

UNIVERSIDAD DE CANTABRIA

PROGRAMA DE DOCTORADO EN INGENIERÍA INDUSTRIAL:
TECNOLOGÍAS DE DISEÑO Y PRODUCCIÓN INDUSTRIAL



TESIS DOCTORAL EN RÉGIMEN DE COTUTELA CON LA UNIVERSIDAD DE SFAX (TÚNEZ)

**Contribución al estudio del comportamiento
dinámico de engranajes planetarios en el estado
no estacionario en la presencia de fallos**

PHD THESIS

**Contribution to the study of the dynamic
behavior of planetary gears in nonstationary
regimes in presence of defects**

Realizada por: AYOUB MBAREK

Dirigida por: PROF. DR. FERNANDO VIADERO RUEDA

PROF. DR. FAKHER CHAARI

Escuela de Doctorado de la Universidad de Cantabria

Santander 2019



Doctoral Thesis

Presented at

National School of Engineers of Sfax

In partial fulfillment of the requirements to obtain

DOCTORAT

in Mechanical Engineering

Presented by

Ayoub MBAREK

Contribution to the study of the dynamic
behaviour of planetary gears in non-
stationary regimes in presence of defects

September 24th - 2019

Dissertation committee:

Pablo García Fernández	Associate Professor, University of Cantabria	President
M. José Antunes	Professor at IST Lisbon -Portugal	Reviewer
M. Fehmi Najjar	Professor at EPT - Tunisia	Reviewer
M. Mohamed Taktak	Associate Professor, FSS, Sfax Tunisia	Member
M. Fakher Chaari	Professor, ENIS, Sfax-Tunisia	Supervisor
M. Fernando Viadero Rueda	Professor, University of Cantabria	Supervisor
M. Alfonso Fernández Del Rincón	Professor, University of Cantabria	Co-Supervisor
M. Mohamed HADDAR	Professor, ENIS, Sfax-Tunisia	Co-Supervisor
M.Ahmed Hammami	Assitant Professor, ENIG, Gabes-Tunisia	Co-Supervisor

Acknowledgments

In the research work, the personal effort must enlist the help of a group that supports individual activity, thus allowing collectively achieved objectives. In this sense, I have been fortunate to have the support of the Laboratory of Mechanics, Modeling and Production, of the National School of Engineers of Sfax-Tunisia and Group of Mechanical Engineering, University of Cantabria-Spain.

I express my sincere gratitude to my directors of this thesis Professor Fagher Chaari and Professor Fernando Viadero Rueda for their guidance and support throughout this research.

I want to express my deep appreciation to each member of this laboratory and this group for their help and support, starting with Professor Mohamed Haddar and Professor Alfonso Fernández Del Rincon.

I am grateful to Professor Ahmed Hammami for his helpful advice. I would like to thank my tutor Professor Pablo García Fernández who created a friendly working atmosphere in the Laboratory of Mechanical Engineering, University of Cantabria-Spain.

I express my gratitude to Professor José Antunes, Professor Fehmi Najar and Professor Pablo García Fernández for accepting to participate in the examination committee of this doctoral thesis.

I want to sincerely my thanks to my family and all my friends for their continuous support and encouragement without which this work would not have been possible.

Abstract

The present PhD study is focused on analyzing the dynamic behavior of planetary gear transmissions in non-stationary conditions in presence of defects. The strategy of this thesis is based on building a numerical model which is referred to a test bench composed of a test planetary gear set mounted back to back with reaction gear set which allow the power recirculation.

First of all, modal analysis techniques were studied to characterize the dynamic behavior of the system. a comparative study between three modal analysis techniques was carried out in order to determine the modal properties in different running condition. Stabilization diagram and Modal assurance criterion were used to estimate the obtained modes. Experimental and numerical modes of each technique were compared and discussed. In addition, the effect of load and meshing stiffness variation on the modal parameters were highlighted.

The study of the dynamic behavior of the model corresponding to the test bench was performed initially in stationary conditions where the speed and the torque are constant. Modulation sidebands are highlighted through numerical simulations issued from a three-dimensional model and experimental measurements. Influence of the gravity of carrier on the dynamic response were also investigated taking into account the interaction between meshing gears, the weight of the planet carrier systems. Then, the dynamic behavior under non-stationary excitations such as the variable load, variable speed and run up regimes was investigated. Time frequency analysis was developed to characterize frequency of vibration signals issued from non-stationary operating conditions. Numerical results obtained by the Short Time Fourier Transform are validated through vibration measurements on test bench during operation under these conditions. However, a non linear model of the model taking into account the Hertzian stiffness was developed and studied in non stationary regime presented by the variable load and run up regime.

Finally, the dynamic response of the system in presence of two kinds of defect was analyzed and discussed in stationary and non stationary regimes. Order tracking method was used to identify the defects in run up and variable loading condition for the simulated and experimental determined signals.

RESUMEN

La presente tesis aborda el análisis del comportamiento dinámico de transmisiones planetarias en condiciones no estacionarias considerando la presencia de defectos. La estrategia adoptada se basa en un doble planteamiento que combina un modelo numérico y su contraste experimental. En relación con el enfoque numérico, se ha desarrollado un modelo de un banco de ensayos de transmisiones planetarias dispuesto en una configuración de recirculación de potencia mecánica. Este mismo banco se ha utilizado para llevar a cabo la campaña experimental.

En una primera fase, se han estudiado diversas técnicas de análisis modal experimental con el fin de caracterizar el comportamiento dinámico del sistema. Se realizó un estudio comparativo entre tres técnicas de análisis modal experimental con el propósito de establecer los parámetros modales del banco de ensayos en distintas condiciones de funcionamiento. Se utilizaron los diagramas de estabilización y el criterio de aseguramiento modal para la estimación de los modos y frecuencia de vibración. Los modos experimentales y numéricos obtenidos empleando cada una de las técnicas han sido evaluados de forma comparativa. Además, se ha resaltado el impacto que tiene la magnitud de la carga a transmitir y sus consecuencias en la rigidez de engrane sobre los parámetros modales.

El estudio del comportamiento dinámico del modelo correspondiente al banco de ensayos se realizó inicialmente en condiciones estacionarias donde la velocidad y el par son constantes. Se han destacado las bandas laterales de modulación mediante simulaciones numéricas obtenidas a partir de un modelo tridimensional y su contraste con los registros experimentales. La influencia de la gravedad del porta-satélites en la respuesta dinámica también se ha investigado teniendo en cuenta la interacción entre la rigidez de engrane y el peso del porta-satélites. Posteriormente, se analizó el comportamiento dinámico bajo excitaciones no estacionarias como carga variable, velocidad variable y maniobras de arranque y parada. El análisis tiempo-frecuencia ha sido utilizado para caracterizar el contenido de frecuencia de las señales de vibración emitidas desde condiciones de operación no estacionarias. Los resultados numéricos obtenidos por la Transformada de Fourier de corto plazo (STFT) se validan mediante mediciones de vibración en el banco de ensayos operando en estas condiciones.

Además, se desarrolló y estudió un modelo no lineal de la transmisión planetaria que tiene en cuenta la rigidez hertziana en regímenes no estacionarios.

Finalmente, la respuesta dinámica del sistema en presencia de dos tipos de defectos fue analizada tanto en régimen estacionario como no estacionario. Para ello, se han utilizado técnicas de seguimiento de órdenes con el fin de identificar la presencia de defectos en maniobras de arranque / parada y con condiciones de carga variables tanto sobre las señales experimentales como simuladas.

Table of contents

List of figures.....	viii
List of tables.....	xi
Nomenclature.....	xii
Abbreviations.....	xiv
Introduction	1
Chapter 1: Literature review:	3
1 Introduction	4
2 Models of PG in literature:	5
2.1 Lumped-parameters models (LPM):	6
2.2 Finite elements models:	7
2.3 Hybrid models:	8
3 Mesh stiffness:	8
4 Mesh Damping:	11
5 Modal parameters:	12
6 Non-stationary operating conditions:	13
6.1 The run up:.....	13
6.2 Run-down:	15
6.3 Variable loading regime:	16
6.4 Variable speed:	17
7 Gear defects:	18
7.1 Geometrical defects :	18
7.1.1 Planet position errors :	18
7.1.2 Misalignment errors:	19
7.1.3 Eccentricity:	19
7.2 Teeth errors :.....	21
7.2.1 Tooth profile errors:	21
7.2.2 Pittings:	22
7.2.3 Crack:	23
7.2.4 Tooth breakage:	23
8 Vibration signals processing:.....	24
8.1 Statical analysis of the signals:	25
8.2 Time domain descriptions:	26
8.2.1 The root mean square:.....	26
8.2.2 The crest factor:	26
8.2.3 Kurtosis:	26
8.3 Time Synchronous Averaging (TSA):.....	27
8.4 Frequency domain descriptors:.....	27
8.4.1 Fourier transforms:.....	27
8.4.2 Capon Method:.....	28
8.5 Cepstrum analysis:.....	28
8.6 Joint Time-frequency representations: Wigner-Ville transform.....	29
9 Gears fault detection techniques in non-stationary operation:	30
9.1 Short-Time Fourier Transform (STFT):	30

9.2	Wavelet decomposition:	30
9.3	Empirical mode decomposition (EMD)	31
9.4	Hilbert transforms:.....	32
10	Experimental test benches	33
11	Summary of literature review:.....	34
Chapter 2: Description of the test bench and the numerical model		37
1	Introduction	39
2	Test bench description:	39
3	External load:.....	41
3.1	Driving system:.....	41
3.2	Vibration response measurements and signal processing:	43
3.3	Strain gauge:.....	44
3.4	Tachometer and strip band:	45
3.5	Slip ring:	46
3.6	Acquisition system:	46
4	Analytical lumped-parameter model (LPM)	47
4.1	Description of the model	47
4.2	Modal analysis	52
4.3	Classification of modes:	53
4.4	Modal analysis taking into account the gyroscopic effect.....	54
5	Resolution method:.....	55
6	Modal parameter estimation:	57
7	Stabilization diagram:.....	58
8	Conclusion	60
Chapter 3: Modal analysis techniques:		62
1	Introduction:	64
2	Experimental modal analysis.....	64
2.1	Impacts hammer excitation:.....	64
2.2	Vibration measurement:	65
2.3	Frequency response function (FRF):	66
2.4	Natural frequencies damping and modes:	67
2.5	Modal assurance criterion:.....	68
2.6	Mode shapes:	69
3	Influence of meshing stiffness variation on the modal parameter:.....	71
4	Operational modal analysis:	74
4.1	Experimental setup:	74
4.2	Power spectral density function:.....	75
4.3	Natural frequencies and damping identification:.....	76
5	Order based modal analysis:.....	77
5.1	Experimental setup:	77
5.2	Order tracking:.....	78
5.3	Natural frequency, damping and mode:	80
6	Comparison between different modal analyses:	81
7	Modal proprieties sensitivity to load variation using OBMA	83
7.1	Experimental set up:	83
7.2	Effect of load on the dynamic behavior:	84

7.3	Order functions:	89
7.4	Natural frequencies and modal damping sensitivity to the load:.....	92
8	Conclusion:	94

Chapter 4: Dynamic behavior of planetary gear in Stationnary and non-Stationnary conditions:96

1	Introduction	98
2	Stationary regime:.....	98
3	Effect of gravity of carrier on the dynamic behavior of PGs	105
4	Run up regime:	107
5	Variable loading regime	110
6	Variable speed regime	114
7	Conclusion:.....	117

Chapter 5: Non-linear model of planetary gear:.....119

1	Introduction	121
2	Non linear model:	121
2.1	Modelling of gear mesh-stiffness:	121
2.1.1	Bending deflection	121
2.1.2	Fillet foundation deflection.....	122
2.1.3	Contact deflection:	123
2.2	Non linear numerical model:	124
2.2.1	Electric motor modelling:	127
2.2.2	Resolution of the equation of motion:.....	127
2.2.3	Relationship between the non linearity and the non stationary regime	130
3	Influence of combined non linear hertzian contact and non stationary conditions on the dynamic behavior:	130
3.1	Run-up condition:	130
3.2	Variable load regime:	135
4	Conclusion:.....	139

Chapter 6: Dynamic behavior in presence of defect in non-stationary condition:140

1	Introduction:	142
2	Stationary conditions:	142
2.1	Case of spalling defect on the planet:.....	142
2.2	Influence of load on the dynamic response:	147
2.3	Case of combined spalling defect on the planet and crack defect on the sun:	149
3	Non stationary conditions: run up regime:	154
3.1	Case of spalling defect on the planet:.....	154
3.2	Case of combined spalling defect on the planet and crack defect on the sun:	158
4	Conclusion.....	162

Conclusions:.....163

Conclusiones:.....167

Scientific Publications.....172

References:.....173

List of Figures

Figure 1. 1. Dynamics modeling of a planetary gear set (X. Liang et al 2015).....	7
Figure 1. 2. Model of the helical gear : (a) Solid model and (b) finite element mesh (Lin et al., 2016).	8
Figure 1. 3. Evolution of the mesh stiffness $k_{12}(t)$	9
Figure 1. 4. Gear mesh stiffness for the healthy case (Chaari et al., 2009).....	10
Figure 1. 5. Variation of the viscous damping ratio ζ as a function of mesh position (Li and Kahraman, 2011)	11
Figure 1. 6. Evolution of mesh stiffness sun-planets during run up (Hammami et al, 2015).....	14
Figure 1. 7. Meshing stiffness during the run-up (Viadero et al., 2014)	14
Figure 1. 8. Time–frequency analysis during the run-up regime. (Villa et al., 2012)	15
Figure 1. 9. Acceleration measured during run down (Hammami et al., 2015)	16
Figure 1. 10. Load applied to the carrier (Chaari et al, 2013)	16
Figure 1. 12. Time response of acceleration in case of variable loading condition (Chaari et al., 2012).....	17
Figure 1. 13. Conditions of the wind turbine (Zimroz et al, 2011)	17
Figure 1. 14. Gear defects classification (Chaari et al, 2011)	18
Figure 1. 15. Meshing stiffness evolution in presence tangential position error sp-0 sun/planets without errors: sp1,2,3,4 with error (GU and Velez, 2012),.....	19
Figure 1. 16. Contact teeth with misalignment error on the plane of action(Shuting Li, 2015).....	19
Figure 1. 17. Schematic presentation of the eccentricity on a PG system.....	20
Figure 1. 18. Schematic presentation of the eccentricity on the sun gear (Chaari et al., 2005).....	20
Figure 1. 19. Influence of a profile error on the dynamic component of the carrier (a) Healthy case. (b) 20 μm of error . (c) 200 μm of error, (Chaari et al., 2005)	22
Figure 1. 20. Photo of pitting (Liang et al, 2016).....	22
Figure 1. 21. Evolution of mesh stiffness in presence of a crack analytical vs. FE(Chaari et al., 2009).....	23
Figure 1. 22. Gear mesh stiffness evolution with different breakage width. (Chaari et al. 2009)	24
Figure 1. 23. Classification of signals (Randall, 2011)	25
Figure 1. 24. Spectrum and cepstrum (Randall, 1977).....	29
Figure 1. 25. Wigner Ville transforms (Elbadaoui 1999).....	30
Figure 1. 26. Complex Morlet wavelet with different bandwidth parameters (Saxena et al.,2005).....	31
Figure 1. 27. Schematic view (a) real view (b) of the PG test rig (Boguski 2010)	33
Figure 1. 28. View of the "back to back" train test bench (Ligata., 2007)	34
Figure 2. 1. Experimental test bench: (a) General view (b) Applied external load with masses (c) Planetary gear (d) Applied external load with jack.....	40
Figure 2. 2. Layout of the test bench and the used instruments	40
Figure 2. 3. Electric cabinet	42
Figure 2. 4. Window of ramp function generator function of “STARTER” software.....	43
Figure 2. 5. Accelerometer location	44
Figure 2. 6. Calibration of Acelerometers.....	44
Figure 2. 7. Strain gauge location	45
Figure 2. 8. Quarter bridge mode of the strain gauge (LMS SCADAS, 2009)	45
Figure 2. 9. Encoder zebra and tachometer.....	45
Figure 2. 10. Slip ring mounted on the shaft of suns.....	46
Figure 2. 11. PG numerical model	48
Figure 2. 12. Variation of natural frequencies with rotational speed	55
Figure 2. 13. Newmark algorithm	57
Figure 2. 14. Stabilization diagram	60
Figure 3. 1. Impact hammer location	64
Figure 3. 2. (a) Coherence function (b) force window of the hammer.....	65
Figure 3. 3. Accelerometers mounted (a) on the ring gear (b) on the sun and planets of the test ring	65
Figure 3. 4. Layout of the instruments (a) on the ring (b) on the sun.....	66
Figure 3. 5. FRF measured on the: (a) Carrier (b) Planet 1(c) Ring (d) Sun	67
Figure 3. 6. MAC matrices from the mode shapes of the experimental and numerical modes.....	69
Figure 3. 7. Mesh stiffness function (a) Sun-planet (b) Ring-planet.....	71
Figure 3. 8. Waterfall plot of FRF on the test ring (a) Numerical (b) Experimental.....	74
Figure 3. 9. Cross power function determined on the fixed ring (a) Experimental (b) Numerical.....	76
Figure 3. 10. Evolution of rotational speed	79

Figure 3. 11. Order map	80
Figure 3. 12. Order function (a) Order 1 (b) Order 2	80
Figure 3. 13. Mesh stiffness function for the ring- planets (a) and sun-planets (b) on the test gear set during run up.....	84
Figure 3. 14. Experimental time response measured on the fixed ring (a) 200 N-m (b) 400 N-m (c) 600 N-m (d) 800 N-m	85
Figure 3. 15. Numerical time response simulated on the fixed ring (a) 200 N-m (b) 400 N-m (c) 600 N-m (d) 800 N-m	86
Figure 3. 16. Strain gauge signal: red: 200 N-m, green: 400 N-m, blue: 600 N-m, pink: 800 N-m.....	87
Figure 3. 17. Experimental STFT on the fixed ring (a) 200 N-m (b) 400 N-m (c) 600 N-m (d) 800 N-m	88
Figure 3. 18. Numerical STFT on the fixed ring (a) 200 N-m (b) 400 N-m (c) 600 N-m (d) 800 N-m	89
Figure 3. 19. Order map (a) experimental (b) numerical.....	90
Figure 3. 20. Experimental order function measured on the fixed ring (a) 200 N-m (b) 400 N-m (c) 600 N-m (d) 800 N-m	91
Figure 3. 21. Numerical order function simulated on the fixed ring (a) 200 N-m (b) 400 N-m (c) 600 N-m (d) 800 N-m	92
Figure 3. 22. Influence of load on (a) experimental natural frequencies (b) frequency error (c) damping ratio.....	93
Figure 4. 1. Evolution of mesh stiffness on test gear : (a) ring-planet 1 (b) ring-planet 2 (c) ring-planet 3.....	100
Figure 4. 2. Influence of the position of planets on the accelerometer (Hammami. 2015)	101
Figure 4. 3. Force due to rotation of carrier on the test ring.....	102
Figure 4. 4. Time response on the fixed ring (a) Experimental (b) Numerical	102
Figure 4. 5. Spectra of acceleration on the fixed ring (a) Experimental (b) Numerical	103
Figure 4. 6. Zoom of the spectra of acceleration on the fixed ring: (a) Experimental (b) Numerical	104
Figure 4. 7. Ring-planet mesh stiffness.....	105
Figure 4. 8. Spectra of acceleration on the test ring: (a) Numerical (b) Experimental.....	106
Figure 4. 9. Response spectrum of the test ring on the first harmonic of the mesh stiffness: Numerical (a) and experimental (b)	107
Figure 4. 10. Evolution of the rotational speed in case of run up.....	108
Figure 4. 11. Gear mesh stiffness function evolution during run-up regime: (a) ring-planet (b) sun-planet.....	108
Figure 4. 12. Time response of acceleration on the ring (a) measured (b) simulated.....	109
Figure 4. 13. STFT on the fixed ring (a) experimental and (b) numerical	110
Figure 4. 14. External applied load	111
Figure 4. 15. Ring-planet 1 mesh stiffness	112
Figure 4. 16. Time evolution of the acceleration on the fixed ring (a) Experimental (b) Numerical	113
Figure 4. 17. Spectra of acceleration on the fixed ring (a) Experimental (b) Numerical	114
Figure 4. 18. Evolution of rotational speed in case of variable speed.....	115
Figure 4. 19. Time response measured on the fixed ring (a) Experimental (b) Numerical	116
Figure 4. 20. STFT of the acceleration on the test ring (a) Experimental (b) Simulated.	117
Figure 5. 1. Modelling of the spur gear tooth.....	122
Figure 5. 2. Geometrical parameters for the fillet foundation deflection	123
Figure 5. 3. PG torsional model	124
Figure 5. 4. Resolution algorithm (Newmark and Newton-Raphson).....	128
Figure 5. 5. Rotational speed evolution of electrical motor	130
Figure 5. 6. Mechanical characteristics of the driving and driven system.	131
Figure 5. 7. Accelerations measured on the test ring: (a) Numerical (b) Experimental	132
Figure 5. 8. Mesh stiffness evolution, (a) Ring-planet 1(b) sun-planet 1	133
Figure 5. 10. Ring-planet 1 meshing force evolution.....	134
Figure 5. 11. STFT of the acceleration of the ring: (a) Numerical (b) Experimental.....	135
Figure 5. 12. External applied load	136
Figure 5. 13. Ring-Planet 1 meshing stiffness.....	136
Figure 5. 14. Hertzian stiffness between the Ring and Planet 1	137
Figure 5. 15. Transmission error between test ring and planet 1.....	138
Figure 5. 16. Dynamic force between test ring and planet 1	138
Figure 6. 1. Spalling defect located on the planet gear	142
Figure 6. 2. Ring-planet 1 gear mesh stiffness trend in case of combined defect	143
Figure 6. 3. Time response of the acceleration measured on the angular direction (Θ) of the test ring (a) simulated (b) experimental.....	144
Figure 6. 4. Simulated spectra of the acceleration measured on the angular direction (Θ) of the test ring	145
Figure 6. 5. Experimental spectra of the acceleration measured on the angular direction (Θ) of the test ring.....	146

Figure 6. 6. Time response of acceleration on the test ring (a) measured (b) simulated	147
Figure 6. 7. Spectra of acceleration on the test ring (a) measured (b) simulated	148
Figure 6. 8. Crack defect located on the test sun.....	149
Figure 6. 9. Sun-Planet 1 gear mesh stiffness trend in case of combined defect.....	150
Figure 6. 10. Time response of the acceleration measured on the angular direction (θ) of the test ring (a) simulated (b) experimental.....	151
Figure 6. 11. Simulated spectra of the acceleration on the angular direction (Θ) of the test ring	152
Figure 6. 12. Experimental spectra of the acceleration measured on the angular direction (Θ) of the test ring.....	153
Figure 6. 13. Input rotational speed.....	154
Figure 6. 14. Sun-planet 1 mesh stiffness evolution in presence of spalling defect.....	155
Figure 6. 15. Time response of the acceleration measured on the angular direction (θ) of the test ring (a) Experimental (b) Simulated	156
Figure 6. 16. Order map of the acceleration simulated on the test ring.....	157
Figure 6. 17. Zoom around the first ten order of the acceleration measured on the test ring	158
Figure 6. 18. Sun-planet 1 mesh stiffness evolution in presence of combined spalling and crack defects	159
Figure 6. 19. Time response of the acceleration measured on the angular direction (θ) of the test ring (a) simulated (b) experimental.....	160
Figure 6. 20. Order map of the acceleration on the test ring (a) Experimental (b) Numerical	161
Figure 6. 21. Zoom around the first ten order of the acceleration measured on the test ring	161

List of Tables

Table 1. 1. The limits of the existing works.	35
Table 2. 1. Planetary gear basic dimensions	41
Table 2. 2. External torque required in order to achieve the failure	41
Table 2. 3. Motor characteristics	41
Table 2. 4. Characteristics of the frequency inverter.....	42
Table 2. 5. Accelerometers characterization	43
Table 2. 6. PG and shafts parameters.	52
Table 2. 7. Natural frequencies and Vibration modes.	53
Table 3. 1. Modal properties obtained for the static testing.	68
Table 3. 2. Comparison between numerical and experimental mode shapes.	70
Table 3. 3. Modal parameters estimated during OMA.	77
Table 3. 4. Principal order.....	79
Table 3. 5. Modal properties during the run-up test.	81
Table 3. 6. Estimated modal parameters for the three techniques.	82
Table 3. 7. Difference between the results of EMA with respect to the OBMA test.	82
Table 4. 1. PG classification (Inalpolat and Kahraman, 2009).....	99
Table 5. 1. Components of the tooth deflection	127

Nomenclature

Symbol	Meaning
r	Ring
c	Carrier
s	Sun
$P1$	Planet 1
$P2$	Planet 2
K_{rp}	Ring-planet mesh stiffness
K_{sp}	Sun-planet mesh stiffness
k_{cf}	Carrier 's shaft flexural stiffness
k_{sf}	Sun 's shaft flexural stiffness
k_{ct}	Carrier 's shaft torsional stiffness
k_{st}	Sun 's shaft torsional stiffness
k_{ca}	Carrier 's shaft axial stiffness
k_{sa}	Sun 's shaft axial stiffness
ψ_r	Ring-planet pressure angle
ψ_s	Sun-planet pressure angle
m_{ij}	Masses of component i of gear j
I_{ij}	Inertia of component i of gear j
α_m	The operating pressure angle
F	The applied force
s_h	Shear factor
G	Shear modulus
I_i	The inertia
A_i	Area moment
S_i	The tooth cross section
ν	The Poisson ratio
E	The Young modulus
W	Tooth width
S_b	The slip at breakdown
T_b	the torque at breakdown,
$a1$ and $b1$	Constant properties of the motor
f_s	The sun shaft rotational frequency,
Z_s	Teeth number of the sun
Z_r	Teeth number of the ring
s	The proportional drop in the speed
f_{dp}	Frequency of defect of the planet
f_{ds}	Frequency of defect of the sun
T_c	Period of rotation of carrier
w_i	Natural pulsations
φ_i	Vibrations modes
q	Degree of freedom vector
M	Global mass matrix
K_b	Bearing stiffness matrix
$K_e(t)$	Time varying mesh stiffness matrix
K_c	Coupled matrix

C	Damping matrix
$F(t)$	External force
Ψ_r	Ring-planet pressure angle
Ψ_s	Sun-planet pressure angle
α_i	Planet i angular position
α_s	The sun pressure angle
α_r	The ring pressure angle
R_{br}	The rings base radius
R_{bs}	The suns base radius
R_{bp}	The planets base radius
m_{ij}	Masses of component i of gear j
I_{ij}	Inertia of component i of gear j
k_{ijk}	Bearing stiffness of component i of gear j in k direction
f_s	Sampling frequency
Subscripts	
$i=r,c,s,p1,p2,p3$	Ring, carrier, sun, planet1, planet2 and planet3
$j= r,t$	Reaction gear and test gear
$k= u,v,w,\phi,\Psi,\theta$	Denotes axis direction

Abbreviations

(CCF)	Cross Correlation Function
(CPSD)	Cross Power Spectral Density
(DFT)	Discrete Fourier Transform
(EMA)	Experimental Modal Analysis
(LPM)	Lumped Parameter Models
(FEM)	Finite Elements Models
(FFT)	Fast Fourier Transform
(FRF)	Frequency Response Function
(f_m)	Mesh Frequency
(MAC)	Modal Assurance Criterion
(OBMA)	Order Based Modal Analysis
(OMA)	Operational Modal Analysis
(OT)	Order Tracking
(PG)	Planetary Gear
(PSD)	Power Spectral Density
(STFT)	Short Time Fourier Transform

General introduction

Gear reducers are powerful tools for power transmission in various mechanisms including rotating components. Planetary gears, one of the most common types of gearboxes, have the particular feature of transmitting high torque with reduced bulk, lower bearing loads and a relatively low level of vibration and noise. They are used in several fields such as in cars gear transmissions, aircraft engines and wind turbines.

Planetary gears are subjected to various excitations producing vibrations and noise. These excitations can be internal, specific to the actual running of the system, or external, associated with fluctuations in engine torque, load torque and in speed.

Most studies of the dynamic behaviour of planetary gears consider the stationary regime where external forces and velocity are constant over time. In the presence of failures, the vibration diagnosis and related techniques should help to identify the presence of these defects and should not be sensitive to other sources of vibration.

Research objectives

The main objective of this thesis is the study of the dynamic behaviour of planetary gears in the non-stationary regime in the presence of defects. This study will provide a better understanding of their dynamics, especially for vibration analysis during conditional maintenance operations of machines operating in non-stationary regimes.

A model based approach combined with experimental investigation will be adopted to reach this objective. Modal characterization of the transmission will be first achieved. Then, the influence of internal and external excitations on the vibration response of the system will be done. In addition, the behaviour in presence of both non stationary conditions and combined defects will be investigated using advanced signal processing techniques. Correlations between numerical results issued from the developed model and the experimental results will be done for all the developments in this thesis.

Outline of the thesis

The outline of the chapters is given below:

The first chapter in this work is dedicated on a deep bibliographic study on the dynamic behaviour of planetary gear transmissions including the description of the technological

function and the modelling methods. The different techniques to characterize the non stationary conditions and the most frequent defect diagnostics methods are enumerated. Finally, the tools used to detect defects under non stationary regimes are cited.

In the second chapter, the back to back planetary gear test bench and all the equipment used for the measurement and data acquisition of vibration signals such as software and hardware are presented. Also, a numerical model referred to this bench is developed and the equations of motion are derived.

To understand and characterize the dynamic behaviour of the planetary gears, we focus in the third chapter on modal analysis. Three modal analysis techniques which are the experimental modal analysis (EMA), the operational modal analysis (OMA) and the order based modal analysis (OBMA) are presented in order to identify modal parameters such as natural frequencies and damping ratios. These parameters are identified experimentally and compared to others obtained numerically. In addition, the impact of load on modal parameters is investigated using OBMA.

In chapter 4, the dynamic behaviour of the two stages planetary gear system is studied in stationary and non stationary conditions. A three-dimensional model was used to simulate the dynamic behaviour which is compared to that issued from the bench. Frequency characterization of the planetary gear and effect of loading variation on frequency content are studied. In addition, the dynamic behaviour of back-to-back planetary gear is studied in the cases of variable speed, run up and run down regimes.

A theoretical study of the influence of non-linear Hertzian stiffness on the dynamic behaviour of the planetary gear system is investigated in the chapter 5. A general formulation for computing the gear meshing stiffness functions taking into account the Hertzian contact is developed. Also, a torsional lumped parameters model referred to the real system is established. The dynamic response of the system is studied in the cases of run up and variable loading conditions.

In the last chapter, the dynamic behaviour of planetary gearbox system in presence of defects is highlighted. Two kinds of defects which are spalling and crack defects are studied numerically and experimentally in stationary and non stationary conditions. The influence of defects on the vibration response of the system is detailed.

Chapter 1: Literature review

Chapter 1: Literature review

Sommaire

1	Introduction	5
2	Models of PG in literature:	5
2.1	Lumped-parameters models (LPM):	6
2.2	Finite elements models:	7
2.3	Hybrid models:	8
3	Mesh stiffness:	8
4	Mesh Damping:	11
5	Modal parameters:	12
6	Non-stationary operating conditions:	13
6.1	The run up:.....	13
6.2	Run-down:	15
6.3	Variable loading regime:	16
6.4	Variable speed:	17
7	Gear defects:	18
7.1	Geometrical defects :	18
7.1.1	Planet position errors :	18
7.1.2	Misalignment errors:	19
7.1.3	Eccentricity:	19
7.2	Teeth errors :	21
7.2.1	Tooth profile errors:	21
7.2.2	Pittings:	22
7.2.3	Crack:	23
7.2.4	Tooth breakage:	23
8	vibration signals processing:	24
8.1	Statical analysis of the signals:	25
8.2	Time domain descriptions:	26
8.2.1	The root mean square:.....	26
8.2.2	The crest factor:	26
8.2.3	Kurtosis:	26
8.3	Time Synchronous Averaging (TSA):.....	27
8.4	Frequency domain descriptors:.....	27
8.4.1	Fourier transforms:.....	27
8.4.2	Capon Method:.....	28
8.5	Cepstrum analysis:.....	28
8.6	Joint Time-frequency representations: Wigner-Ville transform.....	29
9	Gears fault detection techniques in non-stationary operation:	30
9.1	Short-Time Fourier Transform (STFT):	30
9.2	Wavelet decomposition:	30
9.3	Empirical mode decomposition (EMD)	31
9.4	Hilbert transforms:.....	32
10	Experimental test benches	33
11	Summary of literature review:	34

1 Introduction

Nowadays, gear transmissions are upon the most popular power transmission systems due to their ability to transmit torque and speed, their compactness and their reliability.

A planetary gear (PG) system is like the arrangement of the planets in a solar system. A sun-gear located at the center of the mechanism, is in mesh with several planets orbit around it. The planets are mounted on a carrier which can either be fixed or rotating.

The PG systems allow the transmission of high torque and be used in different speed configurations. It consists of four types of moving components:

- The sun (S): it is an external gear used usually as an input component of the gear train and drives the planets.
- Planets (P): their number varies from 3 to 6. They rotate around their axes and around the sun.
- The carrier (C): includes the axes on which are mounted the planets, it is often the output component of the planetary gear transmission.
- The ring (R): It is an internal gear. It can also be the housing of the whole transmission (fixed ring).

In this chapter, a literature review on the dynamic characterization of PG is presented. The different developed models and the most influencing parameters such as mesh stiffness, mesh damping and modal parameters are detailed. In a second section, the non-stationary conditions in which the PG are widely operating like the variable speed, variable load, run up and run-down regimes are discussed. Different damage cases and defects that can affect these systems are presented and the main techniques for detection and characterization, of non stationary excitations are detailed. In the last section, the powerful techniques and methods for defects detection in non stationary conditions are listed.

2 Models of PG in literature:

To study PG dynamic behaviour, several models has been developed in literature.

The main methodologies used to model gear mechanisms are the lumped parameter models (LPM), the finite elements models (FEM) and the hybrid models which combine the two latter models.

Several PG dynamics models were proposed over the last 30 years. Most of them were LPM dedicated to the prediction of vibration characteristics of PG sets. A great majority of them are

either purely torsional or two-dimensional ones. In a review from 1988, (Ozguven and Houser, 1988) studied mathematical models used in gear dynamics. (August and Kasuba, 1986) developed a torsional model of a planetary gear set. The obtained results indicate that floated suns have a limited interest for high-speed cases. In the work of (Parker and Lin, 2004), a good selection of phase shift between planets has shown to reduce the vibration of the planetary gear. (Kahraman, 2001) developed different torsional models of gear sets and studied the free vibrations proprieties under different kinematic configurations resulting in different speed ratios. (Lin and Parker, 1999) reported a bi-dimensional LPM of PG with equally spaced planets to study its modal proprieties.

Moreover, in the case of helical gears, few studies were devoted to their dynamic behaviour modelling and simulation. Usually three-dimensional LPM are used. We can find the model developed by (Eritenel and Parker, 2009) which is dedicated to the study of modal proprieties. Furthermore, other models consider nonlinearities such as the one presented by (Ambarisha and Parker, 2007). They studied the impact of different parameters like the nonlinear jumps and chaotic motions on dynamic behavior. The obtained results were compared with those obtained from FEM. Most of the cited models were developed and simulated under stationary operations, while other works considered the non-stationary conditions (Hammami et al., 2015; Bartelmus, 2010, Chaari et al., 2013). The gyroscopic effect was considered in modelling (Cooley et al. 2012, Meirovitch, 1974) as well as the carrier gravity. Many works have been established to study the effect of gravity of carrier, (Hammami et al, 2015); (Guo et al., 2012). (Guo and Parker, 2010) showed that gravity will disorder the planets symmetry and can cause tooth wedging under certain conditions. (Qiu and Chu, 2015) developed a lumped parameter model of the spur planetary gear that correlates the effect of gravity; tooth separation, backside contact and bedplate tilt.

2.1 Lumped-parameters models (LPM):

The lumped parameter models are very efficient to describe and characterize the dynamic behavior of the components and systems under certain assumptions. In the case of planetary gear system, the gear components are modeled with mass and inertia whereas the contacts between these components are modeled by rigid spring with high stiffness and damping values. Dynamic modeling of the PG was initiated by (Cunliffe, 1974) who used LPM that allowed studying the vibration response for a PG with fixed carrier.

Figure 1.1 shows a LPM of a PG set (Liang et al. 2015). Each element is considered as rigid body having three degrees of freedom: one rotation and two translations. The meshing stiffness function and the bearing were modeled using spring-damper system, respectively.

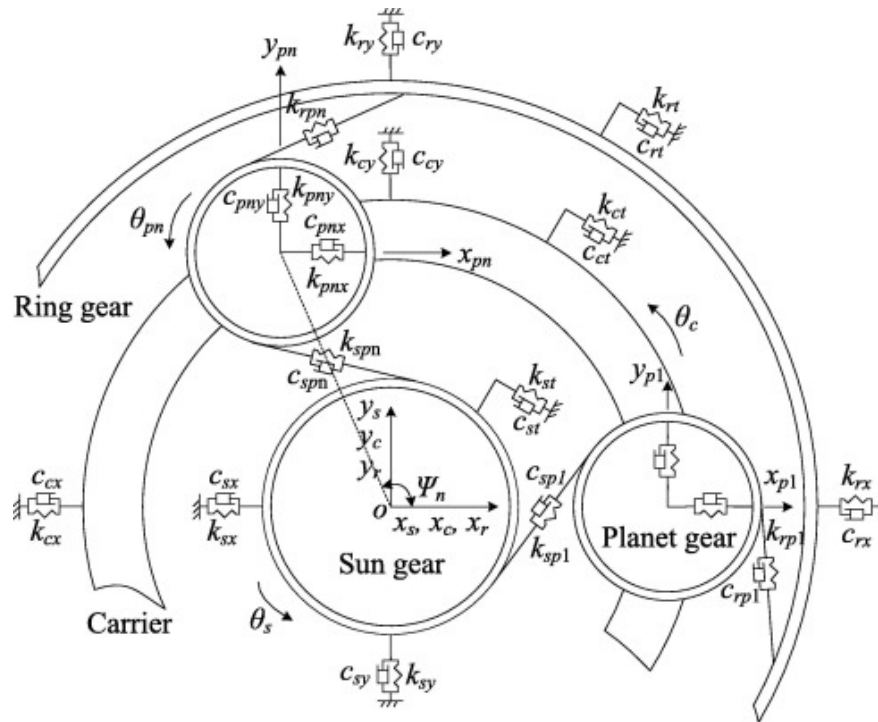


Figure 1. 1. Dynamics modeling of a planetary gear set (X. Liang et al 2015)

2.2 Finite elements models:

The FEM were basically built to overcome lack of accuracy in LPM.

Several parameters like gear tooth deflections, mesh stiffness and stresses were considered so that the complex shape of PG dynamics is better described.

(Guo and Parker, 2012) used FEM of rolling element bearings in order to study the contact behavior between the race and rolling elements. They compared the obtained results to others obtained experimentally (Royston and Basdogan 1998).

(Lin et al., 2016) proposed the FEM to deal with dynamic contact and impact problems of gears. This method is efficient in computation for gear drives in the small contact region involved in teeth meshing.

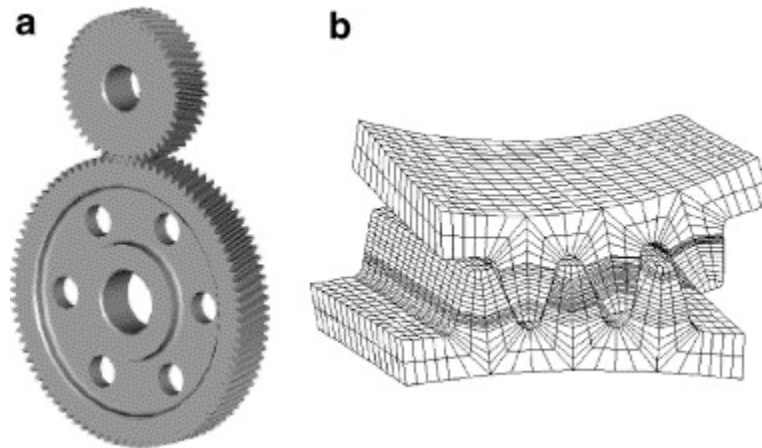


Figure 1. 2. Model of the helical gear : (a) Solid model and (b) finite element mesh (Lin et al., 2016).

2.3 Hybrid models:

A hybrid model is a combination of the two previous models, the contact between teeth is modeled by FEM and the rest of gear body is modeled using LPM. This model shows efficiency when studying planetary and epicyclic trains (Abousleiman and Vex, 2006). Authors claim that ring-gear flexibility modifies static load distributions and critical tooth speeds on internal meshes. The main advantages of these models is their closeness to real object systems, however they need high CPU time.

The presented models are characterized by several influencing function. Mesh stiffness and damping are examples of those functions that will be detailed in the next sections.

3 Mesh stiffness:

Mesh stiffness is one of the main source of excitation in gear systems, this excitation is always present even when the gears are perfectly manufactured and mounted. It depends on many parameters such as the number of teeth in contact, gear face width, the contact ratio, profile modifications, and applied torque.

Computation of stiffness is based generally on the calculation of the tooth deflection as mentioned by (Timoshenko and Baud 1924) and Weber (Weber, 1949). For a given loading position, the equivalent stiffness K_m is the sum of the flexural-shear stiffness K_f and the body of the gear K_v .

$$K_m = 1 / \left(\frac{1}{K_f} + \frac{1}{K_v} \right) \quad (1.1)$$

In the case of a pinion (1) and a wheel (2) in mesh, the equivalent meshing stiffness K_{12} is obtained by summing the stiffness K_1 of the pinion, the stiffness of the wheel K_2 and the contact stiffness (K_h) as following :

$$K_{12} = 1 / \left(\frac{1}{K_1} + \frac{1}{K_2} + \frac{1}{K_h} \right) \quad (1.2)$$

The mesh stiffness calculation depends of the tooth engagement. Velex (Velex, 1988) has shown that it is possible to represent the meshing stiffness as a slot function for the spur gears, the maximum value is observed when two pairs of teeth are engaged (maximum contact length) , the minimum value is for a single pair of teeth in contact (minimum contact length). (Lin and Parker, 2002), (Lin and Parker, 2000a), (Maatar, 1995) approximated this variation using a square wave function (Figure 1.3).

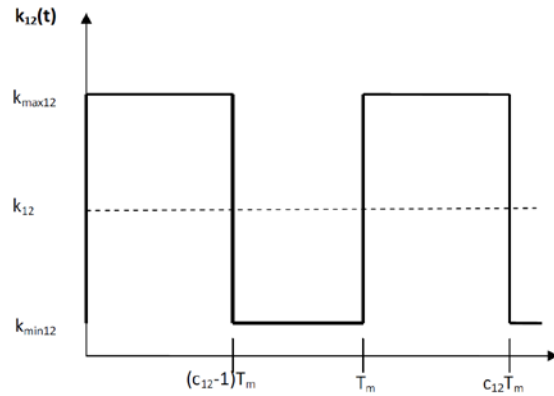


Figure 1. 3. Evolution of the mesh stiffness $k_{12}(t)$

c_{12} is the contact ratio of the transmission. T_m is the meshing period. k_{max12} , k_{min12} and k_{12} represent respectively the values of the maximum, the minimum and the average values of the mesh stiffness.

The Fourier series expansion of $K_{12}(t)$ yields to:

$$k_{12}(t) = k_{12} + \frac{\Delta k}{\pi} \sum_{i=1}^{\infty} \frac{1}{i} \left[\sin \left((2i\pi(c_{12} - 1)) \cos \left(\frac{2i\pi t}{T_m} \right) + (1 - \cos((2i\pi t(c_{12} - 1))) \sin \left(\frac{2i\pi t}{T_m} \right) \right) \right] \quad (1.3)$$

Where :

$$k_{12} = k_{max12}(c_{12}-1) + (2 - c_{12})k_{min12} \quad (1.4)$$

$$\Delta k = k_{max12} - k_{min12} \quad (1.5)$$

The mesh stiffness function is a time varying function, it depend on the number of tooth in contact. The contact periodically changes from one to two.

In Henriot (Henriot, 1985) works, a formula for k_{12} in case of spur teeth is presented. It is expressed in $N / \mu m / m$ where:

$$k_{12} = b / (A_1 + A_2 / Z_1 + A_3 / Z_2) \quad (1.6)$$

With $A_1 = 0.04723$, $A_2 = 0.15551$, $A_3 = 0.25791$ and b is the width of tooth.

(Chaari et al., 2009) developed an analytical approach (eq 1.7) to model the meshing functions; the obtained results were compared to those obtained by FEM.

$$K_i = 1 / \left(\frac{1}{K_{b1}} + \frac{1}{K_{f1}} + \frac{1}{K_{b2}} + \frac{1}{K_{f2}} + \frac{1}{K_h} \right) \quad (1.7)$$

K_{b1}, K_{b2}, K_{f1} and K_{f2} denotes respectively the bending stiffness and the fillet-foundation stiffness of pinion and wheel teeth. K_h is the stiffness of Hertzian contact.

Figure 1.5 displays the gear mesh stiffness computed analytically. During $(c-1) T_e$, the gear mesh stiffness reaches a maximum value but it's minimal during $(2-c) T_e$. “c” and “ T_e ” are respectively the contact ratio and the period of gear meshing.

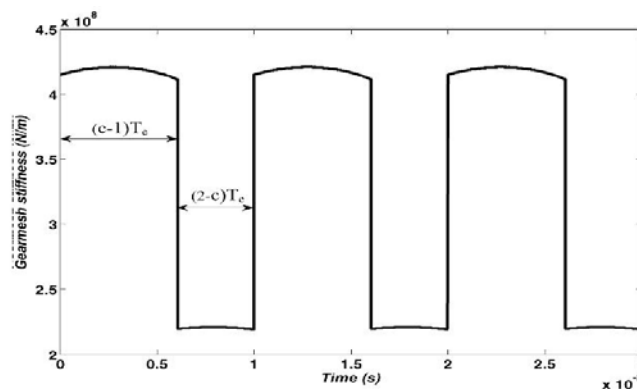


Figure 1. 4. Gear mesh stiffness for the healthy case (Chaari et al., 2009)

(Fernández et al., 2013) used an analytical approach considering the tooth deflection, bending defection and the Hertzian stiffness which is decomposed into local non linear deflection and global linear deflection.

4 Mesh Damping:

For a gear set in a complex mechanical system, the sources of energy dissipation are various. As example, we can cite the mesh damping which has an important effect for resonance vibration. Since the contact between teeth is lubricated, damping is considered viscous. (Li and Kahraman, 2011) showed that the damping is not constant for certain operating conditions and can be considered as a periodic function varying in time with a fundamental frequency equal to the frequency of gear meshing. Also, the damping average increase with the increased torque while it decreases to increasing of the rotation speed and lubricant temperature. In author's analysis of the gear dynamic models; they noticed that the damping value reduces with the increasing of speed, due to the increased film thicknesses. The evolution of damping ratio along the line of action under the same contact conditions are given in Figure 1.6.

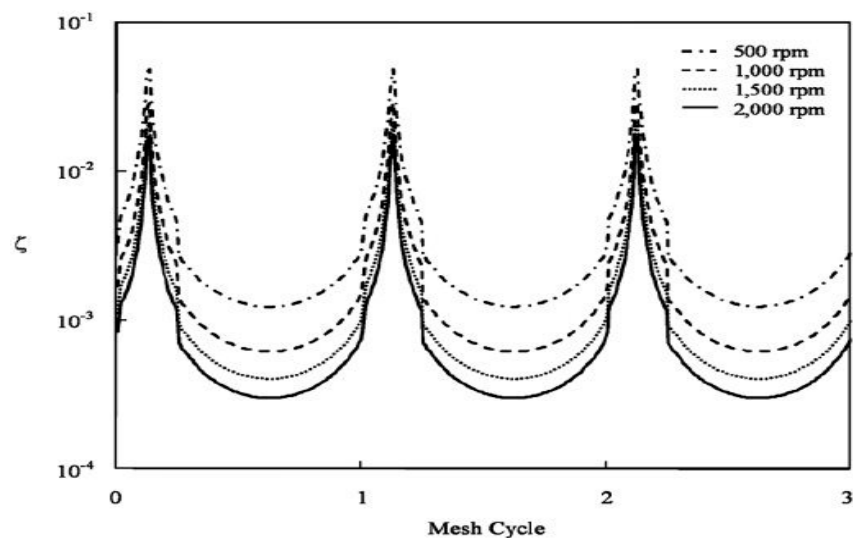


Figure 1. 5. Variation of the viscous damping ratio ζ as a function of mesh position (Li and Kahraman, 2011)

Most other authors introduce an equivalent viscous modal damping, (Al-shyyab and Kahraman, 2007), (Viadero et al., 2014). For models with one or more degrees of freedom, the modal damping coefficient can be written by:

$$c_i = 2m\omega_i\zeta_i \quad (1.8)$$

Another approach was developed by Rayleigh (1877) in which damping is proportional to both mass and stiffness matrices:

$$C = \alpha M + \beta K \quad (1.9)$$

Where α and β are two constants (Dhatt and Touzot, 1981).

5 Modal parameters:

Planetary gears have distinct vibration mode structure because of their cyclic symmetry. Typically, modal parameters are the natural frequencies, the modal damping and the mode shapes. These parameters were first computed for LPM.(Li and Parker, 1999a; Cunliffe et al., 1974; Botman, 1976), and later validated with FEM (Ambarisha and Parker, 2007) and experiments (Ericson and Parker, 2013). (Cunliffe et al., 1974) determined the vibration modes of a 13 DOF planetary gear model. They grouped modes into low frequency “bearing modes” and high frequency “tooth modes,” but did not identify the vibration structure. (Botman, 1976) determined the vibration of a $3N+9$ DOF planetary gear model (N is; the number of planets). When analyzing a gear system with three-planets, he classified the vibration modes and grouped them into two classes named “axisymmetric” and “non axisymmetric” according to the planets’ motion. (Kahraman 1994) found a third mode type when analyzing a planetary gear system with four-planets that wasn’t observed by (Botman, 1976). It was called a “counter-phased mode”. Furthermore, (Wu and Parker, 2010) investigated the modal proprieties of PG with equal planet spacing taking into account the elastic deformation of the ring as well the influence of the unequal planet spacing. (Eritenel and Parker, 2009) investigated the modal properties of three-dimensional helical PG model and they studied also the influence of torque on modal parameter. The obtained results were correlated with others obtained by experiments and FEM. (Bu and Wu, 2012) developed a generalized dynamic model for herringbone PG train in order to investigate its modal properties. Vibration modes of compound PG were studied by (Kiracofe and Parker, 2007) and (Guo and Parker, 2010). (Cooley and Parker, 2012) studied the vibration properties of high-speed planetary gears and they took into account the gyroscopic effects.

What stand out in those works is that the identification of modal parameters vary from one system to another depending on the number degree of freedom. Modal parameters are very important to comprehend and characterize the system. However, gear system are widely operating in non-stationary conditions, so that the identification of modal parameters under these regime could be an interesting research area. Aalso, the influence of these regime on parameter is worth to be investigated.

As mentioned in the previous section, modal parameters are very important in order to define and figure out the complex system.

The most recent trend is achieve modal identifications using the responses of structures in normal operation, when these are excited by unmeasured broadband distributed forces (turbulence, traffic, ...). Such an approach is particularly useful when dealing with large structures, especially in civil engineering (bridges, buildings), where the excitation is difficult. In this regard, recent works by Gentile & Saisi (2007), Zhang et al (2010) and Magalhães et al (2011) can be consulted.

However, for small or medium sized structures, such as those of interest in this report, it is relatively easy to produce measured broadband excitations (most often by impact using an instrumented hammer). It is then possible to directly measure vibratory responses normalized to excitation, in the time domain, in the form of impulse responses, $h_{ij}(t) = h(r_i, r_j, t)$ or in the frequency domain in the form of transfer functions $H_{ij}(\omega) = H(r_i, r_j, t)$, where r_i and r_j are the coordinates of the points excitation and response, respectively.

The gear are widely exploited in different running conditions. For further insight in the dynamic behavior of PG, several non-stationary conditions were treated in literature.

6 Non-stationary operating conditions:

Most of rotating machinery are operating under time varying speed/loading conditions. These non stationary regimes are widely observed in wind turbines, mining machinery, automotive cars and helicopter transmissions. As examples of the non-stationary condition, we can cite the run up and the run down, repetitive run up and run down regimes during operations could be very critical especially when the system is overloaded. Variable speed and the variable loading conditions during steady state regime is considered also as a non-stationary giving rise to amplitude and frequency modulations

6.1 The run up:

The motor torque must always exceed the resistant torque during run-up regime. In case of PG models, this regime affects the mesh stiffness function. (Hammami et al., 2015) and (Khabou et al., 2011) studied the evolution of mesh stiffness during run-up regime, they noticed that the vibration increase when the speed and the accelerating torque increase.

Figure 1.7 illustrates the evolution of meshing stiffness during run up regime.

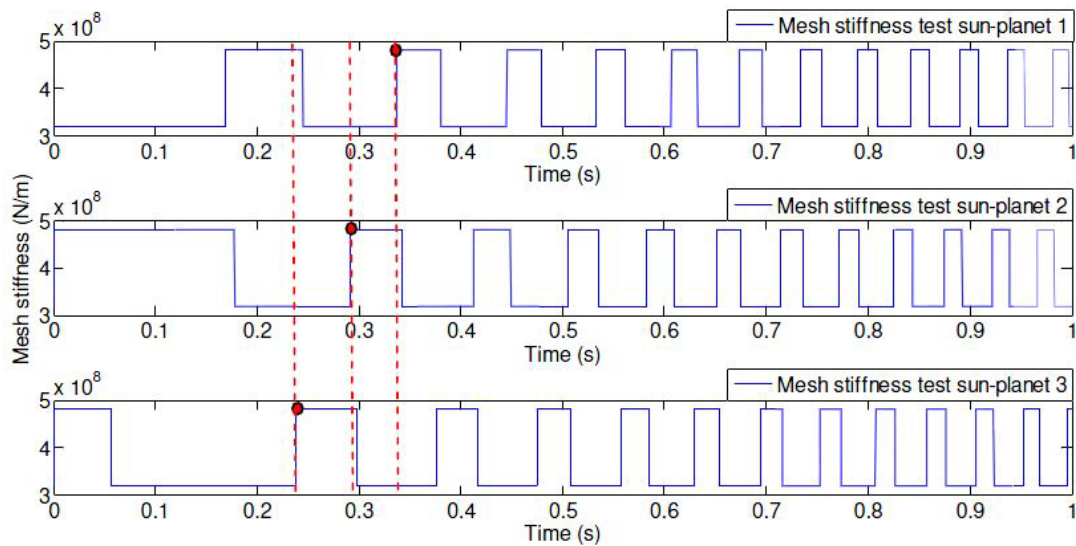


Figure 1. 6. Evolution of mesh stiffness sun-planets during run up (Hammami et al, 2015)

The mesh stiffness evolution was studied also by (Viadero et al., 2014); they modelled the meshing stiffness during run-up considering mesh function shapes as a sinusoidal function, (Figure.1.8).

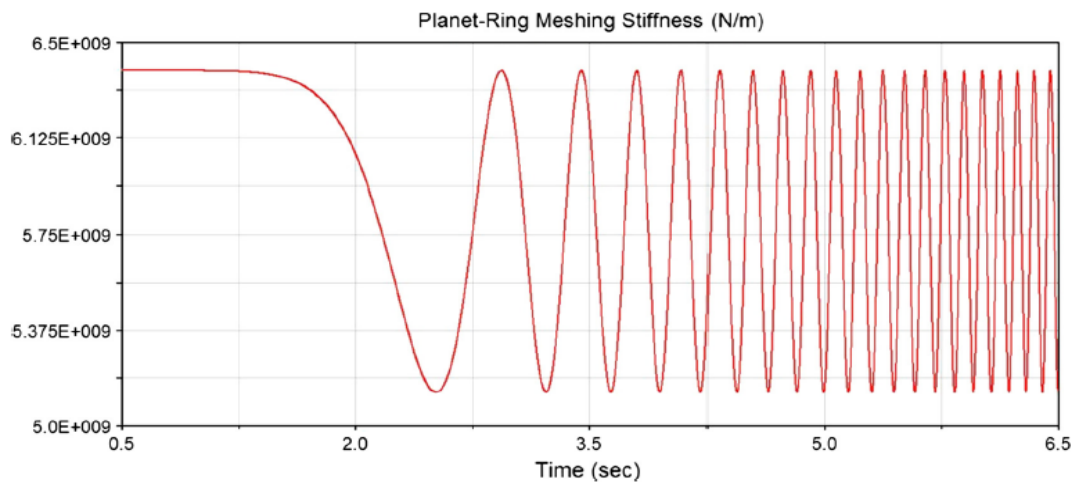


Figure 1. 7. Meshing stiffness during the run-up (Viadero et al., 2014)

Furthermore, in the run-up and by using the time-frequency analysis, (Villa et al., 2012) identified the gear mesh frequency and the characteristic natural frequencies of the gear system. The vibration is increasing in time due to the increasing of speed, (figure 1. 9).

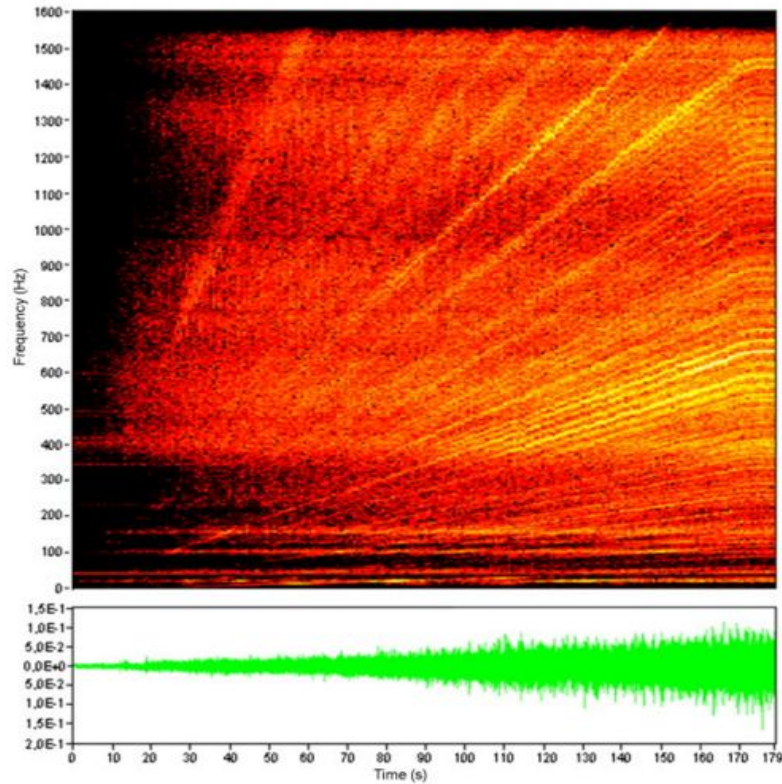


Figure 1. 8. Time–frequency analysis during the run-up regime. (Villa et al., 2012)

6.2 Run-down:

During the run down regime, the period of meshing increases as the speed decrease. The vibration reaches a maximum value and it is over closely to zero. This regime was studied by many authors, such as (Hammami et al., 2015) by investigating the behavior of back to back PG. The obtained experimental results were correlated to others obtained numerically. Figure 1.10 displays the evolution of the acceleration during the run-down regime.

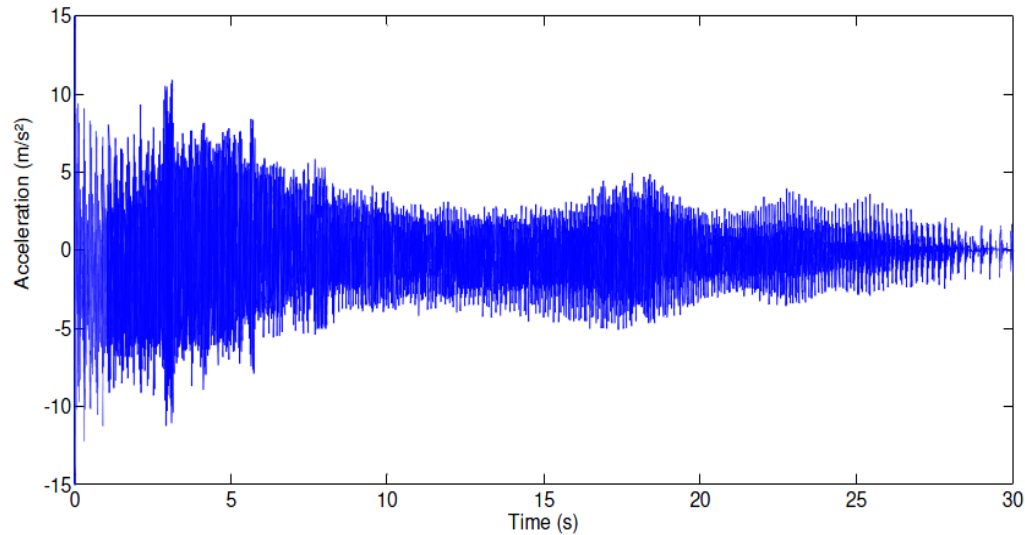


Figure 1. 9. Acceleration measured during run down (Hammami et al., 2015)

6.3 Variable loading regime:

Many researchers have noticed that several machines incorporating PG transmissions like mining machines and wind turbines are subjected to variable loading conditions. The load influences on the mesh stiffness function. When the load increases the contact between teeth increase so the mean mesh stiffness increase(Fernandez et al .2013).

(Chaari et al., 2013) developed a single stage planetary gear model under variable loading conditions applied on carrier giving rise to variability in speed and mesh stiffness function (Figure 1.11).

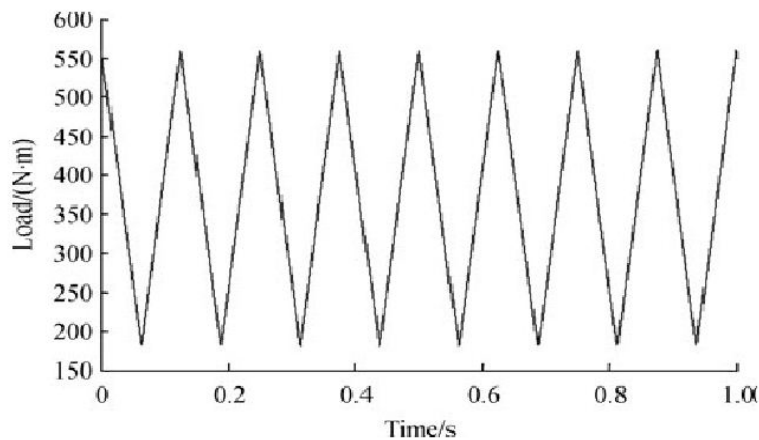


Figure 1. 10. Load applied to the carrier (Chaari et al, 2013)

The recorded time response signal confirmed the presence of amplitude and frequency modulation as mentioned in Bartelmus works (Bartelmus 2001; Bartelmus 1992). Figure 1. 11 shows the acceleration simulated on the sun gear.

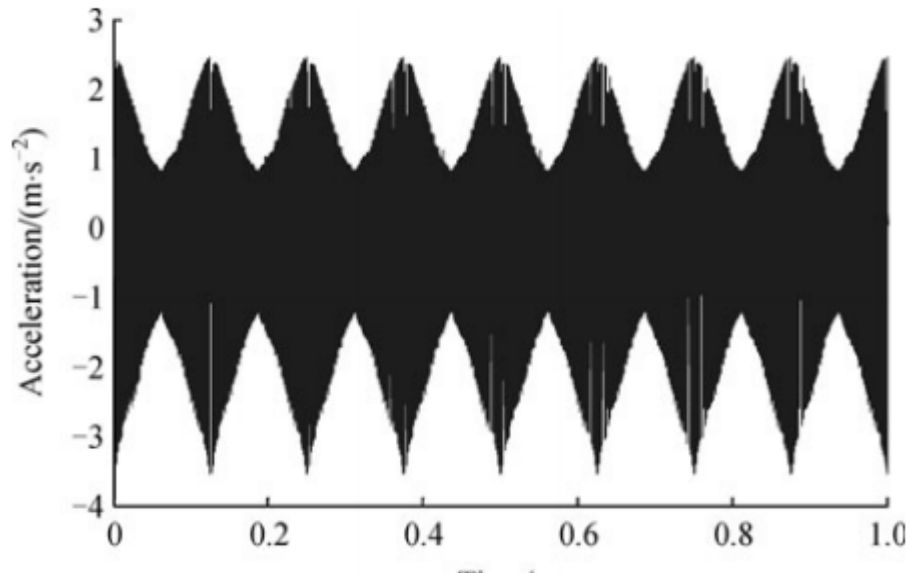


Figure 1. 12. Time response of acceleration in case of variable loading condition (Chaari et al., 2012)

Different load shapes were studied in literature such as cyclic load (Bartelmus et al, 2010), harmonic load (Chaari et al., 2012), and also some special load shapes (Hammami et al., 2016).

6.4 Variable speed:

Gear systems are widely subjected to speed fluctuation. . In the case of a wind turbine for example, the speed is changing very quickly so that the generated power will fluctuate in consequence, therefore, (Zimroz et al, 2011) investigated its influence on the diagnosis feature.

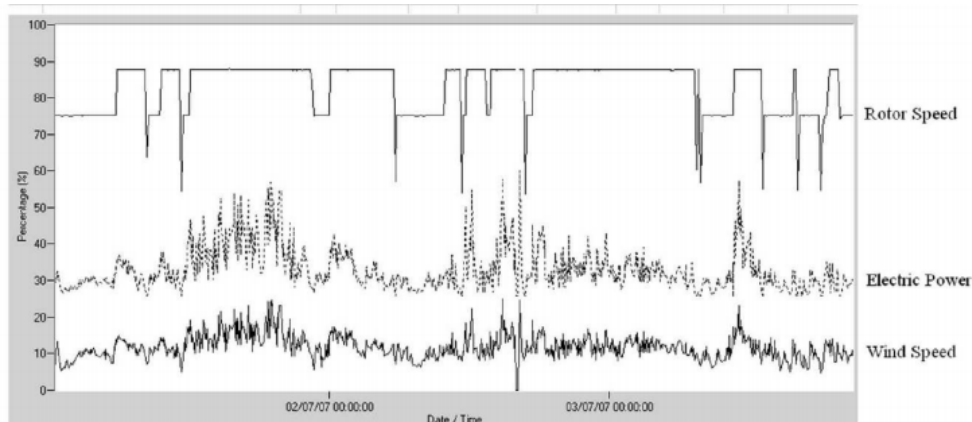


Figure 1. 13. Conditions of the wind turbine (Zimroz et al, 2011)

The non stationary regimes are the main external source of excitation that could be a major source of development of defect. Gear defects will be treated in the next section.

7 Gear defects:

PG are widely used in various power transmission applications because of their characteristics like high load capacity, but they can be affected by several defects reducing their performance and giving rise to undesirable noise and vibration.

Different types of defect like mounting defects, manufacturing defects can appear in these systems. (Chaari et al., 2011) classified gear defects (Figure 1.14) into geometrical defects and tooth defects.

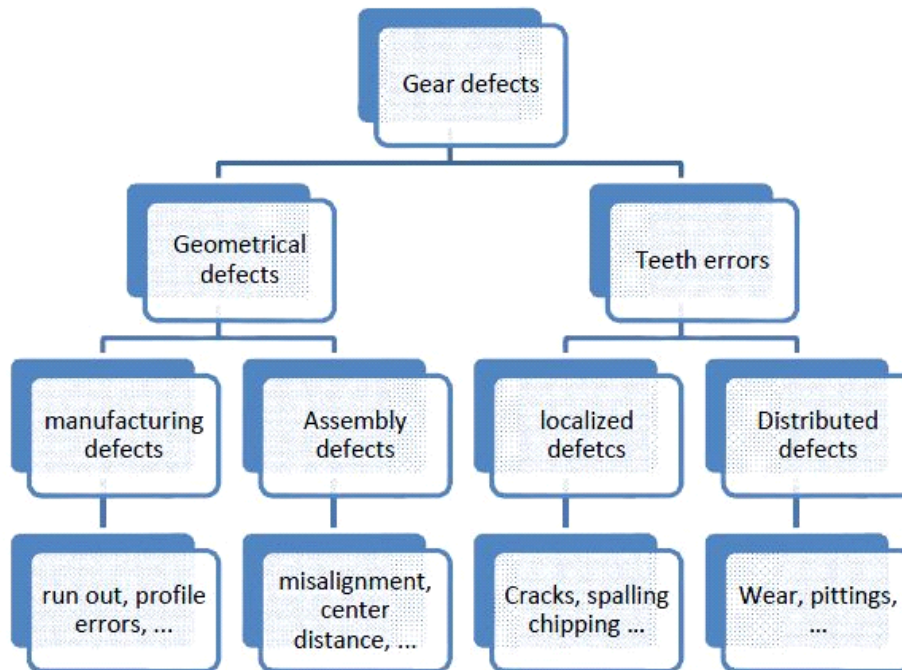


Figure 1. 14. Gear defects classification (Chaari et al, 2011)

7.1 Geometrical defects :

7.1.1 Planet position errors :

In PG systems, planet position error is defined as an error in the location of the planet centers. The error can be decomposed into radial error and tangential position error. The radial error can slightly modify distances between centers, pressure angles whereas the tangential errors strongly modify planet load sharing. In the work of (GU and Vex, 2012), the influence of position error was introduced in mesh stiffness of helical PG as perturbation by adding a radial and tangential position error on the coordinates of the planets components. Figure 1.15 shows the influence of

planet position errors on sun-planet mesh function. it is noticeable that the planet position errors causes an amplification on the tooth load which affect the dynamic behavior.

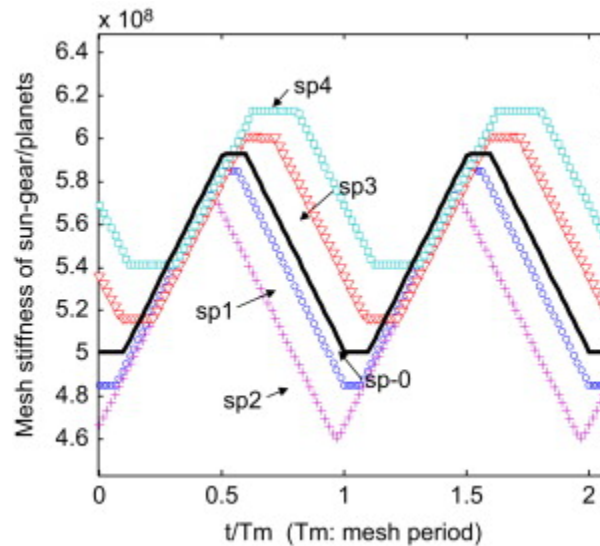


Figure 1. 15. Meshing stiffness evolution in presence tangential position error sp-0 sun/planets without errors: sp1,2,3,4 with error (GU and Velez, 2012),

7.1.2 Misalignment errors:

For single pinion-gear pair, misalignments are three-dimensional error distributions that can be separated into deviation and inclination.

(Shuting Li, 2015) studied the misalignments error in pinion-wheel gear system. .

The misalignment error of the gear shafts can be expressed by an inclination angle of the contact teeth on the plane of action as shown in Figure1.16.

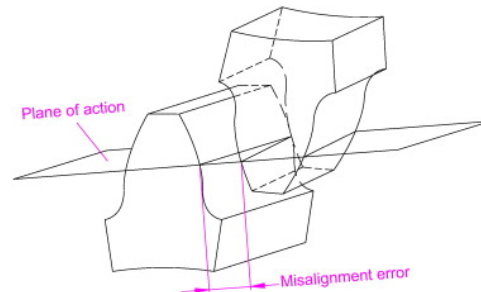


Figure 1. 16. Contact teeth with misalignment error on the plane of action(Shuting Li, 2015)

7.1.3 Eccentricity:

The eccentricity error expresses the difference between the theoretical and the real rotational axis (Figure 1.17). The modelling of this defect was done by adding a transmission error modelled as displacement on the line of action as studied by (Gu and Velez 2013).

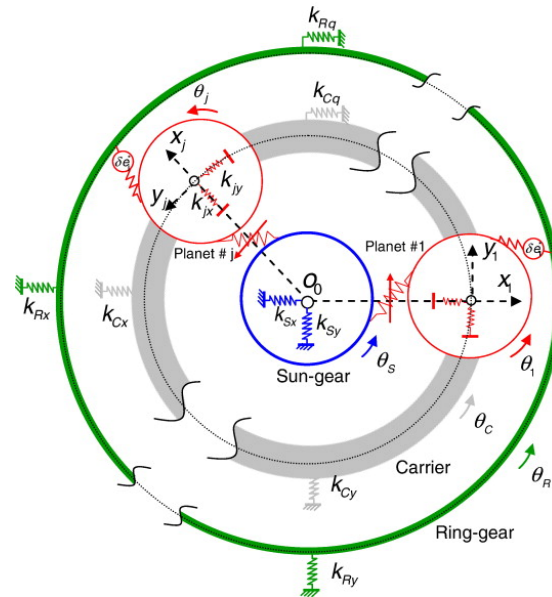


Figure 1. 17. Schematic presentation of the eccentricity on a PG system

This displacement can be introduced in the equation of motion as an exciting force $F(t)$, which represents an amplitude modulation of the gear mesh stiffness by the eccentricity error.

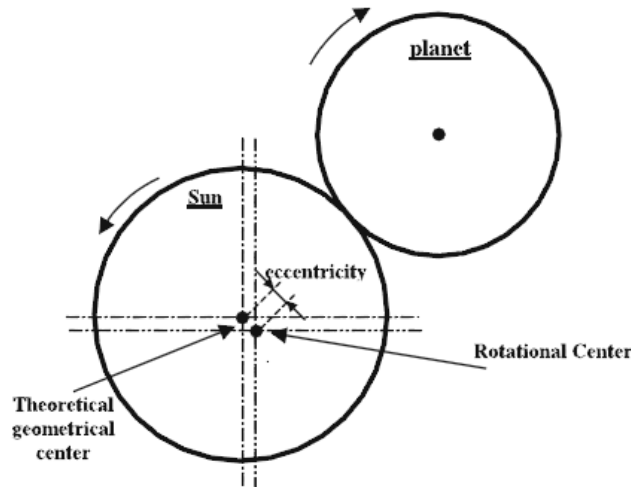


Figure 1. 18. Schematic presentation of the eccentricity on the sun gear (Chaari et al., 2005)

It is expressed as follows (Chaari et al., 2005):

$$F(t) = e_{sn}(t)K_e(t) \quad (1.10)$$

$$e_{sn}(t) = \bar{e}_s \sin\left(\frac{2\pi f_e}{Z_s} t + \xi_{sn}\right) \quad (1.11)$$

where $K_e(t)$ is the time varying mesh stiffness function, \bar{e}_s denotes the eccentricity modulus, Z_s is the tooth number of the sun, and ξ_{sn} is the mesh phasing difference between the sun and planets. This fault usually found in sun or planets. (GU and Vex, 2013) investigated eccentricity errors

modeled in a LPM of a PG in which deflections, errors and gear geometry are detailed and summarized in a differential set of equation. In the presence of errors, rigid-body positions and motions were perturbed giving rise to initial separations between tooth flanks and inertial excitations.

7.2 Teeth errors :

7.2.1 Tooth profile errors:

Tooth profile error is the summation of the deviations measured perpendicular to the actual profile between the actual tooth profile and the correct involutes curve which passes through the pitch point.

These types of defects can be modelled with an exciting force $F(t)$ that represents an amplitude modulation of the gear mesh stiffness signal by the profile error signal $E_{sn}(t)$ (Chaari et al., 2005).

$$F(t) = E_{sn}(t)K_e(t) \quad (1.12)$$

$$e_{sn}(t) = \sum_{m=1}^{\infty} \bar{E}_{sm} \sin(2\pi f_e m t + \xi_{sn}) \quad (1.13)$$

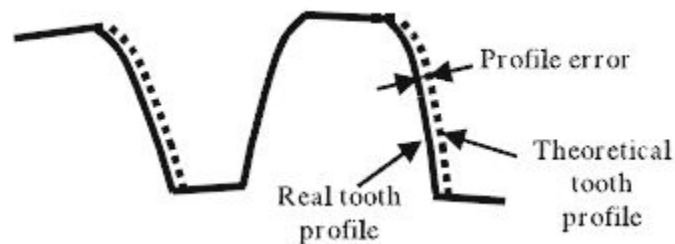


Figure 1. 19. Schematic diagram of a profile error (Chaari et al., 2005)

Figure 1.20 shows the influence of profile errors on the carrier bearing. With the increasing of profile error, the amplitude of mesh frequency (f_e) increase due to the modulation effect issued from profile error .

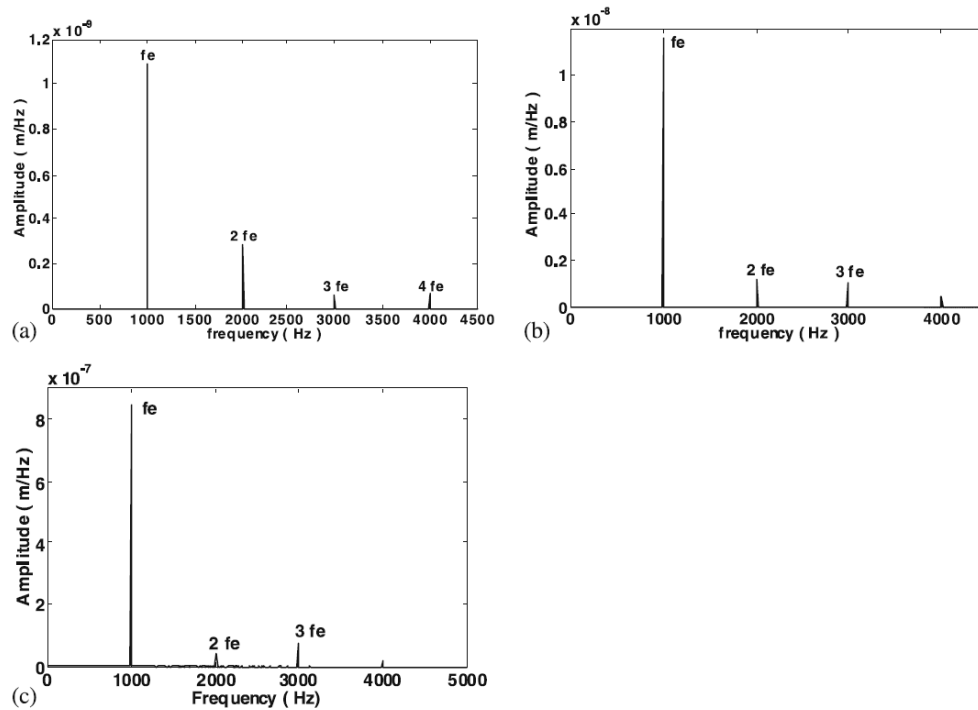


Figure 1. 19. Influence of a profile error on the dynamic component of the carrier (a) Healthy case. (b) 20 μm of error . (c) 200 μm of error, (Chaari et al., 2005)

7.2.2 Pittings:

Pittings are deep holes, which affect all the teeth, particularly in the area of the pitch circle. This damage mostly occurs on relatively hard structural steel gears, and therefore more fragile, sensitive to the cumulative effects of overstressing.

(Liang et al, 2016) proposed an analytical method to compute the gear mesh stiffness in presence of pitting defect considering the severity of pitting (figure 1.20). The pitting are considered in circular shape.

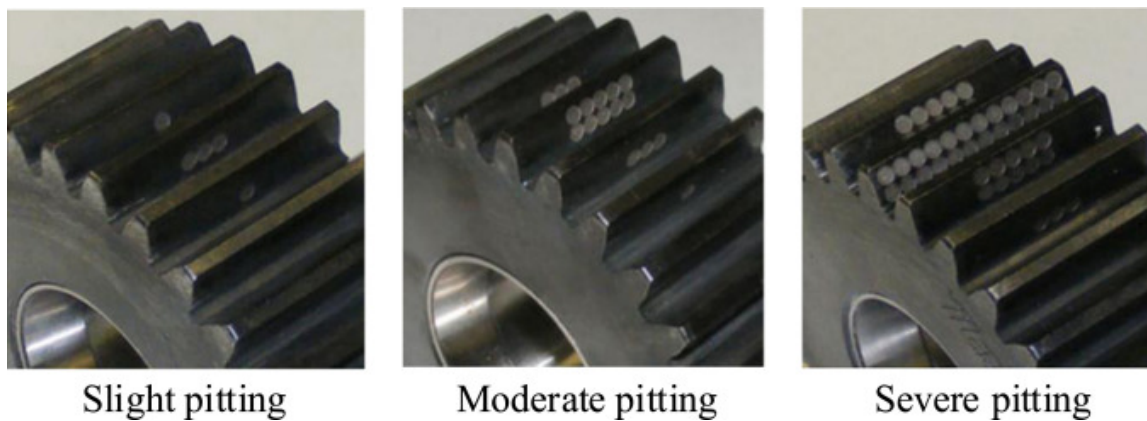


Figure 1. 20. Photo of pitting (Liang et al, 2016)

7.2.3 Crack:

The crack defect is a consequence of stress at the tooth foot that exceeds the fatigue limit of the material and it is generally located on the flank of the tooth stressed in tension. In modeling, cracks affects mainly the mesh stiffness function. (Chaari et al., 2009) used an analytical different method to model mesh stiffness in presence of crack affecting teeth. As shown in Figure.1.22, the effect of crack on mesh stiffness appears through the reduction of mesh stiffness. The mesh stiffness decreases when the length of tooth cracks increase.

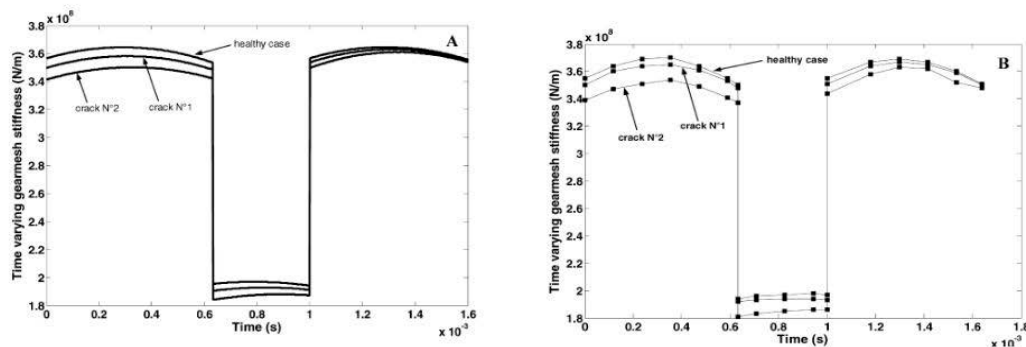


Figure 1. 21. Evolution of mesh stiffness in presence of a crack analytical vs. FE(Chaari et al., 2009)

7.2.4 Tooth breakage:

Tooth breakage faults in gear transmissions can be modeled by a stiffness reduction.

When the breakage size increased, a variation on the dynamic response appears.

(Chaari et al. 2009) reported the influence of tooth breakage on gear mesh stiffness; The effect of breakage defects on mesh stiffness and dynamic response of a one stage gear system was highlighted. Figure 1. 1 shows the evolution of gear mesh stiffness in presence of different size of teeth breakage.

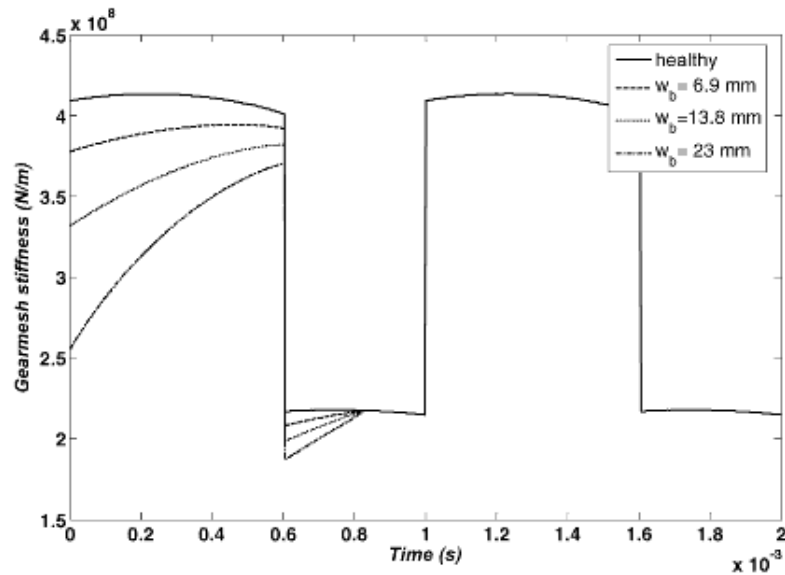


Figure 1. 22. Gear mesh stiffness evolution with different breakage width. (Chaari et al. 2009)

Detection of defects in stationary and non-stationary regimes requires usually special tools. Vibration analysis and signal processing is mainly used to analyze the dynamic behavior of gear transmissions, whether in healthy or damaged cases. The most important signal processing techniques will be enumerated in the next section.

8 vibration signals processing:

Vibration signals can be classified based on their statistical properties. (Randall, 2011) reported that signals can be divided into “stationary signal” characterized by their invariant statistical properties and “non-stationary signal” characterized by their variant statistical properties that vary in time. Figure 1.24 shows this classification.

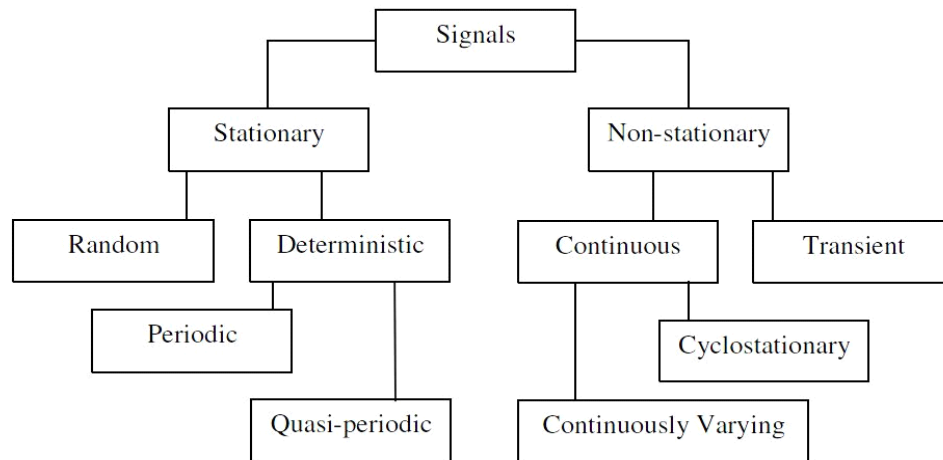


Figure 1. 23. Classification of signals (Randall, 2011)

8.1 Statical analysis of the signals:

The statistical analysis uses the first statistical moments of the probability density of the vibration signal. The signal amplitude distribution can be expressed as a probability density function. Computing the first-moment statistics probability density function of signal amplitudes allows characterizing the overall shape of a signal without a trace. it defines the average value 's' , it is expressed by:

$$m_1 = \bar{s} = \int_{-\infty}^{\infty} s \cdot p(s) ds \quad (1.14)$$

Moment of order 2, which corresponds to the variance, identifies the dispersion of random variables around the mean value and is expressed by:

$$m_2 = \sigma^2 = \int_{-\infty}^{\infty} (s - \bar{s})^2 p(s) ds \quad (1.15)$$

Moment of order 3 represents the distribution amplitude of the signal with respect to a maximum. The measure of this dissymmetry is given by:

$$m_3 = \frac{1}{\sigma^3} = \int_{-\infty}^{\infty} (s - \bar{s})^3 p(s) ds \quad (1.16)$$

Moment of order 4, called also kurtosis represents the flattening rates distribution; it gives an assessment about the peak of curve summit importance.

$$m_4 = \frac{1}{\sigma^4} = \int_{-\infty}^{\infty} (s - \bar{s})^4 p(s) ds \quad (1.17)$$

8.2 Time domain descriptions:

8.2.1 The root mean square:

The Root Mean Square (RMS) of a time signal is an important features since it is directly related to its energy. The RMS measure the power content of the vibration signature, Bigret et al, 1995.). It can be expressed as follow:

$$RMS = \sqrt{\frac{1}{T} \int_0^T S^2(t) dt} \quad (1.18)$$

S (t) is a time signal observed over period T:

8.2.2 The crest factor:

It is a derivative indicator of the effective value, generally used for detection of specific pulse or shock present in the vibration signal and it is defined by:

$$F = \frac{A_c}{A_{eff}} \quad (1.19)$$

With: A_c maximum value of the signal and A_{eff} :RMS signal.

8.2.3 Kurtosis:

The Kurtosis represents the flattening rates of the distribution of a signal; it gives an evaluation of the importance of the peak of the curve.

Kurtosis is a measure of peaks, and it is a good indicator of signal impulsiveness in the context of fault detection for rotating components, it is expressed as:

$$kurtosis(s) = \frac{1}{\sigma^4} = \int_{-\infty}^{\infty} (s - \bar{s})^4 p(s) ds \quad (1.20)$$

$$Kurtosis(x) = \frac{E\{(x - \mu)^4\}}{\sigma^4} - 3 \quad (1.21)$$

Where μ and σ denotes the mean and standard deviation of a time series x and E is the expectation operation.

The“minus3”at the end of this formula is to make the kurtosis of the normal distribution equal to zero. The Spectral kurtosis (SK) is a tool able to detect non-Gaussian components in a signal and it can determine the frequency of the excited component, Dwyer, R. (1983).

This is a quantity without dimension, it is often compared to the value of the kurtosis of a Gaussian signal which is 3 in theory. This parameter allows detection of pulses or shocks in the vibration signal.

8.3 Time Synchronous Averaging (TSA):

The (TSA) is an efficient tool for detection of gear defects. It is based on collecting a vibration time signal of the considered gear and then averaging the signal over a number of revolutions. The resulting signal represents the meshing of teeth over one cycle in which the faulty tooth can be identified. TSA can be expressed as (Miller, 1999):

$$y_{TSA}(t) = \frac{1}{N} \sum_{i=0}^{N-1} y(t + iT_s) \quad (1.22)$$

where:

y (t): is the measured and resampled time signal,

N: is the number of gear revolutions in the signal,

L: is number of samples in one revolution

T_s: is the resampled period.

8.4 Frequency domain descriptors:

Spectral analysis is an efficient tool for the treatment of mechanical vibration signals.. The spectral analysis is characterized by its ability to dissociate and identify vibration sources as a function of the kinematic characteristics of the various components and their speed of rotation.

8.4.1 Fourier transforms:

The Fourier transform allows the decomposition of a time signal into its component frequencies.

The Fourier transform of a time signal x (t) is given by:

$$X(f) = \int_{-\infty}^{\infty} x(t) e^{-2\pi i f t} dt \quad (1.23)$$

If this signal has a finite energy, its discrete Fourier transform can be defined by:

$$X(f) = \sum_{k=-\infty}^{\infty} x(k) e^{-2\pi i k f} \quad (1.24)$$

The Fourier transform represents a basic tool for spectral analysis. It is applied in case of the continuous deterministic time signals. Then, the theory was extended to random processes sampled stationary. Finally, fast algorithms calculating the Fourier transform were developed

making it an interesting method used in several applications.

8.4.2 Capon Method:

The Capon method is developed to estimate the power spectral density of a signal for each frequency. To apply this method, $x(n)$ a signal is filtered to obtain a signal $y(n)$:

$$y(n) = -\sum_{k=0}^p a_k .x(n-k) \quad (1.25)$$

The a_k coefficients must satisfy the following restriction:

$$\sum_{k=0}^p a_k e^{-j2\pi k f_i} = 1 \quad (1.26)$$

This method of spectral estimation approximates the spectral density at a defined frequency by the power output of a filter which contains its contribution to this frequency. However, this output also contains a residual error due to the contribution of other frequencies. This error is lower when the filter order is high.

8.5 Cepstrum analysis:

The cepstrum is a non-linear operator analyzing vibration signals. It is used in the detection of noise as well as in monitoring vibration of rotating machines. The mathematical definition of the Cepstral analysis is (Randall, 2013):

$$s = \mathbf{TF}^{-1}[\mathbf{Ln}|S(v)|] \quad (1.27)$$

Where S is the signal's Fourier transform.

Figure.1.25 shows the passage from spectrum to cepstrum.

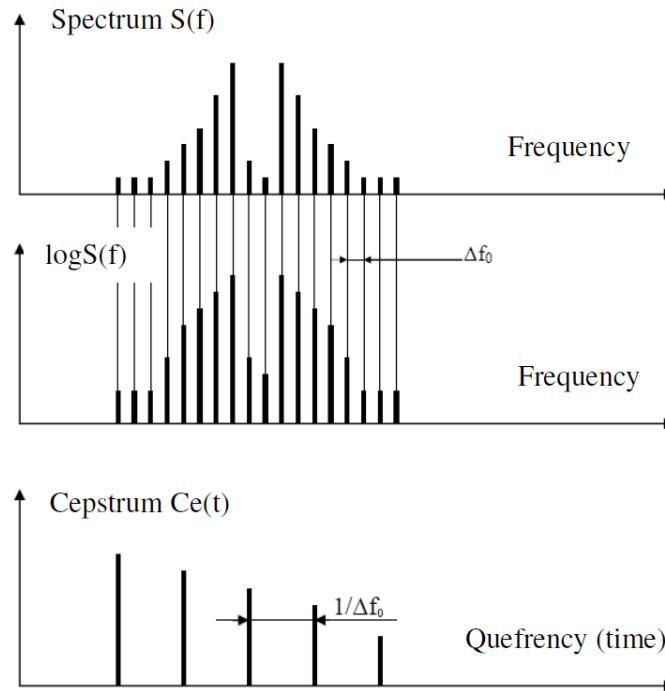


Figure 1. 24. Spectrum and cepstrum (Randall, 1977)

8.6 Joint Time-frequency representations: Wigner-Ville transform

Time-frequency analysis includes techniques that investigate signals in both time and frequency domains using different time-frequency representations.

This technique allows 2D analysis of a signal through one of a plurality now transformations such as the Wigner-Ville transform (TWV).

The (WVT) is a non-linear transformation that combines 1D-2D data with a dimension for frequencies and a second dimension for the time. This method provides time-frequency decomposition with no restrictions on the time and frequency resolutions. It is suitable for the analysis of non- stationary signals since it does not require assumptions about the original signal. Given a function $f(u)$, the Wigner-Ville transform is defined by:

$$W(t, w) = \frac{1}{2\pi} \int_{-\infty}^{\infty} \overline{f\left(t - \frac{u}{2}\right)} f\left(t + \frac{u}{2}\right) e^{-iwu} du \quad (1.28)$$

This transformation can be interpreted as the power spectral density of the instantaneous signal. Figure 1.26 shows the transformed Wigner Ville smoothed signal vibration recorded on more than 3 revolutions of the gearbox pinion. The impacts of defects are clearly identifiable. The presence of energy outside the meshing fundamental frequency shows the existence of a defect

(around 1350 Hz here).

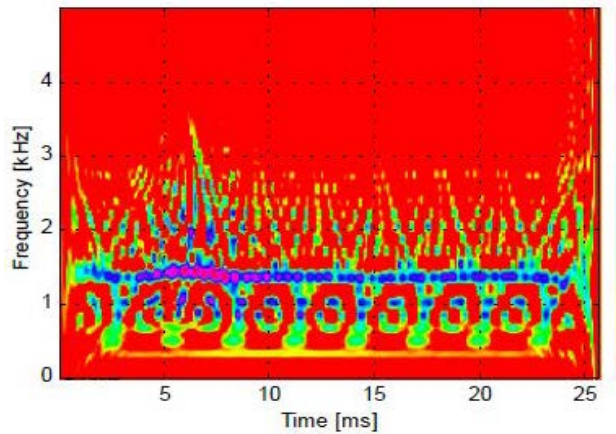


Figure 1. 25. Wigner Ville transforms (Elbadaoui 1999)

The above presented techniques are limited to stationary regimes cases. They are not able to track eventual change of frequency content of signals. For this reason, faults detection techniques in non stationary regimes are required.

9 Gears fault detection techniques in non-stationary operation:

9.1 Short-Time Fourier Transform (STFT):

The Short Time Fourier Transform (STFT) is applied to windows Short data represented in the time domain, (Shin et al. 1993). It is a development that extends the standard Fourier transform technique to manage non-stationary data. The Short-Time Fourier Transform (STFT) of a function $f(u)$ is given by:

$$F(w, t) = \int_{-\infty}^{\infty} \bar{g}(u-t) f(u) e^{-2\pi i w u} du \quad (1.29)$$

With \bar{g} is the complex conjugate of the function $g(u)$ and t is the time parameter.

9.2 Wavelet decomposition:

A vibration signal has usually a broad spectrum.

The wavelet analysis decomposes a signal into smooth oscillating functions called wavelets. It offer a good localization in both time and frequency domain. Typically, the wavelet transform is based on a family of wavelets created by dilatation s and translation u of a mother wavelet $\psi(t)$.

The wavelet transform is used to divide a time function in wavelets. There are two types of wavelet transforms continuous (CWT) and discrete (DWT). The continuous wavelet transforms (CWT) considers factors dilation and translation and is given by equation (1.30). Unlike Fourier transform, continuous wavelet transform could construct a time-frequency representation of a signal by providing the easy location in time and frequency, (Flandrin, 1993).

$$CWT(a,b) = \frac{1}{\sqrt{|a|}} \int_{-\infty}^{\infty} f(t) \psi^* \left(\frac{t-b}{a} \right) dt \quad (1.30)$$

Where a stands for the expansion factor or the index of scale and b is the data translation factor. $\Psi(t)$ denotes a continuous function of time and frequency and $\psi^*(t)$ denotes the conjugate complex $\psi(t)$. The CWT coefficients of complex type are defined with a module and a phase.

In the case of a discrete set of wavelets (DWT), the signal can be divided into two frequency bands. The low frequency band is known as the level Approximate (A) and the high frequency band is known as the Detail (D), (Saxena et al., 2005). Figure 1.26 shows the Morlet wavelets in both the time and frequency domains.

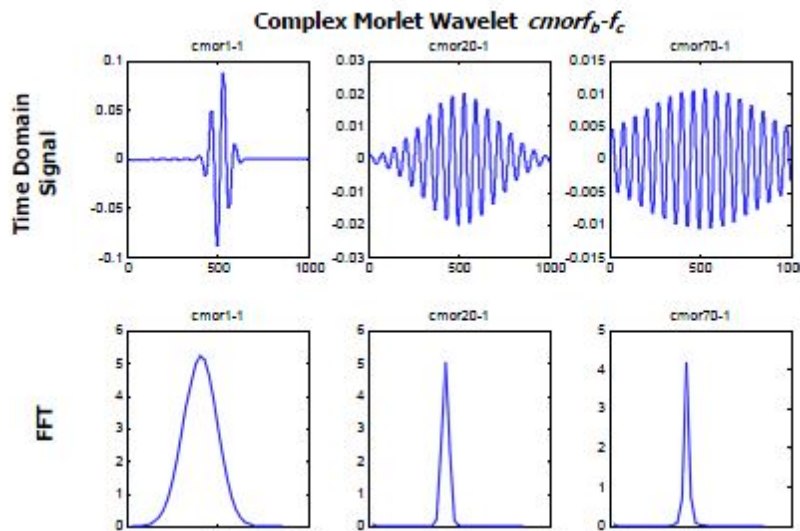


Figure 1. 26. Complex Morlet wavelet with different bandwidth parameters (Saxena et al.,2005).

9.3 Empirical mode decomposition (EMD)

EMD consists in decomposing a signal into some intrinsic mode functions IMFs and one residue (Huang et al., 1998). It is a self-adaptive signal processing method that can be applied to non-linear and non-stationary process perfectly. This technique is very efficient to diagnose gear

defects.

After an iterative computation of an original signals $x(t)$, the original signals are decomposed as follows:

$$x(t) = \sum_{i=1}^n c_i(t) + r_n(t) \quad (1.31)$$

Where $c_1(t), c_2(t), \dots, c_n(t)$ are the I -nth IMFs and $r_n(t)$ is the residue.

The differences among the original vibration signals in various gear running conditions may be subtle. Moreover, EMD analysis can be used to extract the features which can reflect the differences of several running conditions. The main purpose of using EMD for signal decomposition is to find the most exact information about the fault.

9.4 Hilbert transforms:

Hilbert transform is a time-domain convolution that outline one real time-history into another (Wu et al.2012). It is expressed by:

$$H[x(t)] = \frac{1}{\pi} \int_{-\infty}^{+\infty} \frac{x(\tau)}{t - \tau} d\tau \quad (1.32)$$

Where t is time, $x(t)$ is a time domain signal, and $H[x(t)]$ is the Hilbert transform of $x(t)$. The non-stationary characteristics of the modulating signal are not affected by this method because Hilbert transform is a frequency-independent 90° phase shifter. Hilbert transform allow the extraction of the Amplitude and phase modulation functions, $a_m(t)$ and $b_m(t)$, respectively. The demodulation is concluded by building a complex-valued time-domain signal, $A[x(t)]$, which can be expressed as below:

$$A[x(t)] = x(t) + i * H[x(t)] = a(t)e^{i\varphi(t)} \quad (1.33)$$

The resulting complex time-domain signal can be converted from the real/imaginary format to the magnitude/phase format given below:

$$a(t) = \sqrt{x^2(t) + H^2[x(t)]} \quad (1.34)$$

$$\varphi(t) = \arctan \frac{H[x(t)]}{x(t)} \quad (1.35)$$

The Hilbert transform produces a complex time series. The envelope is the magnitude of this complex time series and represents an estimate of the modulation present in the signal because of

sidebands. It allows modulation in signals caused by a faulty gear. In addition, it removes carrier signals and this will decrease the influence of irrelevant information for the purpose of gearbox fault detection and be helpful for identification of the fault in the time–frequency plot via visual inspection.

10 Experimental test benches

To confirm the developed models and the different influencing function in gear systems, several planetary gearbox test bench were built. Experimental validation should provide this field of knowledge with valuable and reproducible data about the dynamic behavior of the transmissions. The data acquisition systems are also very important.

(Boguski 2010) used a PG test machine in order to study its dynamic effects under quasi-static conditions (Figure 1.27). In this test bench, the motor is connected to a torque meter. A torque sensor is connected to the sun gear. Two optical encoders are used to control the speed of the sun and the carrier.

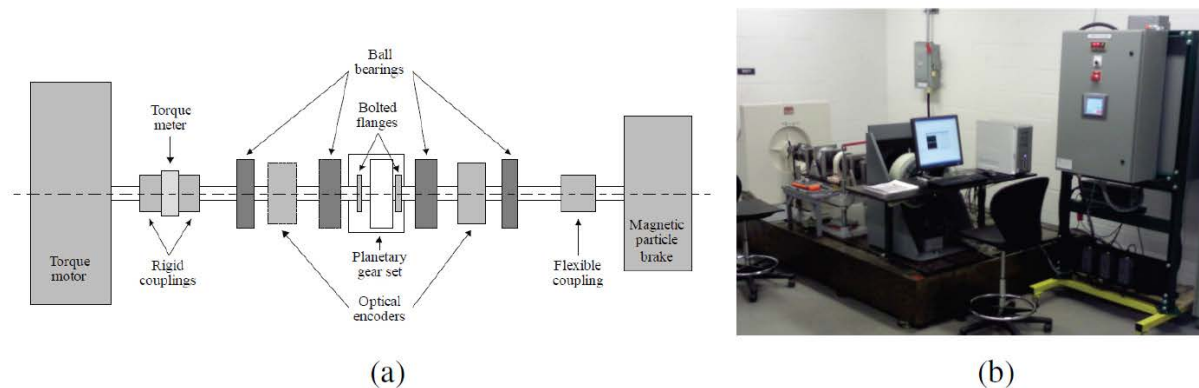


Figure 1. 27. Schematic view (a) real view (b) of the PG test rig (Boguski 2010)

Immonen (Immonen et al., 2012) performed a series of experience on the gearbox of a water turbine composed of two stages of PG trains to detect defects in both stages.

Ligata (Ligata., 2007) studied the load distribution in a epicyclic gear with helical teeth. The purpose of his work was the determination of charge transmitted by each planet by varying the number of planets, the transmitted torque and the position defect value at the first satellite. By using the same bench test (Figure 1.11), Inalpolat (Inalpolat, 2009) presented a theoretical and experimental investigations on modulating sidebands observed in spectra of acquired vibration signals.



Figure 1. 28. View of the "back to back" train test bench (Ligata., 2007)

Practically, the vibrations generated by the epicyclic gear train are measured by a sensor mounted on the outer part of the fixed ring. With the rotation of the planet carrier, a periodic variation of the amplitudes of vibration is observed when the satellites pass close to the location of the fixed sensor.

11 Summary of literature review:

The fundamental purpose of the research in this area found in literature is to study and to characterize the dynamic behavior of PG systems under different running conditions using such models and techniques. Three main models were proposed. Models should take into account the influence of the internal and external excitations on the dynamic behavior of PG system as well as the impact of any kind of defect on the vibration response and the identification of modal properties.

Given the fairly limited literature, it can be concluded that there is a need to develop more lumped parameter models, allowing the extraction of modal parameters in different working conditions and be able to study the effects of internal and the external excitations on the vibration response. The models can also expand to several signal processing tools used generally for the identification of defects in any working condition case.

A complete model should be able to incorporate all the cited parameters and functions providing further insight into the dynamic behavior of the PG systems.

Table 1.1 shows the contribution of this thesis compared to the existing literature.

Table 1. 1. The limits of the existing works.

Discussion of existing literature	Proposed Approaches in this thesis
Few works dedicated to the analysis of dynamic behavior for complex configurations of PG.	A back to back configuration of planetary gear set will be investigated,
A torsional lumped parameter or a plane model PG are widely used which are for limited use in different studied cases.	A three-dimensional lumped parameter model referred to a complex configurations of PG will be developed.
The modal parameters are widely extracted when the system is in a static state	Identification and extraction of modal properties when the system is running under non stationary regimes.
The impact of the non-linear Hertzian contact on the dynamic response in non stationary conditions is not treated. Gear mesh stiffness functions are widely computed as a square function which is not really the case.	An analytical approach taking into account the impact of non-linear Hertzian stiffness on the dynamic behavior of PG system in non-stationary condition will be studied.
No rigorous numerical vs. experimental analysis for the dynamics of complex PGs in stationary and non stationary operations in presence of defects,	Extensive investigation of the PG set with several case studies including defects in stationary and non-stationary regimes through model based and experimental approaches

Conclusion

In this chapter, a deep review on planetary gear system is presented. The different model existing in literature and their dynamic characterization were described highlighting the main important parameter related to those systems such as the meshing stiffness function and damping. Since most of PG systems are operating in non stationary regime, a focus on these conditions was done. Run up, variable load, run down and variable speed conditions were highlighted as well as the techniques which used to describe them. Moreover, a review on the most influencing gear defects was presented. Techniques allowing the identification of defects in non-stationary operation are also detailed.

The principal remarks issued from this review can be summarized as following:

- The modeling of the dynamic behavior of PG system is based on LPM or FEM or hybrid model.
- The periodic variation of the mesh stiffness is the main internal source of excitation.
- The non stationary conditions are the main sources of external excitation, they modify and change the dynamic behaviour of the PG system.
- The modal parameters and the techniques used to identify them are important to understand the dynamic behavior of the gear system.
- The defect can be classified into geometrical and tooth defect, their presence has an impact on the dynamic response.

Based on this literature review, we are focused on the investigation of the dynamic behavior of PG system in healthy and damage cases. In the next chapter, the used test bench for experimental studies is described and its corresponding dynamic model is proposed.

Chapter 2: Description of the test bench and the numerical model

Chapter 2: Description of the test bench and the numerical model

Sommaire

1	Introduction	39
2	Test bench description:	39
3	External load:	41
3.1	Driving system:	41
3.2	Vibration response measurements and signal processing:	43
3.3	Strain gauge:	44
3.4	Tachometer and strip band:	45
3.5	Slip ring:	46
3.6	Acquisition system:	46
4	Analytical lumped-parameter model (LPM)	47
4.1	Description of the model	47
4.2	Modal analysis	52
4.3	Classification of modes:	53
4.4	Modal analysis taking into account the gyroscopic effect.....	54
5	Resolution method:	55
6	Modal parameter estimation:	57
7	Stabilization diagram:	58
8	Conclusion	60

1 Introduction

Planetary gear transmissions are characterized by their high efficiency and their ability to transmit high loads for different speed conditions. Different investigations were carried out in order to study the behaviour and the characterization of these systems which are practically implemented in several industrial cases. A test bench may be used to study such systems.

In this chapter, a two stage PG with power recirculation and its instrumentation is described. In addition, the used signal processing software and its characteristics are detailed. Then, a numerical model which is referred to this test bench is developed.

2 Test bench description:

Experimental setups are carried out on a test bench developed at the University of Cantabria Spain (figure 2.1). The bench consists of two identical planetary gears connected by two rigid shafts, supported by a rigid housing and driven by an electrical motor which is connected through an elastic coupling. Its speed is controlled by a frequency converter which allows the running of the system under stationary or non-stationary operations. The two-planetary gears are mounted in back to back configuration in order to allow the circulation of power. This architecture is selected to minimize the costs and improve the energy efficiency. A ring, a carrier, a sun and three identical planets are the principal components of each planetary gear set. The first PG is called reaction set characterized by a fixed ring and the second one is called test gear characterized by a free ring.

The connection between the two gear sets is through two rigid shafts: the inner shaft connect on the two suns and the hollow shaft links the carriers.

The external load is obtained by adding masses on a rigid radial arm connected to the reaction ring or by using a jack.

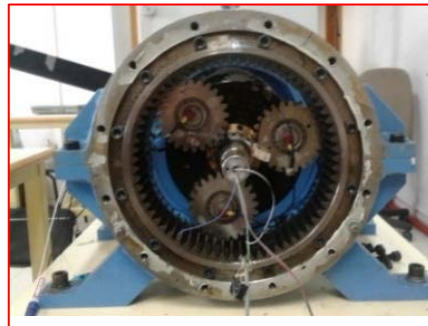
Figure 2.2 and table 2.1 displays the layout of the test bench and the used instruments.



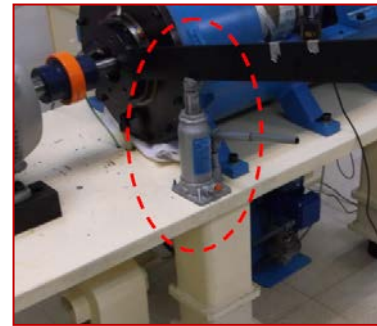
(a)



(b)



(c)



(d)

Figure 2. 1. Experimental test bench: (a) General view (b) Applied external load with masses (c) Planetary gear (d) Applied external load with jack

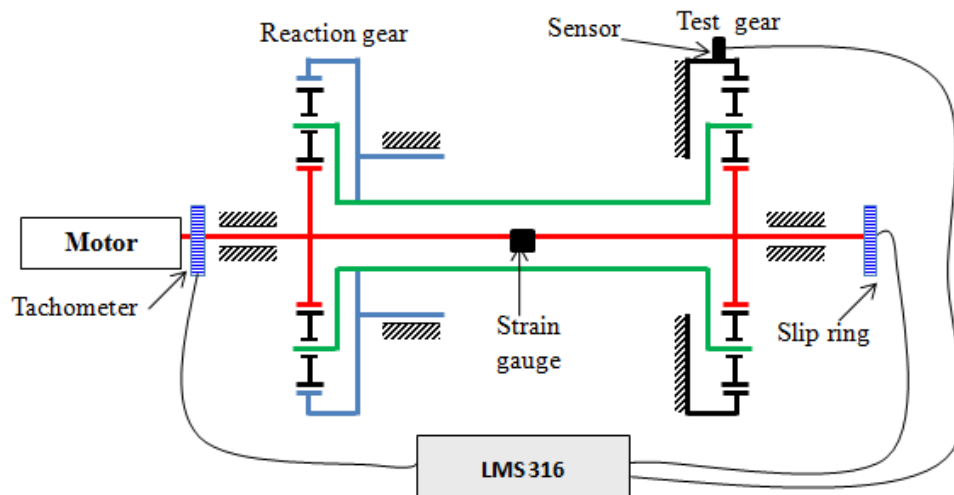


Figure 2. 2. Layout of the test bench and the used instruments

Table 2. 1. Planetary gear basic dimensions

	Sun	Planet (3)	Ring	Carrier
Number of teeth	16	24	65	-
Module (m)	0.00423	0.00423	0.00423	-
Base diameters (m)	0.0614	0.0921	0.2494	0.1728
Tip diameters (m)	0.0699	0.1006	0.2579	0.1813
Pressure angle (rad)	0.4621		0.4621	-

3 External load:

The external torque can be obtained by adding mass or by using a jack. 4000 N.m is the maximum load that can be applied by jack while the load with adding mass can reach 900 N.m.

Based on calculation of load capacity of spur and helical gears” (ISO 6336, 2006), the tangential torque applied on the reaction ring can produce tooth bending and tooth pitting in the sun planet and ring component.

Table 2.2 illustrates the External torque required in order to achieve the failure.

Table 2. 2. External torque required in order to achieve the failure

Contact	Component	Torque producing Bending (N.m)	Torque producing Pitting (N.m)
Sun-Planet	Sun	2644	1100
	Planet	3630	1100
Ring- Planet	Planet	2411	1650
	Ring	47587	9446

Since external torque applied by mass is more accurate than the torque obtained by jack and in order to avoid tooth failure, we will load the transmission by adding mass during the experiments. 1100 N.m is chosen as the maximum load applied on the system.

3.1 Driving system:

An asynchronous electric motor is connected to the sun's shaft to drive planetary sets. Its characteristics are given in table 2.3. It is controlled by a frequency inverter “MICROMASTER 440” with characteristics given in table 2.4 and mounted in the electric cabinet, (figure 2.3).

Table 2. 3. Motor characteristics

Motor type	ABB-MT 90L
Output power (kW)	1.5
Full load speed (rpm)	3000
Full load torque T_f (N m)	1100
Torque starting T_s/T_f	2.7
Ratio breakdown T_b/T_f	5
Slip s_b	0.8
Motor constant a	50
Motor constant b	3

Table 2. 4.Characteristes of the frequency inverter

	Voltage (V)	Current intensity (A)	Frequency (Hz)
Input	380-480	37	47-63
Output	0-Input	32	0-650
Motor	15 kW		



Figure 2. 3. Electric cabinet

This inverter can be configured with the software “STARTER”. This software, developed by “SIEMENS” can be started directly through the frequency converter integrated into PCS 7. With this software, we can control the speed under the stationary condition and command the run up and the run down regimes of the motor.

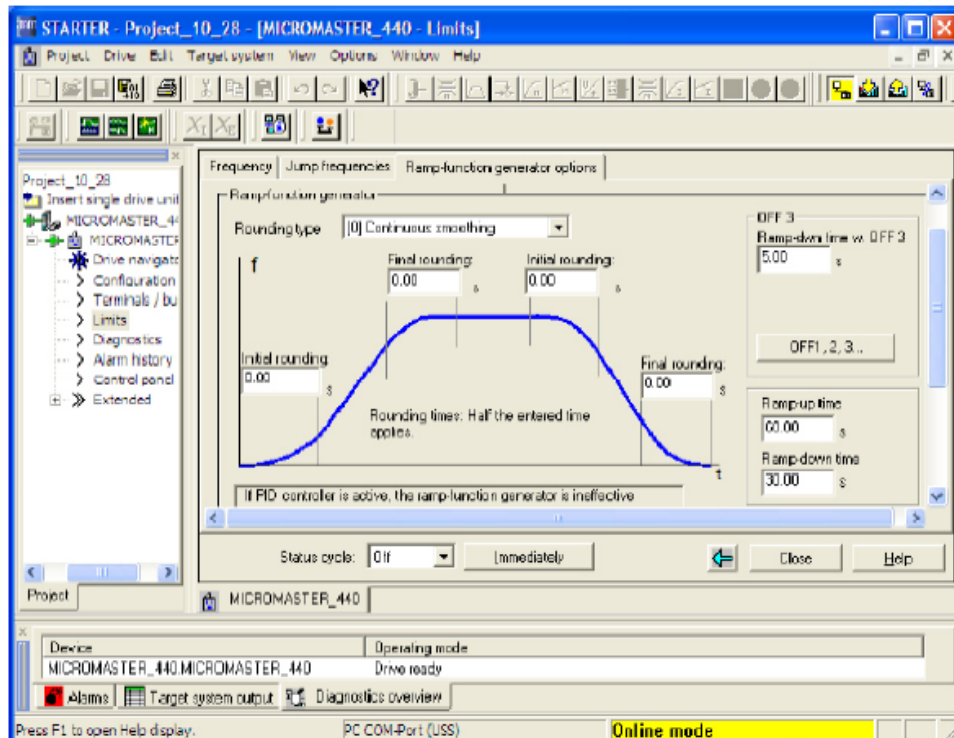


Figure 2. 4. Window of ramp function generator function of “STARTER” software

3.2 Vibration response measurements and signal processing:

To collect the instantaneous accelerations in the inner and the outer components, four tri-axial accelerometers are used,(figure 2.5). Depending on the nature of measurement, those accelerometers are mounted on the tangential direction of the component using a wax.

The sensors are calibrated by using a “Brüel & Kjær” calibration exciter in all used directions (figure 2.6). The calibration frequency is 159.2Hz for $\omega=1000$ rad/s and the level of acceleration is 3.16 m/s². The following table displays the accelerometers characterization.

Table 2. 5. Accelerometers characterization

	1	2	3	4
Serial number	10020	10021	10022	10023
X-Sensitivity (mV/g)	102.6	103.5	101.6	101.6
Y-Sensitivity (mV/g)	101.3	98.68	99.67	103.0
Z-Sensitivity (mV/g)	101.1	104.3	102.6	101.9

Accelerometer signals were recorded using a sampling frequency of 1000 Hz. At this frequency band the acceleration signal are a good option. They provide a clean spectrum that can be integral to a velocity or a displacement spectrum,(Kahraman and Blankenship;1997).

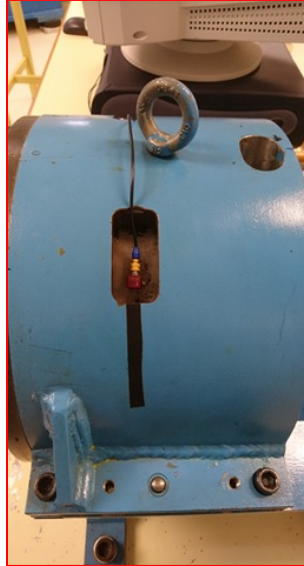


Figure 2. 5. Accelerometer location



Figure 2. 6. Calibration of Accelerometers

3.3 Strain gauge:

In order to estimate the input torque and to identify some vibration modes, a strain gauge is mounted on the sun's shaft using a quarter bridge. Its resistance is 120Ω and its gage factor is 2.7. Figure 2.7 displays the strain gauge location and figure 2.8 shows the schematic diagram of the quarter bridge model.



Figure 2. 7. Strain gauge location

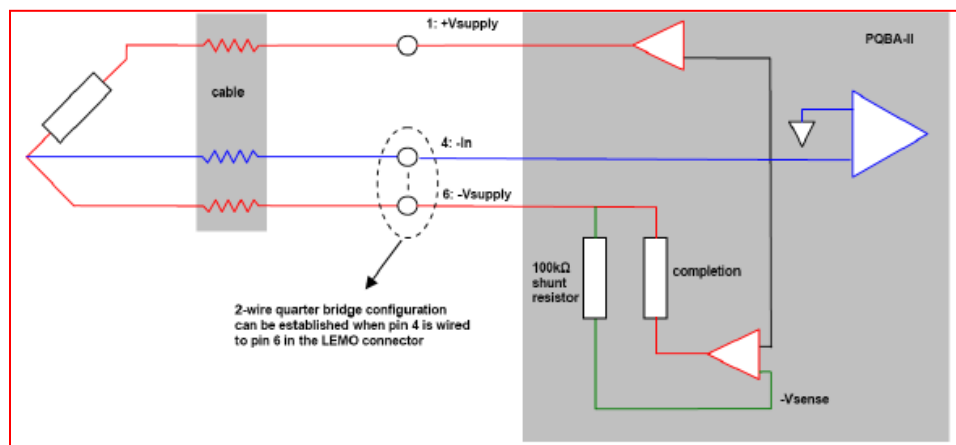


Figure 2. 8. Quarter bridge mode of the strain gauge (LMS SCADAS, 2009)

3.4 Tachometer and strip band:

Figure 2.9 shows the overall speed measurement instrument, it is composed of a tachometer (Compact VLS7) and a zebra stripes encoder with 130 black bands glued and fixed on the hollow shaft in order to measure its instantaneous angular velocity.

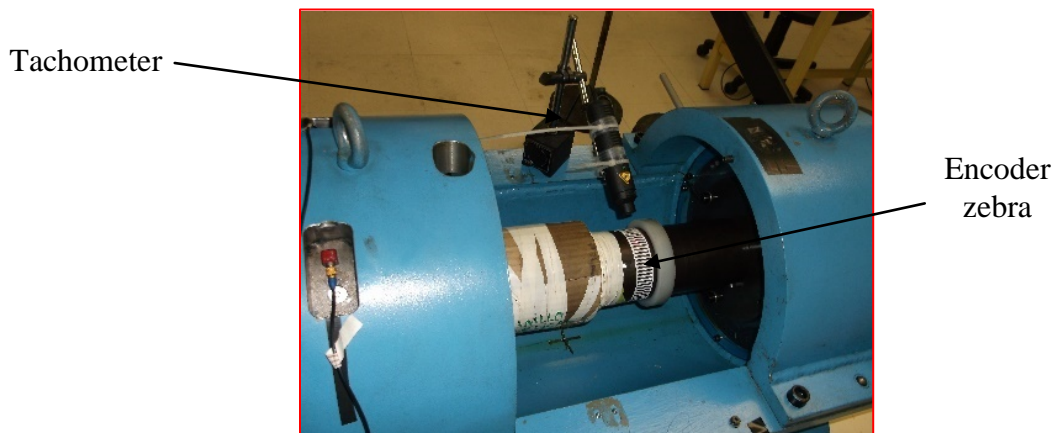


Figure 2. 9. Encoder zebra and tachometer

3.5 Slip ring:

In order to collect the signal issued from the strain gauge, a slip ring was mounted in the extremity of the sun shaft. It allows the connection to the input module of the data acquisition system (Figure.2.10) by 6 pole LEMO connector.

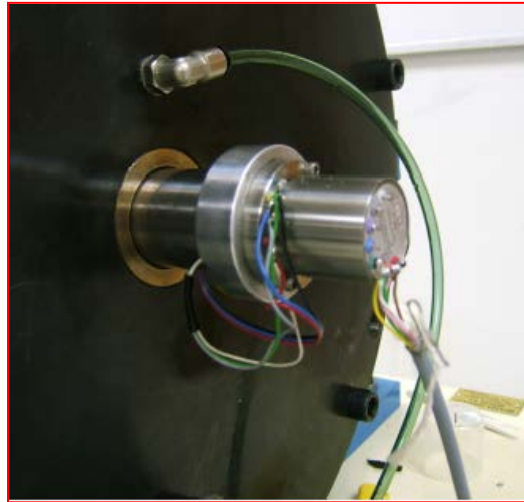


Figure 2. 10. Slip ring mounted on the shaft of suns

3.6 Acquisition system:

Different software are used during the experimental test.

LMS test Lab A15 is used in the different experimental setups such as modal analysis and dynamic test. Also, Starter software is used to drive the electrical motor through the introduction of the different operating conditions.

The recorded signals are recorded and processed an LMS SCADAS 316 system; it includes different modal analysis techniques with different options like the stabilization diagram, the PolyMAX estimation method and the transfer path analysis. It allows also the introduction of the geometry of the structure in the software.

The "LMS SCADAS 316" is a high-performance data acquisition system. It is connected to the computer through 1Gbit Ethernet host interface. This acquisition system is integrated with "LMS Test.Lab", "LMS Test. Xpress" and "LMS CADA-X" software.

"LMS SCADAS 316" includes five different modules: four input modules and one output module.

4 Analytical lumped-parameter model (LPM)

4.1 Description of the model

An analytical model based on the real test rig is developed (figure 2.13). It is a three-dimensional LPM of the studied two PG sets which are reaction PG (r) and test PG (t). A ring (r), a carrier (c), a sun (s) and three planets (p1, p2, p3) are the principal elements of each gear set. Three translation u_{ij} , v_{ij} , w_{ij} and three rotations ϕ_{ij} , Ψ_{ij} , θ_{ij} ($i=c, r, s, p1, p2, p3$; $j=r, t$) are the degree of freedom of each component.

The rotations ϕ_{ij} , Ψ_{ij} and θ_{ij} are replaced by their gear mesh displacements following the procedure given by Karray et al.(2016):

$$\rho_{ijx} = Rb_{ij} \cdot \phi_{ij} \quad \rho_{ijy} = Rb_{ij} \cdot \Psi_{ij} \quad \rho_{ijz} = Rb_{ij} \cdot \theta_{ij} \quad (i=c, r, s, p1, p2, p3; j=r, t). \quad (2.1)$$

Where: Rb_{ij} presents the base circle radius of the sun, the ring, the planet, and the radius of the circle passing through the planet centres for the carrier.

These elements are modelled as rigid bodies with masses m_{ij} and inertias I_{ij} and supported by a bearing with a stiffness k_{ijk} where $i=c, r, s, p1, p2, p3$; $j=r, t$ in direction $k=u, v, w, \phi, \Psi, \theta$. The planets components were modelled as identical and equally spaced

The connections between these components are defined by the gear mesh stiffness functions modelled as linear spring with stiffness K_{rpr1} , K_{rpr2} , K_{rpr3} and K_{spr1} , K_{spr2} , K_{spr3} for the reaction gear set and by the stiffness K_{rpt1} , K_{rpt2} , K_{rpt3} and K_{spt1} , K_{spt2} , K_{spt3} for the test gear set. The shafts connecting the two gear set are modelled by an axial stiffness k_{sa} , k_{ca} ; flexural stiffness k_{sf} , k_{cf} and torsional stiffness k_{st} , k_{ct} , respectively.

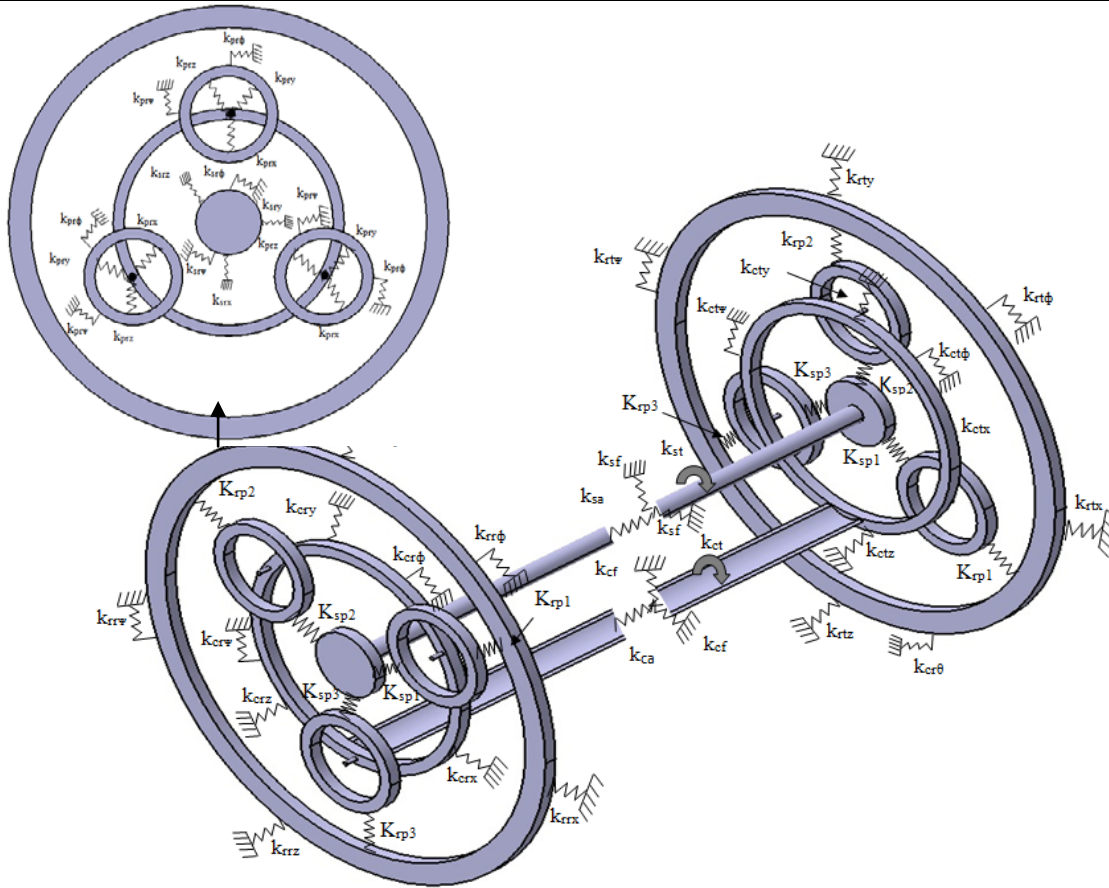


Figure 2.11. PG numerical model

The system's equation of motion is obtained by the procedure given by (Karray et al., 2016). It can be expressed as:

$$M\ddot{q} + C\dot{q} + (K_b + K_e(t))q = F(t) \quad (2.2)$$

q is the degree of freedom vector defined as:

$$q = \begin{Bmatrix} q_r \\ q_t \end{Bmatrix} \quad (2.3)$$

q_r and q_t are the reaction and test gear degree of freedom.

$$q_r = \{U_{cr}, V_{cr}, W_{cr}, \rho_{cxr}, \rho_{cyr}, \rho_{czt}, U_{rr}, V_{rr}, W_{rr}, \rho_{rxr}, \rho_{ryr}, \rho_{rzt}, U_{sr}, V_{sr}, W_{sr}, \rho_{sxr}, \rho_{syr}, \rho_{szr}, U_{1r}, V_{1r}, W_{1r}, \rho_{1xr}, \rho_{1yr}, \rho_{1zt}, U_{2r}, V_{2r}, W_{2r}, \rho_{2xr}, \rho_{2yr}, \rho_{2zt}, U_{3r}, V_{3r}, W_{3r}, \rho_{3xr}, \rho_{3yr}, \rho_{3zt}\} \quad (2.4)$$

$$q_t = \{U_{ct}, V_{ct}, W_{ct}, \rho_{cxt}, \rho_{cxt}, \rho_{czt}, U_{rt}, V_{rt}, W_{rt}, \rho_{rxt}, \rho_{ryt}, \rho_{rzt}, U_{st}, V_{st}, W_{st}, \rho_{sxt}, \rho_{syt}, \rho_{szt}, U_{1t}, V_{1t}, W_{1t}, \rho_{1xt}, \rho_{1yt}, \rho_{1zt}, U_{2t}, V_{2t}, W_{2t}, \rho_{2xt}, \rho_{2yt}, \rho_{2zt}, U_{3t}, V_{3t}, W_{3t}, \rho_{3xt}, \rho_{3yt}, \rho_{3zt}\} \quad (2.5)$$

M denotes the mass matrix, K_b is the bearing and shaft stiffness matrix, $K_e(t)$ is the time varying stiffness matrix and $F(t)$ stand for the external force vector applied to the system.

$$F(t) = \begin{bmatrix} \frac{T_{cr}}{r_{cr}}, \frac{T_{rr}}{r_{rr}}, \frac{T_{sr}}{r_{sr}}, 0, 0, 0, \frac{T_{ct}}{r_{ct}}, \frac{T_{rt}}{r_{rt}}, \frac{T_{st}}{r_{st}}, 0, 0, 0 \end{bmatrix} \quad (2.6)$$

T_{cr} , T_{rr} , T_{sr} , T_{ct} , T_{rt} , T_{st} are the external torque applied respectively in the reaction carrier, the reaction ring, the reaction sun, the test carrier, the test ring and the test sun.

The damping matrix C is given by:

$$C = \alpha M + \beta K \quad (2.7)$$

Where α and β are two constants (Dhatt and Touzot, 1981).

All matrices are presented in what follows:

$$M = \begin{bmatrix} M_t & 0 \\ 0 & M_r \end{bmatrix} \quad (2.8)$$

$$M_i = \begin{bmatrix} M_c & 0 & 0 & 0 & 0 & 0 \\ 0 & M_r & 0 & 0 & 0 & 0 \\ 0 & 0 & M_s & 0 & 0 & 0 \\ 0 & 0 & 0 & M_1 & 0 & 0 \\ 0 & 0 & 0 & 0 & M_2 & 0 \\ 0 & 0 & 0 & 0 & 0 & M_3 \end{bmatrix} \quad i = t, r \quad (2.9)$$

$$M_{ij} = \begin{bmatrix} m_j & 0 & 0 & 0 & 0 & 0 \\ 0 & m_j & 0 & 0 & 0 & 0 \\ 0 & 0 & m_j & 0 & 0 & 0 \\ 0 & 0 & 0 & \frac{I_j}{r_j^2} & 0 & 0 \\ 0 & 0 & 0 & 0 & \frac{I_j}{r_j^2} & 0 \\ 0 & 0 & 0 & 0 & 0 & \frac{2 * I_j}{r_j^2} \end{bmatrix} \quad j=c, r, s, 1,2,3 \quad (2.10)$$

The bearing stiffness matrix K_b

$$K_b = \text{diag}(K_{cr}, K_{rr}, K_{sr}, K_{1r}, K_{2r}, K_{3r}, K_{cb}, K_{rb}, K_{sb}, K_{1b}, K_{2b}, K_{3b}) \quad (2.11)$$

$$K_{ij} = \text{diag}(K_{ijx}, K_{ijy}, K_{ijz}, K_{ij^s}, K_{ij^r}, K_{ij^c}) \quad i=c, r, s, \quad (2.12)$$

$$K_{kjb} = \text{diag}(K_{kjb}, K_{kjb}, K_{kjb}, K_{k^s}, K_{k^r}, 0) \quad k=1,2,3 \quad j=r, \quad (2.13)$$

$$\psi_r = \alpha_i + \alpha_r \quad (2.14)$$

$$\psi_s = \alpha_i - \alpha_s \quad (2.15)$$

The stiffness matrix K_m :

$$K_m = \begin{bmatrix} K_{mr} & 0 \\ 0 & K_{mt} \end{bmatrix} + K_c \quad (2.16)$$

$$K_m = \begin{bmatrix} \sum K_{c1}^n & 0 & 0 & K_{c2}^1 & K_{c2}^2 & K_{c2}^3 \\ 0 & \sum K_{r1}^n & 0 & K_{r2}^1 & K_{r2}^2 & K_{r2}^3 \\ 0 & 0 & \sum K_{s1}^n & K_{s2}^1 & K_{s2}^2 & K_{s2}^3 \\ K_{c2}^1 & K_{r2}^1 & K_{s2}^1 & K_{PP}^1 & 0 & 0 \\ K_{c2}^2 & K_{r2}^2 & K_{s2}^2 & 0 & K_{PP}^2 & 0 \\ K_{c2}^3 & K_{r2}^3 & K_{s2}^3 & 0 & 0 & K_{PP}^3 \end{bmatrix} \quad (2.17)$$

$$K_{pp}^n = K_{c3}^n + K_{r3}^n + K_{s3}^n \quad (2.18)$$

$$K_{\alpha}^n = \begin{bmatrix} \cos^2(\alpha_i) K_{xx} + \sin^2(\alpha_i) K_{yy} & \cos(\alpha_i) \sin(\alpha_i) K_{xx} - \sin(\alpha_i) \cos(\alpha_i) K_{yy} & 0 & 0 & 0 & -\sin(\alpha_i) K_{yz} \\ \cos(\alpha_i) \sin(\alpha_i) K_{xx} - \sin(\alpha_i) \cos(\alpha_i) K_{yy} & \sin^2(\alpha_i) K_{xx} + \cos^2(\alpha_i) K_{yy} & 0 & 0 & 0 & \cos(\alpha_i) K_{yz} \\ 0 & 0 & K_{zz} & \sin(\alpha_i) K_{zx} & -\cos(\alpha_i) K_{zx} & 0 \\ 0 & 0 & \sin(\alpha_i) K_{zx} & \sin^2(\alpha_i) K_{zz} & -\sin(\alpha_i) \cos(\alpha_i) K_{zz} & 0 \\ 0 & 0 & -\cos(\alpha_i) K_{zx} & -\sin(\alpha_i) \cos(\alpha_i) K_{zz} & \cos^2(\alpha_i) K_{zz} & 0 \\ -\sin(\alpha_i) K_{yz} & \cos(\alpha_i) K_{yz} & 0 & 0 & 0 & K_{zz} \end{bmatrix} \quad (2.19)$$

$$K_{r1}^n = K_{rp} \begin{bmatrix} \sin^2(\psi_r) & -\varepsilon \sin(\psi_r) \cos(\psi_r) & 0 & \frac{\varepsilon}{Rb_r} \sin(\psi_r) \cos(\psi_r) & -\frac{1}{Rb_r} \sin^2(\psi_r) & -\varepsilon \sin(\psi_r) \\ -\varepsilon \sin(\psi_r) \cos(\psi_r) & \cos^2(\psi_r) & 0 & -\frac{\varepsilon^2}{Rb_r} \cos^2(\psi_r) & \frac{1}{Rb_r} \sin(\psi_r) \cos(\psi_r) & \varepsilon^2 \cos(\psi_r) \\ 0 & 0 & 0 & 0 & 0 & 0 \\ \frac{\varepsilon}{Rb_r} \sin(\psi_r) \cos(\psi_r) & -\frac{\varepsilon^2}{Rb_r} \cos^2(\psi_r) & 0 & \frac{\varepsilon^2}{(Rb_r)^2} \cos^2(\psi_r) & -\frac{\varepsilon}{(Rb_r)^2} \sin(\psi_r) \cos(\psi_r) & -\frac{\varepsilon^2}{Rb_r} \cos(\psi_r) \\ -\frac{1}{Rb_r} \sin^2(\psi_r) & \frac{\varepsilon}{Rb_r} \sin(\psi_r) \cos(\psi_r) & 0 & -\frac{\varepsilon}{(Rb_r)^2} \sin(\psi_r) \cos(\psi_r) & \frac{1}{(Rb_r)^2} \sin^2(\psi_r) & \frac{\varepsilon}{Rb_r} \sin(\psi_r) \\ -\varepsilon \sin(\psi_r) & \varepsilon^2 \cos(\psi_r) & 0 & -\frac{\varepsilon^2}{Rb_r} \cos(\psi_r) & \frac{\varepsilon}{Rb_r} \sin(\psi_r) & \varepsilon^2 \end{bmatrix} \quad (2.20)$$

$$K_{s1}^n = K_{sp} \begin{bmatrix} \sin^2(\psi_s) & \varepsilon \sin(\psi_s) \cos(\psi_s) & 0 & -\frac{\varepsilon}{Rb_s} \sin(\psi_s) \cos(\psi_s) & \frac{1}{Rb_s} \sin^2(\psi_s) & \varepsilon \sin(\psi_s) \\ \varepsilon \sin(\psi_s) \cos(\psi_s) & \varepsilon^2 \cos^2(\psi_s) & 0 & -\frac{\varepsilon^2}{Rb_s} \cos^2(\psi_s) & \frac{\varepsilon}{Rb_s} \sin(\psi_s) \cos(\psi_s) & \varepsilon^2 \cos(\psi_s) \\ 0 & 0 & 0 & 0 & 0 & 0 \\ -\frac{\varepsilon}{Rb_s} \sin(\psi_s) \cos(\psi_s) & -\frac{\varepsilon^2}{Rb_s} \cos^2(\psi_s) & 0 & \frac{\varepsilon^2}{(Rb_s)^2} \cos^2(\psi_s) & -\frac{\varepsilon}{(Rb_s)^2} \sin(\psi_s) \cos(\psi_s) & -\frac{\varepsilon^2}{Rb_s} \cos(\psi_s) \\ \frac{1}{Rb_s} \sin^2(\psi_s) & \frac{\varepsilon}{Rb_s} \sin(\psi_s) \cos(\psi_s) & 0 & -\frac{\varepsilon}{(Rb_s)^2} \sin(\psi_s) \cos(\psi_s) & \frac{1}{(Rb_s)^2} \sin^2(\psi_s) & \frac{\varepsilon}{Rb_s} \sin(\psi_s) \\ \varepsilon \sin(\psi_s) & \varepsilon^2 \cos(\psi_s) & 0 & -\frac{\varepsilon^2}{Rb_s} \cos(\psi_s) & \frac{\varepsilon}{Rb_s} \sin(\psi_s) & 1 \end{bmatrix} \quad (2.21)$$

$$K_{c2}^n = \begin{bmatrix} -\cos(\alpha_i) K_{xx} & \sin(\alpha_i) K_{yy} & 0 & 0 & 0 & 0 \\ -\sin(\alpha_i) K_{xx} & -\cos(\alpha_i) K_{yy} & 0 & 0 & 0 & 0 \\ 0 & 0 & -K_{zz} & 0 & 0 & 0 \\ 0 & 0 & -\sin(\alpha_i) K_{zz} & 0 & 0 & 0 \\ 0 & 0 & \cos(\alpha_i) K_{zz} & 0 & 0 & 0 \\ 0 & -K_{yy} & 0 & 0 & 0 & 0 \end{bmatrix} \quad (2.22)$$

$$K_{r_2}^n = K_{rp} \begin{bmatrix} -\sin(\psi_r)\sin(\alpha_c) & \varepsilon\sin(\psi_r)\cos(\alpha_c) & 0 & \frac{\varepsilon}{Rb_p}\sin(\psi_r)\cos(\alpha_c) & -\frac{1}{Rb_p}\sin(\psi_r)\sin(\alpha_c) & \varepsilon\sin(\psi_r) \\ \varepsilon\cos(\psi_r)\sin(\alpha_c) & -\varepsilon^2\cos(\psi_r)\cos(\alpha_c) & 0 & -\frac{\varepsilon^2}{Rb_p}\cos(\psi_r)\cos(\alpha_c) & \frac{\varepsilon}{Rb_p}\cos(\psi_r)\sin(\alpha_c) & -\varepsilon^2\cos(\psi_r) \\ 0 & 0 & 0 & 0 & 0 & 0 \\ -\frac{\varepsilon}{Rb_r}\cos(\psi_r)\sin(\alpha_c) & \frac{\varepsilon^2}{Rb_r}\cos(\psi_r)\cos(\alpha_c) & 0 & \frac{1}{Rb_r}\frac{\varepsilon^2}{Rb_p}\cos(\psi_r)\cos(\alpha_c) & -\frac{1}{Rb_r}\frac{\varepsilon}{Rb_p}\cos(\psi_r)\sin(\alpha_c) & \frac{\varepsilon^2}{Rb_r}\cos(\psi_r) \\ \frac{1}{Rb_r}\sin(\psi_r)\sin(\alpha_c) & -\frac{\varepsilon}{Rb_r}\sin(\psi_r)\cos(\alpha_c) & 0 & -\frac{1}{Rb_r}\frac{\varepsilon}{Rb_p}\sin(\psi_r)\cos(\alpha_c) & \frac{1}{Rb_r}\frac{1}{Rb_p}\sin(\psi_r)\sin(\alpha_c) & \frac{\varepsilon}{Rb_r}\sin(\psi_r) \\ \varepsilon\sin(\alpha_c) & -\varepsilon^2\cos(\alpha_c) & 0 & -\frac{\varepsilon^2}{Rb_p}\cos(\alpha_c) & \frac{\varepsilon}{Rb_p}\sin(\alpha_c) & -\varepsilon^2 \end{bmatrix} \quad (2.23)$$

$$K_{s_2}^n = K_{sp} \begin{bmatrix} -\sin(\psi_s)\sin(\alpha_s) & -\varepsilon\sin(\psi_s)\cos(\alpha_s) & 0 & \frac{\varepsilon}{Rb_p}\cos(\alpha_s)\sin(\psi_s) & -\frac{1}{Rb_p}\sin(\alpha_s)\sin(\psi_s) & \varepsilon\sin(\psi_s) \\ -\varepsilon\cos(\psi_s)\sin(\alpha_s) & -\varepsilon^2\cos(\psi_s)\cos(\alpha_s) & 0 & \frac{\varepsilon^2}{Rb_p}\cos(\alpha_s)\cos(\psi_s) & -\frac{\varepsilon}{Rb_p}\sin(\alpha_s)\cos(\psi_s) & \varepsilon^2\cos(\psi_s) \\ 0 & 0 & 0 & 0 & 0 & 0 \\ \frac{\varepsilon}{Rb_s}\cos(\psi_s)\sin(\alpha_s) & \frac{\varepsilon^2}{Rb_s}\cos(\psi_s)\cos(\alpha_s) & 0 & \frac{1}{Rb_s}\frac{\varepsilon^2}{Rb_p}\cos(\alpha_s)\cos(\psi_s) & -\frac{1}{Rb_s}\frac{\varepsilon}{Rb_p}\sin(\alpha_s)\cos(\psi_s) & \frac{\varepsilon^2}{Rb_s}\cos(\psi_s) \\ -\frac{1}{Rb_s}\sin(\psi_s)\sin(\alpha_s) & -\frac{\varepsilon}{Rb_s}\sin(\psi_s)\cos(\alpha_s) & 0 & -\frac{1}{Rb_s}\frac{\varepsilon}{Rb_p}\cos(\alpha_s)\sin(\psi_s) & \frac{1}{Rb_s}\frac{1}{Rb_p}\sin(\alpha_s)\sin(\psi_s) & -\frac{\varepsilon}{Rb_s}\sin(\psi_s) \\ -\varepsilon\sin(\alpha_s) & -\varepsilon^2\cos(\alpha_s) & 0 & \frac{\varepsilon^2}{Rb_p}\cos(\alpha_s) & -\frac{\varepsilon}{Rb_{st}}\sin(\alpha_s) & \varepsilon^2 \end{bmatrix} \quad (2.24)$$

$$K_{c3}^n = K_{pn} \begin{bmatrix} K_{XX} & 0 & 0 & 0 & 0 & 0 \\ 0 & K_{YY} & 0 & 0 & 0 & 0 \\ 0 & 0 & K_{ZZ} & 0 & 0 & 0 \\ 0 & 0 & 0 & 0 & 0 & 0 \\ 0 & 0 & 0 & 0 & 0 & 0 \\ 0 & 0 & 0 & 0 & 0 & 0 \end{bmatrix} \quad (2.25)$$

$$K_{R_3}^n = K_{rp} \begin{bmatrix} \sin^2(\alpha_c) & -\varepsilon\sin(\alpha_c)\cos(\alpha_c) & 0 & -\frac{\varepsilon}{Rb_p}\cos(\alpha_c)\sin(\alpha_c) & \frac{1}{Rb_p}\sin(\alpha_c)\sin(\alpha_c) & -\varepsilon\sin(\alpha_c) \\ -\varepsilon\cos(\alpha_c)\sin(\alpha_c) & \varepsilon^2\cos^2(\alpha_c) & 0 & \frac{\varepsilon^2}{Rb_p}\sin(\alpha_c)\cos(\alpha_c) & -\frac{\varepsilon}{Rb_p}\sin(\alpha_c)\cos(\alpha_c) & \varepsilon^2\cos(\alpha_c) \\ 0 & 0 & 0 & 0 & 0 & 0 \\ -\frac{\varepsilon}{Rb_p}\cos(\alpha_c)\sin(\alpha_c) & \frac{\varepsilon^2}{Rb_p}\cos(\alpha_c)\cos(\alpha_c) & 0 & \frac{\varepsilon^2}{(Rb_p)^2}\cos^2(\alpha_c) & -\frac{\varepsilon}{(Rb_p)^2}\sin(\alpha_c)\cos(\alpha_c) & \frac{\varepsilon^2}{Rb_p}\cos(\alpha_c) \\ \frac{1}{Rb_p}\sin(\alpha_c)\sin(\alpha_c) & -\frac{\varepsilon}{Rb_p}\sin(\alpha_c)\cos(\alpha_c) & 0 & -\frac{\varepsilon}{(Rb_p)^2}\sin(\alpha_c)\cos(\alpha_c) & \frac{1}{(Rb_p)^2}\sin^2(\alpha_c) & -\frac{\varepsilon}{Rb_p}\sin(\alpha_c) \\ -\varepsilon\sin(\alpha_c) & \varepsilon^2\cos(\alpha_c) & 0 & \frac{\varepsilon^2}{Rb_p}\cos(\alpha_c) & -\frac{\varepsilon}{Rb_p}\sin(\alpha_c) & \varepsilon^2 \end{bmatrix} \quad (2.26)$$

$$K_{S_3}^n = K_{sp} \begin{bmatrix} \sin^2(\alpha_s) & \varepsilon\sin(\alpha_s)\cos(\alpha_s) & 0 & -\frac{\varepsilon}{Rb_p}\cos(\alpha_s)\sin(\alpha_s) & -\sin(\alpha_s) & -\varepsilon\sin(\alpha_s) \\ \varepsilon\sin(\alpha_s)\cos(\alpha_s) & \varepsilon^2\cos^2(\alpha_s) & 0 & -\frac{\varepsilon^2}{Rb_p}\cos(\alpha_s)\cos(\alpha_s) & -\frac{\varepsilon}{Rb_p}\sin(\alpha_s)\cos(\alpha_s) & -\varepsilon^2\cos(\alpha_s) \\ 0 & 0 & 0 & 0 & 0 & 0 \\ -\frac{\varepsilon}{Rb_p}\cos(\alpha_s)\sin(\alpha_s) & -\frac{\varepsilon^2}{Rb_p}\cos(\alpha_s)\cos(\alpha_s) & 0 & \frac{\varepsilon^2}{(Rb_p)^2}\cos^2(\alpha_s) & -\frac{1}{Rb_p}\frac{\varepsilon}{Rb_p}\sin(\alpha_s)\cos(\alpha_s) & \frac{\varepsilon^2}{Rb_p}\cos(\alpha_s) \\ -\sin(\alpha_s) & -\frac{\varepsilon}{Rb_p}\sin(\alpha_s)\cos(\alpha_s) & 0 & -\frac{\varepsilon}{(Rb_p)^2}\sin(\alpha_s)\cos(\alpha_s) & \frac{1}{(Rb_p)^2}\sin^2(\alpha_s) & -\frac{\varepsilon}{Rb_p}\sin(\alpha_s) \\ -\varepsilon\sin(\alpha_s) & -\varepsilon^2\cos(\alpha_s) & 0 & \frac{\varepsilon^2}{Rb_p}\cos(\alpha_s) & -\frac{\varepsilon}{Rb_p}\sin(\alpha_s) & \varepsilon^2 \end{bmatrix} \quad (2.27)$$

Table 2.6 shows the values of the different parameters used in the model which are used in Hammami work,(Hammami 2015).The meshing stiffness are determined by using FEM developed by (Fernandez et al 2013).

Table 2. 6. PG and shafts parameters.

Reaction gear set				
Component	Sun	Planet (3)	Ring	Carrier
Mass [kg]	0.485	1.225	28.1	3.643
Moment of inertia [kgm ²]	$356 \cdot 10^{-6}$	$2045 \cdot 10^{-6}$	$697767 \cdot 10^{-6}$	$21502 \cdot 10^{-6}$
Bearing stiffness [N/m]	$K_{strx}=k_{strz}=1.5 \cdot 10^8$	$k_{prx}=k_{pry}=1.1 \cdot 10^8$	$K_{rtx}=k_{rty}=8 \cdot 10^8$	$K_{crx}=k_{ctz}=1 \cdot 10^8$
	$K_{stz}=3 \cdot 10^8$	$k_{prz}=3 \cdot 10^8$	$K_{rtz}=10 \cdot 10^8$	$K_{ctz}=5 \cdot 10^8$
Torsional stiffness [Nm/rd]	$k_{sr\phi}=k_{sr\nu}=6 \cdot 10^9$	$k_{pr\phi}=k_{pr\nu}=6 \cdot 10^9$	$k_{rr\phi}=k_{rr\nu}=1.5 \cdot 10^9$	$k_{cr\phi}=k_{cr\nu}=610^9$
Meshstiffness[N/m]	$3.5 \cdot 10^8$		$4.5 \cdot 10^8$	-
Test gear set				
Component	Sun	Planet (3)	Ring	Carrier
Mass [kg]	0.485	1.225	28.1	3.643
Moment of inertia [kgm ²]	$356 \cdot 10^{-6}$	$2045 \cdot 10^{-6}$	$697767 \cdot 10^{-6}$	$21502 \cdot 10^{-6}$
Bearing stiffness [N/m]	$K_{stx}=k_{stz}=1.5 \cdot 10^8$	$k_{ptx}=k_{pty}=1.1 \cdot 10^8$	$K_{rtx}=k_{rty}=8 \cdot 10^8$	$K_{crx}=k_{ctz}=1 \cdot 10^8$
	$K_{stz}=3 \cdot 10^8$	$k_{ptz}=3 \cdot 10^8$	$K_{rtz}=10 \cdot 10^8$	$K_{ctz}=5 \cdot 10^8$
Torsional stiffness [Nm/rd]	$k_{st\phi}=k_{st\nu}=5 \cdot 10^9$	$k_{pt\phi}=k_{pt\nu}=610^9$	$k_{rt\phi}=k_{rt\nu}=510^9$ $k_{rt\theta}=7.9 \cdot 10^6$	$k_{ct\phi}=k_{ct\nu}=510^9$
Mesh stiffness[N/m]	$3.5 \cdot 10^8$		$4.5 \cdot 10^8$	-
Shaft stiffness				
	Flexural[N/m]	Torsional [Nm/rd]	Tractional[N/m]	
Sun	$4.9 \cdot 10^5$	$3.73 \cdot 10^4$	4.8510^8	
Carrier	$1.1 \cdot 10^7$	$8.38 \cdot 10^5$	1.2510^9	

4.2 Modal analysis

In order to determine the natural frequencies and the vibration modes of the system, the time varying mesh stiffness between all the components in each gear will be considered by its mean value. The gyroscopic effect was neglected since the system is running under low speed. In this case, the undamped free equation of motion will be:

$$M\ddot{q} + (K_b + K_m)q = 0 \quad (2.28)$$

The Eigen value problem can be expressed as:

$$(-\omega_i^2 M + K_M)\varphi_i = 0 \quad (2.29)$$

Where ω_i is the natural frequencies, φ_i are the vibration modes, M and K_m denotes respectively the mass and the stiffness matrices.

4.3 Classification of modes:

The natural frequencies, its multiplicity and the nature of modes are displayed in table 2.7.

Lin and Parker (1999) classified the vibration modes into three types of modes:

- The rotational (R) and translational (T) vibration modes characterized by their natural frequencies and their multiplicity m ($m=1$ for rotational modes and $m=2$ for translational modes). The rotational modes have a rotational motion of-ring, carrier and sun components and in-phase motion of planets. The translational modes have a translational motion of the sun, carrier and ring.
- The planet modes (P) which depend to the number of planet in the PG set, this kind of modes appears only when the number of planets $N>3$, its multiplicity is $m=N-1$. For the studied case, In the studied PG, the number of planets is three and only rotational and translational modes were observed.

Table 2. 7. Natural frequencies and Vibration modes.

Mode	Multiplicity	Type	Natural frequencies
1	1	R	77
2	1	R	154
3	1	R	172
4	1	R	197
5	1	R	241
6	2	T	291
7	2	T	320
8	1	R	342
9	1	R	384
10	1	R	413
11	1	R	436
12	1	R	-
13	2	T	531
14	1	R	552
15	1	R	592
16	1	R	618
17	2	T	697
18	1	R	720
19	1	R	-
20	1	R	815

4.4 Modal analysis taking into account the gyroscopic effect

Because of the mounting of the planets on a rotating carrier, the centrifugal accelerations and Coriolis effect induced by the rotation of the planet carrier introduce gyroscopic terms in the system modelling. For applications at high speeds, such as the case of aircraft engines (6000 rpm), the gyroscopic effect can alter the stability and dynamic behavior of the system and cannot be ignored.

We recall that the system motion equation including the gyroscopic matrix is written by:

$$M\ddot{q} + \Omega_c G \dot{q} + (K_b + K_e(t) - \Omega_c^2 K_\Omega)q = F(t) \quad (2.30)$$

The eigenvalue problem of the corresponding undamped free system is given by:

$$\{-\omega_i^2 M + j\Omega_c G_r \omega_i + \tilde{K}\} \phi_i = 0 \quad (2.31)$$

with \tilde{K} the matrix mean stiffness of the system written as:

$$\tilde{K} = K_b + K_e - \Omega_c^2 K_\Omega \quad (2.32)$$

G and K_Ω are respectively the gyroscopic matrix and the Centripetal matrix .

$$G = \text{Diag} (G_t, G_r). \quad (2.32)$$

$$G_i = \text{Diag} (G_c, G_r, G_s, G_1, \dots, G_n); i=t,r. \quad (2.33)$$

$$G_j = \begin{bmatrix} 0 & -2m_j & 0 & 0 & 0 & 0 \\ -2m_j & 0 & 0 & 0 & 0 & 0 \\ 0 & 0 & 0 & 0 & 0 & 0 \\ 0 & 0 & 0 & 0 & 0 & 0 \\ 0 & 0 & 0 & 0 & 0 & 0 \\ 0 & 0 & 0 & 0 & 0 & 0 \end{bmatrix}, \quad j = c, r, s, 1, \dots, n, \quad (2.34)$$

$$K_\Omega = \text{Diag} (K_{\Omega t}, K_{\Omega r}). \quad (2.35)$$

$$K_{\Omega i} = \text{diag}(K_{\Omega C}, K_{\Omega R}, K_{\Omega S}, K_{\Omega 1}, \dots, K_{\Omega n}); i=t,r. \quad (2.36)$$

$$\text{with : } K_{\Omega j} = \text{diag}(m_j, m_j, 0, 0, 0, 0); \quad j = c, r, s, 1, \dots, n, \quad (2.37)$$

According to literature (...) Gyroscopic effect will be responsible of the separation of double translational modes into distinct ones as the speed increases. Figure 2.12 shows the change in the value of the 7th and 8th natural frequencies according to the speed of rotation of the planet carrier .

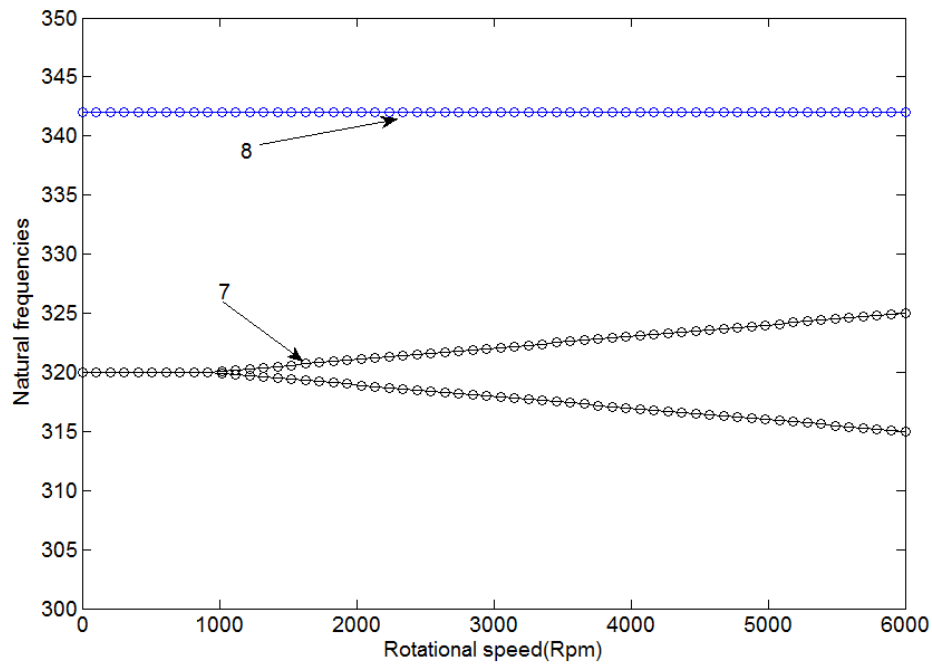


Figure 2. 12. Variation of natural frequencies with rotational speed

It is clearly seen the separation of the translation al mode 7 as Ω_c increase. However rotational mode 8 remain unchanged.

Seen that the studied system will run under low rotational speed, the gyroscopic effect will be neglected.

5 Resolution method:

To solve the equations of motion, step by step integration methods are usually used. These methods proved to be well adapted to linear equations with periodic coefficients. The most commonly used time method is the implicit method of Newmark due to its numerical stability and interesting computation time ratio-precision for industrial applications (Dhatt, 1984). However, it requires a judicious choice of integration parameters and initial conditions. The solution is given in the time domain; the transition to the frequency domain is performed by a Fourier transform of the reply. The concept of this method is to solve at each time step the time discredited equation of motion given by

$$M\ddot{q} + C\dot{q} + K(t)q = F(t) \quad (2.38)$$

The state of the system at a time $t_{n+1}=t_n+\Delta t$ is calculated according to the known state at time t_n with Δt considered the time step. This scheme considers two independent parameters “ a ” and “ b ” to write the Taylor series developments of displacement and velocity (Yannick, 2004):

$$\dot{q}_{n+1} = \dot{q}_n + \Delta t(1-b)\ddot{q}_n + \Delta t b \ddot{q}_{n+1} \quad (2.39)$$

$$q_{n+1} = q_n + \Delta t \dot{q}_n + \Delta t^2 \left(\frac{1}{2} - a\right) \ddot{q}_n + \Delta t a \ddot{q}_{n+1} \quad (2.40)$$

Substituting the two equations (2.39) and (2.40) in the equilibrium equation (2.2) written in time domain, we obtain the following equation:

$$(M + b\Delta t C + a\Delta t^2 K) \ddot{q}_{n+1} = f_{n+1} - C(\dot{q}_n + (1-b)\Delta t \ddot{q}_n) - K(q_n + \Delta t \dot{q}_n + \Delta t^2 \left(\frac{1}{2} - a\right) \ddot{q}_n) \quad (2.41)$$

The resolution with a Newmark scheme is achieved by a predictor-corrector approach.

Equation (2.38) becomes in the following simplified form:

$$\tilde{M} \ddot{q}_{n+1} = f_{n+1} - C^p \dot{q}_{n+1} - K^p q_{n+1} \quad (2.42)$$

Where:

$$\tilde{M} = M + b\Delta t C + a\Delta t^2 K \quad (2.43)$$

$$\dot{q}_{n+1}^p = \dot{q}_n + (1-b)\Delta t \ddot{q}_n \quad (2.44)$$

$$q_{n+1}^p = q_n + \Delta t \dot{q}_n + \left(\frac{1}{2} - a\right) \Delta t^2 \ddot{q}_n \quad (2.45)$$

\dot{q}_{n+1}^p and q_{n+1}^p are the predictions of speed and displacement and corresponds to the beginning of the Taylor's development.

Equation (2.33) calculates the acceleration and then corrects the speed and displacement through the following relationships:

$$\dot{q}_{n+1} = \dot{q}_{n+1}^p + \Delta t b \ddot{q}_{n+1} \quad (2.46)$$

$$q_{n+1} = q_{n+1}^p + \Delta t^2 a \ddot{q}_{n+1} \quad (2.47)$$

Figure 2.13 shows the algorithm of Newmark method.

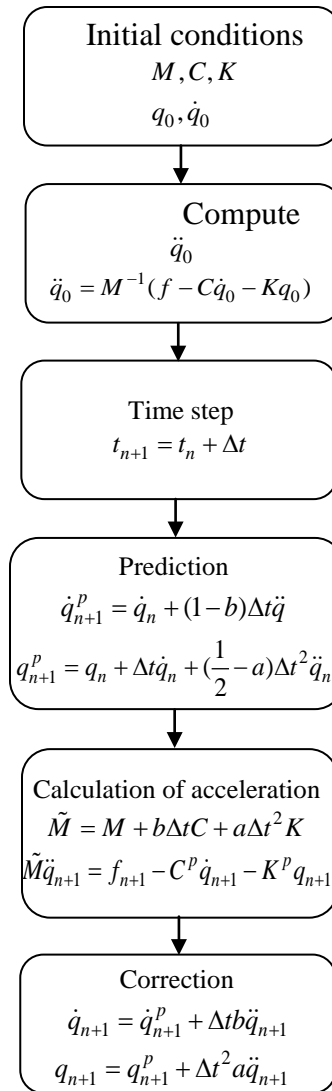


Figure 2. 13. Newmark algorithm

6 Modal parameter estimation:

Different modal parameters estimations can be done using LMS test Lab 15 A acquisition system. In this version, the PolyMAX Modal parameter estimation is implemented. It is a further evolution and a poly-reference version of the (LSCF) estimation method.

This method is characterized by the fact that the singular value decomposition SVD step to decompose the residues can be avoided and that closely spaced poles can be separated.

The PolyMAX method needs Frequency Response Function (FRFs) or Cross Correlation Function (CCF) or Order Function (OF) as primary data and after that identifies a right matrix-fraction model.

$$[H(\omega)] = [B(\omega)][A(\omega)]^{-1} \quad (2.48)$$

$[H(\omega)]$ is the FRF matrix containing the FRFs between all m inputs and all l outputs.

The numerator and the denominator polynomial matrix are defined as:

$$\langle B_o(\omega) \rangle = \sum_{r=0}^p \Omega_r(\omega) \langle \beta_{or} \rangle \quad (2.49)$$

$$\langle A(\omega) \rangle = \sum_{r=0}^p \Omega_r(\omega) \langle \alpha_r \rangle \quad (2.50)$$

Where $\Omega_r(\omega)$ are the polynomial basis functions and p is the polynomial order. β_{or} and α_r are two polynomial coefficients.

In this approach, the participation factors are available when constructing the stabilization diagram (Eq 2.40). Based on the right matrix-fraction model and after reducing the normal equations, the poles and modal participation factors are identified as the eigenvalue and eigenvectors of their matrix.

$$[H(\omega)] = \sum_{i=1}^n \frac{\{v_i\} \langle l_i^T \rangle}{j\omega - \lambda_i} + \frac{\{v_i^*\} \langle l_i^H \rangle}{j\omega - \lambda_i^*} - \frac{LR}{\omega^2} + UR \quad (2.51)$$

where n is the number of modes; \bullet^* is the complex conjugate of a matrix; $\{v_i\}$ are the mode shapes; l_i^T are the modal participation factors and λ_i are the poles, which occur in complex-conjugated pairs and are related to the eigen frequencies ω_i and damping ratios ξ_i as follows:

$$\lambda_i, \lambda_i^* = -\xi_i \omega_i \pm j \sqrt{1 - \xi_i^2} \omega_i \quad (2.52)$$

LR, UR denotes the lower and upper residuals due to the influence of the out-of-band modes in the considered frequency band.

This procedure allows constructing a stabilization diagram for increasing the model orders and using stability criteria for natural frequencies, damping ratios and mode shapes.

7 Stabilization diagram:

The stabilization diagram is an efficient tool to extract modal parameters. The diagram uses an Frequency Response Function (FRF) or Order Function (OF) or Cross Power Spectral Density (CPSD) as input data. Another function called mode indicator function (MIF) (green) can be added to help identifying resonances.

In Figure 2.14, an example of stabilization diagram using the FRF is displayed. Different indicators appear on the diagram: v is vector and s stands for stable pole.

The procedure for selecting stable pole is as bellow:

The model size must be increased until the poles stabilize. Then, the 2nd or 3rd "s" can be selected after the stabilization of the pole. The maximum possible of stable pole must be selected. This procedure is iterative until obtaining the real mode.

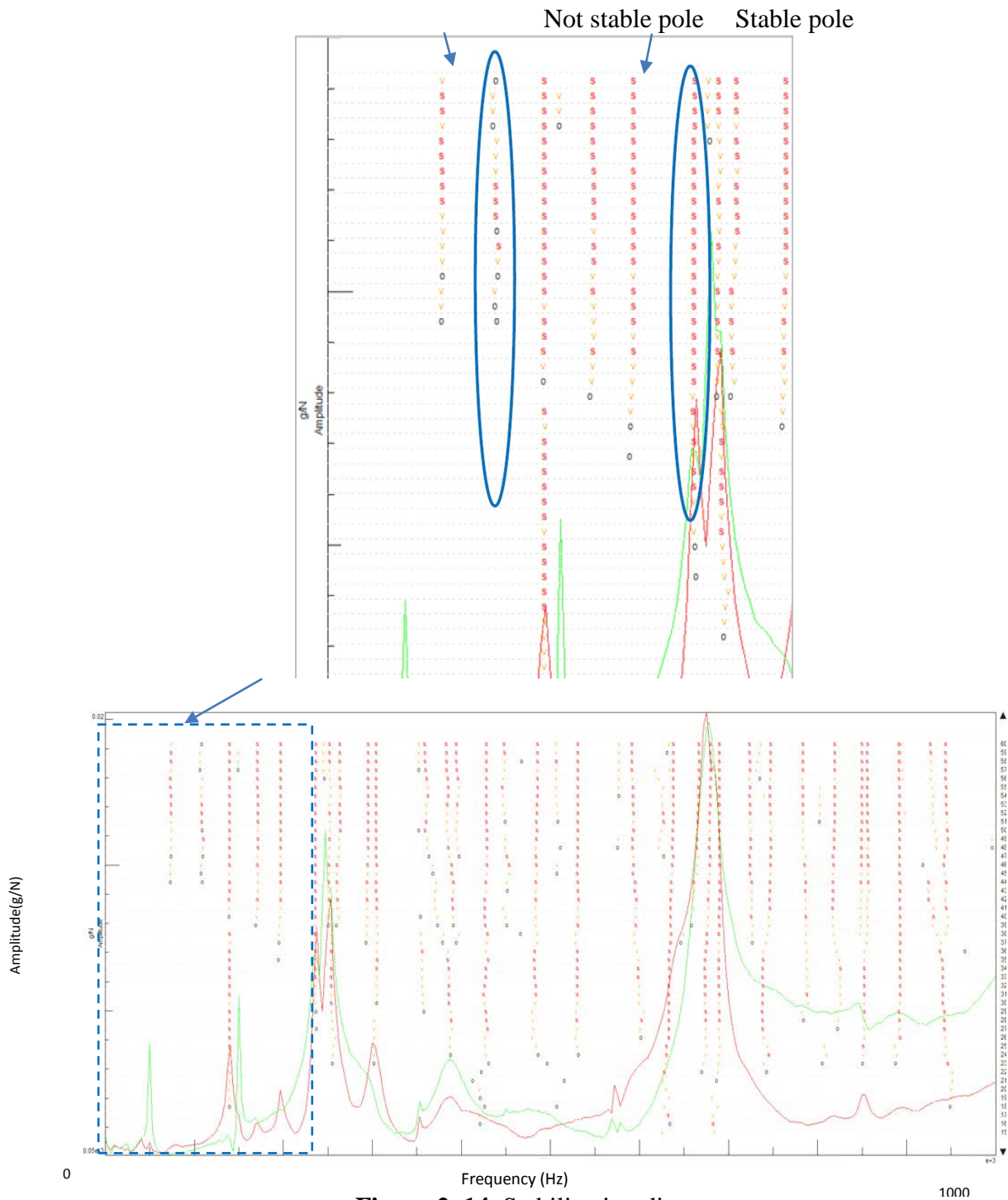


Figure 2. 14. Stabilization diagram

8 Conclusion

In this chapter, a PG test bench with power mechanical recirculation is presented; this special configuration can run under stationary and non stationary conditions.

For the collection of measurement, accelerometers and strain gauge are used to record the signals in the different components. Moreover, LMS Test.Lab software is used to visualize and to precede the signal in the different experiments.

Based on this test bench, a linear three-dimensional LPM of PG is developed. The natural frequencies and the vibration modes are detailed.

Using the test bench and the developed three-dimensional model, a comparison between modal analysis techniques will be highlighted in the next chapter.

Chapter 3: Modal analysis techniques

Chapter 3: Modal analysis techniques

Sommaire

1	Introduction:	64
2	Experimental modal analysis	64
2.1	Impacts hammer excitation:.....	64
2.2	Vibration measurement:	65
2.3	Frequency response function (FRF):	66
2.4	Natural frequencies damping and modes:	67
2.5	Modal assurance criterion:.....	68
2.6	Mode shapes:	69
3	Influence of meshing stiffness variation on the modal parameter:.....	71
4	Operational modal analysis:	74
4.1	Experimental setup:	74
4.2	Power spectral density function:.....	75
4.3	Natural frequencies and damping identification:.....	76
5	Order based modal analysis:.....	77
5.1	Experimental setup:	77
5.2	Order tracking:.....	78
5.3	Natural frequency, damping and mode:	80
6	Comparison between different modal analyses:	81
7	Modal proprieties sensitivity to load variation using OBMA	83
7.1	Experimental set up:	83
7.2	Effect of load on the dynamic behavior:	84
7.3	Order functions:	89
7.4	Natural frequencies and modal damping sensitivity to the load:.....	92
8	Conclusion:.....	94

1 Introduction:

Modal analysis techniques are used to identify the critical frequencies and corresponding vibration modes of a structure. Three modal analysis techniques which are the experimental modal analysis (EMA), the operational modal analysis (OMA) and the order based modal analysis (OBMA) are presented. All these techniques are applied to the studied complex PG system test bench. The modal parameters are identified using each technique experimentally and compared to others obtained numerically. In addition, the influence of load on modal parameters is investigated using EMA and OBMA.

2 Experimental modal analysis

2.1 Impact hammer excitation:

Typically, experimental modal analyses are carried out by the help of the hammer or shaker excitations. In the studied cases, the EMA is performed using an impact hammer excitation with sensitivity 1 mV/N. The impact tests were performed on the arm of the test of PG in order to excite the rotational mode and on planets and sun of the test gear in order to excite the translational mode, (Figure 3.1). Ten impacts were performed during each test and then averaged using modal testing tools.



Figure 3. 1. Impact hammer location

The sampling frequency was selected as 1000 Hz.

The coherence function was used as a data quality assessment tool which identifies how much of the output signal is related to the measured input signal.

When the coherence is close to 1, the measurements can be considered as repeatable; otherwise, they aren't. In the studied case, the coherence is close to 1 along the frequency bandwidth but it can

go below 0.5-0.6 in particular zones. In this case, the presence of natural frequencies cannot be confirmed. Nevertheless, the reduction of coherence can be explained as well by the complex path between the measurement point and the impact point.

A force window was applied to the signal immediately after the impulse; Figure 3.2 shows the coherence function and the input random force.

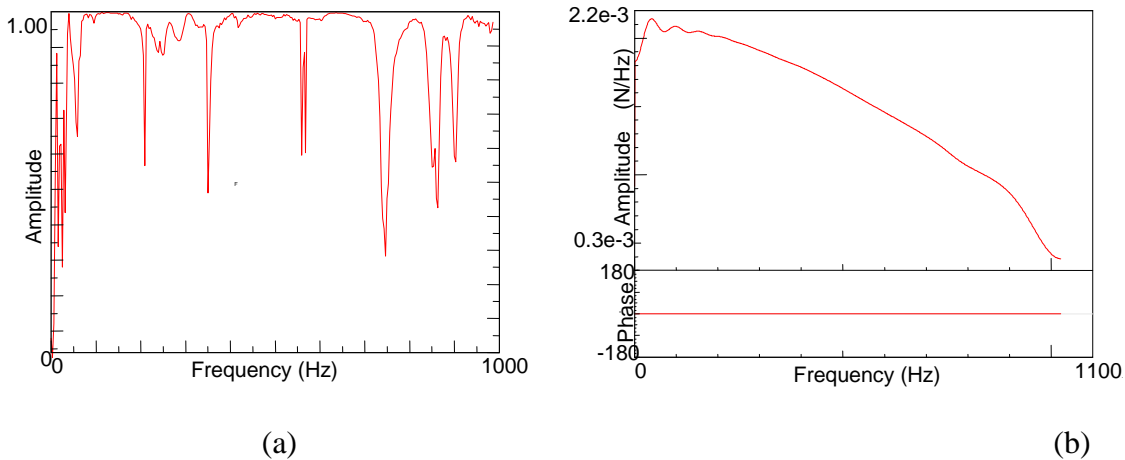


Figure 3. 2. (a) Coherence function (b) force window of the hammer

2.2 Vibration measurement:

During measurement, triaxial accelerometers are used to record the vibration signals (figure 3.3).

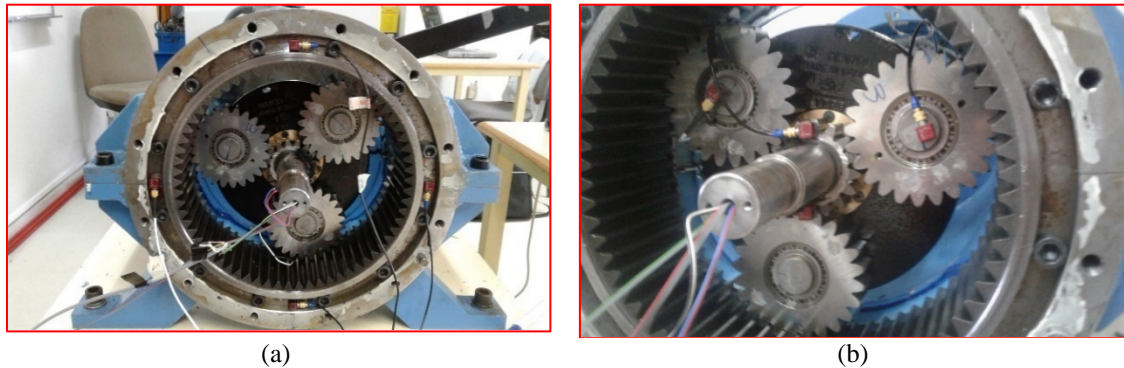


Figure 3. 3. Accelerometers mounted (a) on the ring gear (b) on the sun and planets of the test ring

In EMA tests, the angular accelerations of the different components are measured; sensors are mounted following a kinematic orientation as shown in Figure 3.4. In addition, only the tangential components of the acceleration are considered because the radial components cancel each other (Corey,1962),(Kahraman and Blankenship,1997).

For the ring, four transducers are fixed equally spaced to measure the acceleration of the fixed ring. The tangential recorded accelerations of all sensors are $a_{a,r}$, $a_{b,r}$, $a_{c,r}$ and $a_{d,r}$.

The ratio of the sum of the four averaged recorded signals over the mounting ring's radius $r_{m,r}$ yields the angular acceleration of the ring $\ddot{\theta}_r$:

$$\ddot{\theta}_r = \frac{a_{a,r} + a_{b,r} + a_{c,r} + a_{d,r}}{r_{m,r}} \quad (3.1)$$

For the other components, two sensors are fixed equally spaced on the tangential direction to measure the angular acceleration of the carrier, sun and the three planets. The tangential recorded accelerations of all accelerometers are denoted by $a_{a,s}$, $a_{b,s}$, respectively.

The ratio of the sum of the two averaged recorded signals over the mounting radius of component i (i =carrier, sun and planets) $r_{m,i}$ yields the angular acceleration of the ring $\ddot{\theta}_i$:

$$\ddot{\theta}_i = \frac{a_{a,i} + a_{b,i}}{r_{m,i}} \quad (3.2)$$

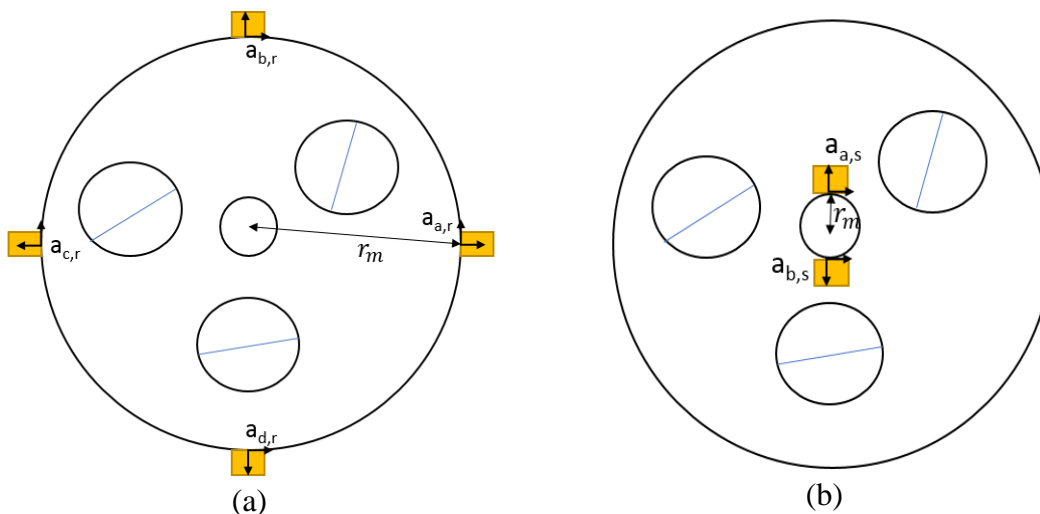


Figure 3. 4. Layout of the instruments (a) on the ring (b) on the sun

2.3 Frequency response function (FRF):

The FRF quality and impact location are very important in the case of modal testing.

Six FRF responses are selected to identify the modal parameters. Figure 3.5 displays the FRF measured on the ring, the sun, the carrier and the planet1 of the test PG for an impact done on the arm.

The obtained experimental results are compared to those issued from the LPM.

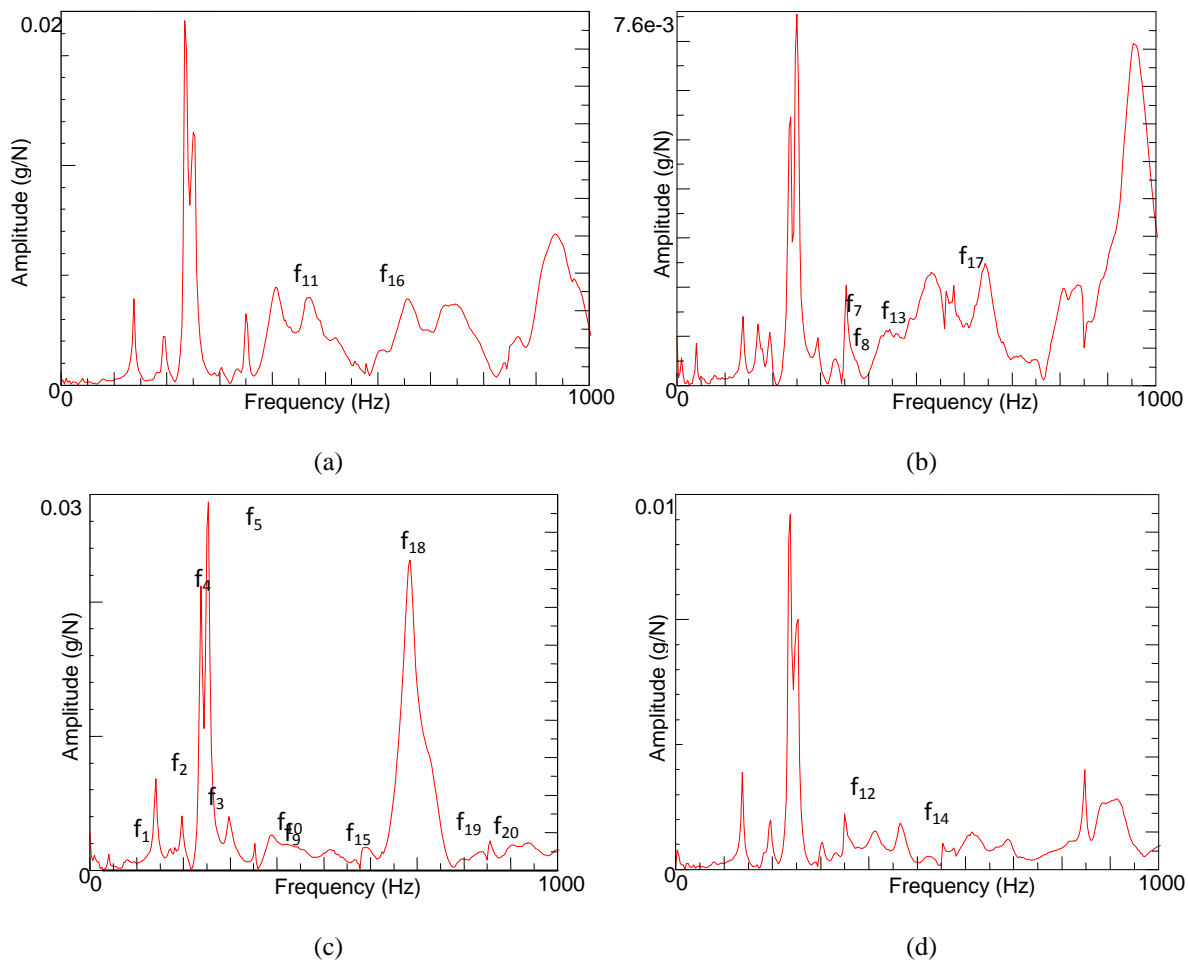


Figure 3. 5. FRF measured on the: (a) Carrier (b) Planet 1(c) Ring (d) Sun

As a preliminary result, it can be noticed that the dynamic response in various degrees of freedom is qualitatively and quantitatively different.

The FRF on test ring which is the fixed component reveals the majority of natural frequencies.

2.4 Natural frequencies damping and modes:

From the preceding investigation, 20 modes are identified: 16 rotational and 4 translational, the nature of these modes are identified using Eigen value problem. For each mode, the modal damping and the natural frequency were identified.

The obtained modes were estimated by using the stabilization diagram as well as the damping and natural frequencies.

The comparison between the natural frequencies determined from the experimental impact tests and the numerical model, the multiplicity of each mode and the damping ratio are displayed in table 3.1.

Table 3. 1. Modal properties obtained for the static testing.

Mode	Multiplicity	Type	Experimental	Numerical	Error (%)	Damping ratio (%)
1	1	R	76	77	1,30	0.77
2	1	R	136	154	11,69	1.36
3	1	R	169	172	1,74	1.61
4	1	R	195	197	1,02	1.49
5	1	R	251	241	-4,15	1.06
6	2	T	301	291	-3,44	1.57
7	2	T	325	320	-1,56	1.41
8	1	R	352	342	-2,92	0.38
9	1	R	378	384	1,56	2.00
10	1	R	406	413	1,69	2.04
11	1	R	436	436	0,00	2.09
12	1	R	466	-	-	2.06
13	2	T	526	531	0,94	2.16
14	1	R	558	552	-1,09	0.08
15	1	R	578	592	2,36	0.65
16	1	R	604	618	2,27	2.19
17	2	T	687	697	1,43	0,96
18	1	R	755	720	-4,86	1.28
19	1	R	783	-	-	1.65
20	1	R	803	815	1,47	1.57

2.5 Modal assurance criterion:

To estimate the quality of the obtained mode shapes, the Modal Assurance Criterion (MAC) is used. First, the auto MAC is computed separately from the numerical and experimental mode shape to investigate the validity of the estimated modes. Then, the MAC between both experimental and numerical is determined to compare two mode shapes obtained from two different modal parameter estimation processes (numerical modal analysis and experimental modal analysis). The MAC between two mode shape vectors can be expressed as follows (Pastor et al.,2012):

$$MAC = MAC(\{\hat{D}\}_j, \{D\}_l) = \frac{\left| \{\hat{D}\}_j^T \cdot \{D\}_l^T \right|}{(\{\hat{D}\}_j^T \cdot \{\hat{D}\}_j^*) (\{D\}_l^T \cdot \{D\}_l^*)} \quad (3.3)$$

Where:

$\{\widehat{D}\}$ and $\{D\}$ are respectively the numerical and experimental mode shapes.

Figure 3.6 shows the results for different mode sets combinations. The MAC values of 1 mean that the two modes are correlated; whereas a MAC value of 0 means the two vectors are orthogonal.

The determination of the angular acceleration using equations (3.1) and (3.2) for each component and the use of the torsional LPM allow the building of the mode shapes for all the modes.

Only the correlated modes are selected, the orthogonal ones are neglected.

From 20 modes, only five modes are identified as consequence their mode shapes are plotted .

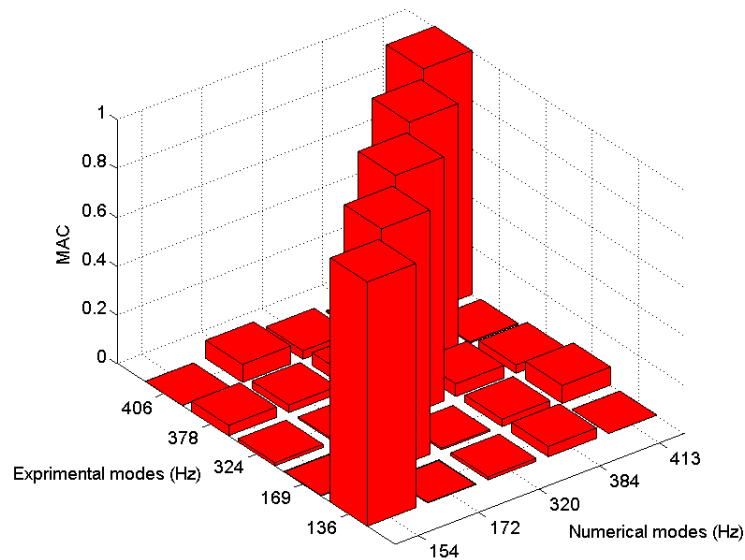


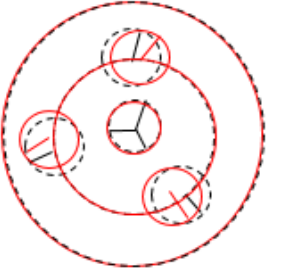
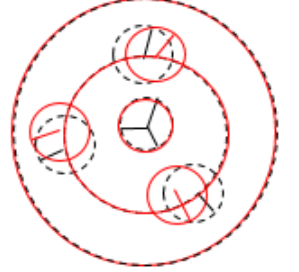
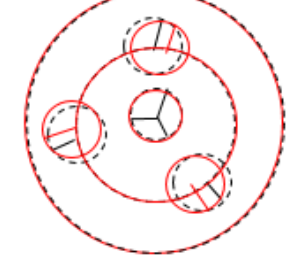
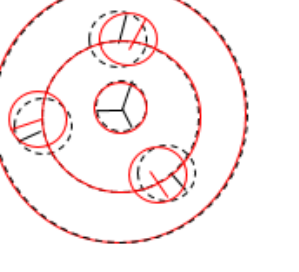
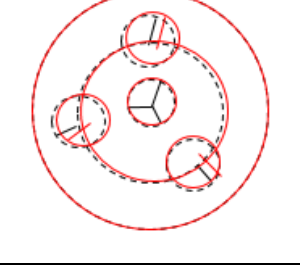
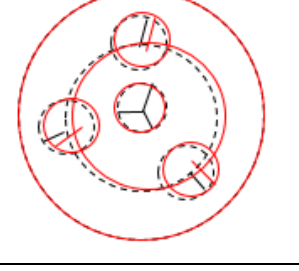
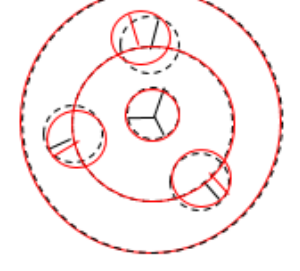
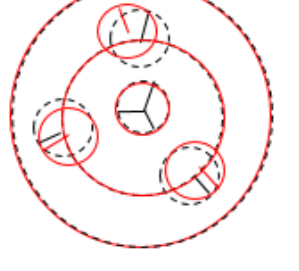
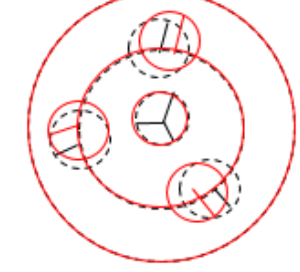
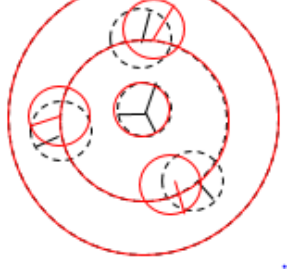
Figure 3. 6. MAC matrices from the mode shapes of the experimental and numerical modes

2.6 Mode shapes:

Table 3.2 shows the first five modes validated by the MAC: Four rotational modes (154 Hz, 172 Hz, 384 Hz, and 406 Hz) and one translational mode (320 Hz). It highlights also the difference between the experimental and numerical modes.

The experimental mode shapes are plotted according to each degree of freedom magnitude and phase in the impacts tests, while the numerical mode shapes provided the mode shapes directly from the eigenvalue problem.

Table 3. 2. Comparison between numerical and experimental mode shapes.

Mode (Hz)	Experimental	Numerical	Interpretation
154 (R)			Planets move in phase
172 (R)			Planets move in phase
320 (T)			Carriers have pure translation
384(R)			Planets move in phase
406(R)			Planets move in phase

What stands out in the previous table is that experimental and numerical mode shapes plotted are close to each other. In addition, the planets set have the same modal deflection and move in phase for the rotational modes. While, the carriers have a pure translation in the translational mode.

3 Influence of meshing stiffness variation on modal parameters:

Mesh stiffness function is the most important function in gear transmission. It is classified as the principal source of vibration. Several developments have been done in literature in order to model it. In this context, (Fernandez et al., 2013) used finite elements modelling and Hertzian contact theory to model mesh functions. Authors start by defining the tooth geometry using the parameters of gear transmission and then compute the gear contact point by considering the analytic formulation of the involute-involute contact. Then, two phenomena were considered: the first one is the nonlinear local deformations near the contact area where an analytical non-linear Hertzian formulation for local deflections is used. The second is the tooth body deflections. Two-dimensional finite elements model of teeth in contact is carried out in order to validate this methodology. The proposed procedure was adopted to model the mesh function.

The main purpose of this part is to study the impact of mesh stiffness variation during one meshing period on the modal parameter. The spaces between planets were considered with regular interval and the contact sun-planets and ring planets were sequentially phased.

Figure 3.7 displays the mesh stiffness functions.

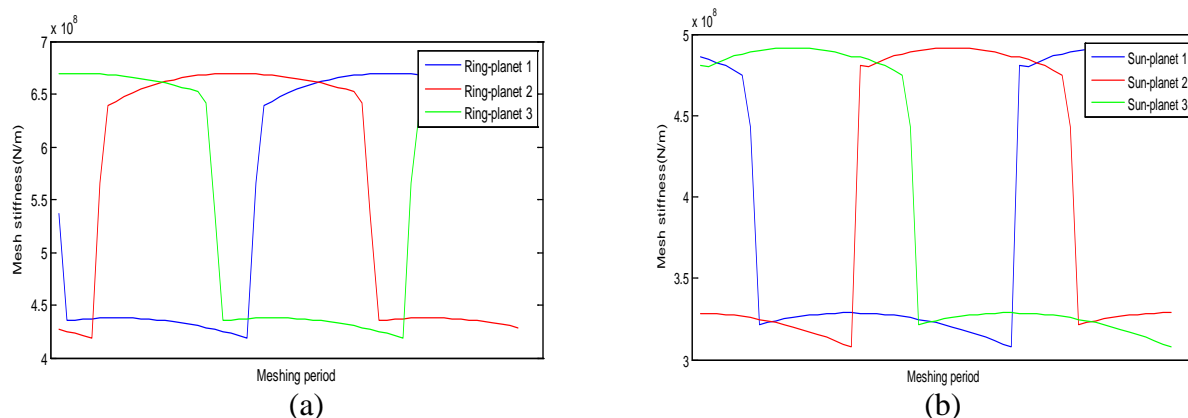
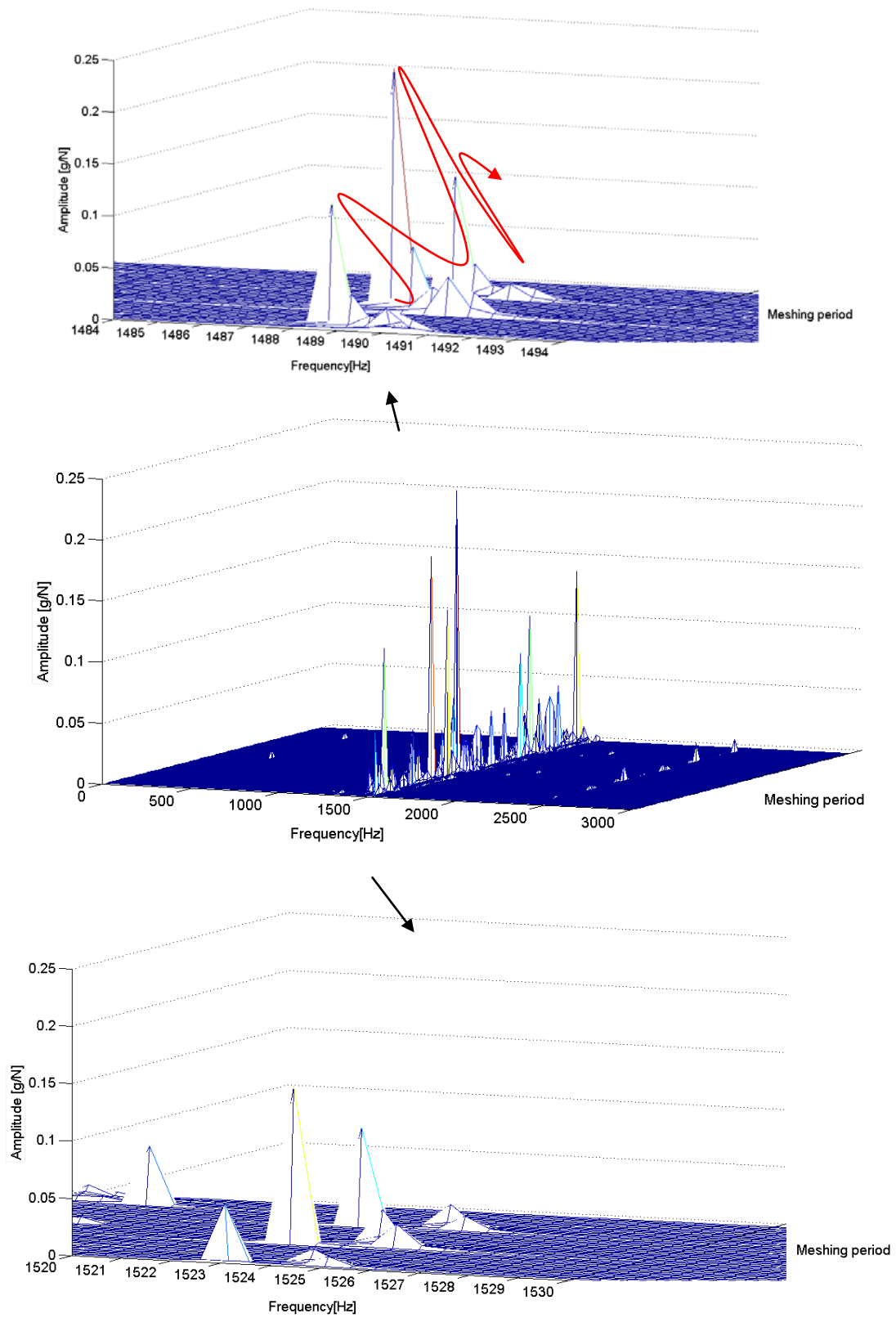


Figure 3. 7. Mesh stiffness function (a) Sun-planet (b) Ring-planet

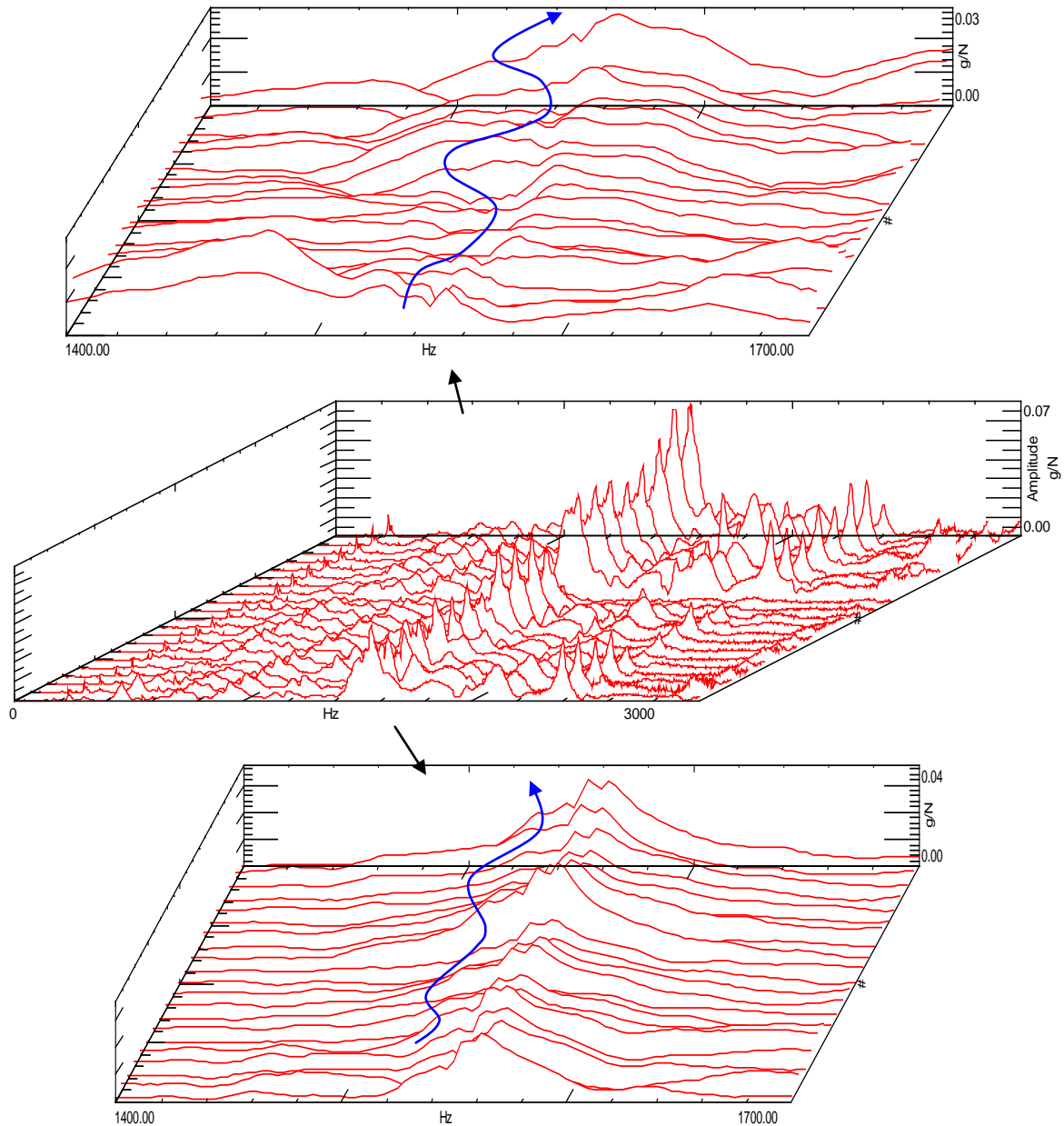
The meshing period was subdivided into equidistant point. For each point FRF were determined experimentally and numerically. The evolution of the FRF respecting the mesh stiffness values in one meshing period are displayed in Figures 3.8a and 3.8b. For both numerical and experimental

results, the variation of mesh stiffness introduced a slight deviation on FRF amplitude presented by a deviation of natural frequencies. Moreover, this deviation is repeated three times in one meshing period. This behaviour is explained by the fact that the contact sun-planets and ring planets are sequentially phased and the number of planets is three. What stands out in Figures 3.8.a and 3.8.b is the variation of natural frequencies, a variation by 2% in the numerical results and by 3% in the experimental results is observed.

Furthermore, the variation of FRF amplitude during the meshing period which is caused by the variation of contact points location between mating teeth and the variation of meshing stiffness values.



(a)



(b)

Figure 3. 8. Waterfall plot of FRF on the test ring (a) Numerical (b) Experimental

4 Operational modal analysis:

4.1 Experimental setup:

Experimental measurements were carried out when the system is running in stationary conditions (the input load and input speed are fixed). The accelerations were measured on the test ring.

4.2 Power spectral density function:

Experimentally, LMS test lab requires Power Spectral Density (PSD) function as input data, whereas, analytically, OMA is applied after computing the PSD function. First of all, the Welch's method can be applied by computing the Discrete Fourier Transforms DFT of the time response signal (G. Arfken 1985):

$$Y(w) = \sum_{k=0}^{N-1} w_k y_k \exp(-jwk\Delta t) \quad (3.4)$$

where N is the length of y_k . y_k and $Y(w)$ are respectively the input signal and output signal respectively, w_k : denotes the time window and Δt is the time increment.

After determining the DFT, Cross Correlation Function (CCF) is obtained using the following equation (E. Orlowitz, A. Brandt 2013):

$$E_{21}(m) = \frac{1}{\sum_{k=0}^{N-1} |w_k|^2} Y_1(w) Y_2^H(w) \quad (3.5)$$

$Y_1(w)$ is the conjugate DFT of y_1 , which is the reference, and $Y_2(w)$ is the DFT of y_2 in the frequency domain. Moreover, the inverse of this product produces a biased correlation function.

The Cross Power Spectral Density (CPSD) functions are identified experimentally and numerically and the different modal parameters are extracted using the stabilization diagram.

Now, after getting the experimental and the numerical CPSD, the stabilization diagram is used to estimate the experimental modal proprieties whereas the numerical modal proprieties are identified directly by solving the eigenvalue problem.

Figures 3.9.a and 3.9.b show respectively the CPSD on the fixed ring obtained by the experimental test and the numerical model.

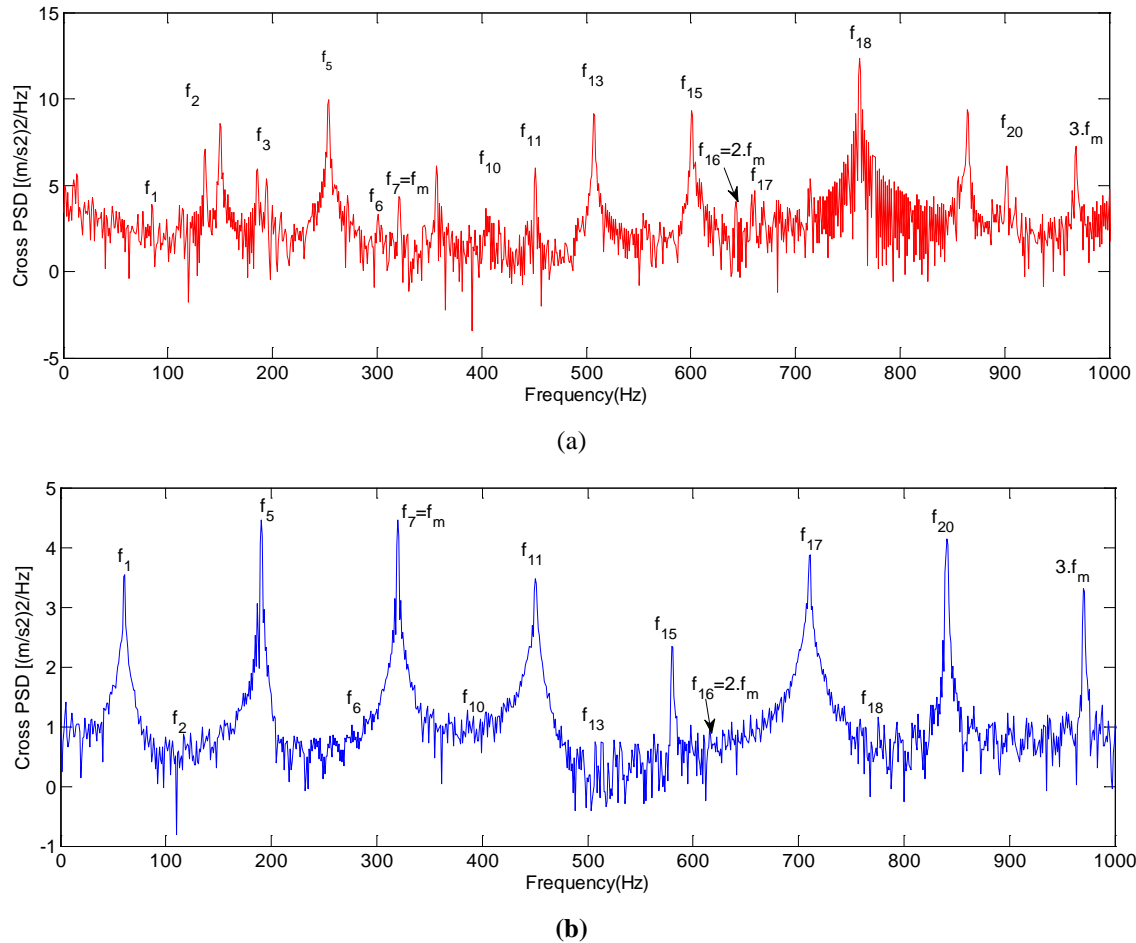


Figure 3. 9. Cross power function determined on the fixed ring (a) Experimental (b) Numerical

It can be also observed through figure 3.9 that the gear mesh frequency and harmonics appear on the CPSD function. A distinction on amplitude and a frequency is observable both on experimental and numerical cases.

The amount of difference on amplitude is explained by the fact that several parameters like the housing, the elastic coupling and the effect of friction are not considered in the model. Concerning the difference in frequency, the experimental CPSD contains more natural frequencies than the numerical CPSD. This distinction is explained by several phenomena and parameters such as the white noise, the effect of temperature as well as the elastic coupling connecting the motor shaft to the gear shaft. Other modes related to structure are not considered in the numerical model for example the arm, the motor and the housing.

4.3 Natural frequencies and damping identification:

In order to identify modal parameters, we follow the same procedure adopted in EMA.

The identified modes are listed in table 3.3 associated with their multiplicity, damping and natural frequencies.

Table 3.3. Modal parameters estimated during OMA.

Mode	Multiplicity	Experimental	Analytical	Error (%)	Damping (%)
1	1	74	75	-1,35	3,34
2	1	129	132	-2,33	3
3	1	248	260	-4,84	3,11
4	2	298	300	-0,67	3,42
5	2	322	323	-0,31	3,01
6	1	394	391	0,76	3,27
7	1	432	436	-0,93	3,51
8	2	540	521	3,52	2,29
9	1	570	592	-3,86	3,11
10	1	629	618	1,75	3
11	2	643	649	-0,93	3,12
12	1	747	781	-4,55	2,85
13	1	888	910	-2,48	3,07

It is clear in table 3.3 that the error between the analytical and experimental natural frequencies is lower than the error determined using EMA. Also, data from this table shows precisely the value of the error for each mode. This phenomenon can be explained the impact of the meshing stiffness variation on the natural frequencies as mentioned in section 3. The natural frequencies can change from a point to another in one meshing period. It is also noticed that the modes ($f_3, f_4, f_8, f_9, f_{12}, f_{14}, f_{19}$) are missing. This fact is may be due to that these modes are not excited in stationary conditions,. For this reason, another type of OMA is required.

5 Order based modal analysis:

5.1 Experimental setup:

In order to overcome the problem raised by the use of EMA and OMA, Order Based Modal identification OBMA is implemented. In this method, the measurements are carried out during run up regime. During this regime, there will be cross of several natural frequencies.

The variation of speed during this regime is performed by the help of the frequency converter Micromaster 440 as well as LMS test lab “acquisition system”.

5.2 Order tracking:

While the speed is variable, the order tracking (OT) method should be used in order to estimate order function, (Fyfe and Munck, 1997).

Several OT methods could be used such as Time Domain, Sampling-Based Fast Fourier Transform (FFT), Angle domain, Vold-Kalman (VK) Filter-Based and Time Varying Discrete Fourier. In the studied case, the angle domain is selected as order technique during OBMA test. Data are acquired with a uniform Δt and then resembled to the angle domain using an adaptive digital resampling algorithm. As a result, the uniform Δt data become uniformly spaced angle data $\Delta \theta$. The amplitude and phase estimates of the orders are obtained by processing the recorded signals with a Discrete Fourier Transform (DFT) instead of an FFT for computational flexibility in performing the transform without being restricted to a power of two numbers of samples. In order to achieve the time domain data to angle domain data transformation, a reference signal must be selected to define the time instant at which the uniform angular intervals have been spaced. Usually, this signal is considered to be the tachometer signal measured on a reference shaft of the operating machine.

The kernels of the Fourier transform were computed as shown in Eqs. (3.6) and (3.7), where o_m is the order which is being analyzed:

$$a_n = \frac{1}{N} \sum_{n=1}^N x(n\Delta\theta) \cos(2\pi o_m n\Delta\theta) \quad (3.6)$$

$$b_n = \frac{1}{N} \sum_{n=1}^N x(n\Delta\theta) \sin(2\pi o_m n\Delta\theta) \quad (3.7)$$

Frequency and orders are closely the same: a measure of events over an observation frame. The order should be multiple; they can be computed according to the following expression:

$$Order = \frac{freq.rot.In}{freq.rot.out} \quad (3.8)$$

During this test, the structure is excited instantly using the frequency inverter. A ramp of speed was applied on the structure at 1300 rpm over 15s as shown in the following figure:

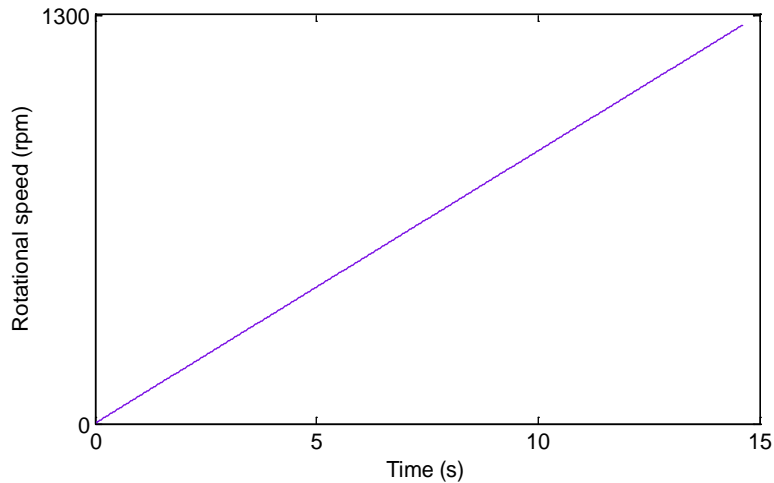


Figure 3. 10. Evolution of rotational speed

The principal order can be resumed in the following table.

Table 3. 4. Principal order

Order	Correspondence Order	Correspondence meshing frequency
1	12.88	1.GMF
2	25,25	2.GMF
3	38.49	3.GMF
4	51.32	4.GMF
5	64.15	5.GMF

The frequency at which a rotating system is operating can be calculated from an order and the rotational speed (expressed in rpm) via the equation below:

$$Frequency = \frac{(order).rpm}{60} \quad (3.11)$$

After measurements, order map is plotted (figure 18). It is clear from the figure that the tachometer detects only 12.88 and 25, 25. This error may be caused by the vibration issued from the test bench, the tachometer vibrates also and the accurateness of the encoder zebra can cause a variation on mesh order. Also, error can be caused by the fact that the extremity of the encoder zebra are not matching well.

Figure 3.1 show the OT map.

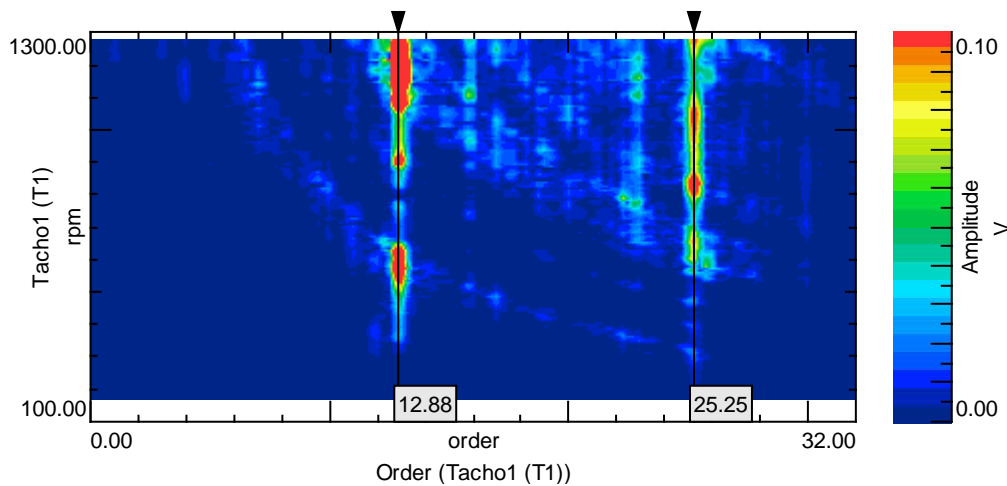


Figure 3.11. Order map

Only the two first orders are displayed in figure 3.11. The order 12.88 corresponds to the first meshing order while the order 25.25 is that of the 2nd gear mesh order. Therefore, the OT will be achieved by examining in details these orders and ignoring all the others.

The order resolution was set from 0.01 for a maximum order equal to 32.

Figure 3.2 displays the two first selected orders measured on the test gear ring.

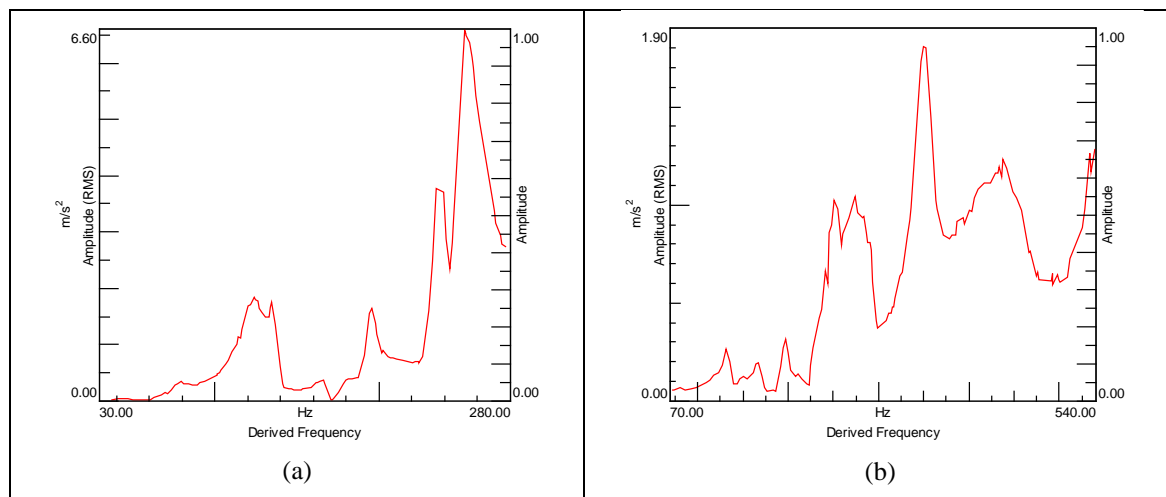


Figure 3.12. Order function (a) Order 1 (b) Order 2

While examining figure 3.3, some peaks can be identified directly even before applying the Polymax method to these orders to extract the modal parameters.

5.3 Natural frequencies, damping and modes:

Before applying the PolyMAX method to order function and using stabilization diagram, the modal parameters can be estimated.

Table 3.4 shows a comparison between the numerical and experimental natural frequencies using OT during the run-up test as well as the amount of error and the damping ratio of each mode.

Table 3. 5. Modal properties during the run-up test.

Mode	Experimental	Analytical	Error (%)	Damping ratio (%)
1	72	77	6,49	3,2
2	125	154	18,83	3,6
3	159	172	7,56	3,3
4	191	197	3,05	3,7
5	250	241	-3,73	3
6	294	291	-1,03	3,41
7	325	320	-1,56	3,13
8	354	342	-3,51	3,5
9	375	384	2,34	3,76
10	404	413	2,18	3,7
11	441	436	-1,15	3,29
12	471	-	-	3,15
13	521	531	1,88	3,41

The difference between the achieved experiments and the analytical model results is noticeable. The frequency error is lower, and the modal damping is higher than that obtained by the EMA.

6 Comparison between different modal analyses:

The comparison between the different techniques is presented through contrasting the natural frequency modal damping and the random error (table 3.5).

It is clearly noticed from this table that the natural frequencies identified with EMA are close to those by OBMA. In the other hand, some natural frequencies are missed for the OMA.

The variation of natural frequencies is related to several factors like the evolution of temperature in the inner component as well as the variation of the boundary conditions and the influence of gear mesh stiffness.

The difference between the three methods is more accentuated when identifying damping ratio.

The modal damping increases when moving from EMA to OMA and OBMA.

Table 3. 6. Estimated modal parameters for the three techniques.

Mode	Analytical	EMA		Frequency Error (%)	OMA		Frequency Error (%)	OBMA		Frequency Error (%)
		f_e (Hz)	Damping ratio (%)		f_e (Hz)	Damping ratio (%)		f_e (Hz)	Damping ratio (%)	
1	77	76	0.77	1,3	74	3,34	-1,35	72	3.2	6,49
2	154	136	1.36	11,69	129	3	-2,33	125	3.6	18,83
3	172	169	1.61	1,74	-	-	-	159	3.3	7,56
4	197	195	1.49	1,02	-	-	-	191	3.7	3,05
5	241	251	1.06	-4,15	248	3,11	-4,84	250	3	-3,73
6	291	301	1.57	-3,44	298	3,42	0,76	294	3.41	-1,03
7	320	325	1.41	-1,56	322	3,01	-0,31	325	3.13	-1,56
8	342	352	1.38	-2,92	-	-	-	354	3.5	-3,51
9	384	378	2.00	1,56	-	-	-	375	3.76	2,34
10	413	406	2.54	1,69	394	3,27	0,76	404	2.7	2,18
11	436	436	2.09	0	432	3,51	-0,93	441	3.29	-1,15
12	-	466	2.04	-	-	-	-	471	2.15	-
13	531	526	2.16	0,94	540	2,29	3,52	521	3.41	1,88

Let's focus on the difference between EMA and OBMA. These two methods allow the identification of almost all frequencies. Table 3.7 shows the difference between identified natural frequencies and damping using EMA and OBMA techniques.

Table 3. 7. Difference between the results of EMA with respect to the OBMA test.

Difference of	EMA vs OBMA	
	f_n [%]	d_n [%]
1	4	2.43
2	11	2.24
3	10	1.69
4	4	2.21
5	1	1.9
6	7	1.8
7	0	1.7
8	-2	2.1
9	3	1.7
10	2	0.16
11	-5	1.2
12	-5	0.11
13	5	1.25

It can be concluded from table 3.6 that the estimated dampings have a smaller deviation between the two tests than the estimated natural frequencies. This fact is expected since the inaccuracy of the frequency estimates is well known to be larger than the damping estimation (Orlowitz and Brandt 2017). The results coming from EMA are closed to others obtained OBMA results. The amount of difference can be due to the variation of behavior of such parameter from a static test to dynamic one.

Following these results, it is assumed that OBMA technique is an efficient technique to understand the dynamic behavior of the system and is more useful in the extraction of the modal proprieties.

7 Modal proprieties sensitivity to load variation using OBMA

In this section, the influence of load on modal parameters of the back-to-back PGs is investigated. The experimental tests were carried when the test bench is excited in run up condition for different levels of load. The obtained results were compared to others obtained numerically.

7.1 Experimental set up:

For the dynamic test, the motor is driven in run up. The sensors are mounted on the two rings in a tangential direction in order to extract the angular accelerations of the components and an optical tachometer is used to measure the instantaneous angular velocity.

For both experiments and numerical simulation, a random speed between 0 and 1000 rpm is imposed to the electrical motor over 15 s.

For signal processing, Spectrogram is plotted for both experimental and numerical vibration signals. It provides very useful information about the evolution of gear mesh frequencies and harmonics. Numerically, a Matlab function “Spectrogram” with a Hamming window of 1000 samples and 50% overlap giving a frequency resolution of 2 Hz/line is implemented for simulated vibration signals. OT method, as mentioned in the previous chapter, will be adopted to remove speed fluctuations from the signal and enable the tuning of order function to have a confident analysis with high accuracy. After the OT process and removing the fluctuations of speed from the signal, order function can be extracted.

To estimate the most important orders, an angle domain OT method was developed and stabilization diagram is adopted to extract the modal parameters for each load level.

7.2 Effect of load on the dynamic behavior:

The same load levels used previously in EMA are used in the dynamic test and implemented in the numerical model. The main load influence is in the gear meshes stiffness. The stiffness functions mean value increase when the loads increase (Fernandez et al., 2013). Also, the influence of load on the inertia and mass of the reaction ring is considered too.

However, these functions are modelled as square functions according to (Lin and Parker, 1999); (Maatar, 1995).

During the run-up regime, (Viadero et al., 2014), (Khabou et al., 2011) claim that the period of mesh stiffness function decrease when the speed increase,

Figure 3.13 shows the evolution of ring-planets and sun-planets gear mesh stiffness functions on the test gear set during run-up.

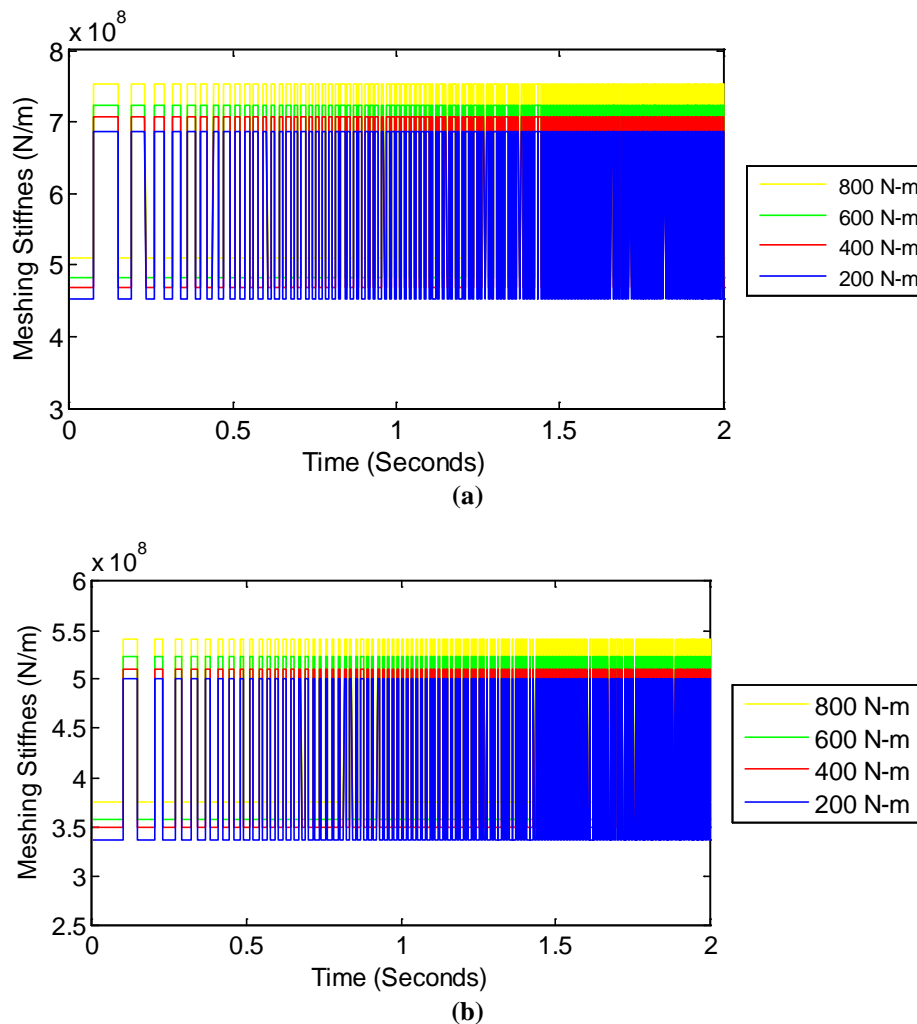


Figure 3. 13. Mesh stiffness function for the ring- planets (a) and sun-planets (b) on the test gear set during run up

After taking into account this gear mesh stiffness function in the equation of motion, time response is computed, whereas the measured acceleration of the fixed ring is recorded for the different load levels. It can be noticed from the figures 3.14 and 3.15 that the vibration amplitude is increasing respectively with time. This matter could be explained by the way that during the run-up regime the speed and the accelerating torque is increasing allowing the increase of vibration. The influence of loading condition on dynamic behavior during start-up regime on the measured and simulated acceleration is manifested by the increasing of vibration level with the increasing of load. This phenomenon can be explained to the influence of several parameters like the elastic coupling, the contact friction and the effect of the oil film stiffness (Xiao et al 2019). Figures 3. 14 and 3. 15 display the acceleration measured and simulated on the fixed ring.

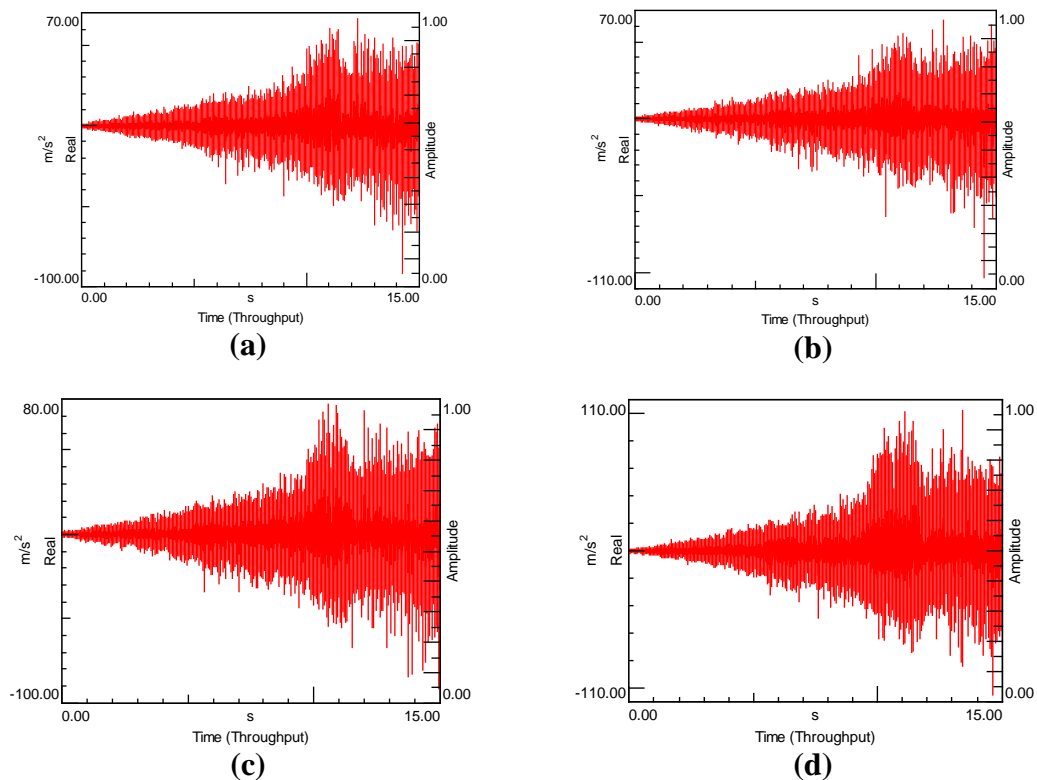


Figure 3. 14. Experimental time response measured on the fixed ring (a) 200 N-m (b) 400 N-m (c) 600 N-m (d) 800 N-m

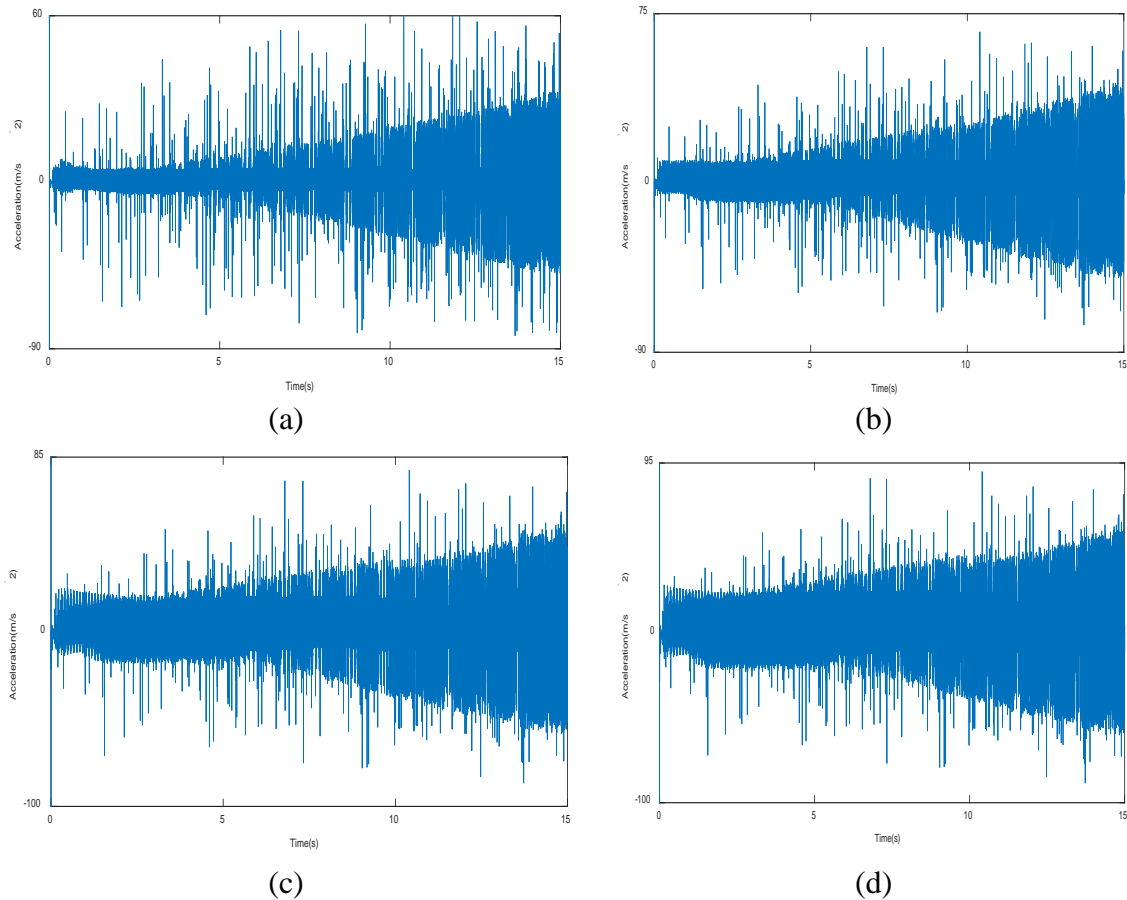


Figure 3. 15.Numerical time response simulated on the fixed ring (a) 200 N-m (b) 400 N-m (c) 600 N-m (d) 800 N-m

It is noticed that the acceleration amplitude increases as the load increase. This phenomenon is related to the increasing of the meshing stiffness amplitude and the decrease of the period of teeth in contact when the speed increases. This fact can introduce instability on the system. (Drago 2009) confirmed that the run up regime is critical when the system is loaded.

The measurement is also carried out on the inner shaft that connects the two suns. Figure 3.16 shows the time response signal issued from the strain gauge placed in the inner shaft. The magnitude of this input load is well noticeable on the gauge signal; also the trend of the strain gauge signal is with agreement with the input speed.

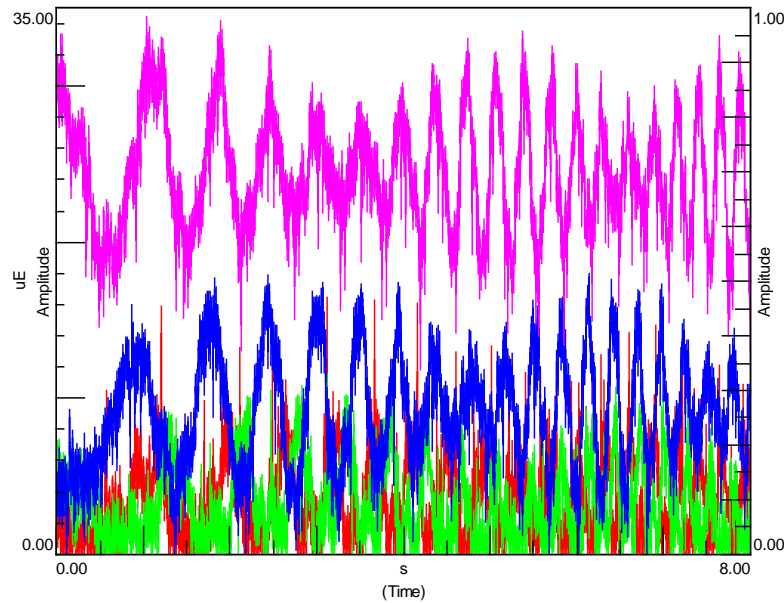


Figure 3. 16. Strain gauge signal: red: 200 N-m, green: 400 N-m, blue: 600 N-m, pink: 800 N-m

The collected signals from the strain gauge are processed with the stabilization diagram in order to estimate the modal parameters related to the shaft. As mentioned, the system was driven in run-up regime, so it is excited in non constant period as consequence the meshing frequencies cannot be not harmonic. For this reason, a time-frequency presentation (Short Time Fourier Transform) is used.

Figure 3.17 and 3.18 display the STFT issued from simulation and experiment for acceleration on the test ring gear. An interesting energy increase is remarked in the spectrograms between 0 and 1 kHz band proving an excitation of structural resonances. Oblique lines appear on the STFT map showing the increase of the gear mesh frequency and its harmonics. Furthermore, vertical lines are observed and there are particular zones where the higher amplitude corresponds to the cross of some natural frequencies of the system allowing their immediate identification.

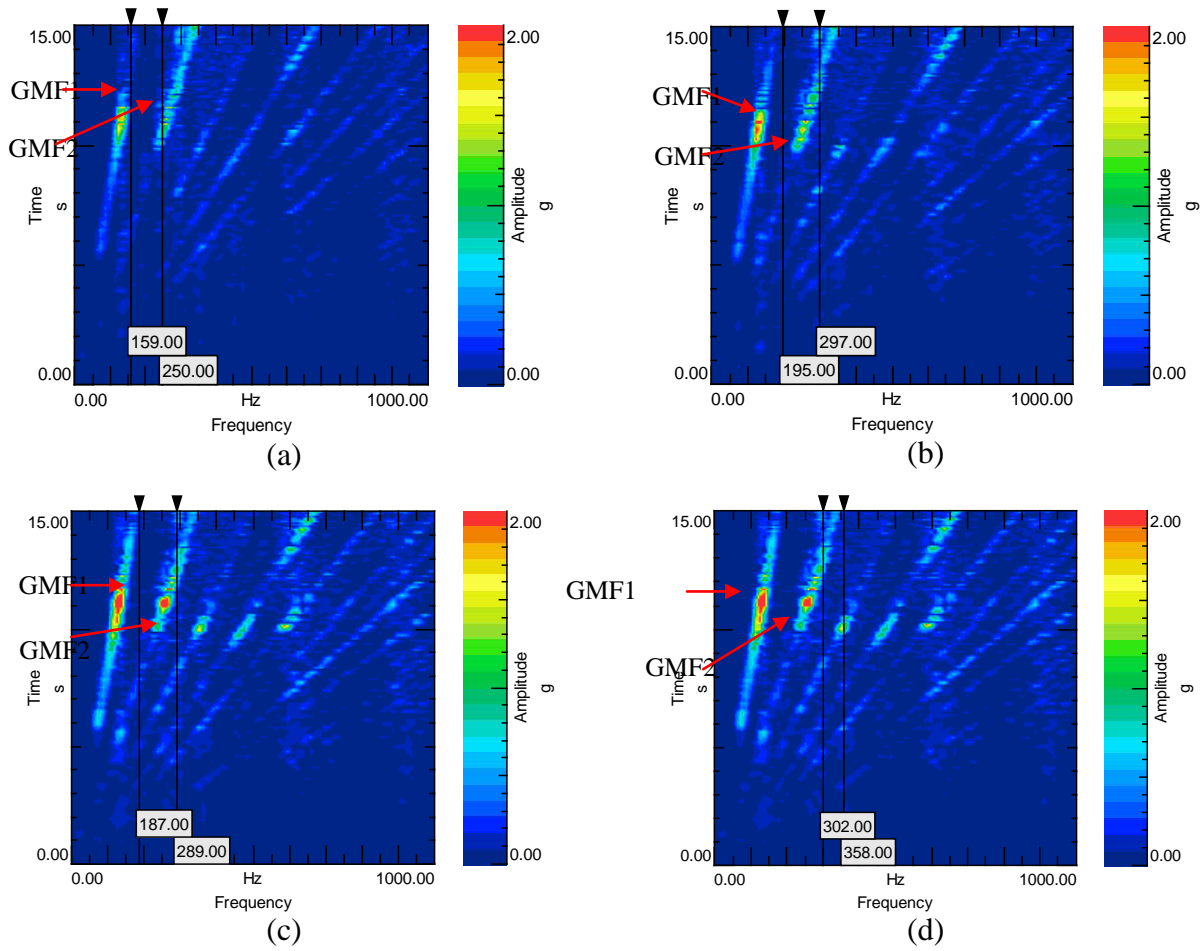


Figure 3. 17. Experimental STFT on the fixed ring (a) 200 N-m (b) 400 N-m (c) 600 N-m (d) 800 N-m.

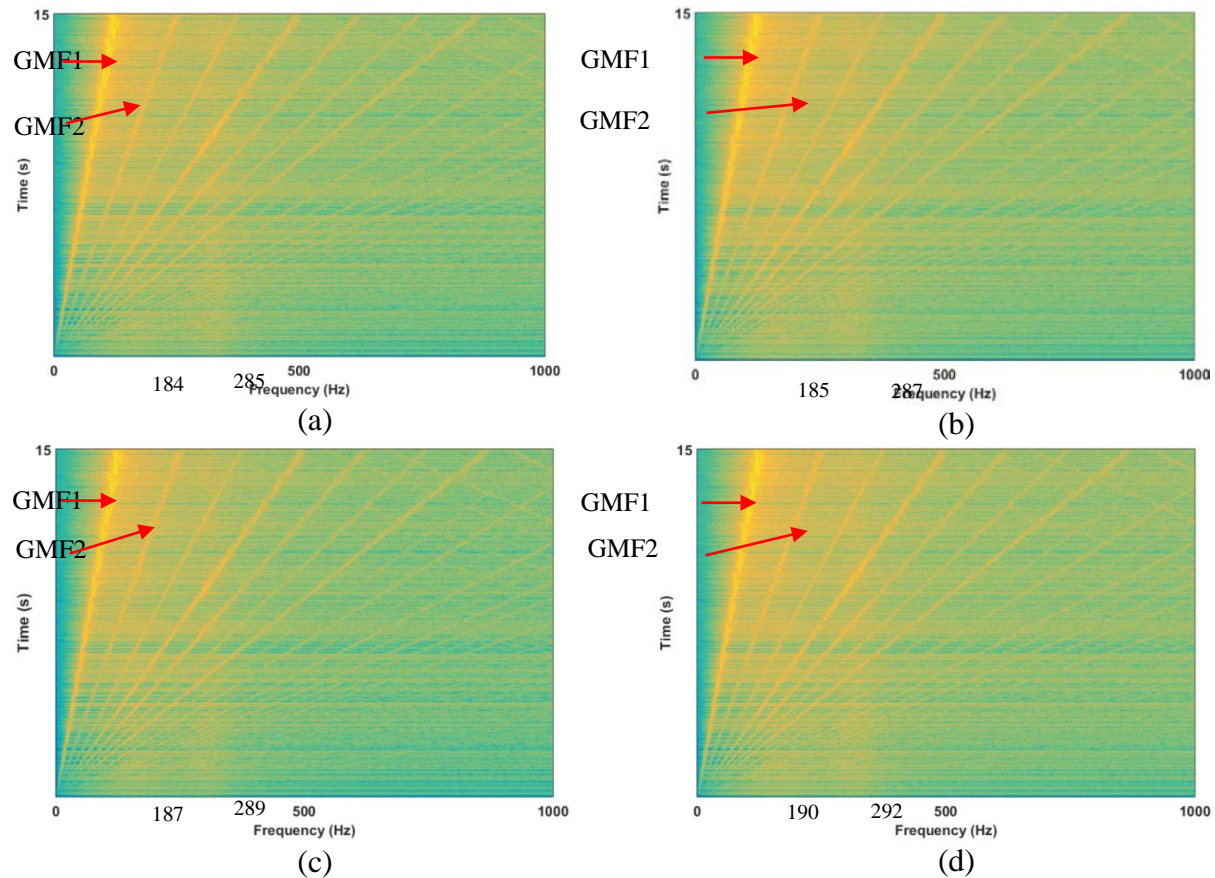


Figure 3. 18. Numerical STFT on the fixed ring (a) 200 N-m (b) 400 N-m (c) 600 N-m (d) 800 N-m.

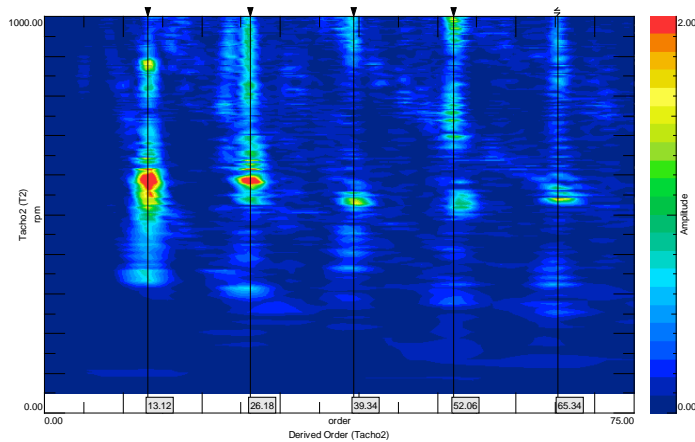
It can be noticed that the amplitude of gear mesh frequency increase with load. An important energy distribution are presented on the second gear mesh frequency, this phenomenon was highlighted by Mitchell (Mitchell, 1982). He defined an intermediate frequency band which is produced by the resonance of gear components of a turbine generator. In our case, during run up regime, with the increasing of the speed, the period of double teeth pairs contact decrease. Also, the contact area between teeth increase which leads to an increasing of meshing forces, a variation of the pressure angle and therefore an increase of the contact ratio (Hammami et al 2016),(Fernandez et al 2013). Moreover, the inertia and the mass of the reaction ring gear increase when masses are added.

7.3 Order functions:

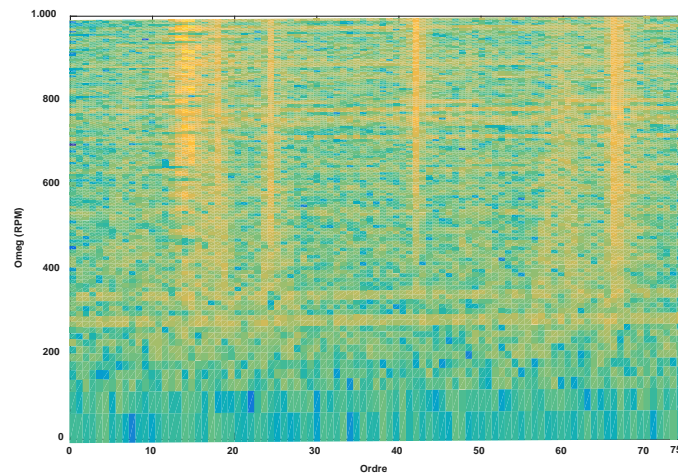
To track the order, angle domain method is used. This method was investigated experimentally and numerically. It uses tachometer signal as input data as well as the response signal.

Figure 3.19 illustrates the obtained OT map during the experimental and numerical test.

The most important orders observed on the order maps are displayed in the following figure.



(a)



(b)

Figure 3. 19. Order map (a) experimental (b) numerical

Typically, the principal order corresponding to the mesh frequency should be multiple to consider its harmonics. It is noticed a slight difference between the presented numerical and experimental order map. This difference can be explained by the influence of some parameters such as the way how the strip band is rolled and the influence of the white noise issued from the test bench. Meanwhile, the order resolution was set from 0.01 for a maximum order equal to 75.

In order to estimate the modal parameters, order 65 will be processed in the order map.

Figure 3.20 and 3.21 show respectively the experimental and numerical order “65” for the different levels of load.

The effect of load appears on order response since the amplitude of accelerations increases as the load increase.

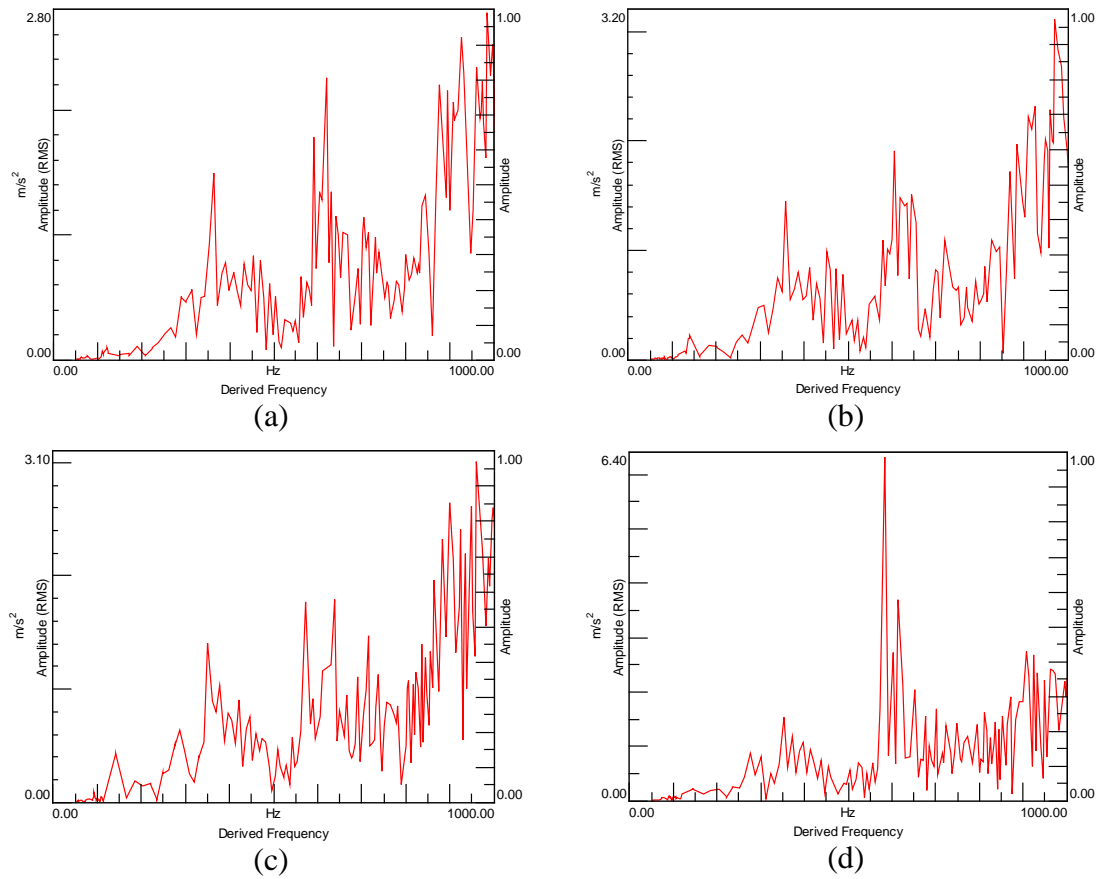


Figure 3. 20. Experimental order function measured on the fixed ring (a) 200 N-m (b) 400 N-m (c) 600 N-m (d) 800 N-m.

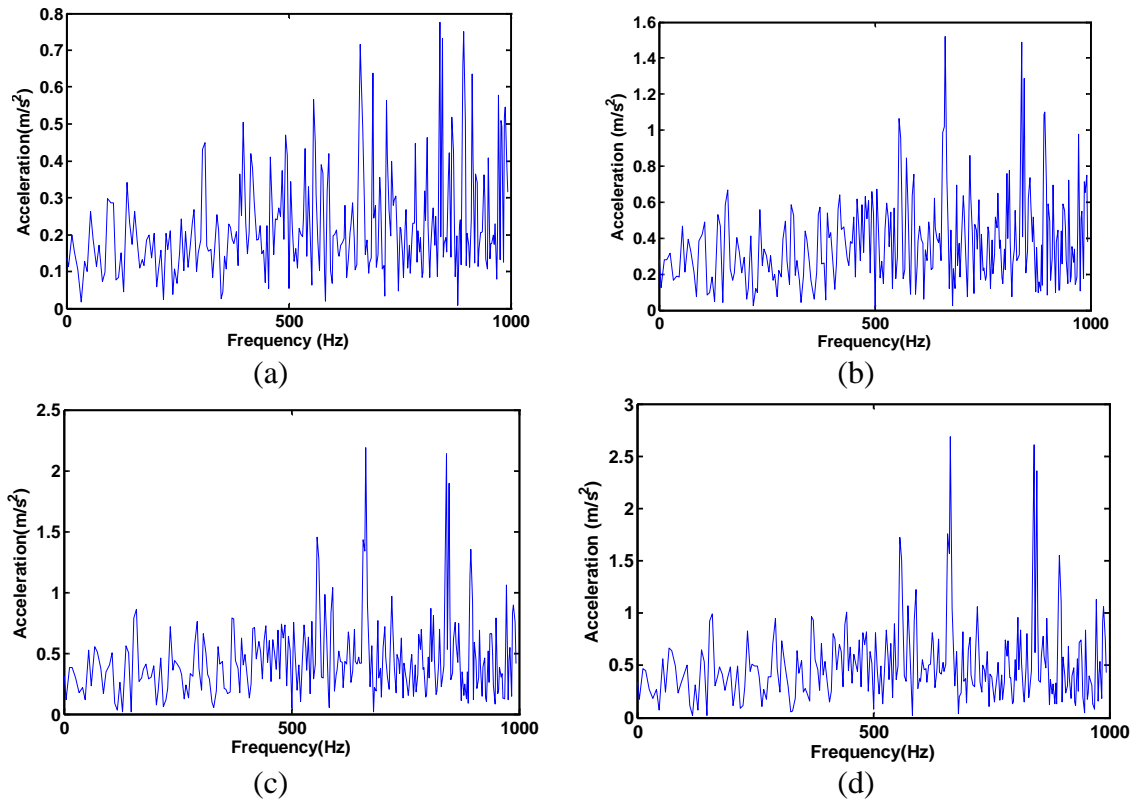
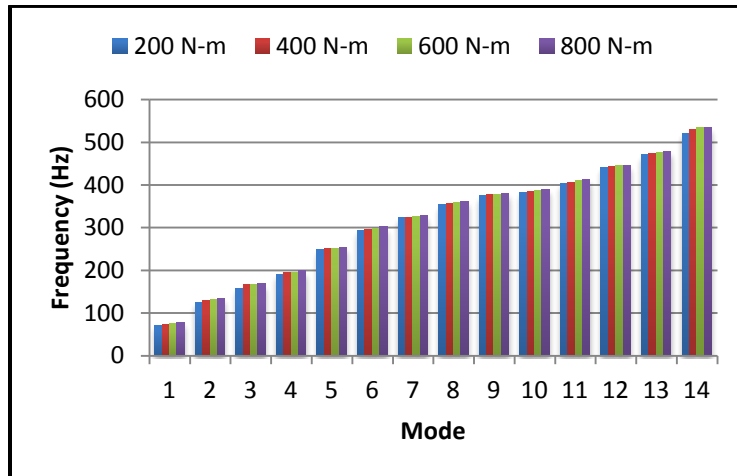


Figure 3. 21. Numerical order function simulated on the fixed ring (a) 200 N-m (b) 400 N-m (c) 600 N-m (d) 800 N-m

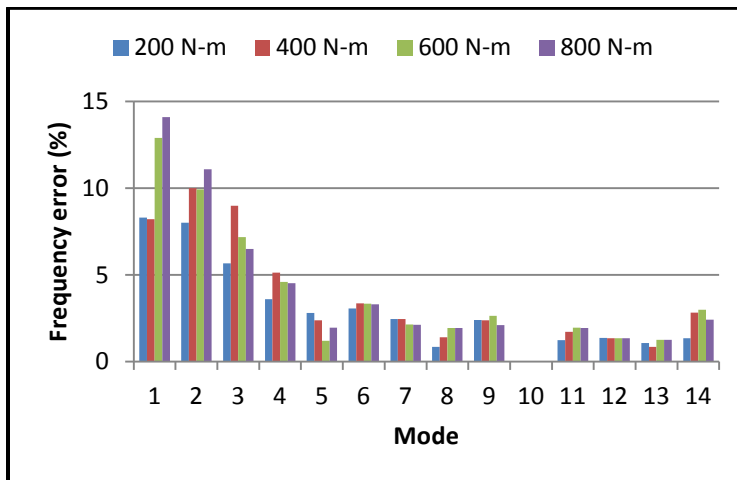
7.4 Natural frequencies and modal damping sensitivity to the load:

The OBMA techniques allow the estimation of modal parameters during run up condition and using order function.

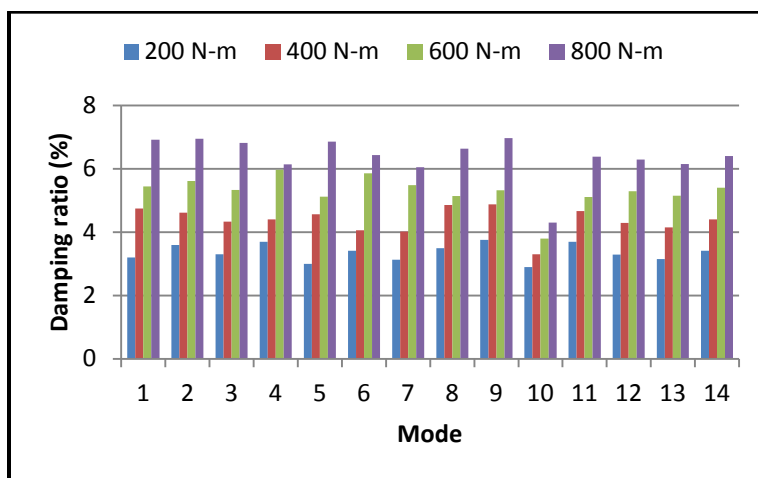
The effect of load on modal parameters is well noticeable confirming that natural frequencies and modal damping depends on it. With increasing the load, the contact area between teeth increase, so the bending and fillet stiffness increase as well as mesh stiffness function. Thus, it was expected because of the mass matrix, stiffness matrix and the damping matrix change, (Ericson and Parker (2014)).



(a)



(b)



(c)

Figure 3. 22. Influence of load on (a) experimental natural frequencies (b) frequency error (c) damping ratio.

Fourteen modes are estimated experimentally for the different load cases. The natural frequencies (Figure 3. 4.a) and the modal damping (Figure 3. 5.c) are varying according to the load variation as well as the frequency error (Figure 3. 6.b).

Obviously, natural frequencies and modal damping varies. Figure 3.22.b shows the frequencies errors between experimental test and numerical results. The error related to mode 10 is missing because the natural frequency associated to the shaft was identified only experimentally. The observed errors are due to the fact that bearings are considered as isotropic. Moreover, this phenomenon is caused by the influence of mesh stiffness variation on the modal proprieties. The natural frequencies may change by about 3%. Also an important deviation appears on the modal damping.

8 Conclusion:

In this chapter, three modal analyses techniques which are EMA, OMA and OBMA are applied on PGs with power recirculation in order to extract the modal parameters. For EMA, natural frequencies, damping ratio and modes shapes are identified; the MAC is used in order to compare the experimental and numerical modes shapes. The influence of meshing stiffness variation on the modal properties is highlighted.

For the OMA and OBMA, only natural frequencies and modal damping are identified. A comparison between identified natural frequencies using these three techniques are performed, the comparison is based on natural frequencies and modal damping.

It is noticed that the comparison is difficult because the OMA technique suffers from missing modes. This phenomenon is due to the fact that some modes cannot be excited during the stationary conditions. For this reason, a comparison between the EMA and the OBMA is presented.

No significant differences are found between the modal parameters obtained by EMA and OBMA. The natural frequencies are deviated by less than 11% and those of the damping ratios by less than 2.43%.

In addition, OBMA is an interesting technique allowing the identification of the modal proprieties of system that works under its real conditions. Moreover, the effect of load on modal properties by using the OBMA is investigated and the experimental results are correlated to results obtained by the numerical model. Angle domain OT method is developed and correlated to experimental

results. The important order is extracted and highlighted in the text. Stabilization diagram is used to extract the natural frequencies and the modal damping.

After using modal analysis techniques to characterize the PG system, a further study on the dynamic behavior of the system in non stationary regimes will be highlighted in the next chapter

**Chapter 4: Dynamic behavior of planetary gear in
stationary and non-stationary conditions**

Chapter 4: Dynamic behavior of planetary gear in stationary and non-stationary conditions

Sommaire

1	Introduction	98
2	Stationary regime:.....	98
3	Effect of gravity of carrier on the dynamic behavior of PGs	105
4	Run up regime:	107
5	Variable loading regime	110
6	Variable speed regime	114
7	Conclusion:	117

1 Introduction

The gearbox systems are frequently running under variable loading and variable speed conditions. The diagnosis and the characterization of those systems under the non stationary regime is a challenge for research and investigation. In this chapter, the dynamic behavior of PGs is investigated in stationary condition, run up regime, variable speed and variable loading conditions. The experimental measurements are compared to the numerical results computed through developed model.

2 Stationary regime:

In this section, the system is set to run under fixed input speed (1500 rpm) and fixed input load (300N-m). Sensors are mounted on both fixed and free ring and the accelerations are recorded on the test ring where the sensors are mounted. The time responses were determined experimentally and computed from the model presented in chapter 2. A complete characterization of the system leading to modulation sidebands of PG sets due to rotation of the planet carrier will be presented. In this context, Inalpolat and Kahraman (Inalpolat and Kahraman, 2009), presented a classification of the PG based on the sidebands and the mesh phasing functions, (Table 4.1).

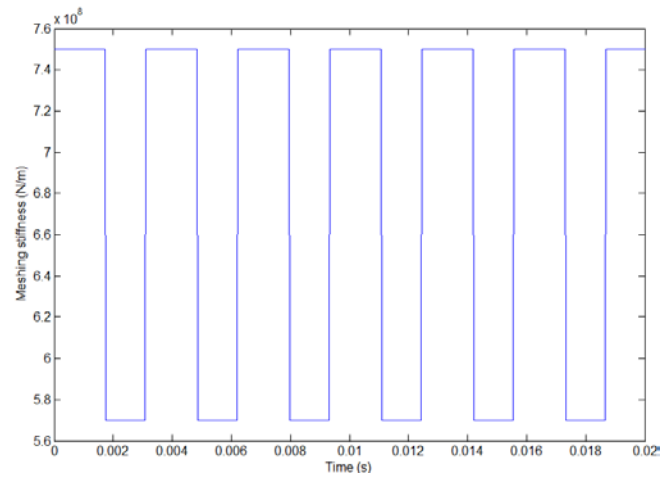
Table 4. 1. PG classification (Inalpolat and Kahraman, 2009).

N	1	2	3	4	5
Case	Planets equally-spaced and in-phase	Planets equally-spaced and sequentially phased	Planets Unequally-spaced and in-phase	Planets unequally-spaced and sequentially phased.	Planets unequally-spaced and arbitrarily phased.
Spacing of planets	$\psi_i = \frac{2\pi(i-1)}{N}$	$\psi_i = \frac{2\pi(i-1)}{N}$	$\psi_i \neq \frac{2\pi(i-1)}{N}$	$\psi_i \neq \frac{2\pi(i-1)}{N}$	$\psi_i \neq \frac{2\pi(i-1)}{N}$
Phasing of gear meshes	$\frac{z_r \psi_i}{2\pi} = n$ (n : integer)	$\frac{z_r \psi_i}{2\pi} \neq n$ $\sum_{i=1}^N Z_r \psi_i = m\pi$	$\frac{z_r \psi_i}{2\pi} = n$	$\frac{z_r \psi_i}{2\pi} \neq n$ $\sum_{i=1}^N Z_r \psi_i = m\pi$	$\frac{z_r \psi_i}{2\pi} \neq n$ $\sum_{i=1}^N Z_r \psi_i \neq m\pi$

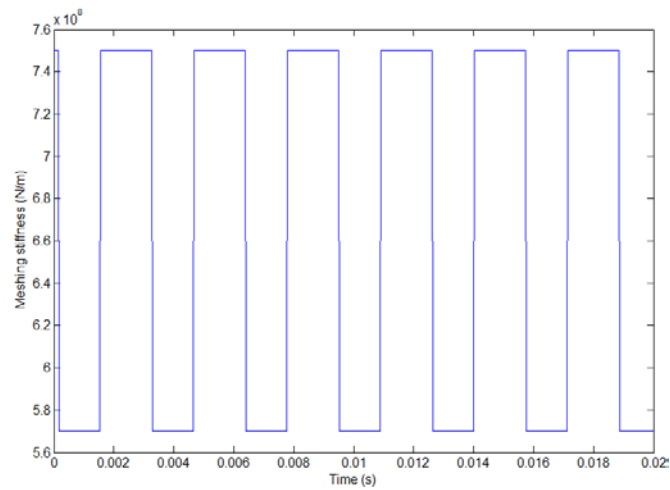
Our studied PG falls in case n° 2. In fact, three equally spaced planets are considered for each PG. The ring planets and sun planets meshing stiffness functions are modeled as square functions taking into account the mesh phasing.

The position of each planet i ($i=1, 2, 3$) in each stage j ($j=r, t$) is defined by angle ψ_{ij} . The 3 planets positions of the reaction gear set are $(0, 2\pi/3, 4\pi/3)$ whereas the 3 planets positions of the test gear set are $(\pi/3, \pi, 5\pi/3)$. All of the angles are measured according to a rotating frame linked to the carrier. Sequentially phased, meshes stiffness are considered for the two sets since $\frac{z_r \psi_{ij}}{2\pi} \neq k$ and $\sum_{n=1}^N z_r \psi_{ij} = m\pi$ where k and m are integers. The mesh phasing was considered too.

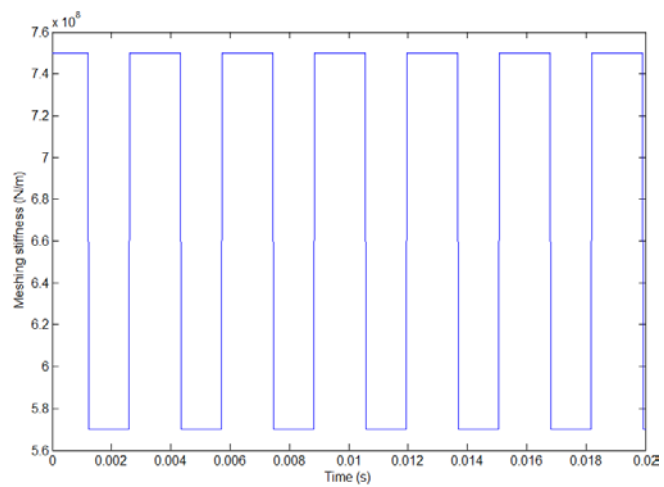
Figure 4.1 shows the evolution of ring-planet 1 mesh stiffness.



(a)



(b)



(c)

Figure 4. 1. Evolution of mesh stiffness on test gear : (a) ring-planet 1 (b) ring-planet 2 (c) ring-planet 3

It can be seen through the figure that a change in the number of pairs in contact ,the meshing stiffness is maximal when the pair tooth in contact.

In case of PG, mesh stiffness fluctuation is the main source of excitation for stationary regime.

For the test rig, the structure is excited by the $f_m=320$ Hz and its harmonics when the motor is running at 1498.5 rpm. The same conditions are adopted for the simulations.

Thus, an individual influence of each planet on the accelerometer will be assumed for a duration T_c/N ($N=3$: number of planets). Hence, the signal reaches its maximum when a planet i approach to the location of the accelerometer, and then diminishing to zero at the next period. It is a periodic phenomenon, so, when a planet i approach to the sensor mounted on the ring, its effect will increase for the first $T_c/2N$ time period, reaching its maximum and then it is decreased to zero at the end of the next $T_c/2N$ time period.

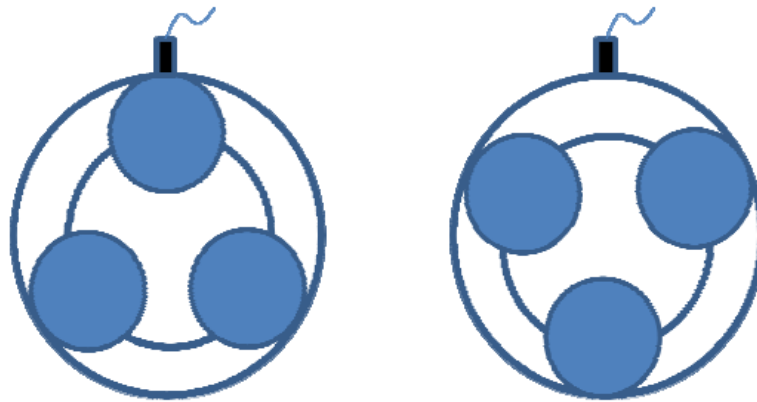


Figure 4. 2. Influence of the position of planets on the accelerometer (Hammami. 2015)

A Hanning function is modeled to represent this phenomenon.

$$w(t) = \frac{1}{2} \left(1 - \cos\left(\frac{2\pi Nt}{T_c}\right) \right) \quad (4-1)$$

In the case of perfect load sharing, a weighting function is used respecting the position of the planet:

$$w_{nj}(t) = \frac{1}{2} \left(t - \cos\left(\frac{\psi_{nj} T_c}{2\pi}\right) U_{nj}(t) \right) \quad (4-2)$$

$U_{nj}(t)$ can be expressed as :

$$U_{nj}(t) = \sum_{i=1}^N \left\{ u \left[t - \left(\frac{(i-1)N + n - 1}{N} \right) T_c \right] - u \left[t - \left(\frac{(i-1)N + n}{N} \right) T_c \right] \right\} \quad (4-3)$$

Where terms $u(t-a)$ are unit step functions that ensure the influence of planet n on the accelerometer and lasts only for a period of $T_c/3$.

The force due to the rotation of carrier is:

$$F_j(t) = \sum_{i=1}^N w_{nj}(t) U_{nj}(t) F_{nj} \cos(Z_r w_c t + Z_r \psi_{nj}) \quad (4-4)$$

In this case, the added force that takes into account the effects of the individual passage of each planet close to the accelerometer has a period $T_c/3=0.2027s$. Figure 4.3 shows the evolution of this force on the test ring.

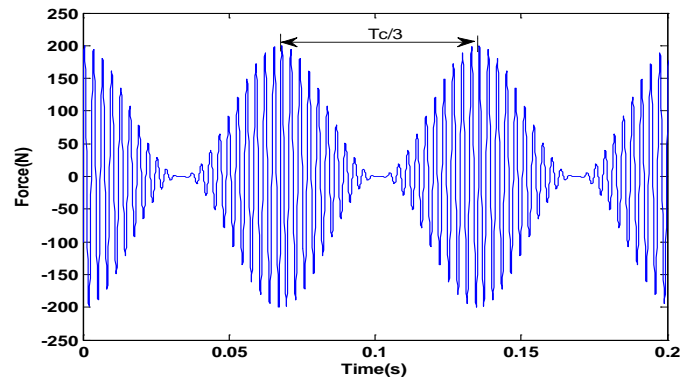


Figure 4. 3. Force due to rotation of carrier on the test ring

Figure 4.4 shows the simulated and measured acceleration on the test ring in time domain.

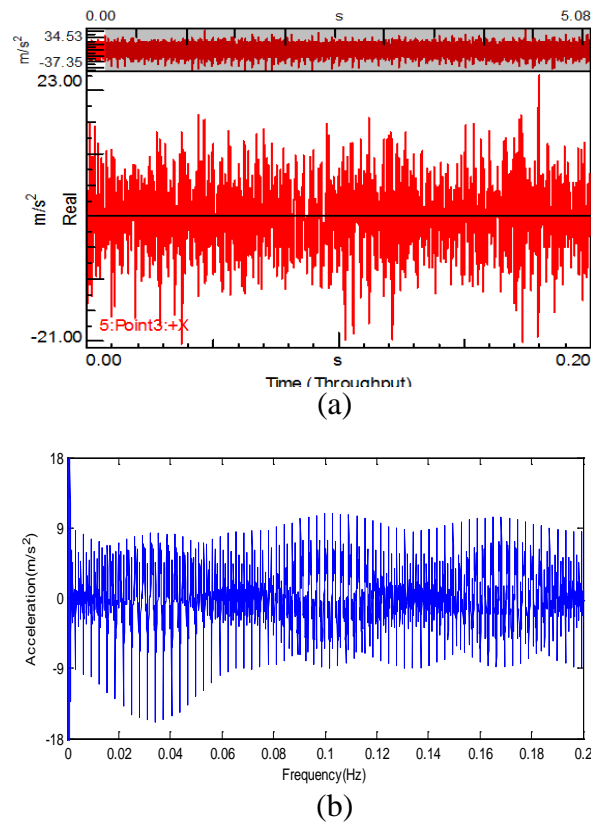


Figure 4. 4. Time response on the fixed ring (a) Experimental (b) Numerical

From figure 4.4, modulation amplitude can be detected in the numerical simulation and the experimental results as mentioned by (Inalpolat and Kahraman, 2009). This modulation is related principally to the force due to the rotation of carrier figure 4.3.

In figure 4.5, the spectra of acceleration measured and simulated on the test ring are presented. We notice that the dynamic component of the test ring is dominated by the f_m . Also, lateral sidebands are active around the f_m ; this fact confirmed the modulation amplitude presented in figure 4.5.

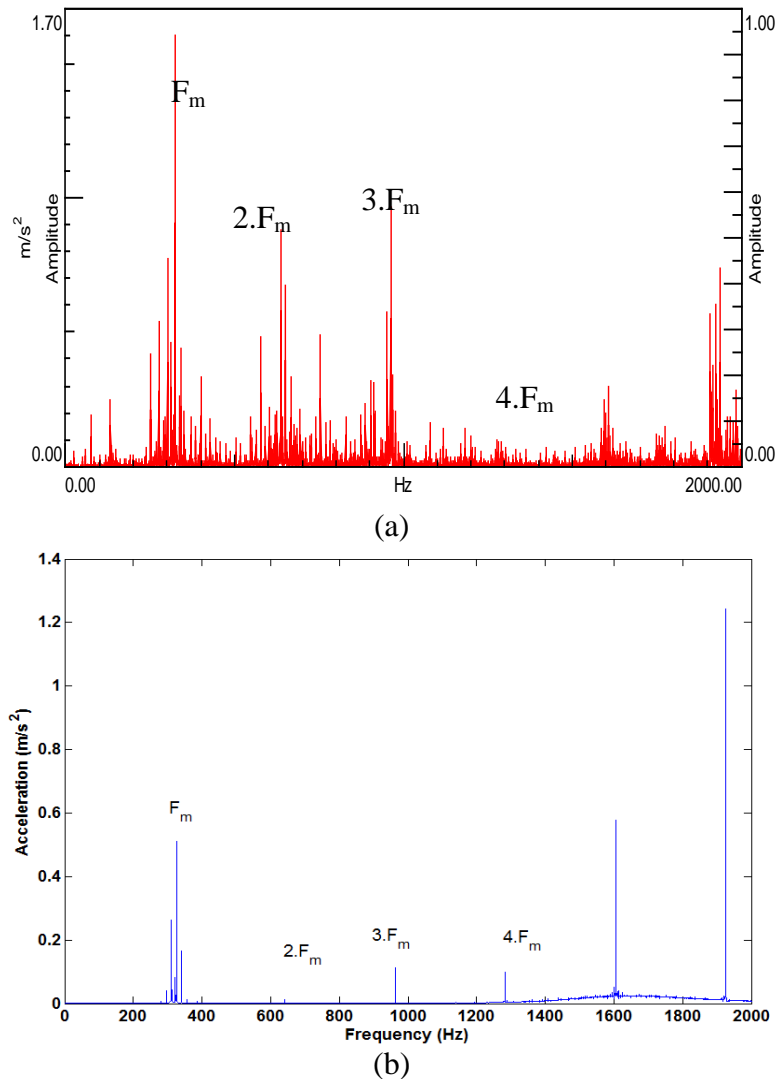


Figure 4. 5. Spectra of acceleration on the fixed ring (a) Experimental (b) Numerical

A zoom around the first f_m is displayed in figure 4.6. These sidebands frequency appears at $3.n.f_c$ (n : integer). This can be explained by the force due to the carrier which was considered in the numerical model and detected experimentally.

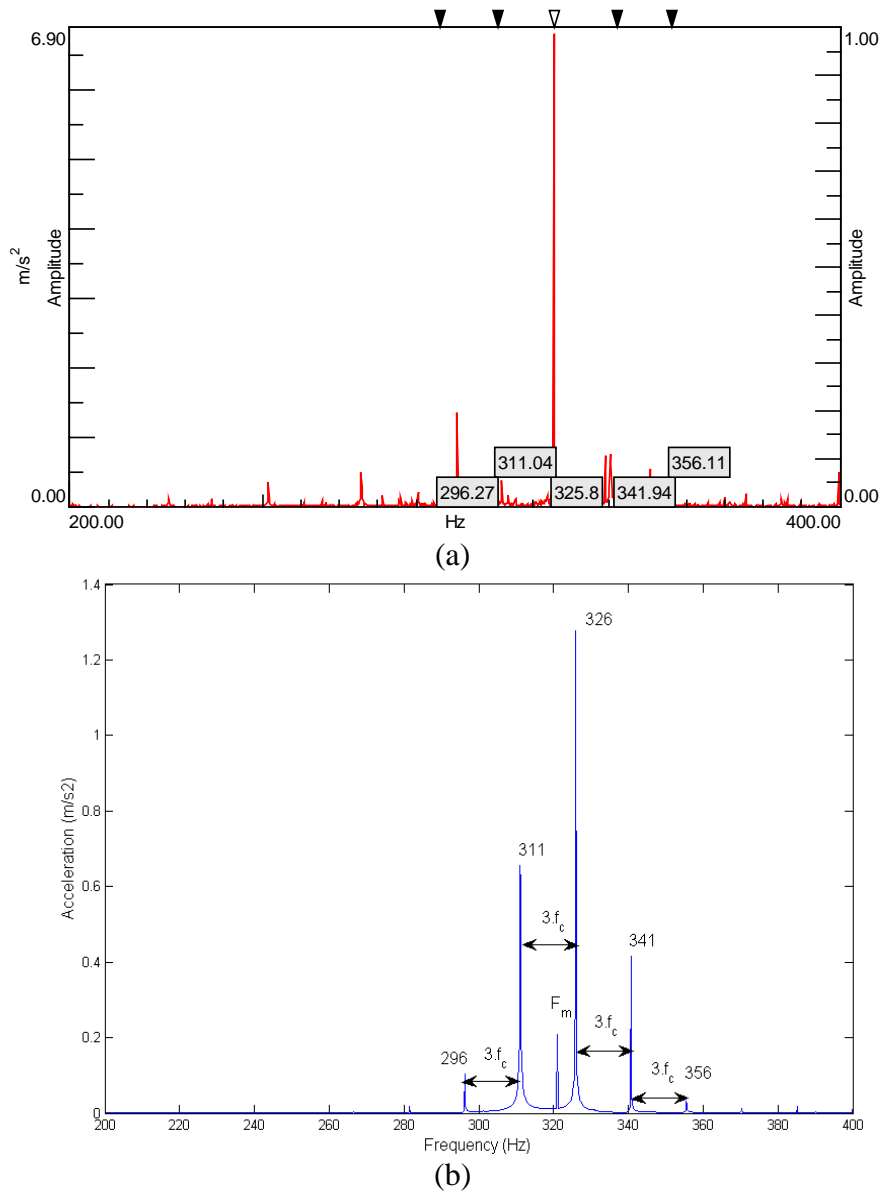


Figure 4. 6. Zoom of the spectra of acceleration on the fixed ring: (a) Experimental (b) Numerical
 It is noticeable that the sidebands are not symmetric to $f_m=320$ Hz, they respect the symmetric position to $f_{max}=325$ that is nearest to f_m , also they respect this condition:

$$|f_{max} - f_m| \leq \frac{1}{2} \cdot N \cdot f_c \quad (4.5)$$

In fact, (McFadden and Smith 1985) studied this behavior, they affirm that the largest component is usually at the nearest harmonic of the planet carrier speed which is a multiple of 3 (the number of planets).

On the experimental spectra (Figure 4.6.a) another sidebands with frequency $m \cdot f_c$ (m : integer) are detected which are related to the gravity of the carrier. However, only the f_m appears on the numerical spectra (Figure 4.6.b).

The difference between the simulated and the experimental results is related to transmitted load, the contact ratio and the damping ratio. Also, parametric instability is observed leading to unstable running regimes. The damping has a significant effect on the system stability, its increase reduces the unstable regions. Besides, increasing of meshing stiffness leads to the enlargement of the unstable regions (Yang et al 2019).

3 Effect of gravity of carrier on the dynamic behavior of PGs

The carriers' components in the studied PG system are heavy; their gravity can impact on the distances between the planets, the ring and the sun components. When the system run, these distances will be varying in time. This fact is periodic, it affects directly on gear meshing. When the distance between gears (sun-planets and ring-planets) increase, the amplitude of meshing stiffness decrease and vice versa which leading to a variation on the mean value of these functions. Based on finite element method proposed by (Fernandez et al., 2013) the gear mesh stiffness functions are determined.

Figure 4.7 shows the evolution of gear mesh stiffness ring-planets during one period of rotation of carrier with effects of gravity of carrier. These functions will be integrated in the numerical model.

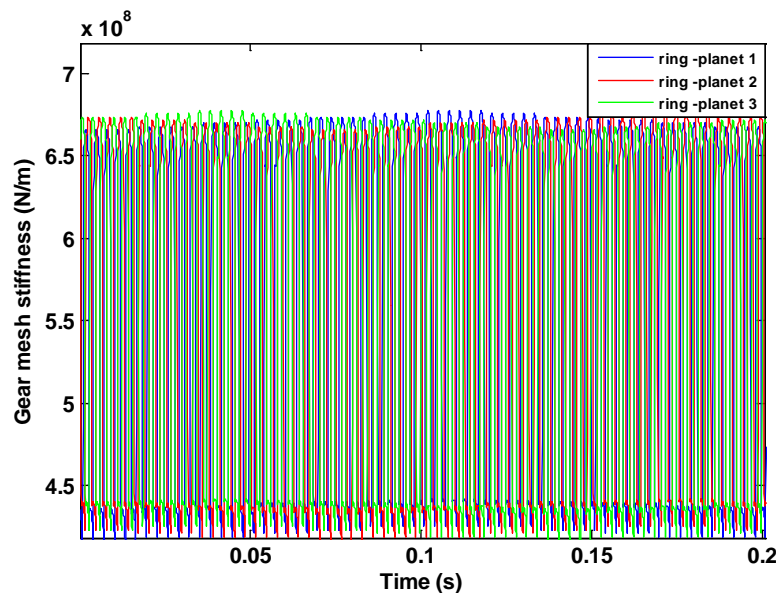
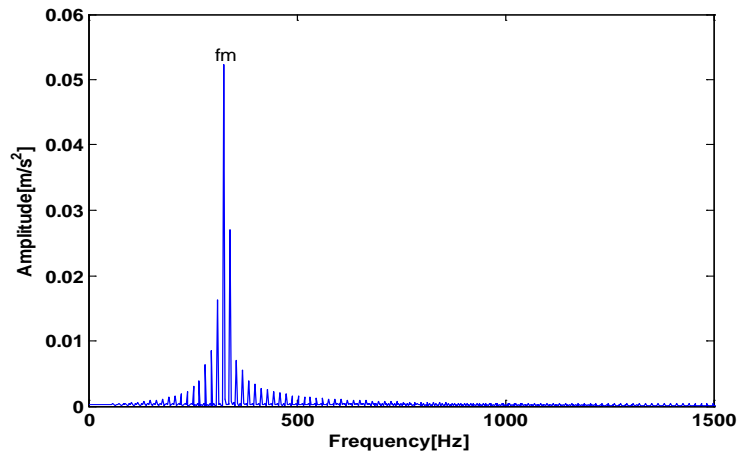


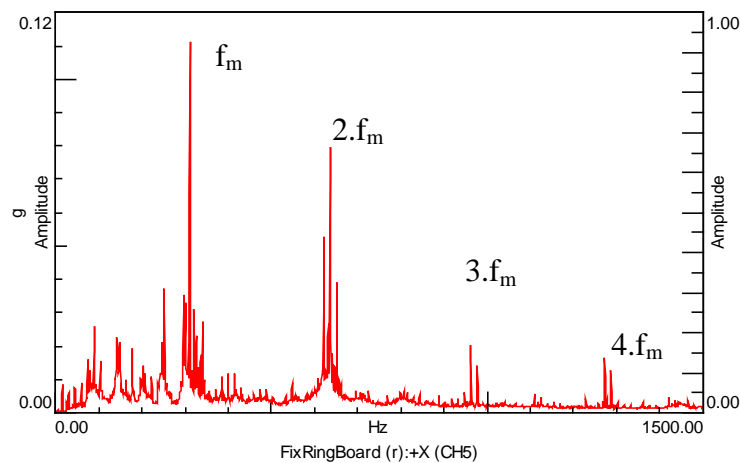
Figure 4. 7. Ring-planet mesh stiffness

The results are obtained for the input rotational speed of motor 1498.5 rpm and an external load 100 Nm.

The spectrum of acceleration of the test ring is dominated by f_m (320.66 Hz) and its harmonics. Obtained numerical results are correlated with the experimental results.(figure 4.8).



(a)



(b)

Figure 4. 8. Spectra of acceleration on the test ring: (a) Numerical (b) Experimental

A zoom around the first f_m is displayed in figure 4.9; based on the frequency characteristics of the sidebands, two kinds of sidebands are noticed, sidebands due to the influence of the rotation of carrier as explained in section 2 which have symmetric behaviour, their associated frequency is $3.n.f_c$ (n : integer), and the other sidebands are caused by the gravity of carrier ,they are also multiple, their associated frequency is $m.f_c$ (m : integer). As example we can cite 281.2Hz, 286.1 Hz, 345.3 Hz, and 350.3 Hz as mentioned on figure 4.9.They are missing in the spectra (figure 4.9-a) when the gravity of carrier was neglected in simulation.

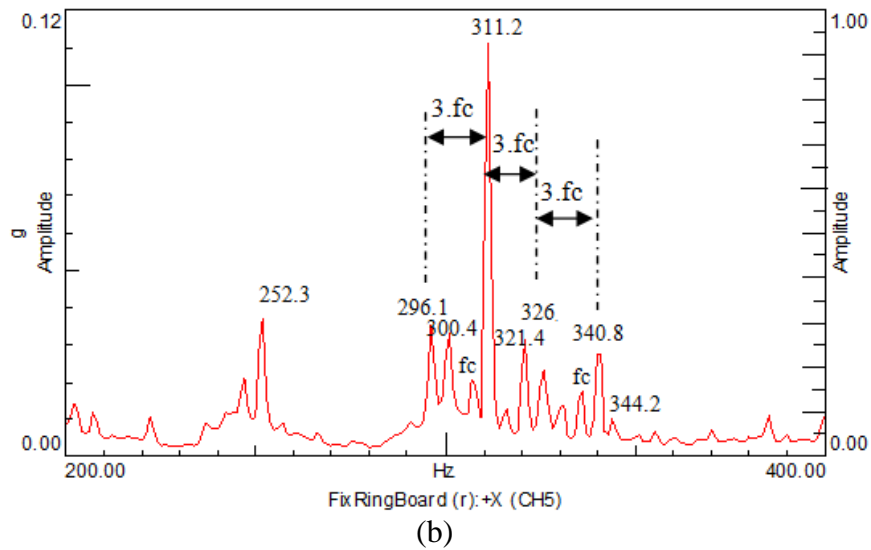
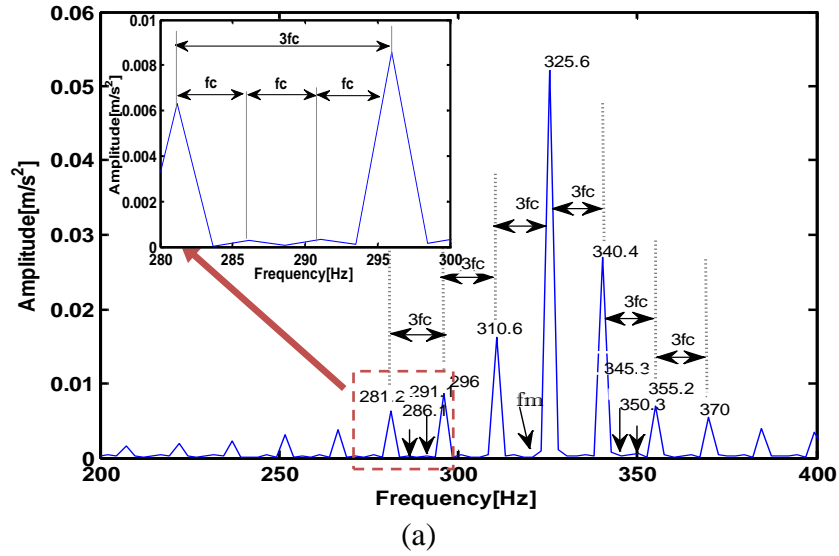


Figure 4. 9. Response spectrum of the test ring on the first harmonic of the mesh stiffness: Numerical (a) and experimental (b)

4 Run up regime:

The run up regime is obtained by using the frequency converter; the gearbox was driven from 0 to 500 rpm over 15 s.

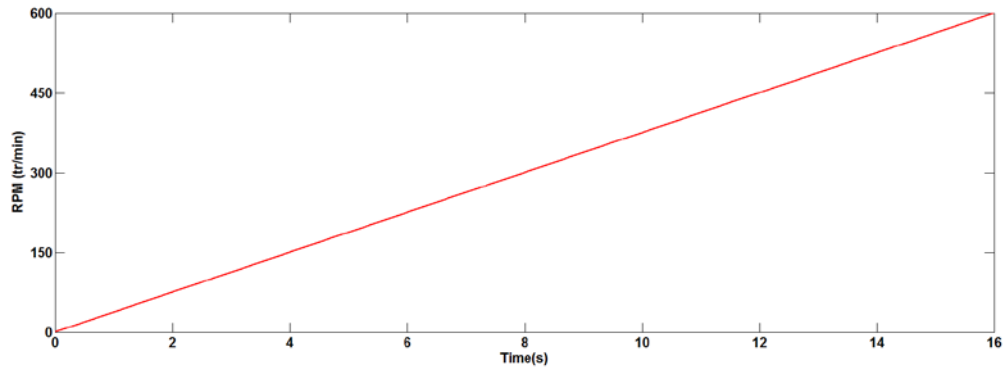


Figure 4.10. Evolution of the rotational speed in case of run up

During run-up regime, when the rotational speed increase the period of time varying stiffness period decreases (Viadero et al., 2014, Hammami et al., 2015). Figure 4.11 displays the trend of ring-planet and sun-planet mesh stiffnesses function.

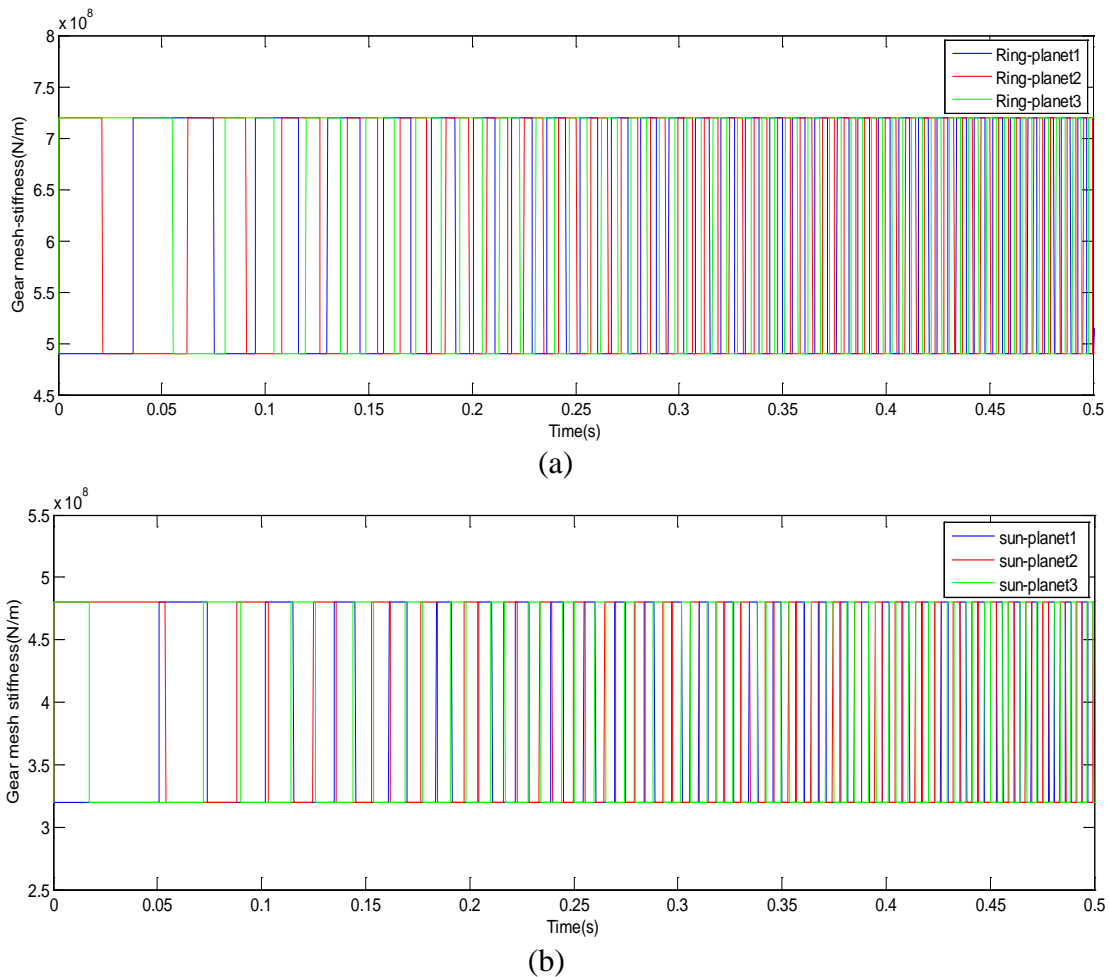
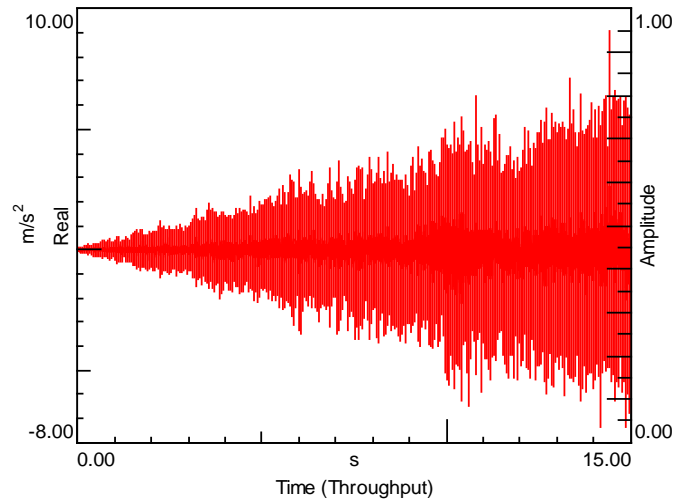
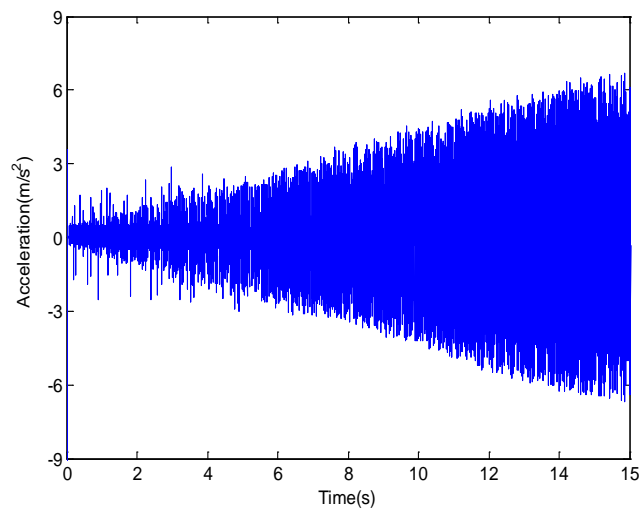


Figure 4.11. Gear mesh stiffness function evolution during run-up regime: (a) ring-planet (b) sun-planet

During this regime, the system is excited by the time varying meshing stiffness (see Figure 4. 9). It can be noticed that with the increasing of speed, the torque increase and as consequence the amplitude of vibration increase.



(a)



(b)

Figure 4. 12. Time response of acceleration on the ring (a) measured (b) simulated

During run up regime, the period of meshing stiffness function is not constant. So, in order to characterize accurately the evolution of acceleration a time frequency map done by Short Time Fourier Transforms (STFT) is presented. Figure 4.13 displays the measured and simulated (STFT) of test ring of the acceleration.

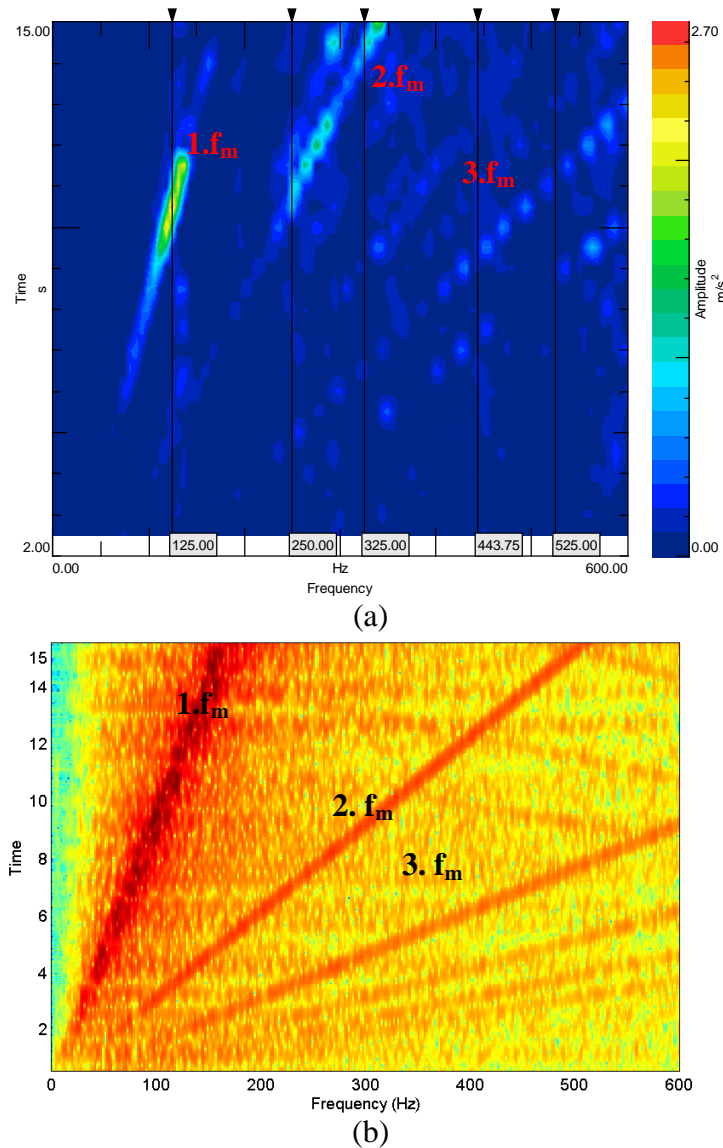


Figure 4. 13. STFT on the fixed ring (a) experimental and (b) numerical

From figure 4.13, the evolution of the f_m and its harmonics during measurement and simulation is observable by the inclined line showing their evolution in time and highlighting the frequency and amplitude modulation. The amplitude is important for $1 \times f_m$ because it is related principally to the (Hammami. 2015).The frequency modulation of frequency is related mainly to the gear meshing function having variable period. Besides, vertical lines appears on the map proving the presence of some natural frequencies of the structure.

5 Variable loading regime

In order to show the effect of loading conditions on the dynamic behaviour of the system, the load shape presented in figure 4.14 is applied to the system during experiments and for simulation. As

mentioned previously, the external load can be obtained by adding mass on the arm which is connected to the test ring.

The speed during this regime is fixed at 600 rpm by the speed controller.

The load is applied manually by adding and removing masses. The loading period T_L is fixed to 1 s.

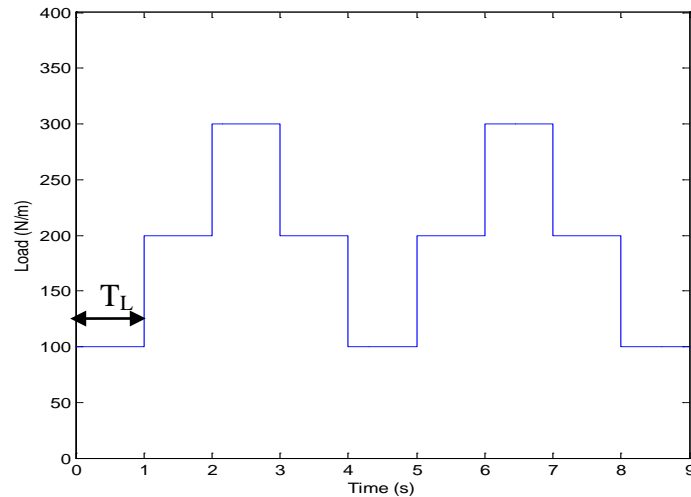


Figure 4. 14. External applied load

The mesh stiffness function follows the same trend of the load, this is related principally to the sensitivity of hertzian contact to the load which will be discussed in the next chapter. Moreover, the amplitude of variation of the external load introduces a variation on the amplitude of the time varying stiffness function (Figure 4.15). Also the contact ratio increases as indicated by (Fernandez et al, 2013).

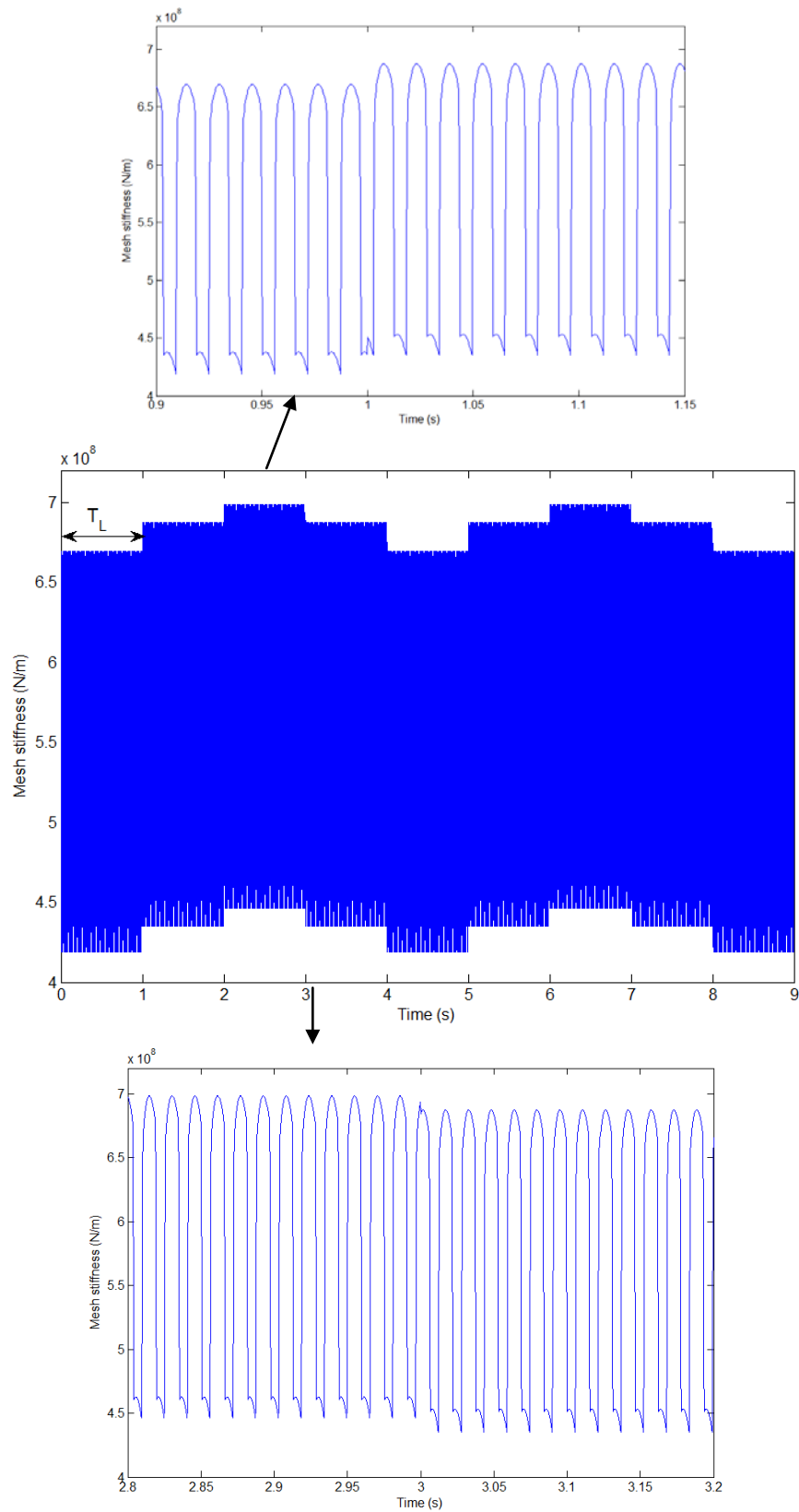
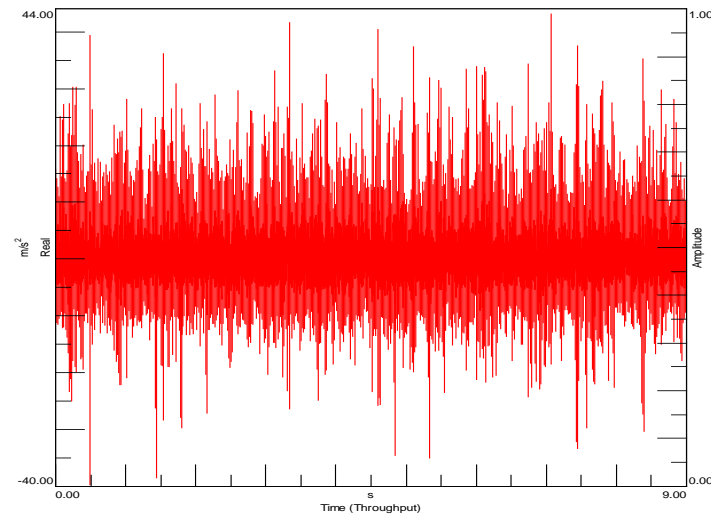
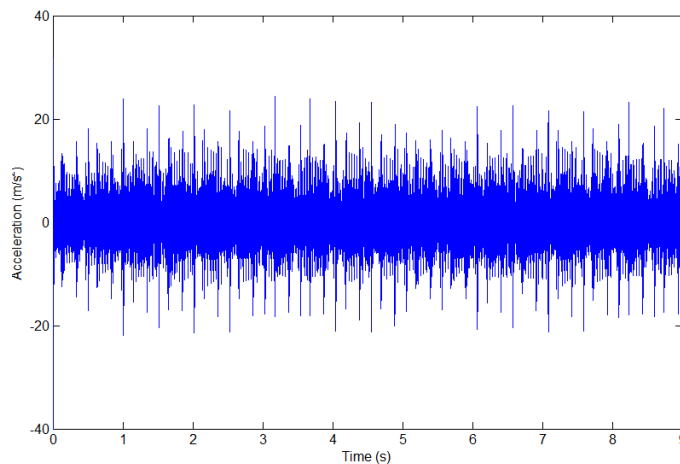


Figure 4. 15. Ring-planet 1 mesh stiffness

It can be noticed from figure 4.16 that the variation of the external load causes an amplitude modulation on the measured and simulated acceleration on the test ring. The load variation (figure 4.14) creates a change in the amplitude of vibration on time response signal. With the increasing of load, the vibration amplitude increase.

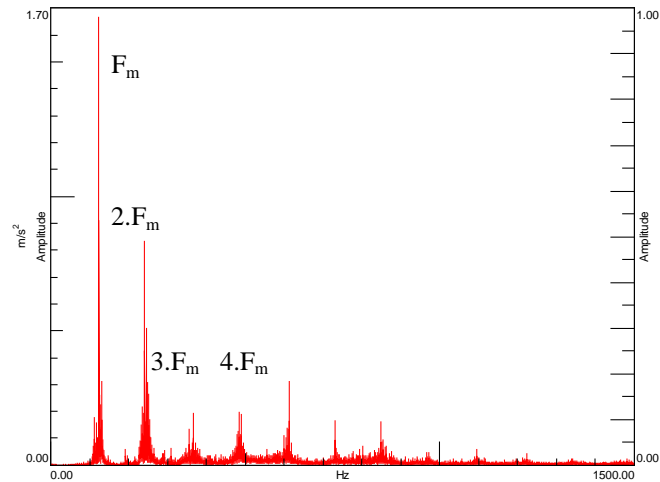


(a)

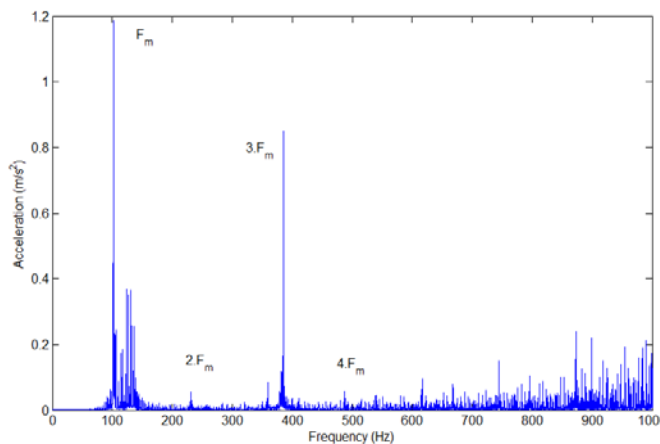


(b)

Figure 4. 16. Time evolution of the acceleration on the fixed ring (a) Experimental (b) Numerical In the studied cases, the input speed is fixed at 590 rpm by the frequency inverter. it is well observed in the spectra shown in figure 4.17 that the fundamental gear mesh frequency is dominant. It can be moved to the second GMF if the amount of the introduced load will increase.(Hammami et al., 2016)



(a)



(b)

Figure 4. 17. Spectra of acceleration on the fixed ring (a) Experimental (b) Numerical

High activity of sidebands is noticed for experimental spectra than that numerical. This fact can be explained by several effect presented during the experimental measurement such as the white noise, the presence mounting errors as well as the noise issued from the motor.

6 Variable speed regime

In this section, the dynamic behavior in variable speed regime is studied. The variation of speed is performed using the frequency inverter.

The input speed has a sawtooth shape with speed ranging from 500 to 1200 rpm as shown in Figure 4.18. However, the load is fixed to 300 N-m.

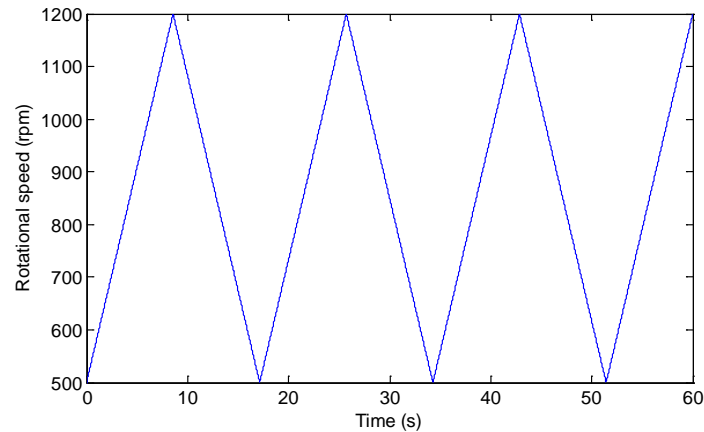
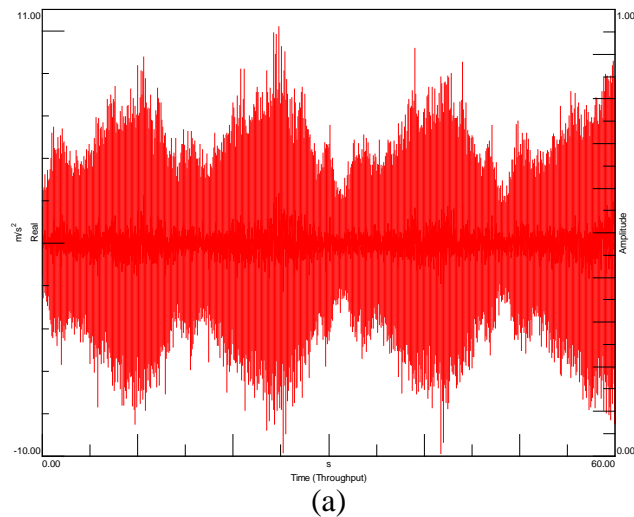


Figure 4.18. Evolution of rotational speed in case of variable speed.

During the acceleration of motor, the period of mesh stiffness function decreases as we increase the speed whereas during the deceleration of motor, the period of mesh stiffness function increases as we decrease the speed. The time response of the acceleration on the fixed ring is shown in Figure 4.19. Vibration signals are modulated by the variation of speed. Amplitude reaches its maximum values when the speed is maximum, (Zimroz et al, 2011).



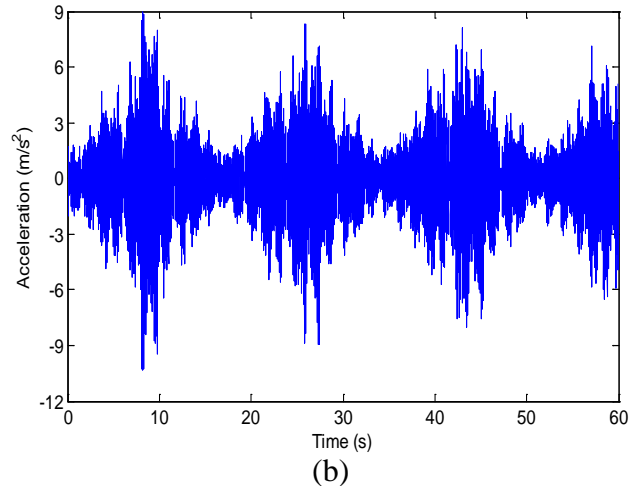
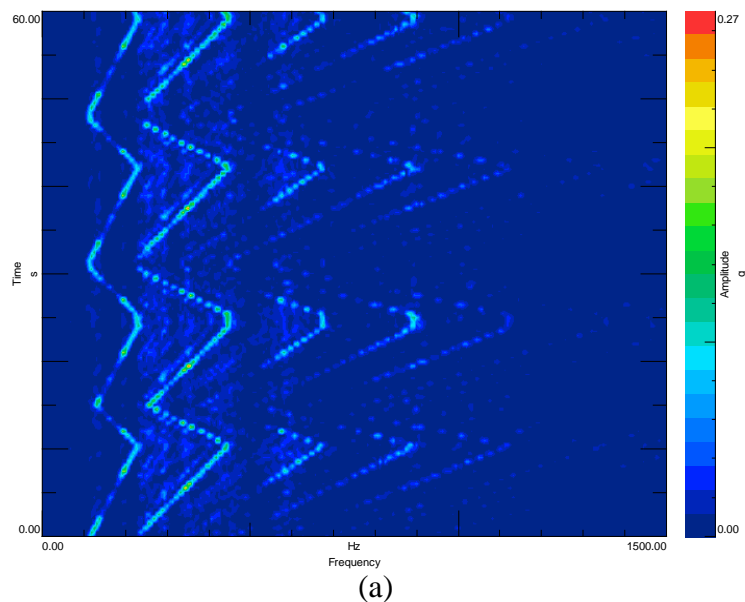
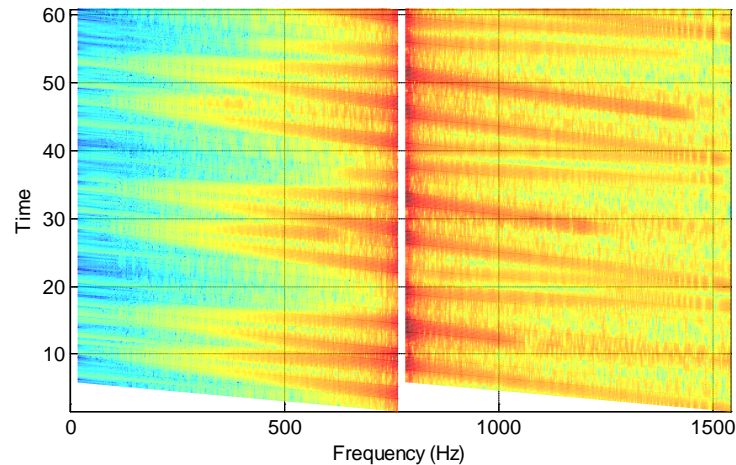


Figure 4.19. Time response measured on the fixed ring (a) Experimental (b) Numerical.

In fact, the meshing frequency is not constant. If we represent the (STFT) of the simulated and measured accelerations on the test ring (Figure 4.20), it is noticeable the presence of inclined lines from the right to the left due to the increase of the meshing frequency (increase of speed) and its harmonics inclined lines from the left to the right due to the decrease of the meshing frequency (decrease of speed) and its harmonics.





(b)

Figure 4. 20. STFT of the acceleration on the test ring (a) Experimental (b) Simulated.

The theoretical STFT (figure 4.20.b) present vertical lines showing the presence natural frequencies at 241Hz and 815Hz while the natural frequencies presented in the experimental result (figure 4.20.a) are on the neighborhood of the frequencies, 136 Hz, 195Hz and 301 Hz. This regime is widely present in gear transmission. Moreover, it is very important to characterize the dynamic behaviour since natural frequencies can be excited.

7 Conclusion:

In this chapter, a series of simulations and measurement under stationary and non-stationary regimes has been performed using the developed numerical model and the experimental test rig. The main remarks are highlighted as following:

- In the case of stationary regime (fixed load and speed), the dynamic response show that the meshing frequency and its harmonics dominate the spectra of acceleration.
- The gravity of the carrier impact on the vibration response through the apparition of the sidebands corresponding to the frequency of carrier.
- Time frequency representations done by STFT could be an efficient tool to analyze the dynamic response of the system in non-stationary regimes.
- The non-stationary nature of the response was highlighted by the fact that the variability of the loading will induce a variability of the speed and consequently a variability of the meshing frequency and its harmonics.

- A double modulation is observed in the response signals: an amplitude modulation in the temporal responses is induced by the variation of the applied load and a frequency modulation induced by the variation of the speed of rotation.

The dynamic behavior of the PG system in the stationary and non stationary regimes is related principally to the meshing function. In the studied cases, these functions are modeled as linear function but in reality they are not due to the Hertzian contact.

In the next chapter, the influence of the non-linear Hertzian stiffness on the dynamic behavior of the system in stationary and non-stationary condition will be highlighted.

Chapter 5: Non-linear model of planetary gear

Chapter 5: Non-linear model of planetary gear

Sommaire

1	Introduction	121
2	Non linear model:	121
2.1	Modelling of gear mesh-stiffness:	121
2.1.1	Bending deflection	121
2.1.2	Fillet foundation deflection.....	122
2.1.3	Contact deflection:	123
2.2	Non linear numerical model:	124
2.2.1	Electric motor modelling:	127
2.2.2	Resolution of the equation of motion:.....	127
2.2.3	Relationship between the non linearity and the non stationary regime	130
3	Influence of combined non linear hertzian contact and non stationary conditions on the dynamic behavior:	130
3.1	Run-up condition:	130
3.2	Variable load regime:	135
4	Conclusion:	139

1 Introduction

PG systems operate often under non stationary conditions. These systems remain a major source of noise and vibration due to the internal or external excitations. The internal excitations for these transmissions are generally due to the meshing process. The computation of the mesh stiffness function is generally performed in literature by a local approach considering Hertzian stiffness between the teeth in contact or by overall approach considering the bending stiffness of the tooth and fillet foundation stiffness. In this chapter, the dynamic behavior of the PG system will be investigated in non stationary conditions taking into account the non-linear Hertzian stiffness. The study of the Hertzian contact is of great importance for computing the transmission errors of the gear, the stiffness of teeth as well as dynamic loads applied to the teeth and also for the investigation of the vibration response of gear system as well as for the designers to estimate the capacity of the load transmission of gears.

2 Non linear model:

2.1 Modelling of gear mesh-stiffness:

The ring-planets and the sun-planets mesh stiffness are modelled by setting in series the bending stiffness K_b , the fillet stiffness K_f and the Hertzian stiffness K_h .

$$K_i = 1 / \left(\frac{1}{K_{b1}} + \frac{1}{K_{f1}} + \frac{1}{K_{b2}} + \frac{1}{K_{f2}} + \frac{1}{K_h} \right) \quad (5.1)$$

The meshing stiffness function $K_i(t)$ is obtained through the knowledge of the number of teeth pairs in contact (Velex, 1988). Considering a rotational speed N of the motor, the meshing period is defined by:

$$T_g = \frac{z_s \cdot z_r}{(z_s + z_r)} \frac{N}{60} \quad (5.2)$$

2.1.1 Bending deflection

The bending deflection δ_b of a tooth is modelled as in (Chaari et al. 2008):

$$\delta_b = F \cdot \cos^2 \alpha_m \sum_{i=1}^n e_i \left\{ \frac{d_i - e_i d_i + \frac{1}{3} e_i^2}{E \bar{I}_i} + \frac{1}{s_h \bar{G} \bar{A}_i} + \frac{\tan^2 \alpha_m}{\bar{A}_i E'} \right\} \quad (5.3)$$

Where α_m is the operating pressure angle, F denotes the applied force, s_h stands to a shear factor, G is the shear modulus, e_i and d_i are defined in Figure 5.1, E' , I_i and A_i are computed according to the following equations:

$$E' = \frac{E(1-\nu)}{(1+\nu)(1-2\nu)} \quad (5.4)$$

$$1/\bar{I}_i = (1/I_i + 1/I_{i+1})/2 \quad (5.5)$$

$$1/\bar{A}_i = (1/A_i + 1/A_{i+1})/2 \quad (5.5)$$

I_i , A_i , S_i , ν and E denotes respectively the moment of inertia, the tooth cross section, the Poisson ratio and the Young's modulus.

The bending stiffness k_b can be obtained by:

$$k_b = \frac{F}{\delta_b} \quad (5.6)$$

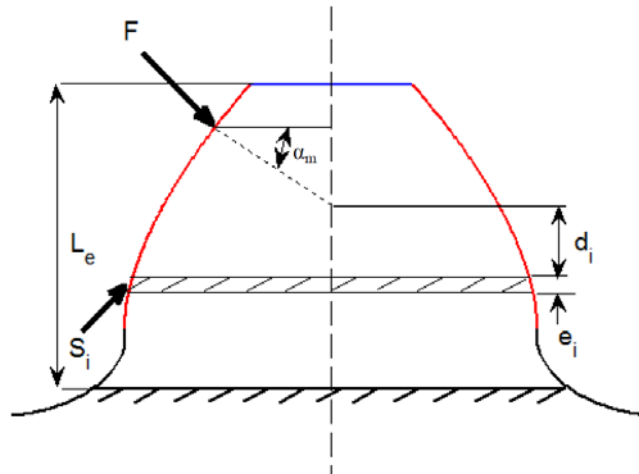


Figure 5. 1. Modelling of the spur gear tooth

2.1.2 Fillet foundation deflection

The analytical expression of fillet foundation deflection is given by equation (5-7) assuming that the variation of stress is linear and constant, (Muskhelishvili ,1975).

$$\delta_f = \frac{F \cdot \cos^2 \alpha_m}{WE} \left\{ L^* \left(\frac{u_f}{S_f} \right)^2 + M^* \left(\frac{u_f}{S_f} \right) + P^* (1 + Q^* \tan^2 \alpha_m) \right\} \quad (5.7)$$

S_f and u_f are shown in Figure 5.2 and W is the tooth width. The coefficients L^* , M^* , P^* and Q^* can be obtained by polynomial functions (Sainsot et al., 2004).

$$X_i^*(h_{fi}, \theta_f) = A_i/\theta_f^2 + B_i h_{fi}^2 + C_i h_{fi}/\theta_f + D_i/\theta_f + E_i h_{fi} + F_i \quad (5.8)$$

$h_{fi} = r_f/r_{int}$, h_{fi} and θ_f are defined in Figure 5.2.

The bending stiffness can be defined by:

$$k_f = \frac{F}{\delta_f} \quad (5.9)$$

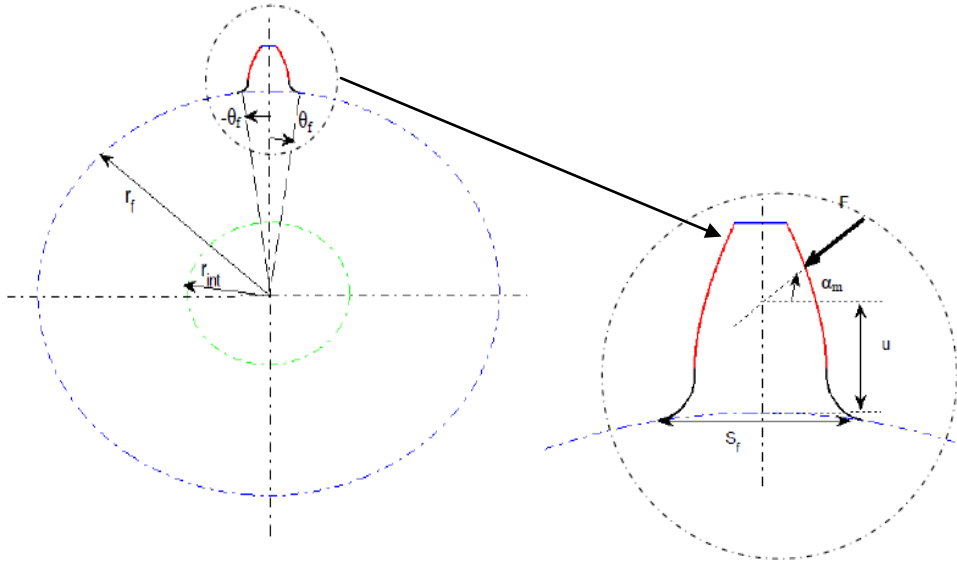


Figure 5. 2. Geometrical parameters for the fillet foundation deflection

2.1.3 Contact deflection:

The contact deflection equation in the case of elastic deformation involving line contact between solid bodies is derived by (Harsha, 2006):

$$\delta_h = \frac{4.05 F_0^{0.925}}{10^5 l_{eff}^{0.85}} \quad (5.10)$$

Where l_{eff} is the length over which teeth are in contact. It is equal to the width of the tooth in the case of one pair of teeth is in contact and twice when two pairs of teeth are in contact. The non-linear contact force is given by:

$$F_h = 56065.703.1_{eff}^{0.92} .\delta_h^{1.08} \quad (5.11)$$

Hence, the non-linear stiffness is expressed by:

$$k_h = \frac{F_h}{\delta_h} = 56065.703.1_{eff}^{0.92} .\delta_h^{0.08} \quad (5.12)$$

2.2 Non linear numerical model:

In order to study the influence of the nonlinear Hertzian contact, a torsional lumped parameter is developed.

The masses and the inertia are $m_c, I_c, m_r, I_r, m_s, I_s, m_{p1}, I_{p1}, m_{p2}, I_{p2}, m_{p3}, I_{p3}$ for the carrier, the ring, the sun and the three planets respectively.

The same meshing stiffness functions used for the tridimensional model are also adopted in this model.

The planets are linked respectively to the reaction ring by the ring planets mesh stiffness K_{rr1}, K_{rr2} and K_{rr3} and to the reaction sun by the sun planets mesh stiffness K_{sr1}, K_{sr2} and K_{sr3} . The same functions are used in the test gear with K_{rt1}, K_{rt2} and K_{rt3} are ring planets mesh stiffness and K_{st1}, K_{st2} and K_{st3} sun planets mesh stiffness.

The sun's shaft and the carrier's shaft are modeled respectively by the torsional stiffness k_{st} and k_{ct} .

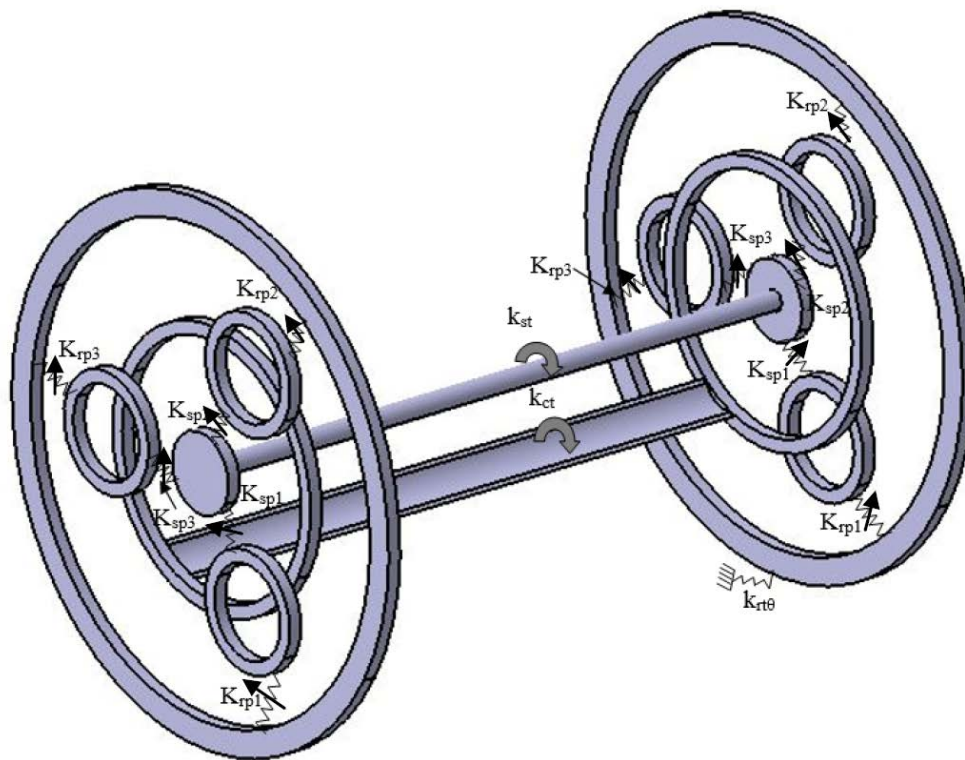


Figure 5. 3. PG torsional model

The system equation of motion is:

$$M\ddot{q} + C\dot{q} + K_c q + F_{nl} = F_{ext}(t) \quad (5.13)$$

$$q = \{\theta_{cr}, \theta_{rr}, \theta_{sr}, \theta_{p1r}, \theta_{p2r}, \theta_{p3r}, \theta_{ct}, \theta_{rt}, \theta_{st}, \theta_{p1t}, \theta_{p2t}, \theta_{p3t}\}^T \quad (5.14)$$

is the vector degree of freedom of the system and M is the mass matrix.

$$M = \begin{bmatrix} M_r & 0 \\ 0 & M_t \end{bmatrix} \quad (5.15)$$

$$M_i = \begin{bmatrix} \frac{I_{ci}}{r_{ci}} + n.m_p & 0 & 0 & 0 & 0 & 0 \\ 0 & \frac{I_{ri}}{r_{ri}} & 0 & 0 & 0 & 0 \\ 0 & 0 & \frac{I_{si}}{r_{si}} & 0 & 0 & 0 \\ 0 & 0 & 0 & \frac{I_{p1i}}{r_{p1i}} & 0 & 0 \\ 0 & 0 & 0 & 0 & \frac{I_{p2i}}{r_{p2i}} & 0 \\ 0 & 0 & 0 & 0 & 0 & \frac{I_{p3i}}{r_{p3i}} \end{bmatrix} \quad i=r,t \quad (5.16)$$

$$K_e(t) = \begin{bmatrix} K_{mrK} & 0 \\ 0 & K_{mt} \end{bmatrix} + K_c \quad (5.17)$$

$$K_{mr} = \begin{bmatrix} \sum_{i=1}^3 (K_{sri}(t) + K_{rri}(t)) & -\sum_{i=1}^3 K_{rri}(t) & -\sum_{i=1}^3 K_{rri}(t) & K_{rr1}(t) - K_{sr1}(t) & K_{rr2}(t) - K_{sr2}(t) & K_{rr3}(t) - K_{sr3}(t) \\ -\sum_{i=1}^3 K_{rri}(t) & \sum_{i=1}^3 K_{rri}(t) & 0 & -K_{rr1}(t) & -K_{rr2}(t) & -K_{rr3}(t) \\ -\sum_{i=1}^3 K_{sri}(t) & 0 & \sum_{i=1}^3 K_{rri}(t) & K_{sr1}(t) & K_{sr2}(t) & K_{sr3}(t) \\ K_{rr1}(t) - K_{sr1}(t) & -K_{rr1}(t) & K_{sr1}(t) & K_{rr1}(t) + K_{sr1}(t) & 0 & 0 \\ K_{rr2}(t) - K_{sr2}(t) & -K_{rr2}(t) & K_{sr2}(t) & 0 & K_{rr2}(t) + K_{sr2}(t) & 0 \\ K_{rr3}(t) - K_{sr3}(t) & -K_{rr3}(t) & K_{sr3}(t) & 0 & 0 & K_{rr3}(t) + K_{sr3}(t) \end{bmatrix} \quad (5.18)$$

$$K_{mt} = \begin{bmatrix} \sum_{i=1}^3 (K_{sri}(t) + K_{rri}(t)) & -\sum_{i=1}^3 K_{rri}(t) & -\sum_{i=1}^3 K_{rri}(t) & K_{rr1}(t) - K_{sr1}(t) & K_{rr2}(t) - K_{sr2}(t) & K_{rr3}(t) - K_{sr3}(t) \\ -\sum_{i=1}^3 K_{rri}(t) & \sum_{i=1}^3 K_{rri}(t) & 0 & -K_{rr1}(t) & -K_{rr2}(t) & -K_{rr3}(t) \\ -\sum_{i=1}^3 K_{sri}(t) & 0 & \sum_{i=1}^3 K_{rri}(t) & K_{sr1}(t) & K_{sr2}(t) & K_{sr3}(t) \\ K_{rr1}(t) - K_{sr1}(t) & -K_{rr1}(t) & K_{sr1}(t) & K_{rr1}(t) + K_{sr1}(t) & 0 & 0 \\ K_{rr2}(t) - K_{sr2}(t) & -K_{rr2}(t) & K_{sr2}(t) & 0 & K_{rr2}(t) + K_{sr2}(t) & 0 \\ K_{rr3}(t) - K_{sr3}(t) & -K_{rr3}(t) & K_{sr3}(t) & 0 & 0 & K_{rr3}(t) + K_{sr3}(t) \end{bmatrix} \quad (5.19)$$

C denotes the proportional damping matrix expressed by:

$$C = \alpha M + \beta K \quad (5.20)$$

Where α and β are two constants.

$F_{ext}(t)$ presents the external torque vector applied on the system.

$$F_{ext}(t) = \{0, 0, T_m(t), 0, 0, 0, 0, 0, T_r(t), 0, 0, 0\}^T \quad (5.21)$$

The nonlinear force is induced by the Hertzian Stiffness. It is expressed by (Faik and Witteman, 2000) :

$$F_{nl} = \{X\} K_e(t) \{X\}^T \{q\} = \{X\} K_e(t) \delta \quad (5.22)$$

δ is the transmission error and $\{X\}$ is vector of tooth deflection

This equation is adopted in the developed model

$$F_{nl} = (F_{nl,r}, F_{nl,t})^T \quad (5.23)$$

$$F_{nl,j}(t) = \{0, F_{rj}(t), F_{sj}(t), F_{plj}(t), F_{p2j}(t), F_{p3j}(t)\}^T \quad (5.24)$$

$$F_{rj}(t) = -\sum_{i=1}^n K_{rij}(t) \delta_{ri}^j(t) \{r_{1i}, r_{2i}, r_{3i}\}^T \quad (5.25)$$

$$F_{sj}(t) = -\sum_{i=1}^n K_{sij}(t) \delta_{si}^j(t) \{s_{1i}, s_{2i}, s_{3i}\}^T \quad (5.26)$$

$$F_{ij}(t) = -K_{rij}(t) \delta_{ri}^j(t) \{r_{4i}, r_{5i}, r_{6i}\}^T - K_{sij}(t) \delta_{si}^j(t) \{s_{4i}, s_{5i}, s_{6i}\}^T ; \text{avec: } i=1, \dots, n. \quad (5.27)$$

Table 5. 1. Components of the tooth deflection

Coefficients s_i	Coefficients r_i
$s_{1i}=s_{2i}=s_{3i}=-r_{br}$	$r_{1i}=r_{2i}=r_{3i}=-r_{bp}$
$s_{4i}=s_{5i}=s_{6i}=r_{bs}$	$r_{4i}=r_{5i}=r_{6i}=r_{bp}$

With

$$\{X\} = \{r_{bcr}, r_{brr}, r_{bsr}, r_{bp1r}, r_{bp2r}, r_{bp3r}, r_{bct}, r_{btr}, r_{bst}, r_{bp1t}, r_{bp2t}, r_{bp3t}\}^T \quad (5.28)$$

The transmission error δ is a relative displacement along the line of action between planetary gears element and is expressed by (Velex 1988):

$$\delta_{ri}^r = r_{brr} \theta_{rr} + r_{bir} \theta_{ir} \quad (5.29)$$

$$\delta_{ri}^t = r_{brt} \theta_{rt} + r_{bit} \theta_{it} \quad (5.30)$$

$$\delta_{si}^r = r r_{bsr} \theta_{sr} + r_{bir} \theta_{ir} \quad (5.31)$$

$$\delta_{si}^t = r r_{bst} \theta_{st} + r_{bit} \theta_{it} \quad (5.32)$$

2.2.1 Electric motor modelling:

From the kinetic energy theorem, the rotational velocity of an electric motor can be linked to its torque and to the receiver torque by:

$$J \frac{d\Omega}{dt} = T_m - \frac{z_r}{z_p} T_r \quad (5.33)$$

The mechanical characteristic of the motor is the relation between the driving torque and the speed of the motor. It is expressed by

$$T_m = \frac{T_b}{\left(1 + (s_b - s)^2\right) \left(\frac{a}{s} - bs^2\right)} \quad (5.34)$$

Where s_b and T_b are the slip and torque at the breakdown, respectively. a and b are all constant properties of the motor and s is the proportional drop in speed which is given by:

$$s = \frac{N_s - N}{N_s} \quad (5.35)$$

N_s is the synchronous speed and N is the actual rotational speed of the motor. Load torque characteristic T_r is chosen to be proportional to the square of the rotational speed.

$$T_r = h\Omega^2 \quad (5.36)$$

Where h is a coefficient depending on the characteristics of the driven system. Eq. (5.33) is transformed into the following differential equation:

$$\frac{d\Omega}{dt} = \frac{1}{J} \left(T_m(\Omega, t) - \frac{Z_r}{Z_p} T_r(\Omega, t) \right) \quad (5.37)$$

$$(5.38)$$

2.2.2 Resolution of the equation of motion:

The equation of motion is achieved using the classical Newton Raphson method coupled with the implicit Newmark algorithm as shown in the following algorithm.

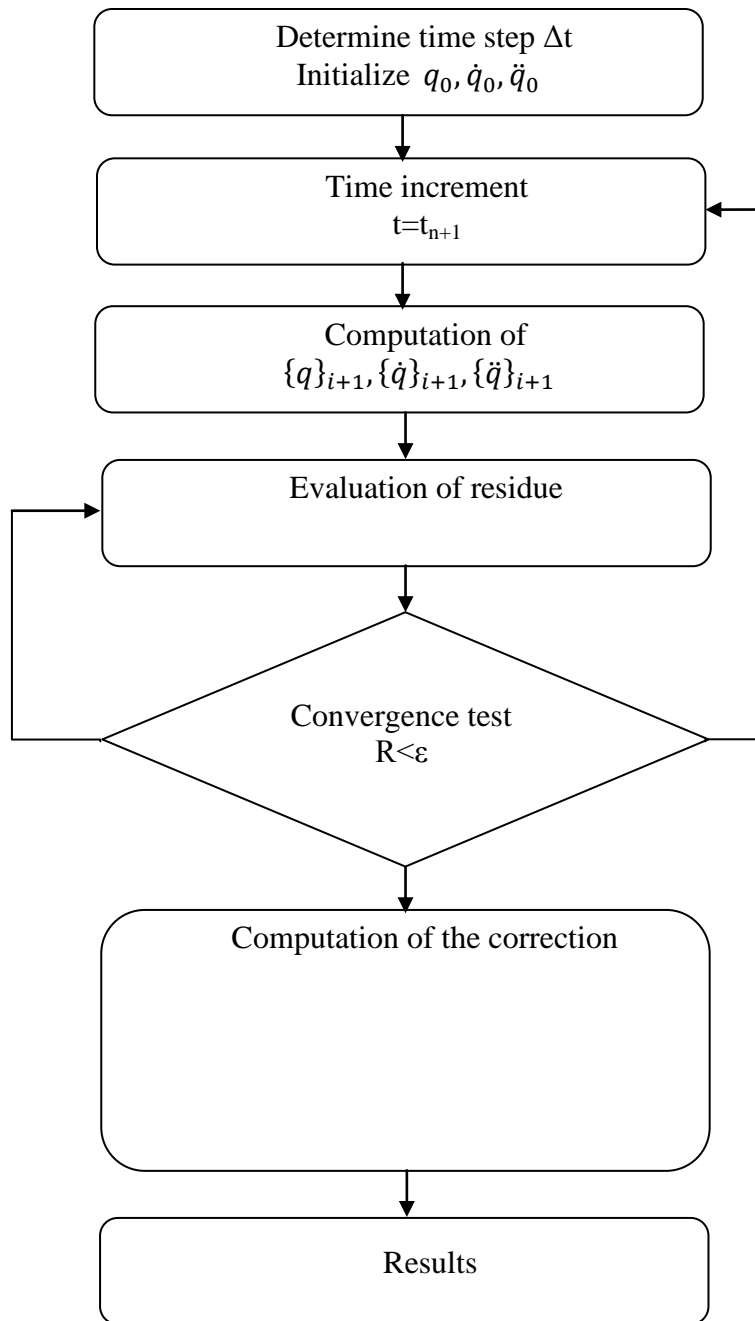


Figure 5. 4. Resolution algorithm (Newmark and Newton-Raphson)

Before applying the Newmark algorithm, we need to compute the initial value corresponding to $q_0, \dot{q}_0, \ddot{q}_0$ and transform the equation of motion.

The system equation of motion given by equation 5.13 can be transformed to an approximated version at time $t = t_{n+1}$

The system equation will be written as :

$$M\{\ddot{q}\}_{n+1} + C\{\dot{q}\}_{n+1} + K_c\{q\}_{n+1} + \{F_{nl}(\{q\})_{n+1}\} = \{F_{ext}(t)\}_{n+1} \quad (5.39)$$

To start the time integration procedure, the initial values of the displacement, velocity, and acceleration vectors are required. These initial values are determined as follows:

$$d_0=q(0), v_0=\dot{q}(0), a_0=\ddot{q}(0)$$

$$\{q\}_{i+1} = \{q\}_i + \Delta t\{\dot{q}\}_i + b\Delta t^2 \left[\left(\frac{1}{2*b} - 1 \right) \{\ddot{q}\}_i + \{\ddot{q}\}_{i+1} \right] \quad (5.40)$$

$$\{\dot{q}\}_{i+1} = \{\dot{q}\}_i + \Delta t * (1-a)\{\ddot{q}\}_i + (a * \Delta t)\{\ddot{q}\}_{i+1} \quad (5.41)$$

Δt denotes the time step between two instants while a and b are the Newmark constants.

Extracting $\{\ddot{X}\}_{i+1}$ from equation (5.40) we obtain:

$$\{\ddot{q}\}_{i+1} = \frac{1}{b * \Delta t^2} [\{q\}_{i+1} - \{q\}_i - \Delta t\{\dot{q}\}_i] - \left(\frac{1}{2*a} \{q\}_i - 1 \right) \{\ddot{q}\}_i \quad (5.42)$$

(5.37) and (5.38) gives :

$$[\overline{K}] \{q\}_{i+1} = \{\overline{F}\}_{i+1} \quad (5.43)$$

Where

$$\begin{aligned} [\overline{K}] \{q\}_{i+1} = \{\overline{F}\}_{i+1} = \{F\}_{i+1} + [M] & \left(\frac{1}{b * \Delta t^2} \{q\}_i + \frac{1}{b * \Delta t} \{\dot{q}\}_i + \left(\frac{1}{2*b} - 1 \right) \{\ddot{q}\}_i \right) + \\ [C] & \left(\frac{a}{b * \Delta t} \{q\}_i + \left(\frac{a}{b} - 1 \right) \{\dot{q}\}_i + \left(\frac{\Delta t}{2} \right) \left(\frac{b}{a} - 1 \right) \{\ddot{q}\}_i \right) \end{aligned} \quad (5.44)$$

So, the residue can be computed as:

$$R = [\overline{K}] \{q\}_{i+1} + F_{nl} - \{\overline{F}\}_{i+1} \quad (5.45)$$

The convergence criterion for the Newton Raphson method coupled with the implicit Newmark algorithm is reached if the residue R is higher than a small predefined value ε .

In the case of the residue R is higher than ε , a correction should be made. At the iteration $k+1$, this residue can be written as a Taylor expansion by:

$$R_{i+1}^{k+1} = R_{i+1}^k + \left. \frac{\partial R}{\partial q} \right|_{i+1}^k \Delta q \quad (5.46)$$

R_{i+1}^{k+1} must be equal to 0, so the correction to be made is:

$$\Delta q = \left(\left. \frac{\partial R}{\partial q} \right|_{i+1}^k \right)^{-1} (-R_{i+1}^k) \quad (5.47)$$

$\{q\}_{i+1}$, $\{\dot{q}\}_{i+1}$ and $\{\ddot{q}\}_{i+1}$ can be determined at the iteration $k + 1$ when Δq is computed.

2.2.3 Relationship between the non linearity and the non stationary regime

In the case of a variable rotation speed or variable loading, the meshing stiffness isn't periodic. An increase in the speed of rotation or increase of load with a decrease in the meshing period. The non-linearity is coupled with the non stationary conditions through the non linear force F_{nl} (5.22). Also, the input torque as mentioned in equation (5.34) will be modified as the non linear Hertzian stiffness is time depend to the input torque and the displacement (equation (5-12)).

3 Influence of combined non linear hertzian contact and non stationary conditions on the dynamic behavior:

In this section; the dynamic behavior simulated from the non linear model will be investigated in two case studies of non stationarity, run up regime and variable loading regime.

3.1 Run-up condition:

By using the Euler method for the resolution of Eq. (5.37), figure 5.5 shows the evolution of the rotational speed of the electrical motor. We can notice the presence of two distinct regimes. The first one called Regime (A) is the stationary regime during which the motor runs under its nominal rotational speed. The second regime (B) is the run-up regime characterized by an increasing of rotational speed.

Figure 5.6 shows the evolution of driving and load torques used for simulation.

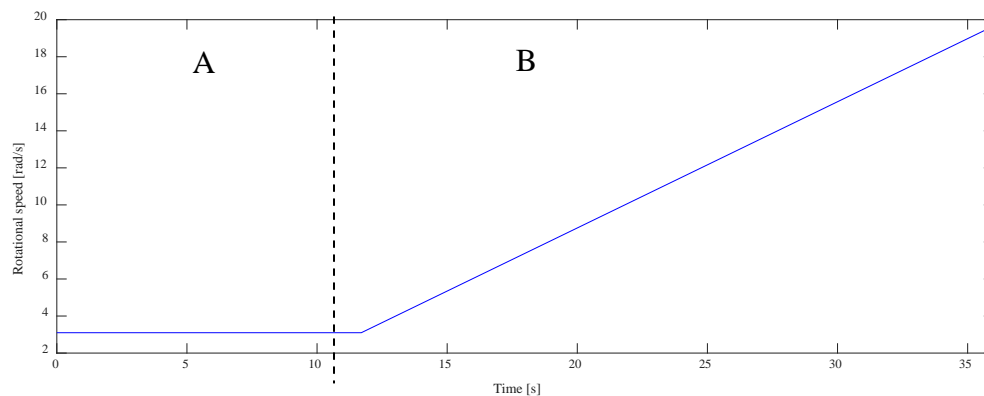


Figure 5. 5. Rotational speed evolution of electrical motor.

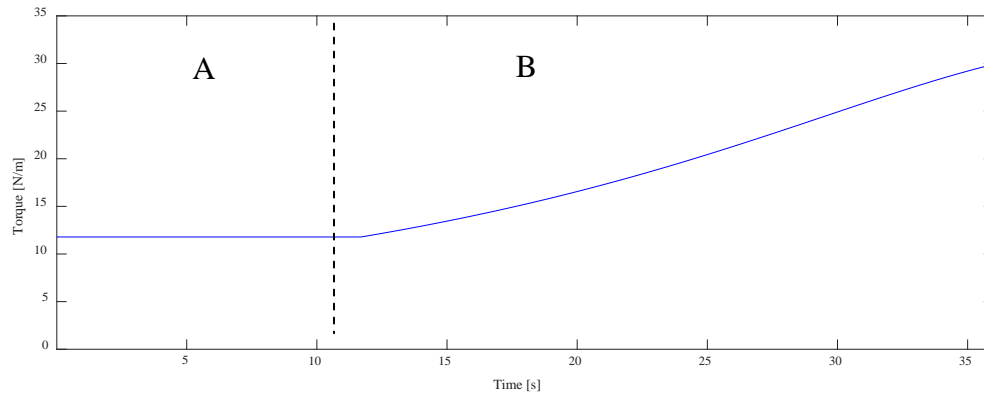
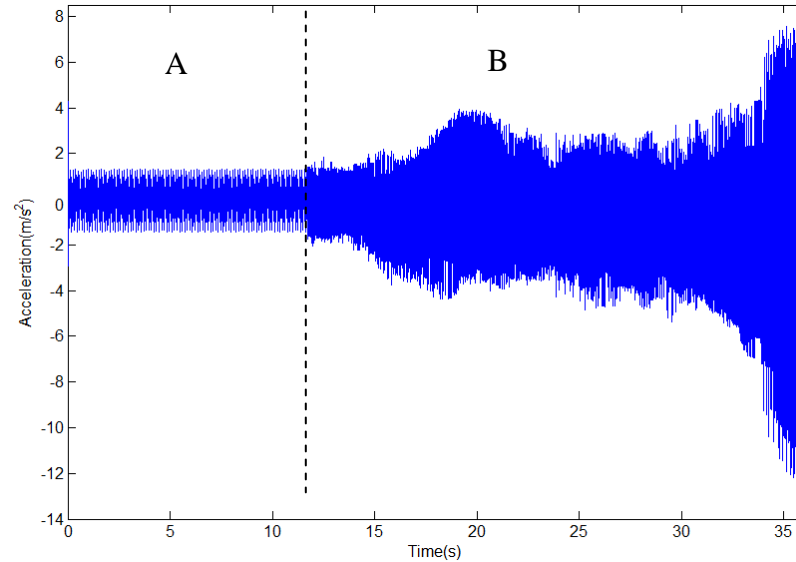
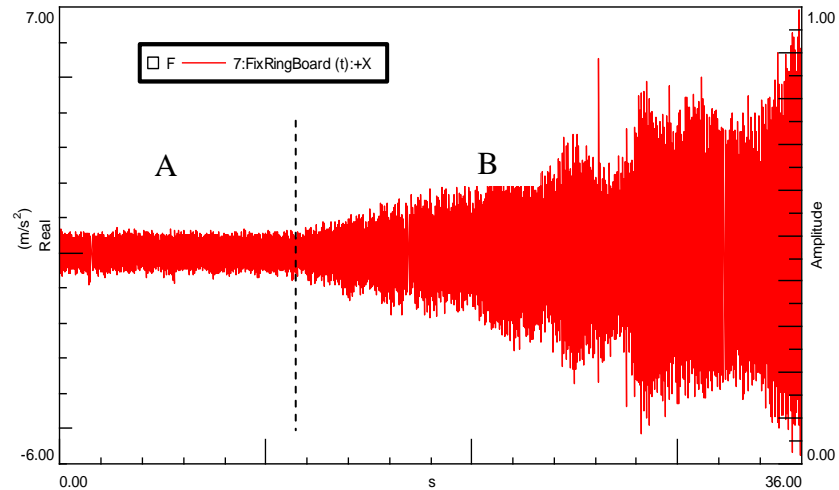


Figure 5. 6. Mechanical characteristics of the driving and driven system.

Figure 5.7 shows the time response of the acceleration measured on the fixed ring. The signal is divided into two parts following the evolution of rotational speed. Part A in which the amplitude of vibration are constant. Part B is run up régime during which we can notice that the vibration is increasing with respect to time. This phenomenon is due to the fact that during run up, the accelerating torque defined by the difference between motor and load torques is increasing giving rise to increased vibration.



(a)



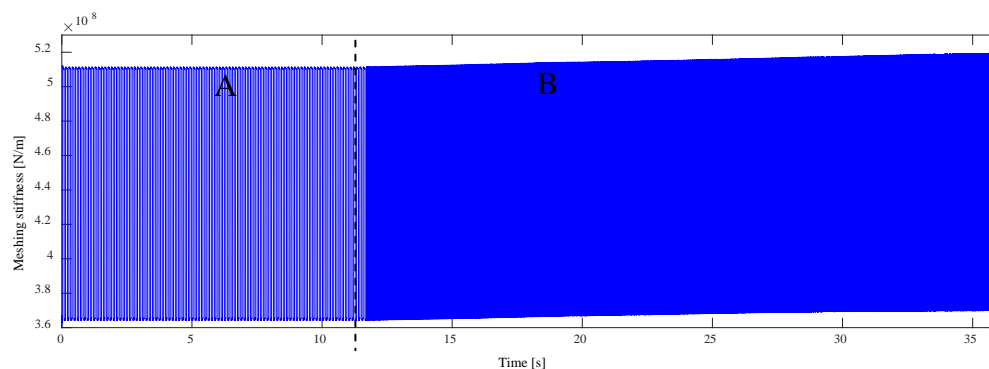
(b)

Figure 5. 7. Accelerations measured on the test ring: (a) Numerical (b) Experimental

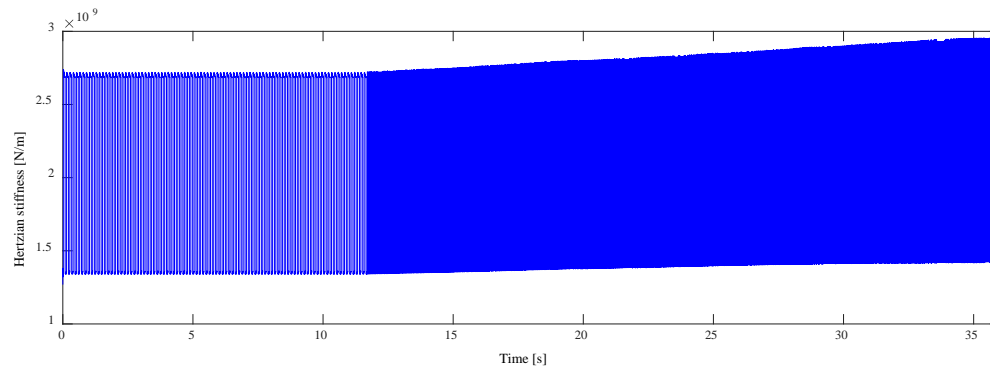
A time varying amplitude evolution of the equivalent mesh stiffness and the Hertzian stiffness is well-observed on figure 5.8.

The gear mesh stiffness are computed according to the procedure given in section 2. The bending and fillet foundation stiffness are computed for the ring, sun and the planets, as described in the following manner and coupled in series with the Hertzian stiffness. It is well observed the time varying evolution of this gear mesh stiffness around a mean value that amplitude is also varying in the run-up regime.

This matter is explained by the time varying teeth pairs in contact. This evolution has the similar shape to the torque value applied on the PG transmission (Figure 5.6).



(a)

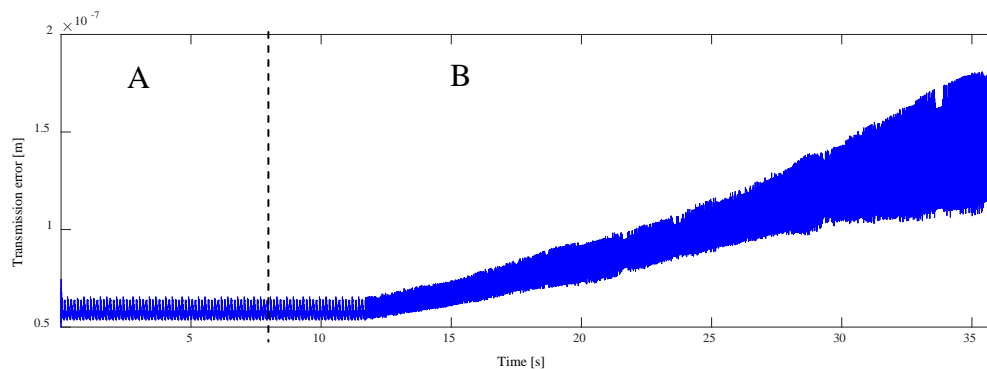


(b)

Figure 5. 81. Mesh stiffness evolution, (a) Ring-planet 1(b) sun-planet 1

The behavior of the Hertzian contact is reflected on the time varying mesh stiffness. In fact, the mean value of this stiffness acquires a maximum value before becoming constant after the run-up regime. This fact can lead several bad consequences especially for transmissions works under frequent start up regime like wear, pitting and spalling defects.

To confirm the influence of run-up regime on gear teeth, the transmission error and inter mesh forces are studied in ring-planets and sun planets mesh zones. The time evolution of transmission error function corresponding to ring-planet1 δ_{s1} is shown in figure 5.9.

**Figure 5. 9.** Transmission error function for the Ring and Planet 1 mesh

As mentioned for the ring acceleration, the same zones were recovered. The transmission errors are constant during the stationary regime (A) and they reach a maximum value during run up regime (B).

The dynamic force on teeth can be computed by:

$$F_d(t) = K_e(t)\delta(t) \quad (5.48)$$

Figure 5.10 shows the evolution of intermesh forces for ring-planet1 gear teeth pairs. We can notice that an overload is applied on teeth during the run-up regime. This phenomenon could absolutely cause effects to the transmission like pitting and bending of the teeth. This phenomena was highlighted by (Freese and Hill 2002),. They confirmed that during run up, electric motors can cause peak torques much higher than recommended for continuous operation which is transmitted by gear teeth.

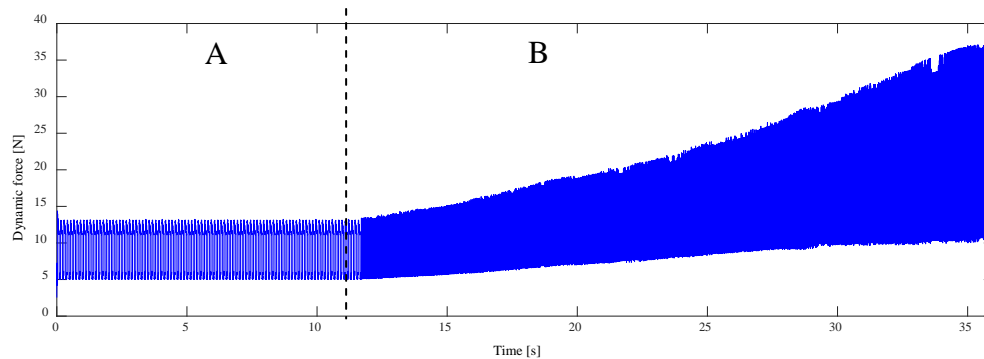


Figure 5. 9. Ring-planet 1 meshing force evolution

In the run up, the meshing frequency is not constant as specified in section To describe the evolution of the frequency content during this phase, a time-frequency map is drawn based on Short Time Fourier Transform (STFT).

Figure 5.11 displays STFT map obtained for acceleration on the test ring. We can notice that the map is divided into two parts. In part A, it is clear that mesh frequency and harmonics are constant over time. Zones with dark yellow correspond to high amplitudes obtained when crossing some Eigen frequencies.

For part (B) inclined lines show the increase of the meshing frequency and its harmonics during run up condition.

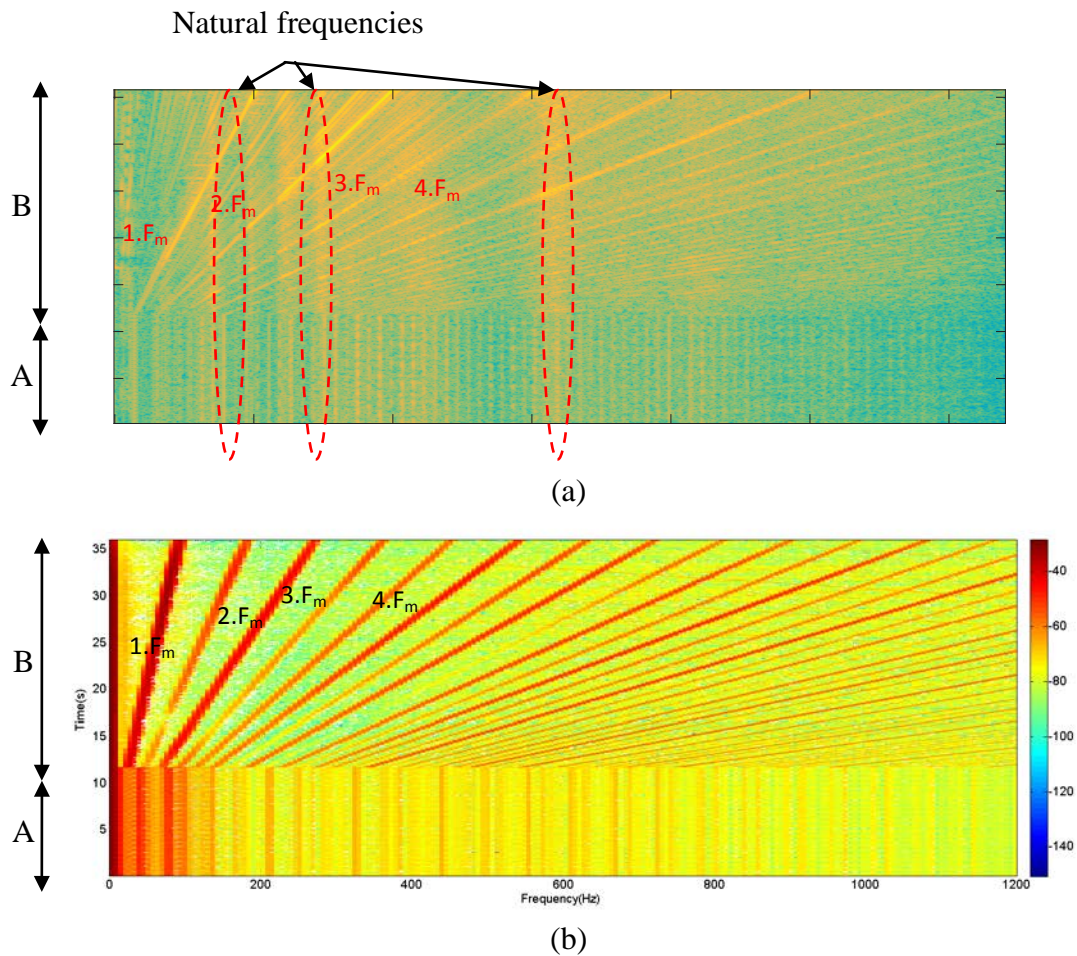


Figure 5. 10. STFT of the acceleration of the ring: (a) Numerical (b) Experimental

3.2 Variable load regime:

A special load shape (Figure 5. 12) was adopted during simulation.

The load in this case is varying with time which can introduce an instantaneous change in the mesh stiffness frequency and then the frequency modulation. In this case, the transmission was supposed driven by the asynchronous motor in which a speed controller impose desired speed evolution and values.

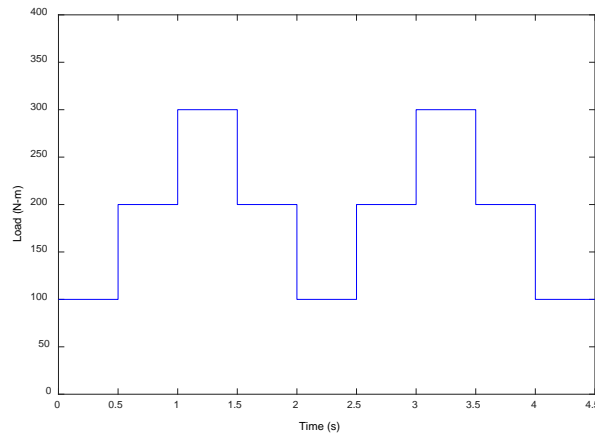


Figure 5.11. External applied load

The variation of the external load introduces a variation on the amplitude of the Hertzian stiffness as a consequence mesh stiffness function and on the period of teeth in contact as shown on (Fig.5.13).

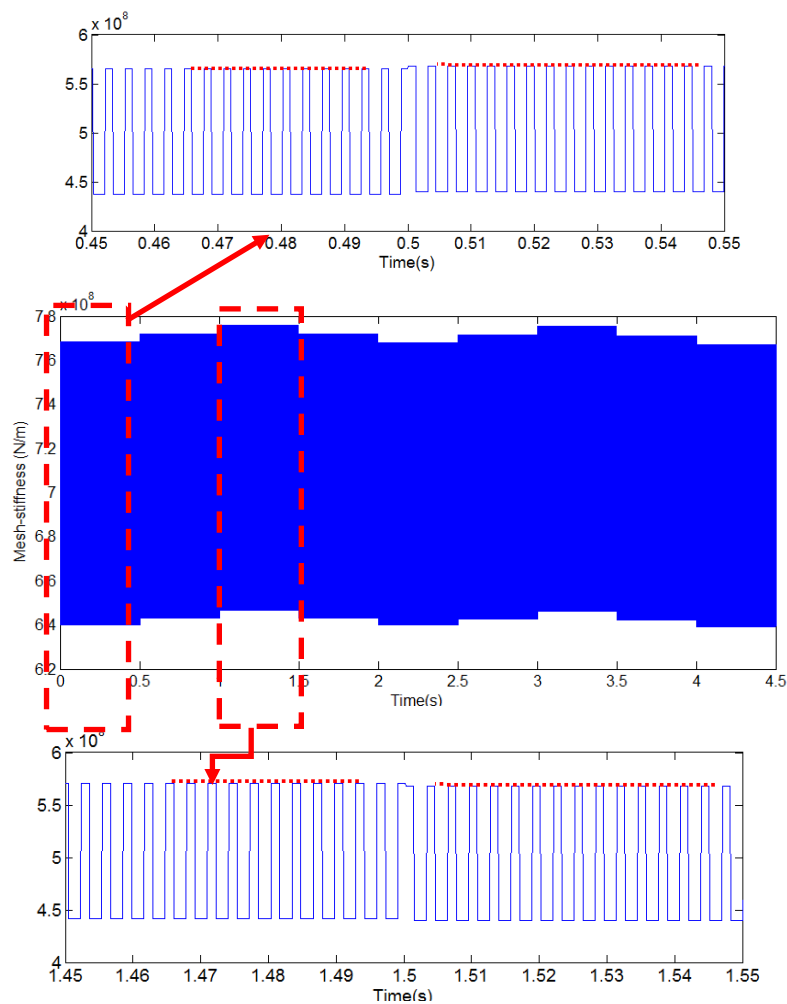


Figure 5.12. Ring-Planet 1 meshing stiffness

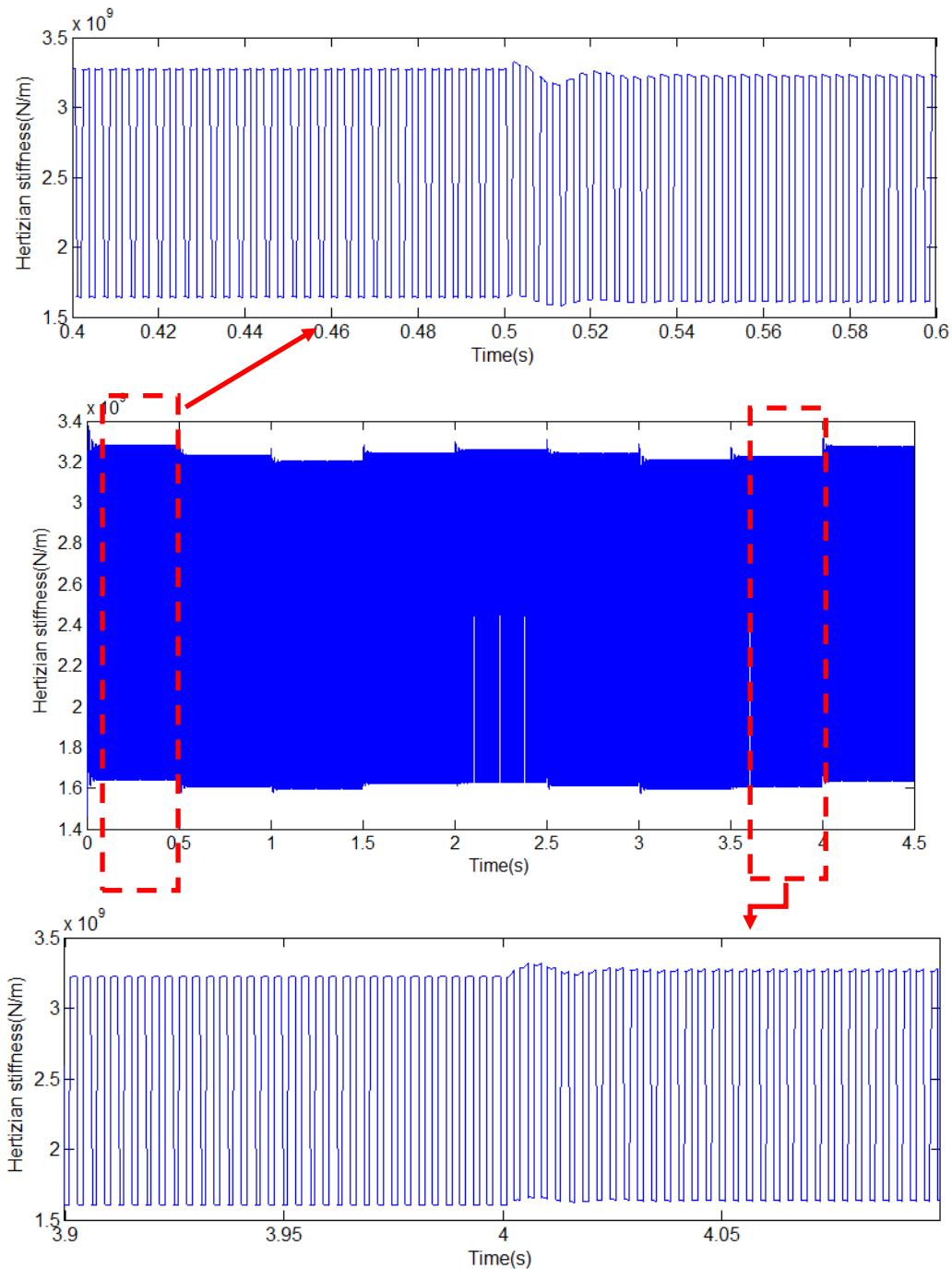


Figure 5. 13. Hertzian stiffness between the Ring and Planet 1

The time varying load applied on the system introduces a variation on different functions such as the transmission error and the meshing forces.

The sensitivity of transmission error to the load is shown in figure 5.15 for test ring-planet1 mesh .

With the increasing of load the contact between teeth increases as well as the dynamic transmission error. The load introduces a variation also on modal parameter (Ericson and Parker 2013). The increasing of load introduces an increasing of stiffness and masses of the system as consequence the natural frequency and modal damping change.

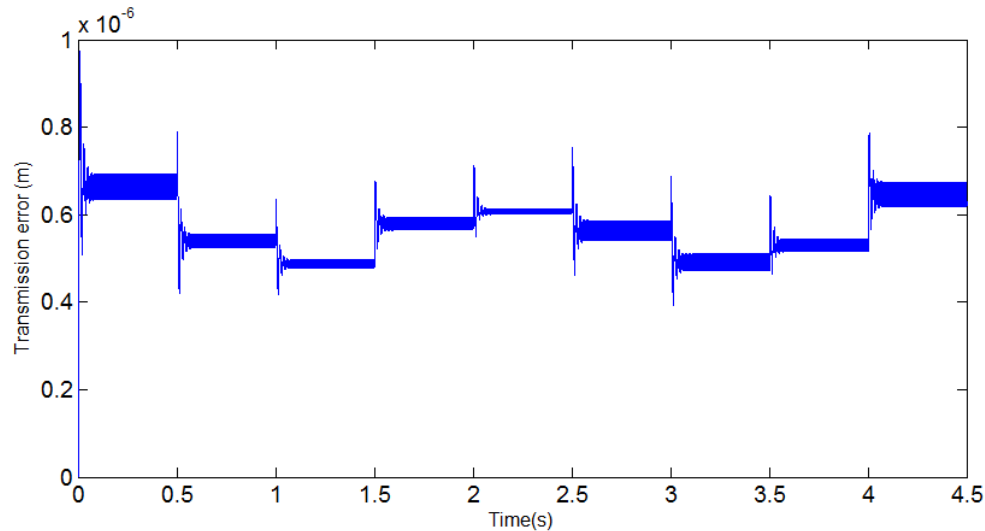


Figure 5. 14.Transmission error between test ring and planet 1

As mentioned for the transmission error, the same behavior was recovered for the meshing forces. With the increasing of load, the contact between teeth increases. This fact induces bending, shear and compression as well as Hertzian contact between teeth which lead a tooth deflection. Moreover, the effort in bearing and teeth varied too which may introduce an increasing in meshing force.

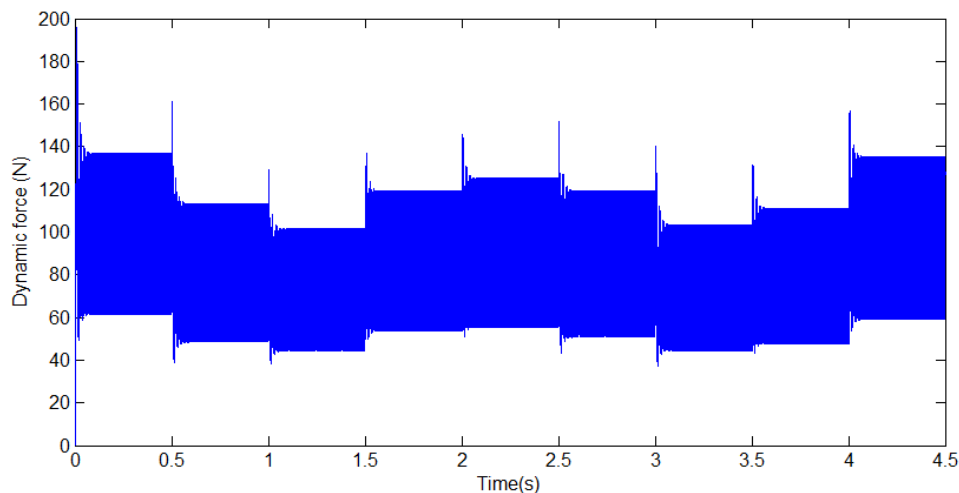


Figure 5. 15. Dynamic force between test ring and planet 1

4 Conclusion:

The dynamic behavior of nonlinear PG model in non-stationary conditions was investigated in this chapter. The nonlinearity due to the Hertzian stiffness was developed and coupled with non stationary condition. In cases of run up, a series of measurement were carried out. The main Results obtained are:

- For the run regime: the time signal determined numerically and experimentally are correlated, during this regime the time varying mesh stiffness is not periodic in the transient regime which causes higher vibration levels when starting an electric motor. The sensitivity of dynamic force and transmission error to the transient regime are also investigated. Hertzian stiffness and the gear mesh stiffness are constant during stationary condition before reaching maximum values of amplitude during run up condition.
- For variable loading condition, obtained results clearly the variability of load induce a variability of Hertzian stiffness, transmission error and meshing force.

The vibration response of the system in non stationary regime in presence of defect will be discussed in the next chapter.

**Chapter 6: Dynamic behavior in presence of defects in
non-stationary conditions**

Chapter 6: Dynamic behavior in presence of defects in stationary and non-stationary conditions

Sommaire

1	Introduction:	142
2	Stationary conditions:	142
2.1	Case of spalling defect on the planet:	142
2.2	Influence of load on the dynamic response:	147
2.3	Case of combined spalling defect on the planet and crack defect on the sun:	149
3	Non stationary conditions: run up regime:	154
3.1	Case of spalling defect on the planet:	154
3.2	Case of combined spalling defect on the planet and crack defect on the sun:	158
4	Conclusion	162

1 Introduction:

PG systems are frequently running under non-stationary operation in which loads or speeds are variable. These conditions affect on the behaviour of the system. In addition, different kind of defects can occur and that are related to teeth or to the geometry of gears. In order to study the behavior of the test bench in presence of teeth defects, two kinds of defects which are spalling and crack are studied through experiments done on the test bench and through simulations using the developed numerical model. The behaviour of the gear system will be studied for these defects and under time varying running conditions.

2 Stationary conditions:

In this section, the effects of spalling and cracked tooth are firstly studied in stationary conditions with constant load and speed. Both defects are created using electro erosion machine and numerically simulated using LPM.

2.1 Case of spalling defect on the planet:

The spalling defects located on the planet impact on the principal excitation source in PG which is the mesh stiffness function.

The defect is identified by its width ω_b (35 mm), its height h_b (2mm) and its thickness t_b (2 mm).

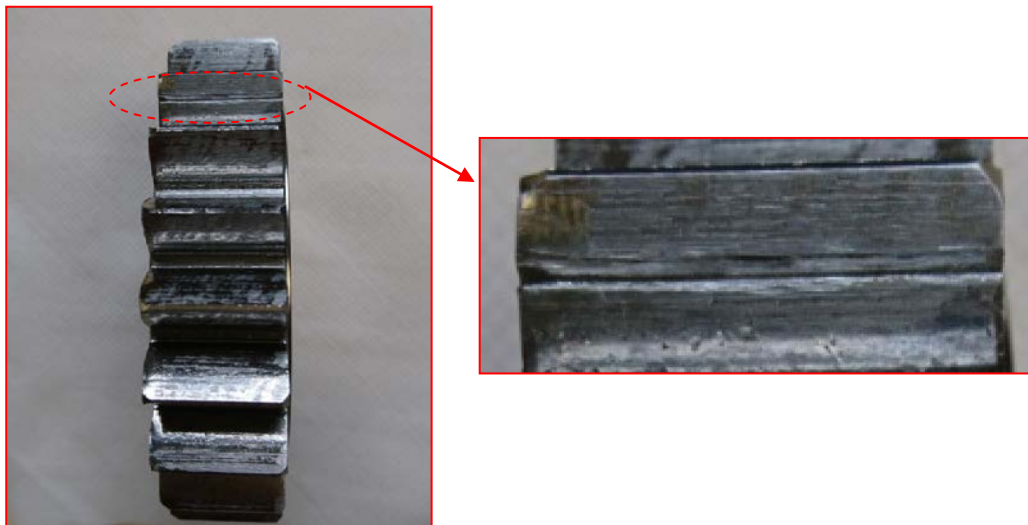


Figure 6. 1. Spalling defect located on the planet gear

Since the defect is located on one of the three planets of the test gear, the sun-planets and ring-planets mesh stiffness functions are modified. This kind of local defect is usually considered having rectangular shape on the tooth flank. The spalling defect can be modelled as indicated by (Chaari et al., 2006) by a reduction in the width of the tooth and as consequence an increasing of the deflection due to the bending. (Ma et al., 2016, Saxena et al. 2016) studied the influence of rectangular spalling shape and its location on meshing function.

Therefore, a fall of gear mesh stiffness when the defected tooth is in contact will occur as presented in figure 6.2. T_{dp} denotes the period of the defected tooth mesh. Its corresponding frequency is expressed by $f_{dp} = ((z_s/z_p) * f_s) - f_c$ where z_s and z_p are respectively the sun and the planet, f_s and f_c present respectively the sun and the carrier; this period is given by $T_{dp} = 1/f_{dp} = 0.22$ s.

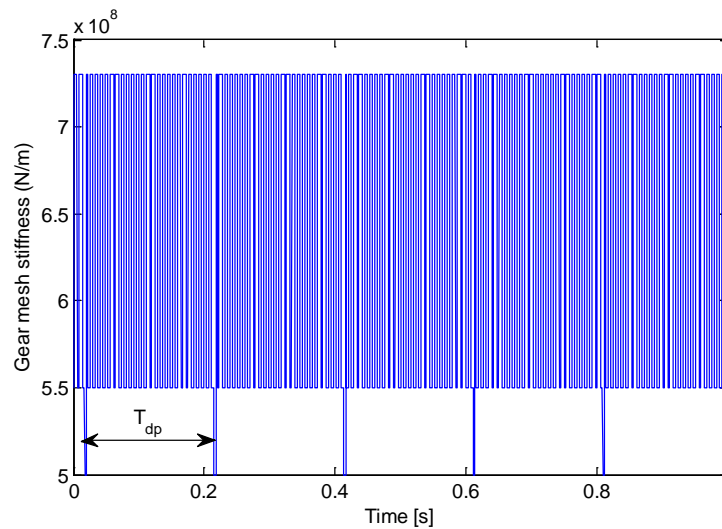
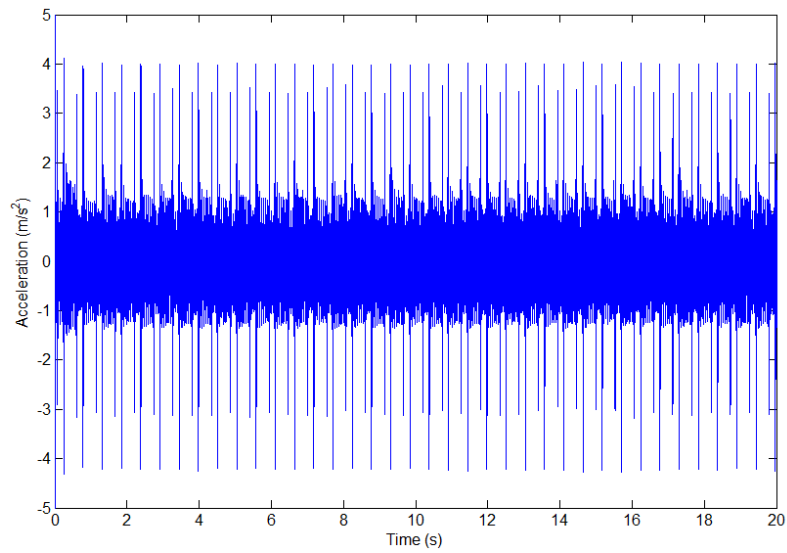


Figure 6. 2. Ring-planet 1 gear mesh stiffness trend in case of combined defect

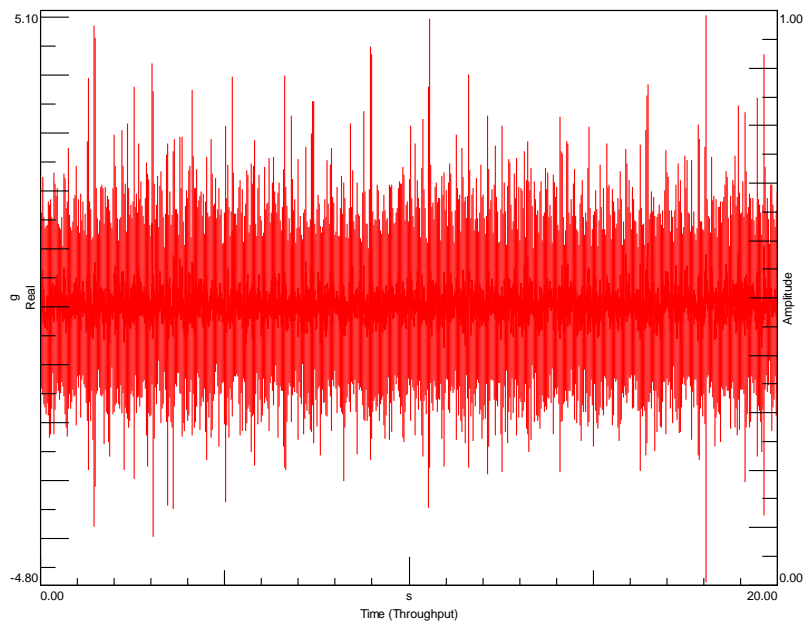
Experimental investigations on the influence of spalling on the vibration response of PG is limited in literature. (Ma and Chen 2012) used time response and spectrum analysis to study the influence of spalling defect on dynamic behaviour of single stage gear transmission.

The simulation and the experimental tests were carried out at fixed speed (590 rpm) and fixed load (100 N.m).

When the damaged tooth enters in contact with another tooth, periodic "impulses" appear in time response as presented in the Figure 6.3. The period T_{dp} of damaged tooth mesh is clearly identified on both simulated and measured time response.



(a)



(b)

Figure 6. 3. Time response of the acceleration measured on the angular direction (Θ) of the test ring (a) simulated (b) experimental

A similar behaviour is shown for both simulation and experimental time signals. However, it is observable that figure 6.3 b is contains much spikes than figure 6.3.a.This fact is related to such parameter like the white noise presented during experimental tests, also, the effect of the elastic coupling which is not considered in the developed model and the presence of mounting errors.

.

The spectrum of the measured and the simulated acceleration on the test ring is displayed in figures 6.4 and 6.5.

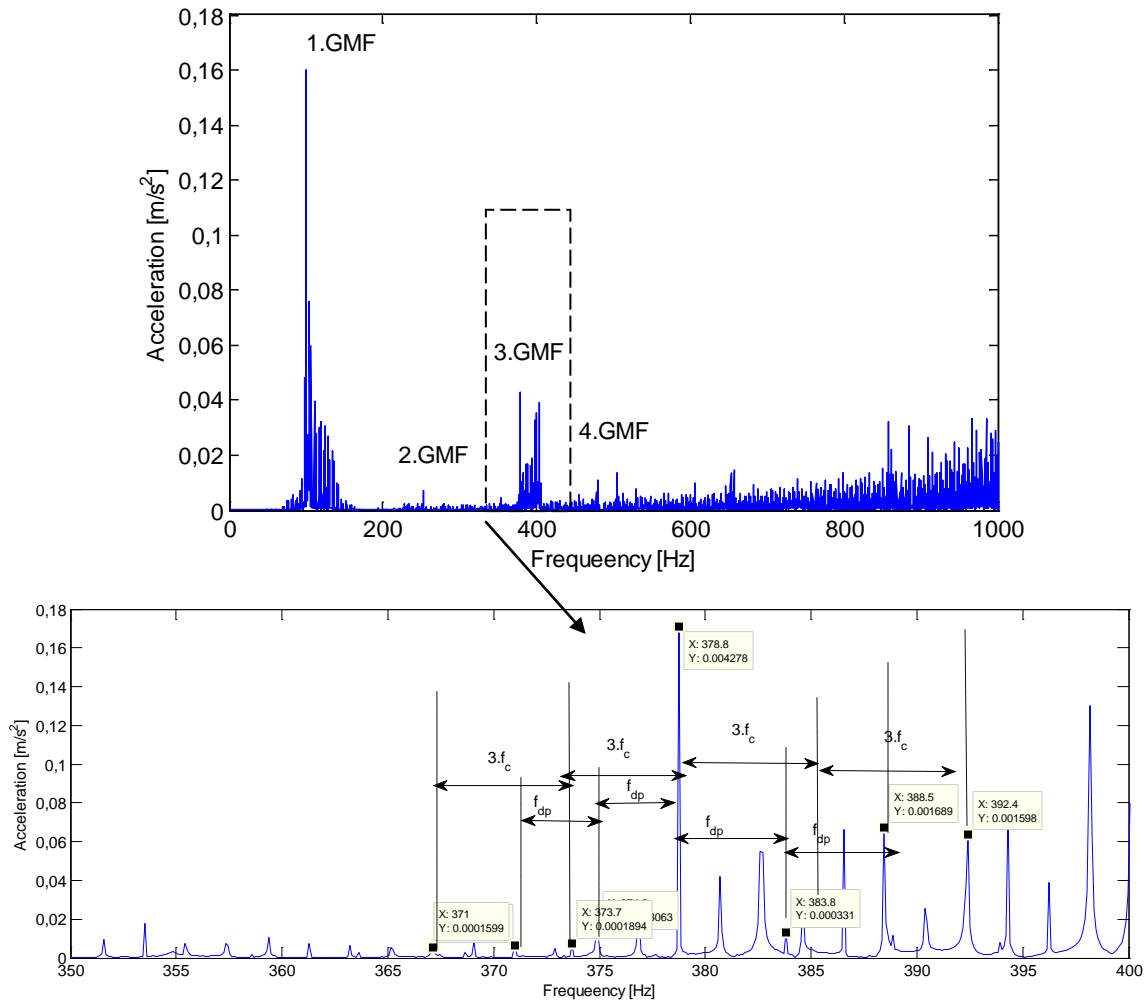


Figure 6. 4. Simulated spectra of the acceleration measured on the angular direction (Θ) of the test ring

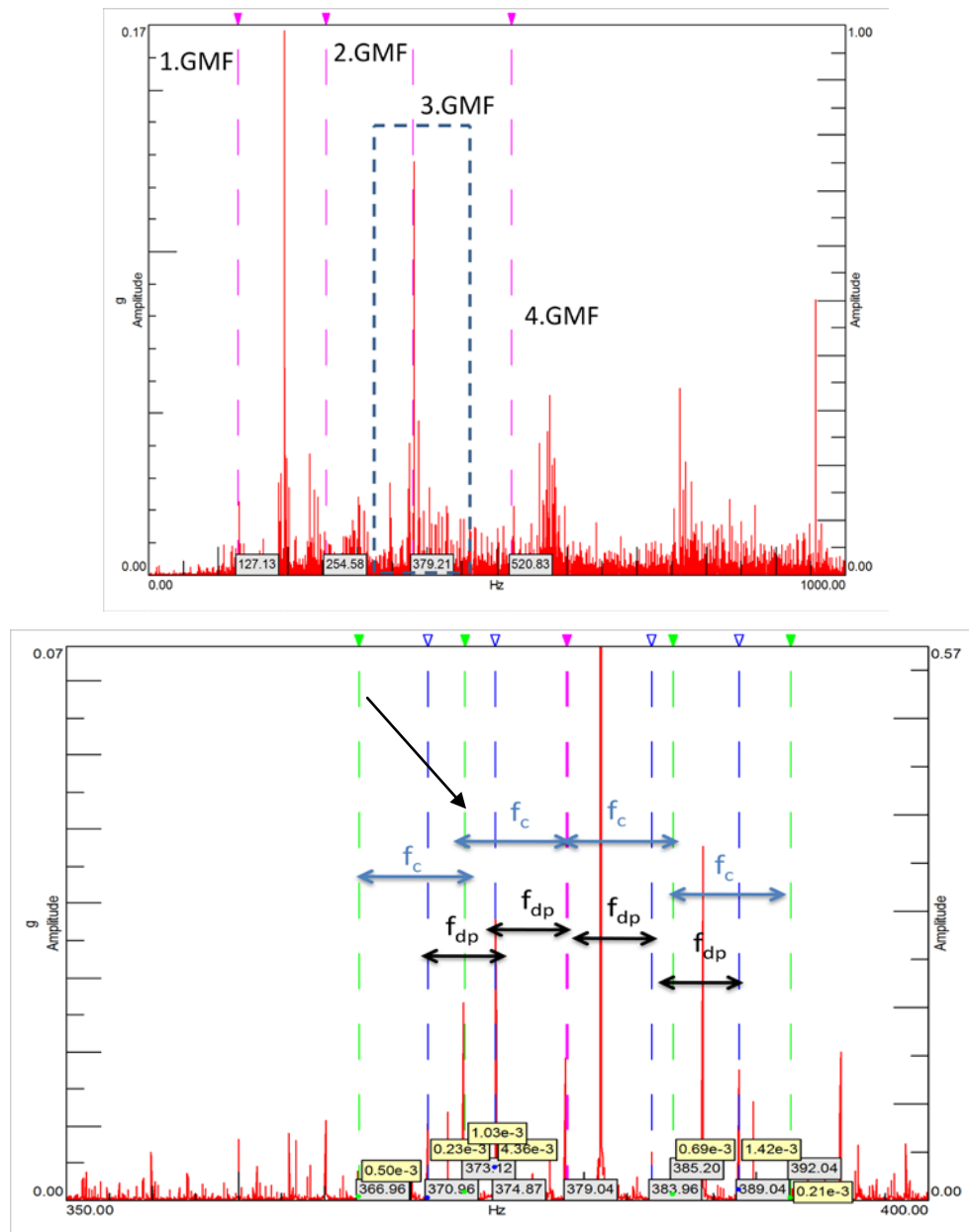


Figure 6. 5. Experimental spectra of the acceleration measured on the angular direction (Θ) of the test ring.

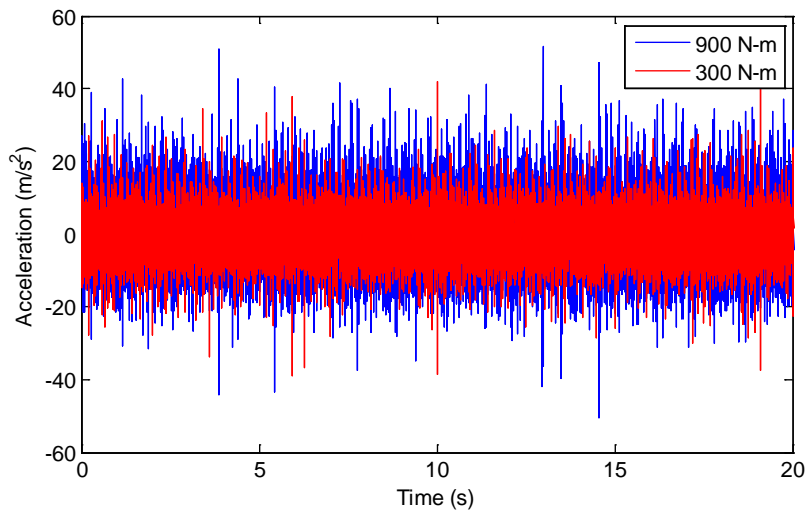
The spectrum of the acceleration measured and simulated on the angular direction (Θ) of the test ring is dominated by f_m and its harmonic. The frequency of the damage is $f_{dp}=1/T_{dp}$, this frequency is noticeable with sidebands around the gear mesh frequency and its harmonics.

The gear mesh frequency is modulated by the frequency of the defected planet and the frequency of the carrier multiplied by three (number of planets). The amplitude of sidebands related to the defect are low due to the geometry of the defect.

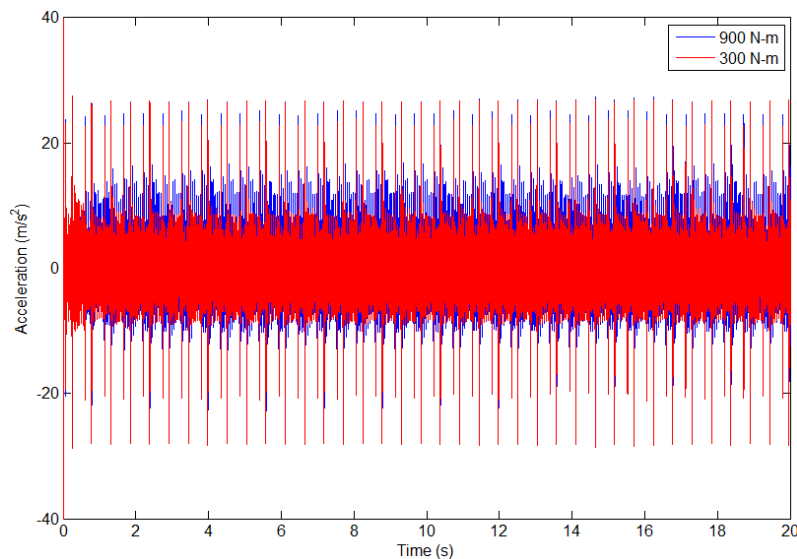
2.2 Influence of load on the dynamic response:

Influence of load on the dynamic response is studied numerically and experimentally. Based on the procedure given by (Fernandez et al, 2013), the meshing stiffness are determined and included in the model. Experimentally, two levels of load (300 N-m and 900 N-m) are studied by adding mass on the arm.

Figure 6.6 shows the time response of acceleration recorded on the angular direction (Θ) of the test ring. Figure 6.7 shows the corresponding spectra.

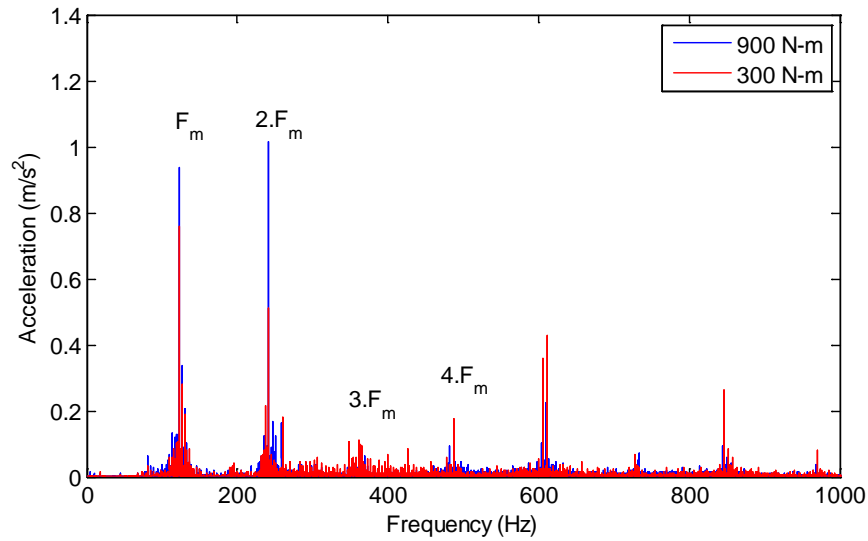


(a)

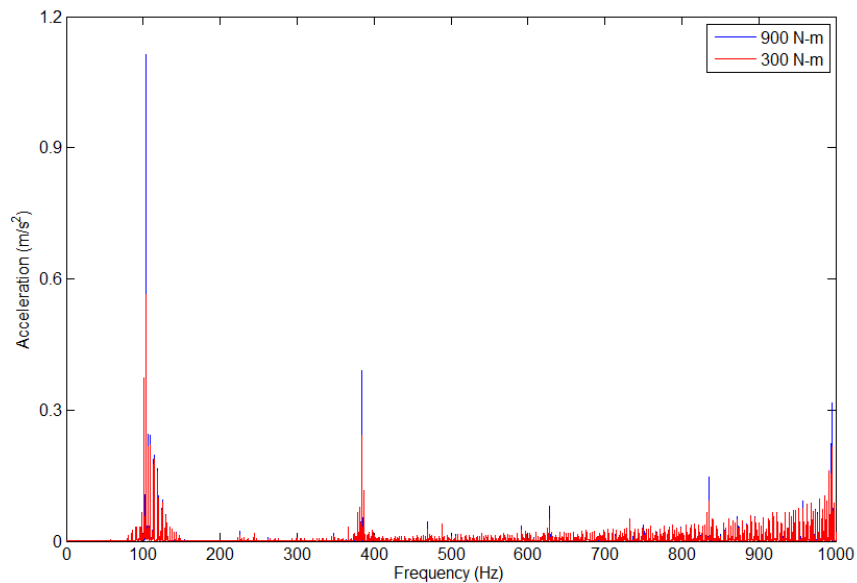


(b)

Figure 6. 6. Time response of acceleration on the test ring (a) measured (b) simulated



(a)



(b)

Figure 6.7. Spectra of acceleration on the test ring (a) measured (b) simulated

It can be observed from figure 6.7 that the increase of load leads to an increase of vibration level. This fact is also detected in frequency domain, the gear meshing frequency and its harmonics increase in amplitude as well as the sidebands around them. Therefore, the amplitude of peaks due to the defect increases. This behaviour confirms the sensitivity of load on meshing function. (Fernandez et al, 2013, Hammami et al 2016), noticed that when the load increase, the contact between teeth increase which lead to an increasing of the stiffness function amplitude. This fact

implies an amplification of vibration amplitude. Also, the meshing stiffness depends on the geometry of the defect, (Liang et al 2016).

2.3 Case of combined spalling defect on the planet and crack defect on the sun:

In this sub-section, a crack defect on the sun of the test gear is added to the existing spalling defect on planet tooth. Figure 6.8 illustrates the location of this defect. The crack initiation and propagation can be caused by several factors like the rim and the web thickness as indicted in Lewicki (Lewicki 2002). The combined two failures impact directly on the mesh functions. Researchers agreed that a tooth crack can be modelled by a reduction in meshing function (Chaari et al., 2006, Cheng et al 2012). In the studied case, this reduction is considered in the sun planet 1 meshing function respecting the period of the defect.

When the cracked tooth enters in contact with another healthy tooth, the time varying mesh function will be modified.

The crack at the sun tooth is identified by its inclination α_f (70°) and its length p_c (5.7 mm).



Figure 6. 8. Crack defect located on the test sun

The fact that the spalling defect is located on the planet 1, and a crack defect is introduced on the sun, two kind of reduction will appears on the ring planet mesh stiffness function following the period of each defect.

The investigations on combined defect are missed in literature. In our work, the PG is submitted to three main independent sources of excitation which are on the meshing phenomenon, the faulty sun and faulty planet.

The signal associated to this kind of defect will lead to combined amplitude modulations and a complex spectrum characterized by the presence of lateral bands spaced by f_{ds} and f_{dp} . The defect frequencies are expressed as follows:

$$f_{ds} = N * (f_s - f_c) \quad (6.1)$$

$$f_{dp} = ((z_s/z_p) * f_s) - f_c \quad (6.2)$$

With f_s and f_c are the rotational frequencies of the sun and the carrier, z_s and z_p are the number of teeth of sun and planets and N is the input speed.

T_{dp} and T_{ds} are respectively the period of the defected planet and sun. In this case, we assume that the meshing function start in mesh with the cracked tooth and then the spalled one.

Figure 6.9 illustrates the evolution of ring-planet 1 mesh stiffness function.

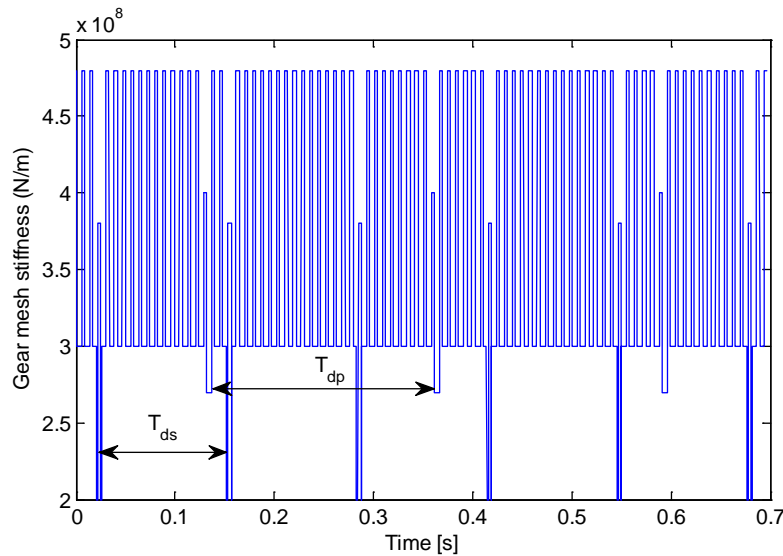
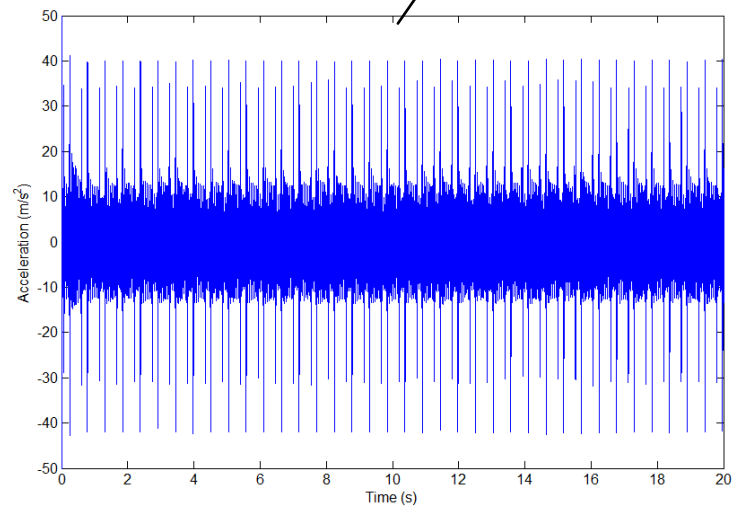
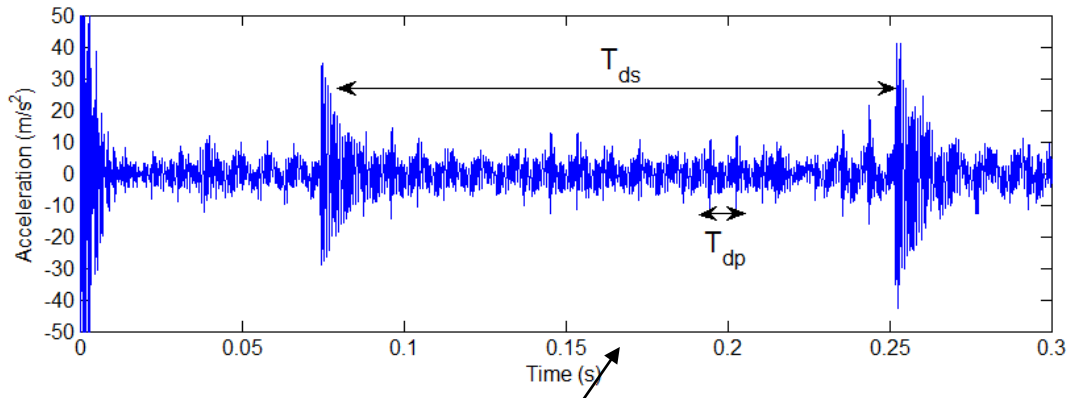


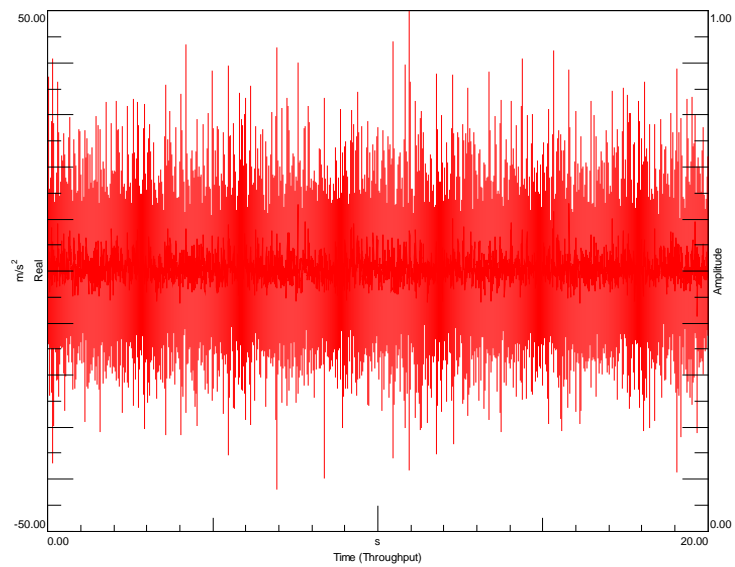
Figure 6.9. Sun-Planet 1 gear mesh stiffness trend in case of combined defect

Figure 6.10 shows the time response of the acceleration measured on the angular direction (θ) of the test ring.

During each period of rotation of carrier, two kinds of peaks are noticed in time responses: peaks related to the faulty sun and the others to the faulty planet (figure 6.10.)



(a)



(b)

Figure 6. 10. Time response of the acceleration measured on the angular direction (θ) of the test ring (a) simulated (b) experimental

As mentioned before, a difference between the time response obtained by experiments and simulation is noticeable. This difference is related to several parameters like the presence of mounting errors, effect of gravity of carrier and noise. Therefore, it is possible through spectra (figures 6.11 and 6.12) to detect the presence of peaks related to both defects by the activity of sidebands around $3xGMF$ that show clearly periodic spikes at f_{dp} and f_{ds}

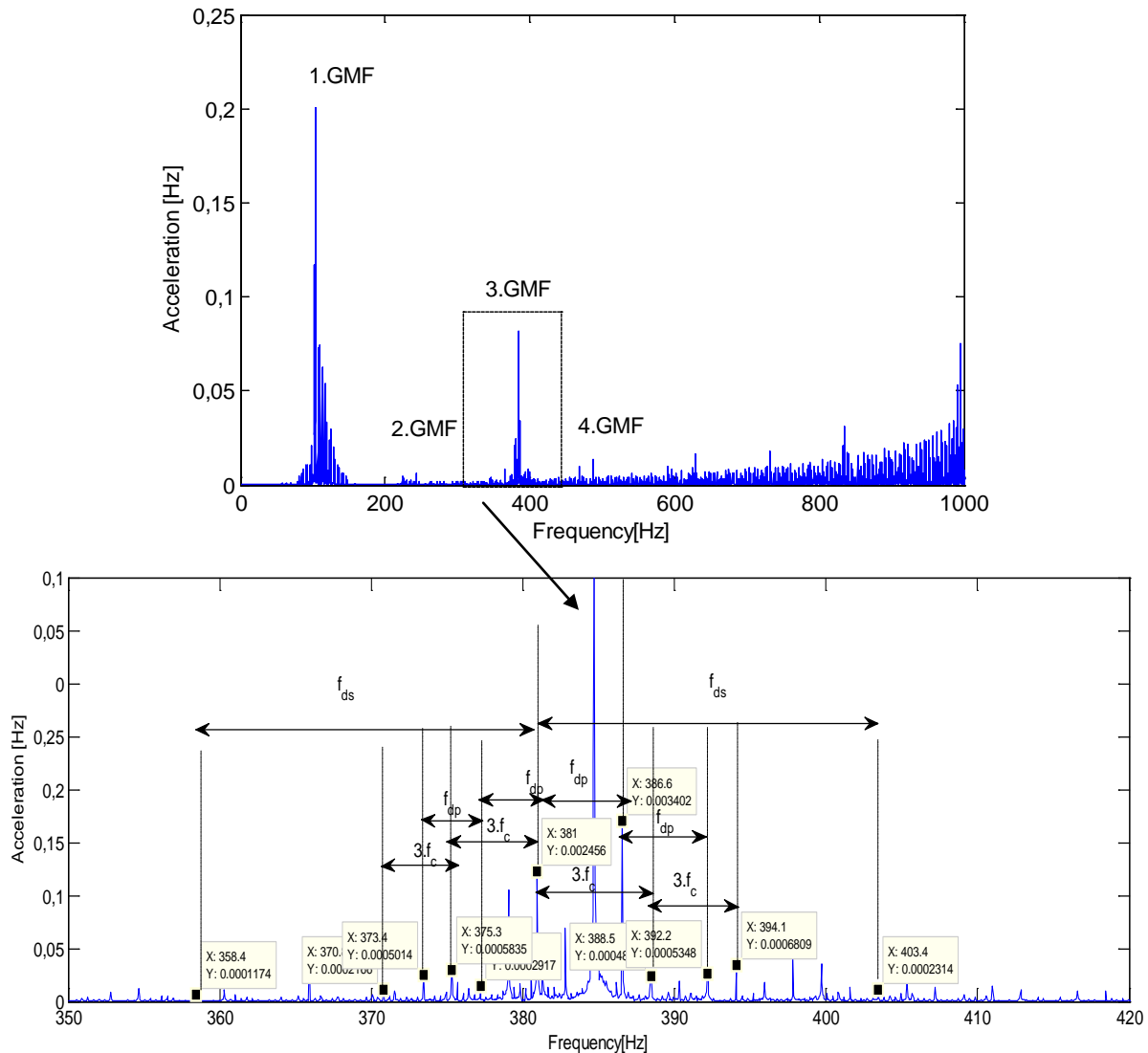


Figure 6. 11. Simulated spectra of the acceleration on the angular direction (Θ) of the test ring

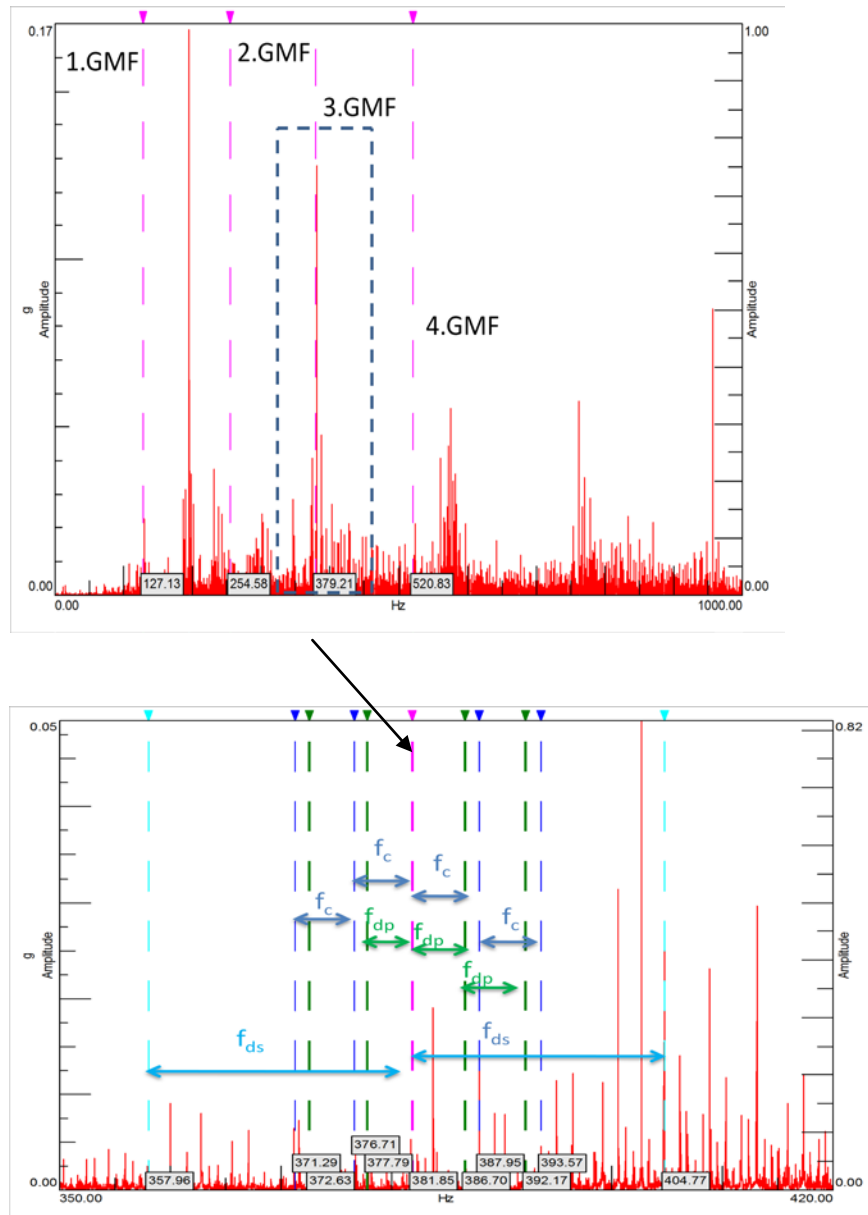


Figure 6.12. Experimental spectra of the acceleration measured on the angular direction (Θ) of the test ring

Figures 6.11 and 6.12 show that the gear mesh frequency is modulated by the frequency of the defected sun, the frequency of the defected planet defect and the frequency of the carrier multiplied by three (number of planets). The sidebands related to the defect are characterized by low amplitude due to the dimension of the defect.

3 Non stationary conditions: run up regime:

In this section, the two kinds of defects studied for stationary regime will be investigated for run up regime.

During run up regime the system is driven to 1000 rpm over 10 s as shown in figure 6.13

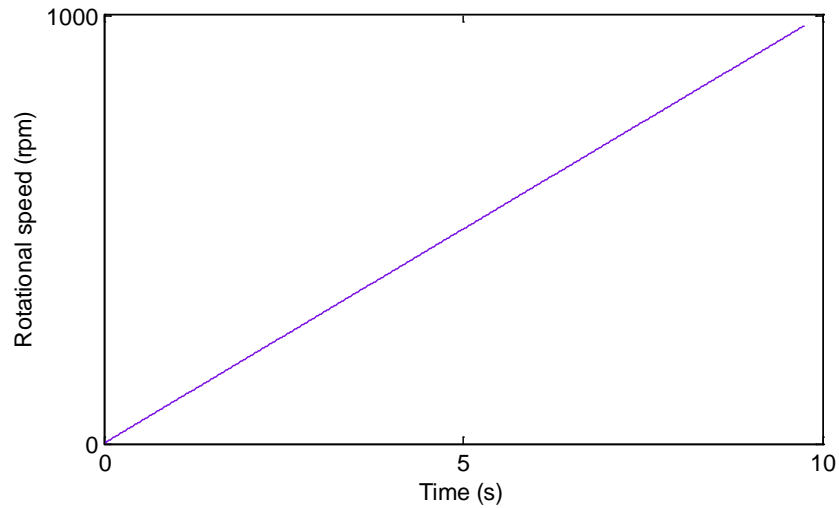


Figure 6. 13. Input rotational speed

3.1 Case of spalling defect on the planet:

Figure 6.16 shows the ring planet meshing stiffness function in presence of defect during run up regime. The time response of acceleration follows the rotational speed trend. The amplitude of vibration increases with time. Besides, peaks are noticed caused by the mesh of the test planet defected tooth. These pulses appear at each meshing of the faulty tooth.

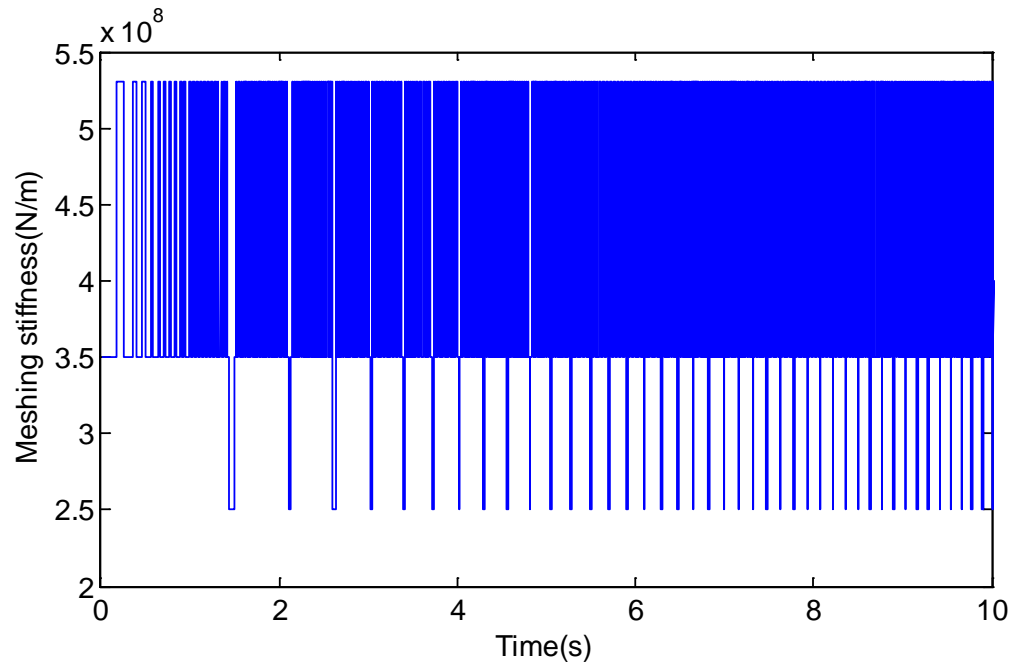
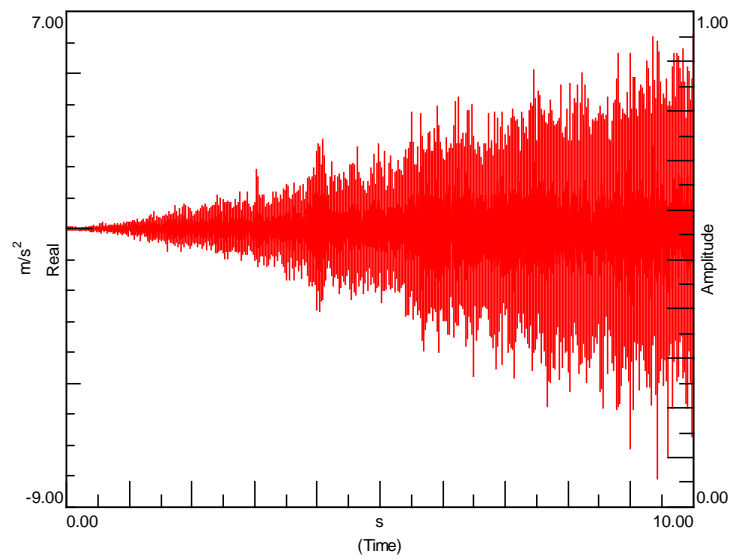
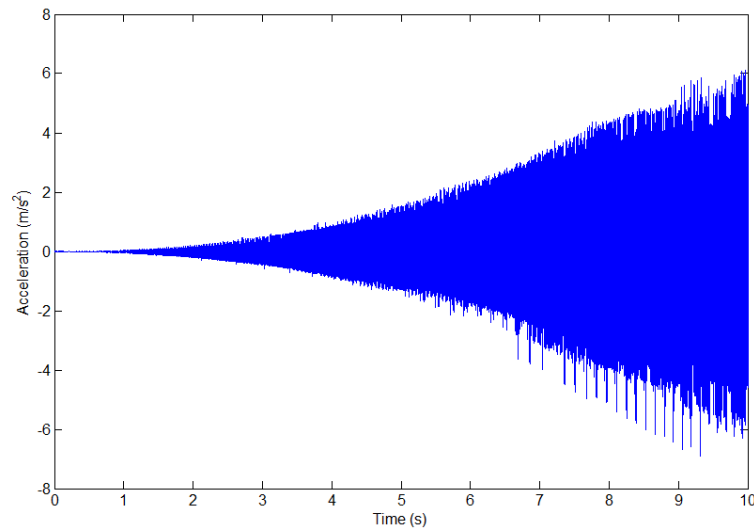


Figure 6. 14. Sun-planet 1 mesh stiffness evolution in presence of spalling defect

Figure 6.15 shows the time response measured and simulated during run up in presence of spalling defect.



(a)



(b)

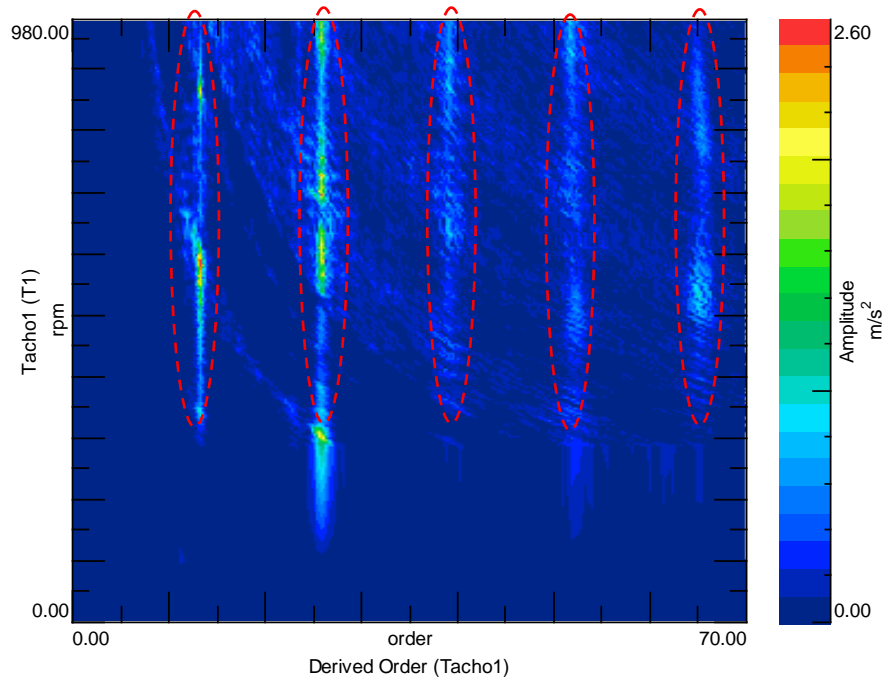
Figure 6. 15. Time response of the acceleration measured on the angular direction (θ) of the test ring (a) Experimental (b) Simulated

The recorded time response gives general information about the presence of the defect but it did not indicate which component is faulty especially when the system runs under non-stationary regime. For this reason, an angular method is proposed in order to define the faulty component.

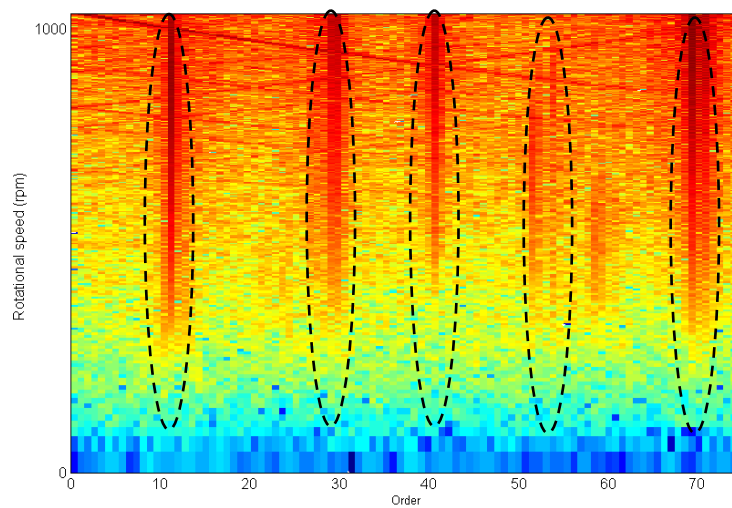
The frequency-based techniques are only applicable for stationary operating conditions. In practice, most of rotating machineries will experience time varying speed conditions. As a result, vibration signals are intrinsically angle-cyclostationarity rather than time-cyclostationarity processes (J. Antoni et al 2004, S. Lu et al 2016). As a consequence, frequency and spectral smearing phenomenon will be observed in the vibration signals; the frequency-based techniques based on assumption of constant rotating speed are no longer applicable. Among the fault diagnosis approaches, order tracking (OT) has been validated to be one of the most effective tools.

The OT method resamples the raw signal with a uniform angle increment, which transforms the irregular signal in time-domain into regular periodic or quasi-periodic signal in the angle-domain. On this basis, the spectral smearing phenomenon will be eliminated in the angular domain. As a consequence, the traditional frequency-based techniques become applicable again for further analysis, (Luo and Mathew (1993).

Figure 6.16 shows the order map of the acceleration of the test ring. The signal is obtained after transforming the time data to angular data using angle domain order tracking. Numerically, the order map is determined based on the procedure explained in chapter 3.



(a)



(b)

Figure 6. 16. Order map of the acceleration simulated on the test ring

The meshing orders are well observed in the figure by the presence of the vertical lines.

The orders presented in this figure are a multiple of the transmission ratio.

A zoom around the ten first orders is displayed in figure 6.17. By computing the order of the faulty planet which is $O_p=2.4$, a slight energy due to this defect is detected.

This order is computed using the following expression:

$$O_p = \frac{z_r + z_p}{z_p + z_s} \quad (6.3)$$

The low energy level can be explained by the small geometry of the defect

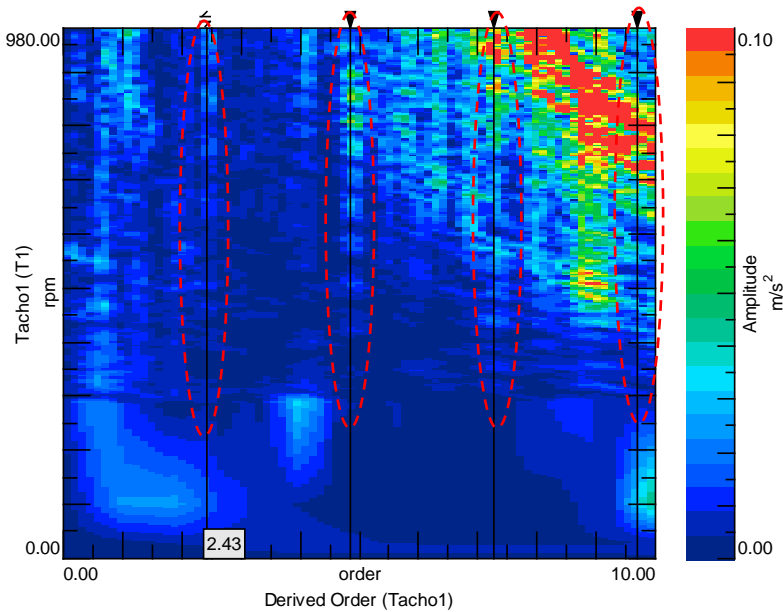


Figure 6. 17. Zoom around the first ten order of the acceleration measured on the test ring

3.2 Case of combined spalling defect on the planet and crack defect on the sun:

The two defects are modelled and implemented in the numerical model. The Sun-planet 1 mesh stiffness function evolution during run up and in presence of combined defects is displayed in figure 6.18.

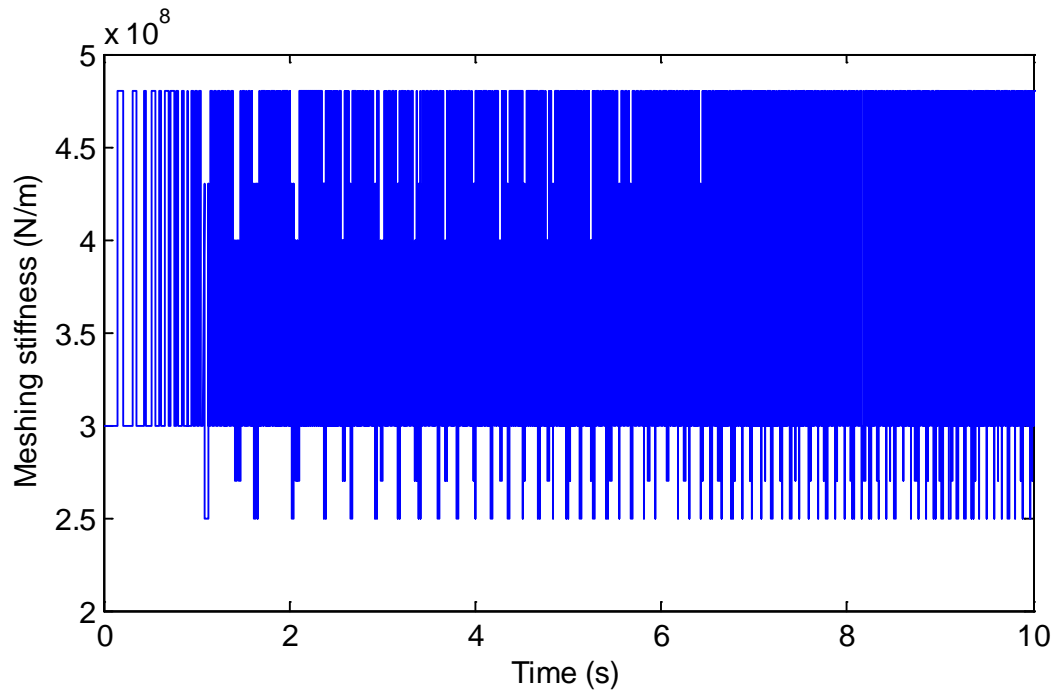
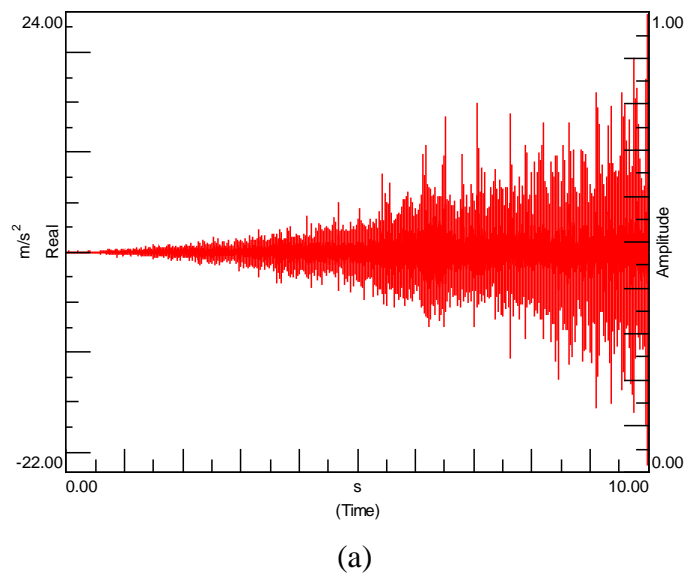
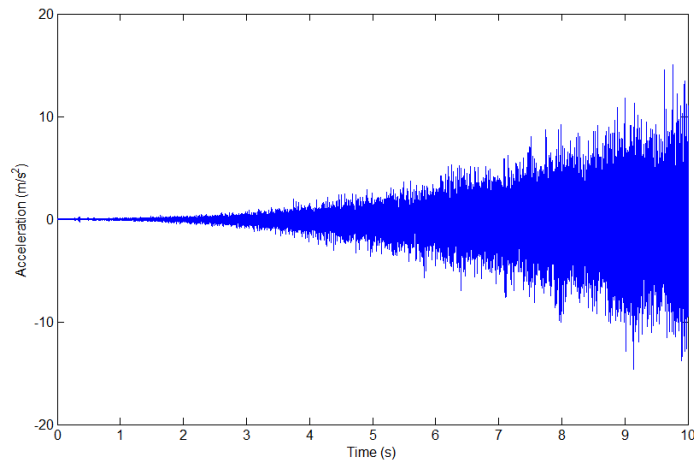


Figure 6. 18. Sun-planet 1 mesh stiffness evolution in presence of combined spalling and crack defects

The time response is recorded for the test bench for the run up regime and in presence of the two defects. Order tracking method is also used to process the time signals.

Figure 6.19 shows the measured and simulated vibration signal on the angular direction (θ) of the test ring.

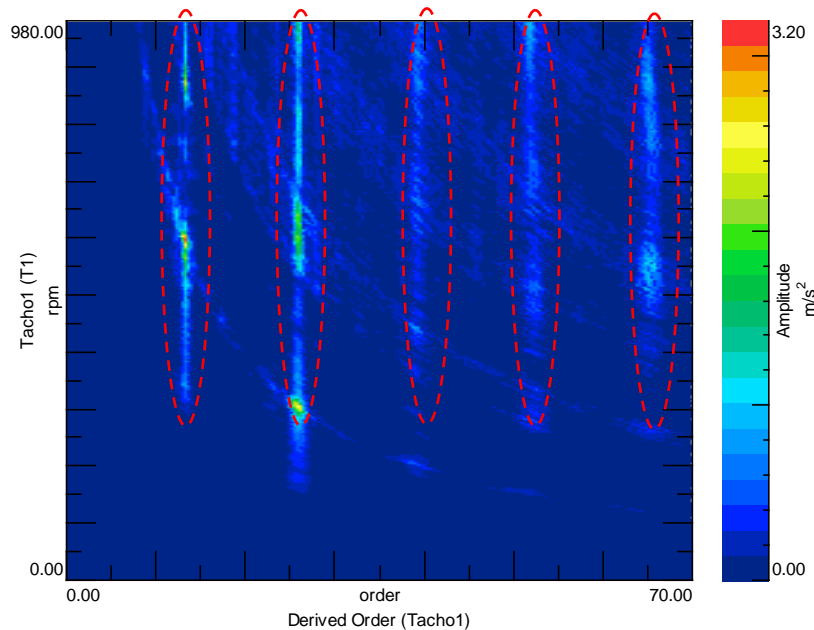




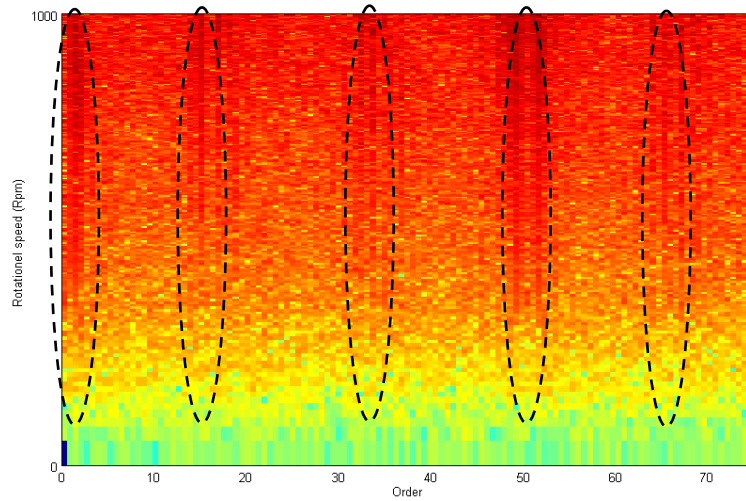
(b)

Figure 6.19. Time response of the acceleration measured on the angular direction (θ) of the test ring (a) simulated (b) experimental

Different peaks appear on the time response signal showing the presence of defect. The PG system, is driven, as mentioned before, in non stationary conditions, the period of defect is variable, so the frequency of the defect during this stage cannot be identified. To identify the orders associated to these defect, order maps are presented in figure 6.20 for measured and simulated signals.



(a)



(b)

Figure 6. 20. Order map of the acceleration on the test ring (a) Experimental (b) Numerical

It is clear from figure 6.20 the presence of vertical lines proving the meshing orders. Also, the meshing orders are observed for simulation.

To detect the presence of defects on the order map, a zoom around the first ten orders is achieved. The order associated to the sun tooth defect is:

$$O_s = \frac{Z_p}{Z_r} \tag{6.4}$$

The spalling and crack defects are characterized respectively by the order $O_p = 2.4$ (pink cursor) and $O_s = 0.4$ (black cursor). The defect orders are harmonic.

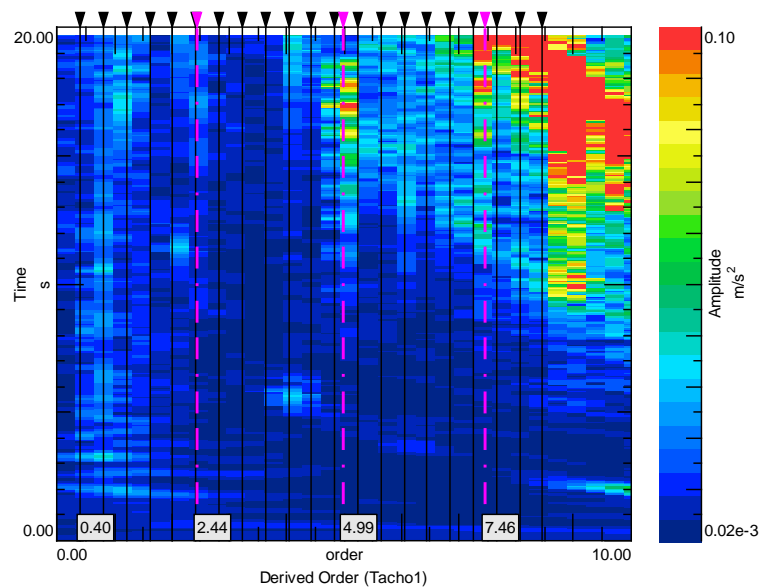


Figure 6. 21. Zoom around the first ten order of the acceleration measured on the test ring

4 Conclusion

In this chapter, the dynamic behaviour of two PGs in presence of defect is discussed using measurement test and simulations issued from the numerical model. The frequency characterization of the system in stationary condition (fixed load and speed) is highlighted in the cases of single and combined defects. Two kinds of defect which are spalling and crack defects are studied. The meshing stiffness functions in presence of defects are modified by a progressive reduction of the meshing stiffness which causes an amplitude modulation of the meshing frequency.

The vibration amplitude is increased in both time and frequency domain comparing to the healthy cases. The amplitude of sidebands depends of the location of the defect (sun or planet). The sensitivity of defect to the load is analyzed for two cases of load. With increasing of load, the amplitude of sidebands referred to the defect increase.

The impacts of defects are also analyzed in non stationary condition during run up regime, by using order tracking method; the defects are identified experimentally and numerically.

Conclusion

This chapter is dedicated to the conclusion of the thesis by presenting the thesis statement and main findings, and finally the author's view, on the scope of further research in this area.

Thesis statement and main findings

In this research work, the dynamic characterization of planetary gear transmission, under stationary and non-stationary operating condition in healthy and damage cases, were achieved. The thesis provided also better knowledge of the planetary gear modals parameters through the implementation and confrontation of different modal analysis techniques in the identification of these parameters especially for different loading conditions. The influence of the external excitation which leads to non stationary conditions was investigated. The incorporation of non linear contact formulation in the mesh stiffness functions allowed the computation of vibration response taking into account Hertzian formulation. On the other hand, the dynamic behaviour of the system in presence of single or combined defect is highlighted especially for non stationary conditions. The results were obtained through the implementation of different dynamic models that are validated through experiments done on test bench.

The principal findings accomplished throughout this research can be summarized as follows:

- A three-dimensional lumped parameter of planetary gear system was developed. The corresponding results were confronted successfully to experimental results issued from test bench.
- Planetary gear natural frequencies and damping ratios were identified using three different modal analysis techniques.
- The mesh stiffness variation impacts on the modal properties of the system.
- The natural frequencies and modal damping depend on the applied loading conditions.
- The non linear Hertzian contact has an effect on the dynamic behavior of the system in non stationary condition.
- The diagnosis of combined teeth defects in non stationary conditions was performed using Order tracking method.

Conclusions

The main conclusions issued from this research work are presented as follows:

In a first step, modal analysis techniques which are EMA, OMA and OBMA were investigated and then compared. A LPM of the gear transmission was used to implement these three techniques numerically jointly with an experimental investigation on a test bench. Using the Stabilization diagram and modal assurance criterion and based on FRFs, a complete thorough modal analysis was done. The natural frequencies, modal damping and mode shapes were identified and correlated to others issued from the LPM. Thus, based on CPSD and order functions respectively for the cases of OMA and OBMA, natural frequencies and damping ratio were extracted numerically and experimentally. However, the building of modes shapes in those cases is difficult due to the limitation of instruments. These two techniques are applied when the system is driven in stationary regime or non-stationary regime (run up or run down conditions). A comparison between these three techniques allowed us to conclude that OBMA technique is close to EMA, but it is powerful for practical engineering application since it allows modal analysis even in non stationary conditions. To provide a further insight in OBMA, the effect of load change and run up on the dynamic characterization is highlighted. Four different loading conditions were treated. It was shown that that the amplitude of meshing forces and the period of teeth double contact increase as the torque level increases. It was found also that inertia of the ring and the average value of mesh stiffness function change. This behavior was noticed on mesh stiffness trends. Moreover, an increase in vibration amplitude on the test ring was observed as well as the spectral density associated to the first (GMF) which moves to second (GMF) harmonic. The results confirmed the fact that when the torque is increased, the contact force between the teeth increase, which lead to an increasing in internal force values at the bearing and the teeth and a fluctuation of the pressure angle and therefore an increase of the contact ratio.

For modal parameters estimation, load plays an important load and contributes significantly to their change. With increasing of the load, natural frequencies and modal damping change. This fact was explained by the increase of mesh stiffness amplitude as well as an increasing of forces transmitted to teeth and bearings.

In a second step, series of simulations and experiments were carried out in stationary regime and under non-stationary operating conditions whether in healthy or damaged cases. What stand out from the obtained results are:

- The dynamic responses of system in healthy case have shown the presence of amplitude modulation on vibration signals explained by the actuating force induced by the rotation of carrier, which is related mainly to the influence of periodic passage of planets close the sensor. The vibration amplitude increase when a planet approaches sensor location.
- The spectrum of acceleration is dominated by the meshing frequency and its harmonics. Sidebands are observed around these components as a consequence of the above cited phenomenon.
- The influence of carrier on the vibration response is identified. In fact, the gravity of carrier creates a variation in the amplitude of meshing function giving rise to sidebands on the spectra spaced by the rotational frequency of carrier.
- Non-stationary conditions which can be found in run up regime, variable speed and variable loading conditions were studied. Two kinds of modulation were observed. An amplitude modulation due to the evolution of the rotational frequency of the carriers' components is noticed. Added to that, a frequency modulation related mainly to gear meshing function is also observed induced by the variability of speed. Short time Fourier analysis was carried out experimentally and numerically in order to characterize frequency content and to identify the speed variation. The STFT showed inclined lines corresponding to the variation of the meshing frequency.
- The influence of the non linear Hertzian contact stiffness between mating teeth on the dynamic behaviour in run up and variable loading conditions was examined. The meshing stiffness amplitude is found to be is non constant. In fact, it is sensitive to the speed and the applied load which affect the vibration response. The sensitivity of dynamic force and transmission error to those regimes were also investigated.

The final part of this thesis is dedicated to the study of the dynamic behaviour of planetary gear system in presence of teeth defects in stationary and non-stationary regimes. The main principal points issued from this study are as follow:

- A reduction on the meshing function respecting the period of rotation of the considered component indicates the presence of defects on the damaged tooth whether in cases of single or combined defect.
- The presence of defect has an impact on time response and spectra by an increase of the vibration amplitude. This is well noticed on meshing frequency amplitude and its harmonics as well as the presence of sidebands which allow the identification of the faulty components.

- The external applied load has an impact on the dynamic response of faulty system. With increasing of load, the vibration amplitude increase. This phenomenon is noticed in time and frequency domain related mainly to the increasing of contact area when the system is loaded.
- The identification of the faulty components in non stationary condition using time response and STFT presentation is limited due to the small geometry of the introduced defect and the change of frequency content over time.
- The Order Tracking method could be the solution for the identification of defects in such conditions. This was demonstrated for single or combined defects detection in run up regime.

This research work contributed to the dynamic characterization of planetary gear system by the identification of modal parameter, the highlight of the influence of internal and external excitations dynamic behaviour of those systems. Moreover, it offers tools for vibration diagnosis that could be used for condition monitoring of machines operating in non stationary condition in healthy and presence of defects.

Future works

As perspective and future works of this thesis we can define the following tasks:

- More kinds of defects whether tooth or geometrical defect can be studied and implemented numerically and in the test bench in order to investigate the dynamic behavior of these system in stationary and non stationary operation.
- More powerful signal processing techniques can be developed allowing the identification and the characterization of these defect.
- Experimentally, different supplementary instruments can be added in the inner component that can be developed allowing a refined measurement of vibration response.
- A common time invariant model based on proportional damping will be developed .

Conclusiones

Este capítulo se dedica a las conclusiones y los principales hallazgos, y finalmente se incluye la opinión del autor sobre el alcance de la investigación y las líneas futuras que quedan abiertas en esta área.

Estado de la tesis y principales conclusiones

En este trabajo de investigación se ha conseguido la caracterización dinámica de una transmisión de engranajes planetarios, en condiciones de operación estacionarias y no estacionarias, para casos sin y con defectos. Este trabajo de tesis también ha proporcionado un mejor conocimiento de los parámetros modales de los engranajes planetarios a través de la implementación y confrontación de diferentes técnicas de análisis modal en la identificación de estos parámetros, especialmente para diferentes condiciones de carga. Se ha investigado la influencia de la excitación externa que conduce a un funcionamiento en condiciones no estacionarias. La incorporación de la formulación del contacto no lineal en las funciones de rigidez de la malla, ha permitido el cálculo de la respuesta vibratoria teniendo en cuenta la formulación hertziana. Por otro lado, el comportamiento dinámico del sistema en presencia de un defecto único o combinado se destaca especialmente en condiciones no estacionarias. Los resultados se obtuvieron a través de la implementación de diferentes modelos dinámicos, que han sido validados mediante ensayos experimentales realizados en un banco de pruebas.

Los principales hallazgos logrados a lo largo de esta investigación se pueden resumir en los siguientes puntos:

- Se ha desarrollado un modelo tridimensional con parámetros concentrados del sistema de engranajes planetarios. Los resultados correspondientes se confrontaron con éxito con los resultados experimentales obtenidos en el banco de pruebas.
- Se han podido identificar las frecuencias naturales de los engranajes planetarios y las relaciones de amortiguamiento utilizando tres técnicas de análisis modal diferentes.
- La variación de la rigidez de engrane afecta a las propiedades modales del sistema.

- Las frecuencias naturales y la amortiguación modal dependen de las condiciones de carga aplicadas.
- El contacto hertziano no lineal tiene un efecto sobre el comportamiento dinámico del sistema en condiciones no estacionarias.
- El diagnóstico de defectos de dientes combinados, en condiciones no estacionarias, se ha realizado mediante un método de análisis de órdenes.

Conclusiones

A continuación se presentan las principales conclusiones obtenidas de este trabajo de investigación:

En un primer paso, se investigaron las técnicas de análisis modal EMA, OMA y OBMA y posteriormente se procedió a una comparación de las mismas. Se utilizó un LPM de la transmisión de engranajes para implementar estas tres técnicas numéricamente, conjuntamente con una investigación experimental sobre un banco de pruebas. Utilizando el diagrama de Estabilización y el criterio de garantía modal y basándose en las FRF, se realizó un análisis modal completo. Las frecuencias naturales, la amortiguación modal y las formas de los modos se identificaron y se correlacionaron con otras emitidas desde el LPM. Por lo tanto, según las funciones de CPSD y de orden, respectivamente, para los casos de OMA y OBMA, las frecuencias naturales y la relación de amortiguación se extrajeron numérica y experimentalmente. Sin embargo, la construcción de las formas de los modos en esos casos es difícil debido a la limitación de los instrumentos. Estas dos técnicas se aplican tanto cuando el sistema se acciona en régimen estacionario como cuando se hace en no estacionario (condiciones de funcionamiento hacia arriba o hacia abajo). Una comparación entre estas tres técnicas ha permitido concluir que la técnica OBMA está cerca de la EMA, pero es potente para aplicaciones prácticas de ingeniería, ya que permite el análisis modal incluso en condiciones no estacionarias. Para proporcionar una visión más detallada de OBMA, se ha resaltado el efecto del cambio de carga y la variación hacia arriba en la frecuencia de funcionamiento en la caracterización dinámica. Se han tratado cuatro condiciones de carga diferentes. Se ha demostrado que la amplitud de las fuerzas de engrane y el período de doble contacto de los dientes aumentan a medida que aumenta el nivel de par. También se ha encontrado que la inercia del anillo y el valor promedio de la función de rigidez de engrane cambian. Este comportamiento se ha notado en las tendencias de la rigidez de engrane.

Además, se ha observado un aumento en la amplitud de la vibración en el anillo de prueba, así como la densidad espectral asociada al primer armónico (GMF) que se mueve hacia el segundo armónico (GMF). Los resultados confirmaron el hecho de que cuando aumenta el par motor, aumenta la fuerza de contacto entre los dientes, lo que conduce a un aumento en los valores de la fuerza interna en el rodamiento y los dientes y una fluctuación del ángulo de presión y, por lo tanto, un aumento de la relación de contacto.

Para la estimación de los parámetros modales, la carga juega un importante papel y contribuye significativamente a su cambio. Con el aumento de la carga, cambian las frecuencias naturales y la amortiguación modal. Este hecho se explica por el aumento de la amplitud de la rigidez de engrane y el aumento de las fuerzas transmitidas a los dientes y rodamientos.

En un segundo paso, se llevaron a cabo unas series de simulaciones y experimentos en régimen estacionario y en condiciones de operación no estacionarias, tanto en casos sin como con defectos. De los resultados obtenidos se destaca lo siguiente:

- La respuesta dinámica del sistema para el caso de ausencia de defectos ha mostrado la presencia de modulación de amplitud en las señales de vibración, hecho que se explica por la fuerza de accionamiento inducida por la rotación del porta satélites, que está relacionada principalmente con la influencia del paso periódico de los planetas cerca de los sensores. La amplitud de la vibración aumenta cuando un planeta se acerca a la ubicación del sensor.
- El espectro de aceleración está dominado por la frecuencia de engrane y sus armónicos. Las bandas laterales se observan alrededor de estos componentes como consecuencia del fenómeno mencionado anteriormente.
- Se ha identificado la influencia del porta satélites en la respuesta vibratoria. De hecho, el efecto de la gravedad sobre el porta satélites crea una variación en la amplitud de la función de engrane que da lugar a bandas laterales en los espectros, espaciados por la frecuencia de rotación del porta satélites.
- Se han estudiado las condiciones no estacionarias que se presentan en casos como al acelerar el sistema, velocidad variable y condiciones de carga variables. Se observaron dos tipos de modulación. Una modulación en amplitud debido a la evolución de la frecuencia de rotación de los componentes de los porta satélites. Además, también se observa una modulación de frecuencia relacionada principalmente con la función de engrane, inducida por la variabilidad de la velocidad. Por ello, se realizó un análisis de Fourier de tiempo corto (STFT), tanto de forma experimental como numérica, con el fin de caracterizar el contenido en frecuencia e identificar la variación de velocidad. El STFT mostró líneas inclinadas correspondientes a la variación de la frecuencia de engrane.

- Se ha examinado la influencia de la rigidez de contacto hertziana no lineal entre los dientes en el comportamiento dinámico en condiciones de carga variable. La amplitud de la rigidez de engrane no es constante. De hecho, es sensible a la velocidad y la carga aplicada y que afectan a la respuesta vibratoria. También se ha investigado la sensibilidad de la fuerza dinámica y el error de transmisión a esos regímenes.

La parte final de esta tesis se ha dedicado al estudio del comportamiento dinámico del sistema de engranajes planetarios en presencia de defectos en los dientes, en regímenes estacionarios y no estacionarios. Los principales aspectos de este estudio son los siguientes:

- Una reducción en la función de engrane que respeta el período de rotación del componente considerado que indica la presencia de defectos en el diente dañado, ya sea en casos de defectos únicos o combinados.
- La presencia de defecto tiene un impacto en la respuesta en el tiempo y en los espectros, debido a un aumento de la amplitud de vibración. Esto se nota bien en la amplitud de la frecuencia de engrane y sus armónicos, así como en la presencia de bandas laterales que permiten la identificación de los componentes defectuosos.
- La carga aplicada externa tiene un impacto en la respuesta dinámica del sistema defectuoso. Con el aumento de la carga aumenta la amplitud de la vibración. Este fenómeno se nota tanto en el dominio de tiempo como en el de la frecuencia, relacionado principalmente con el aumento del área de contacto cuando se incrementa la carga del sistema.
- La identificación de los componentes defectuosos en condiciones no estacionarias utilizando la respuesta en el tiempo y la presentación STFT está limitada debido a la pequeña geometría del defecto introducido y al cambio de contenido en frecuencia a lo largo del tiempo.
- El método de análisis de órdenes podría ser la solución para la identificación de defectos en tales condiciones. Esto se ha demostrado para la detección de defectos simples o combinados en un régimen transitorio de aumento de la velocidad.

Este trabajo de investigación ha contribuido a la caracterización dinámica de un sistema de engranajes planetarios mediante la identificación de parámetros modales, siendo lo más destacado de la influencia en el comportamiento dinámico ante excitaciones internas y externas de esos sistemas. Además, ofrece herramientas para el diagnóstico de vibraciones que podrían usarse para el monitorizado en condición de máquinas que funcionan en condiciones no estacionarias con y sin defectos.

Trabajos futuros

Como perspectiva y trabajos futuros de esta tesis se pueden definir las siguientes tareas:

- Estudiar más tipos de defectos, ya sean en el diente o en la geometría, e implementarse numéricamente y en el banco de pruebas para investigar el comportamiento dinámico de estos sistemas en funcionamiento en régimen estacionario y no estacionario.
- Se pueden desarrollar técnicas de procesamiento de señales más potentes que permitan la identificación y la caracterización de estos defectos.
- A nivel experimental puede ser de interés incluir nuevos instrumentos suplementarios en el componente interno que permitan una medición refinada de la respuesta vibratoria.

Scientific Publications

As result of this work, two research articles are published and five conference papers are presented:

Articles

- Mbarek, A., Hammami, A., Del Rinçon, A. F., Chaari, F., Rueda, F. V., & Haddar, M. (2017). Effect of load and meshing stiffness variation on modal properties of planetary gear. *Applied Acoustics*.
- Mbarek, A., Del Rincon, A. F., Hammami, A., Iglesias, M., Chaari, F., Viadero, F., & Haddar, M. (2018). Comparison of experimental and operational modal analysis on a back to back planetary gear. *Mechanism and Machine Theory*, 124, 226-247.

International conferences papers

- Mbarek, A., Del Rincon, A. F., Hammami, A., Iglesias, M., Chaari, F., Rueda, F. V., & Haddar, M. (2018, March). Dynamic Behavior of Back to Back Planetary Gear in Presence of Pitting Defects. In *International Conference on Acoustics and Vibration*(pp. 16-22). Springer, Cham.
- Mbarek, A., Hammami, A., Del Rincon, A. F., Chaari, F., Rueda, F. V., & Haddar, M. (2017, March). Effect of Gravity of Carrier on the Dynamic Behavior of Planetary Gears. In *International Conference Design and Modelling of Mechanical Systems* (pp. 975-983). Springer, Cham.
- Mbarek, A., , Hammami, Del Rincon, A. F. A., Iglesias, M., Chaari, F., Rueda, F. V., & Haddar, M. (2018, December). Non linear dynamic behavior of planetary gear in run up regime in presence of spalling defect. In *International Conference On Advanced Materials, Mechanics and Manufacturing*.
- Mbarek, A., , Hammami, Del Rincon, A. F. A., Iglesias, M., Chaari, F., Rueda, F. V., & Haddar, M. (2017, June). Non linear dynamic behavior of planetary gear in run up regime. In *International Conference "Condition Monitoring of Machinery in Non-Stationary Operations" CMMNO'2018*. Springer, Cham.

National conferences papers

- Mbarek, A., , Hammami, Del Rinçon, A. F. A., Iglesias, M., Chaari, F., Rueda, F. V., & Haddar, M. (2018, October). Non linear dynamic behavior of planetary gear in run up regime in presence of crack defect. *congrès Tunisian de mécanique*.

References

- Abousleiman, V., & Velez, P. (2006). A hybrid 3D finite element/lumped parameter model for quasi-static and dynamic analyses of planetary/epicyclic gear sets. *Mechanism and Machine Theory*, 41(6), 725-748.
- Al-Shyyab, A., & Kahraman, A. (2007). A non-linear dynamic model for planetary gear sets. *Proceedings of the Institution of Mechanical Engineers, Part K: Journal of Multi-body Dynamics*, 221(4), 567-576.
- Ambarisha, V. K., & Parker, R. G. (2007). Nonlinear dynamics of planetary gears using analytical and finite element models. *Journal of sound and vibration*, 302(3), 577-595.
- Amezketta, M., Iriarte, X., Ros, J., & Pintor, J. M. (2009). Dynamic model of a helical gear pair with backlash and angle-varying mesh stiffness. *Multibody dynamics*, 1-17.
- Arfken, G. (1985). *Discrete Orthogonality--Discrete Fourier Transform*.
- (Botman, 1976) Botman M., *Epicyclic Gear Vibrations*, *Journal of Engineering for Industry*, vol. 96, 1976, p. 811-815.
- Bartelmus, W. (2001). Mathematical modelling and computer simulations as an aid to gearbox diagnostics. *Mechanical Systems and Signal Processing*, 15(5), 855-871.
- Bartelmus, W., & Zimroz, R. (2009). Vibration condition monitoring of planetary gearbox under varying external load. *Mechanical systems and signal processing*, 23(1), 246-257.
- Bartelmus, W., Chaari, F., Zimroz, R., & Haddar, M. (2010). Modelling of gearbox dynamics under time-varying nonstationary load for distributed fault detection and diagnosis. *European Journal of Mechanics-A/Solids*, 29(4), 637-646.
- Bigret, R., & Féron, J. L. (1995). *Diagnostic-maintenance disponibilité des machines tournantes: modeles-mesurages-analyses des vibrations*. Masson.
- Bigret, R., & Féron, J. L. (1995). *Diagnostic-maintenance disponibilité des machines tournantes: modeles-mesurages-analyses des vibrations*. Masson.
- Bu, Z., Liu, G., & Wu, L. (2012). Modal analyses of herringbone planetary gear train with journal bearings. *Mechanism and Machine Theory*, 54, 99-115.
- Chaari, F., Abbas, M. S., Rueda, F. V., del RINCON, A. F., & Haddar, M. (2013). Analysis of planetary gear transmission in non-stationary operations. *Frontiers of Mechanical Engineering*, 8(1), 88-94.
- Chaari, F., Baccar, W., Abbas, M. S., & Haddar, M. (2008). Effect of spalling or tooth breakage on gearmesh stiffness and dynamic response of a one-stage spur gear transmission. *European Journal of Mechanics-A/Solids*, 27(4), 691-705.
- Chaari, F., Bartelmus, W., Zimroz, R., Fakhfakh, T., & Haddar, M. (2012). Effect of load shape in cyclic load variation on dynamic behavior of spur gear system. In *Key Engineering Materials (Vol. 518, pp. 119-126)*. Trans Tech Publications.
- Chaari, F., Fakhfakh, T., & Haddar, M. (2006). Dynamic analysis of a planetary gear failure caused by tooth pitting and cracking. *Journal of Failure Analysis and Prevention*, 6(2), 73-78.
- Chaari, F., Fakhfakh, T., & Haddar, M. (2009). Analytical modelling of spur gear tooth crack and influence on gearmesh stiffness. *European Journal of Mechanics-A/Solids*, 28(3), 461-468.
- Chaari, F., Fakhfakh, T., Hbaieb, R., Louati, J., & Haddar, M. (2006). Influence of manufacturing errors on the dynamic behavior of planetary gears. *The International Journal of Advanced Manufacturing Technology*, 27(7-8), 738-746.
- Chaari, F., Zimroz, R., Bartelmus, W., Fakhfakh, T., & Haddar, M. (2011). Modeling of local damages in spur gears and effects on dynamics response in presence of varying load conditions. *Proceedings of Surveillance*, 6, 1-19.
- Cheng, Z., & Hu, N. (2012). Quantitative damage detection for planetary gear sets based on physical models.

Chinese Journal of Mechanical Engineering, 25(1), 190-196.

Cooley, C. G., & Parker, R. G. (2012). Vibration properties of high-speed planetary gears with gyroscopic effects. *Journal of vibration and acoustics*, 134(6), 061014.

Cooley, C. G., & Parker, R. G. (2012). Vibration properties of high-speed planetary gears with gyroscopic effects. *Journal of vibration and acoustics*, 134(6), 061014.

Corey, V. B. (1962). Measuring angular acceleration with linear accelerometers. *Control Engineering*, 9(3), 79-80.

Cunliffe, F., Smith, J. D., & Welbourn, D. B. (1974). Dynamic tooth loads in epicyclic gears. *Journal of Engineering for Industry*, 96(2), 578-584.

Del Rincon, A. F., Viadero, F., Iglesias, M., García, P., De-Juan, A., & Sancibrian, R. (2013). A model for the study of meshing stiffness in spur gear transmissions. *Mechanism and Machine Theory*, 61, 30-58.

Dhatt, G., & Touzot, G. (1981). *Une présentation de la méthode des éléments finis*. Presses Université Laval.

El Badaoui, M. (1999). Contribution au Diagnostic Vibratoire des Réducteurs Complexes à Engrenages par l'Analyse Cepstrale (Doctoral dissertation, Université Jean Monnet-Saint-Etienne).

Ericson, T. M., & Parker, R. G. (2013). Planetary gear modal vibration experiments and correlation against lumped-parameter and finite element models. *Journal of sound and vibration*, 332(9), 2350-2375.

Ericson, T. M., & Parker, R. G. (2014). Experimental measurement of the effects of torque on the dynamic behavior and system parameters of planetary gears. *Mechanism and Machine Theory*, 74, 370-389.

Eritenel, T., & Parker, R. G. (2009). Modal properties of three-dimensional helical planetary gears. *Journal of Sound and Vibration*, 325(1-2), 397-420.

Faik, S., & Witteman, H. (2000, June). Modeling of impact dynamics: A literature survey. In 2000 International ADAMS User Conference (Vol. 80).

Feese, T., & Hill, C. (2002, October). Guidelines for preventing torsional vibration problems in reciprocating machinery. In Gas Machinery Conference, Nashville, TN, Oct (pp. 7-9).

Flandrin, P. (1998). Temps-fréquence.(2eme édition, revue et corrigée) Editions Hermes.

Fyfe, K. R., & Munck, E. D. S. (1997). Analysis of computed order tracking. *Mechanical Systems and Signal Processing*, 11(2), 187-205.

Gu, X. Y., & Velez, P. (2011). A lumped parameter model to analyse the dynamic load sharing in planetary gears with planet errors. In *Applied Mechanics and Materials* (Vol. 86, pp. 374-379). Trans Tech Publications.

Gu, X., & Velez, P. (2013). On the dynamic simulation of eccentricity errors in planetary gears. *Mechanism and Machine Theory*, 61, 14-29.

Guo, Y., & Parker, R. G. (2010). Purely rotational model and vibration modes of compound planetary gears. *Mechanism and Machine Theory*, 45(3), 365-377.

Guo, Y., & Parker, R. G. (2010). Purely rotational model and vibration modes of compound planetary gears. *Mechanism and Machine Theory*, 45(3), 365-377.

Guo, Y., & Parker, R. G. (2012). Stiffness matrix calculation of rolling element bearings using a finite element/contact mechanics model. *Mechanism and machine theory*, 51, 32-45.

Guo, Y., Keller, J., & LaCava, W. (2012). Combined effects of gravity, bending moment, bearing clearance, and input torque on wind turbine planetary gear load sharing (No. NREL/CP-5000-55968). National Renewable Energy Lab.(NREL), Golden, CO (United States).

- Hammami, A., Del Rincon, A. F., Chaari, F., Santamaria, M. I., Rueda, F. V., & Haddar, M. (2016). Effects of variable loading conditions on the dynamic behaviour of planetary gear with power recirculation. *Measurement*, 94, 306-315.
- Hammami, A., Del Rincon, A. F., Rueda, F. V., Chaari, F., & Haddar, M. (2015). Modal analysis of back-to-back planetary gear: experiments and correlation against lumped-parameter model. *Journal of theoretical and applied mechanics*, 53(1), 125-138.
- Harsha, S. P. (2006). Nonlinear dynamic analysis of a high-speed rotor supported by rolling element bearings. *Journal of Sound and Vibration*, 290(1-2), 65-100.
- Henriot G., *Traité théorique et pratique des engrenages*, tome 1 et 2. Edition Dunod technique, 1985.
- Huang, N. E., Shen, Z., Long, S. R., Wu, M. C., Shih, H. H., Zheng, Q., ... & Liu, H. H. (1998). The empirical mode decomposition and the Hilbert spectrum for nonlinear and non-stationary time series analysis. *Proceedings of the Royal Society of London. Series A: Mathematical, Physical and Engineering Sciences*, 454(1971), 903-995.
- Inalpolat, M., & Kahraman, A. (2009). A theoretical and experimental investigation of modulation sidebands of planetary gear sets. *Journal of sound and vibration*, 323(3-5), 677-696.
- Kahraman, A. (1994). Planetary gear train dynamics. *Journal of Mechanical design*, 116(3), 713-720.
- Kahraman, A. (2001). Free torsional vibration characteristics of compound planetary gear sets. *Mechanism and machine theory*, 36(8), 953-971.
- Kahraman, A., & Blankenship, G. W. (1997). Experiments on nonlinear dynamic behavior of an oscillator with clearance and periodically time-varying parameters. *Journal of Applied Mechanics*, 64(1), 217-226.
- Karray, M., Feki, N., Khabou, M. T., Chaari, F., & Haddar, M. (2017). Modal analysis of gearbox transmission system in Bucket wheel excavator. *Journal of Theoretical and Applied Mechanics*, 55(1), 253-264.
- Kasuba, R., & August, R. (1986). Torsional vibrations and dynamic loads in a basic planetary gear system. *ASME J. Vib., Acoust., Stress, Reliab. Des*, 108, 348-353.
- Khabou, M. T., Bouchaala, N., Chaari, F., Fakhfakh, T., & Haddar, M. (2011). Study of a spur gear dynamic behavior in transient regime. *Mechanical Systems and Signal Processing*, 25(8), 3089-3101.
- Kiracofe, D. R., & Parker, R. G. (2007). Structured vibration modes of general compound planetary gear systems. *Journal of Vibration and Acoustics*, 129(1), 1-16.
- Lewicki, D. G. (2002). Gear Crack Propagation Path Studies-Guidelines for Ultra-Safe Design. *Journal of the American Helicopter Society*, 47(1), 64-72.
- Li, S. (2015). Effects of misalignment error, tooth modifications and transmitted torque on tooth engagements of a pair of spur gears. *Mechanism and Machine Theory*, 83, 125-136.
- Li, S., & Kahraman, A. (2011). A spur gear mesh interface damping model based on elastohydrodynamic contact behaviour. *International Journal of Powertrains*, 1(1), 4-21.
- Li, Z., Jiang, Y., Hu, C., & Peng, Z. (2016). Recent progress on decoupling diagnosis of hybrid failures in gear transmission systems using vibration sensor signal: A review. *Measurement*, 90, 4-19.
- Liang, X., Zhang, H., Liu, L., & Zuo, M. J. (2016). The influence of tooth pitting on the mesh stiffness of a pair of external spur gears. *Mechanism and Machine Theory*, 106, 1-15.
- Liang, X., Zuo, M. J., & Hoseini, M. R. (2015). Vibration signal modeling of a planetary gear set for tooth crack detection. *Engineering Failure Analysis*, 48, 185-200.
- Liang, X., Zuo, M. J., & Liu, L. (2016). A windowing and mapping strategy for gear tooth fault detection of a

planetary gearbox. *Mechanical Systems and Signal Processing*, 80, 445-459.

Lin, J., & Parker, R. G. (1999). Analytical characterization of the unique properties of planetary gear free vibration. *Journal of vibration and acoustics*, 121(3), 316-321.

Lin, J., & Parker, R. G. (2000). Parametric instabilities in planetary gears under mesh stiffness variations. *Journal of Vibration and Acoustics*, in preparation.

Lin, J., & Parker, R. G. (2002). Mesh stiffness variation instabilities in two-stage gear systems. *Journal of vibration and acoustics*, 124(1), 68-76.

Ma, H., Li, Z., Feng, M., Feng, R., & Wen, B. (2016). Time-varying mesh stiffness calculation of spur gears with spalling defect. *Engineering Failure Analysis*, 66, 166-176.

Ma, H., Song, R., Pang, X., & Wen, B. (2014). Time-varying mesh stiffness calculation of cracked spur gears. *Engineering Failure Analysis*, 44, 179-194.

Ma, R., & Chen, Y. (2012). Research on the dynamic mechanism of the gear system with local crack and spalling failure. *Engineering Failure Analysis*, 26, 12-20.

Maatar, M. (1995). Contribution a l'analyse du comportement dynamique de reducteurs a engrenages avec ecarts de forme et défauts de montage (Doctoral dissertation, These de Doctoral. INS A Lyon).

Maatar, M. (1997). Contribution a l'analyse du comportement dynamique de reducteurs a engrenages simple etage. Influence des ecarts de forme et des défauts de montage.

McFadden, P. D., & Smith, J. D. (1985). The vibration produced by multiple point defects in a rolling element bearing. *Journal of sound and vibration*, 98(2), 263-273.

Meirovitch, L. (1974). A new method of solution of the eigenvalue problem for gyroscopic systems. *AiAA Journal*, 12(10), 1337-1342.

Miller, A. J. (1999). A new wavelet basis for the decomposition of gear motion error signals and its application to gearbox diagnostics (Doctoral dissertation, Pennsylvania State University).

Mitchell, T. M. (1982). Generalization as search. *Artificial intelligence*, 18(2), 203-226.

Orlowitz, E., & Brandt, A. (2013). Influence of correlation estimation methods on damping estimates. In 5th International Operational Modal Analysis Conference (IOMAC), Guimarães, Portugal, May 13–15, 2013.

Orlowitz, E., & Brandt, A. (2017). Comparison of experimental and operational modal analysis on a laboratory test plate. *Measurement*, 102, 121-130.

Özgiiven, H. N., & Houser, D. R. (1988). Mathematical models used in gear dynamics—a review. *Journal of sound and vibration*, 121(3), 383-411.

Parker, R. G., & Lin, J. (2003, January). Mesh phasing relationships in planetary and epicyclic gears. In ASME 2003 international design engineering technical conferences and computers and information in engineering conference (pp. 525-534). American Society of Mechanical Engineers.

Pastor, M., Binda, M., & Harčarik, T. (2012). Modal assurance criterion. *Procedia Engineering*, 48, 543-548.

Qiu, X., Han, Q., & Chu, F. (2015). Load-sharing characteristics of planetary gear transmission in horizontal axis wind turbines. *Mechanism and Machine Theory*, 92, 391-406.

Randall, R. B. (1982). Cepstrum analysis and gearbox fault-diagnosis. *Maintenance Management International*, 3(3), 183-208.

Randall, R. B. (2011). *Vibration-based condition monitoring: industrial, aerospace and automotive applications*.

John Wiley & Sons.

Randall, R. B. (2017). A history of cepstrum analysis and its application to mechanical problems. *Mechanical Systems and Signal Processing*, 97, 3-19.

Rayleigh, J. W. S. B. (1899). *Scientific papers* (Vol. 1). University Press.

Royston, T. J., & Basdogan, I. (1998). Vibration transmission through self-aligning (spherical) rolling element bearings: theory and experiment. *Journal of Sound and Vibration*, 215(5), 997-1014.

Sainsot, P., Velex, P., & Duverger, O. (2004). Contribution of gear body to tooth deflections-a new bidimensional analytical formula. *Transactions-American Society of Mechanical Engineers Journal of Mechanical Design*, 126(4), 748-752.

Saxena, A., Parey, A., & Chouksey, M. (2016). Time varying mesh stiffness calculation of spur gear pair considering sliding friction and spalling defects. *Engineering Failure Analysis*, 70, 200-211.

Saxena, A., Wu, B., & Vachtsevanos, G. (2005, June). A methodology for analyzing vibration data from planetary gear systems using complex Morlet wavelets. In *Proceedings of the 2005, American Control Conference, 2005*. (pp. 4730-4735). IEEE.

Shin, Y. S., & Jeon, J. J. (1993). Pseudo Wigner-Ville time-frequency distribution and its application to machinery condition monitoring. *Shock and Vibration*, 1(1), 65-76.

Syngé, J. L. (1955). NI Muskhelishvili, Some basic problems of the mathematical theory of elasticity. *Bulletin of the American Mathematical Society*, 61(5), 445-447.

Timoshenko, S., & Baud, R. V. (1926). Strength of gear teeth. *Mechanical Engineering*, 48(11), 1105-1109.

Velex, P. (1988). *Contribution a l'analyse du comportement dynamique de reducteur a engrenages a axes paralleles* (Doctoral dissertation, Lyon, INSA).

Viadero, F., Fernández, A., Iglesias, M., De-Juan, A., Liaño, E., & Serna, M. A. (2014). Non-stationary dynamic analysis of a wind turbine power drivetrain: Offshore considerations. *Applied Acoustics*, 77, 204-211.

Villa, L. F., Reñones, A., Peran, J. R., & de Miguel, L. J. (2012). Statistical fault diagnosis based on vibration analysis for gear test-bench under non-stationary conditions of speed and load. *Mechanical Systems and Signal Processing*, 29, 436-446.

Weber, C., & Banaschek, K. (1949). *The Deformation of Loaded Gears and the Effect on Their Load Carrying Capacity (Part I)*. DSIR, London.

Wu, T. Y., Chen, J. C., & Wang, C. C. (2012). Characterization of gear faults in variable rotating speed using Hilbert-Huang Transform and instantaneous dimensionless frequency normalization. *Mechanical Systems and Signal Processing*, 30, 103-122.

Wu, X., & Parker, R. G. (2008). Modal properties of planetary gears with an elastic continuum ring gear. *Journal of Applied Mechanics*, 75(3), 031014.

Yannick S., *l'entretènement des ponts mixtes multi poutres ferroviaires*, thèse, INSA de Lyon, 2004.

Zimroz, R., Urbanek, J., Barszcz, T., Bartelmus, W., Millioz, F., & Martin, N. (2011). Measurement of instantaneous shaft speed by advanced vibration signal processing-application to wind turbine gearbox. *Metrology and Measurement Systems*, 18(4), 701-712.

Contribution to the study of the dynamic behaviour of planetary gears in non-stationary regimes in presence of defects

Ayoub MBAREK

Résumé : Ce travail de thèse porte sur l'analyse du comportement dynamique des transmissions à engrenages planétaires dans des conditions non stationnaires en présence de défauts. La stratégie de cette thèse est basée sur la construction d'un modèle numérique qui est référé à un banc d'essai composé d'un train planétaire d'essai monté dos à dos avec un train d'entraînement à réaction qui permet la recirculation de la puissance.

Tout d'abord, des techniques d'analyse modale ont été étudiées pour caractériser le comportement dynamique du système. Une étude comparative entre trois techniques d'analyse modale a été réalisée afin de déterminer les propriétés modales dans différentes conditions de fonctionnement. Le diagramme de stabilisation et le critère d'assurance modale ont été utilisés pour estimer les modes obtenus. Les modes expérimentaux et numériques de chaque technique ont été comparés et discutés. De plus, l'effet de la variation de charge et de la rigidité d'engrènement sur les paramètres modaux a été mis en évidence.

L'étude du comportement dynamique du modèle correspondant au banc d'essai a été réalisée initialement dans des conditions stationnaires où la vitesse et le couple sont constants. Les bandes latérales de modulation sont mises en évidence par des simulations numériques issues d'un modèle tridimensionnel et de mesures expérimentales. L'influence de la gravité du porteur sur la réponse dynamique a également été étudiée en tenant compte de l'interaction entre les engrenages en prise, le poids des systèmes de porte-satellites. Ensuite, le comportement dynamique sous des excitations non stationnaires telles que les régimes de charge variable, de vitesse variable et de montée en régime a été étudié. L'analyse temps-fréquence a été développée pour caractériser la fréquence des signaux de vibration issus de conditions de fonctionnement non stationnaires. Les résultats numériques obtenus par la transformée de Fourier en temps court sont validés par des mesures de vibrations effectuées sur un banc d'essai pendant le fonctionnement dans ces conditions. Cependant, un modèle non linéaire du modèle prenant en compte la rigidité hertzienne a été développée et étudié en régime non stationnaire présenté par la charge variable et le régime de montée en régime.

Enfin, la réponse dynamique du système en présence de deux types de défauts a été analysée et discutée dans les régimes stationnaires et non stationnaires. Une méthode de suivi des commandes a été utilisée pour identifier les défauts de démarrage et les conditions de charge variables pour les signaux simulés et déterminés expérimentalement.

Abstract: The present PhD study is focused on analyzing the dynamic behavior of planetary gear transmissions in non-stationary conditions in presence of defects. The strategy of this thesis is based on building a numerical model which is referred to a test bench composed of a test planetary gear set mounted back to back with reaction gear set which allow the power recirculation.

First of all, modal analysis techniques were studied to characterize the dynamic behavior of the system. a comparative study between three modal analysis techniques was carried out in order to determine the modal properties in different running condition. Stabilization diagram and Modal assurance criterion were used to estimate the obtained modes. Experimental and numerical modes of each technique were compared and discussed. In addition, the effect of load and meshing stiffness variation on the modal parameters were highlighted.

The study of the dynamic behavior of the model corresponding to the test bench was performed initially in stationary conditions where the speed and the torque are constant. Modulation sidebands are highlighted through numerical simulations issued from a three-dimensional model and experimental measurements. Influence of the gravity of carrier on the dynamic response were also investigated taking into account the interaction between meshing gears, the weight of the planet carrier systems. Then, the dynamic behavior under non-stationary excitations such as the variable load, variable speed and run up regimes was investigated. Time frequency analysis was developed to characterize frequency of vibration signals issued from non-stationary operating conditions. Numerical results obtained by the Short Time Fourier Transform are validated through vibration measurements on test bench during operation under these conditions. However, a non linear model of the model taking into account the Hertzian stiffness was developed and studied in non stationary regime presented by the variable load and run up regime.

Finally, the dynamic response of the system in presence of two kinds of defect was analyzed and discussed in stationary and non stationary regimes. Order tracking method was used to identify the defects in run up and variable loading condition for the simulated and experimental determined signals.

Mots clés: engrenage planétaire, regime non stationnaire, défaut, analyse modale, dynamique, essai expérimentaux, modèle numérique

Key-word: planetary gear, non stationary regimes ,defect ,modal analysis ,dynamic, experimental test, numerical model